Time-Dependent Atomistic View on the Electronic Relaxations in Light-Harvesting Systems

by

Carsten Olbrich

A thesis submitted in partial fulfilment
of the requirements for the degree of

Doctor of Philosophy in Physics

Thesis Committee:

Prof. Dr. Ulrich Kleinekathöfer   (Jacobs University Bremen, Germany)

Prof. Dr. Jürgen Fritz   (Jacobs University Bremen, Germany)

Prof. Dr. Thomas Frauenheim   (Universität Bremen, Germany)

Date of Defense: 13 September 2011

Jacobs University Bremen   School of Engineering and Science

Acknowledgment

Abstract

Photosynthesis is certainly one of the most important processes of energy conversion on earth. Plants, algae and some type of bacteria harvest the light energy and convert it into chemical energy. Subsequent to the initial absorption of light, which induces an excitation in a pigment molecule, the absorbed energy is transferred to the so-called reaction center (RC) and induces a charge separation and finally a synthesis of ATP. The transport of the absorbed light energy to the RC happen with almost 100 % quantum efficiency. To this end, certain quantum effects seem to play an important role but are not yet completely understood, for example the recently experimentally observed long-lived quantum coherences in the energy transport. The availability of high-resolution X-ray crystal structures of pigment-protein complexes provides the opportunity to investigate the excitation energy transfer and the related quantum effects on the atomic level. To that purpose, this thesis comprises a multi-scale approach using classical molecular dynamics simulations with subsequently applied electronic structure calculations to compute optical properties and excited state dynamics of light-harvesting (LH) systems without additional parameters. This multi-scale approach was applied to two LH systems: the LH2 complex of a purple bacterium and the FMO complex of a green-sulfur bacterium. Consecutive excitation energies for the individual pigments and the electronic couplings between the pigments were obtained for each of the two complexes. These quantities were combined to a time-dependent Hamiltonians which were subsequently used to calculate optical properties and excitation energy transfer dynamics. Based on the fluctuations of the excited state energies, spectral densities were obtained which serve as necessary input quantities in dissipative quantum dynamics calculations. Additionally, spatial correlations of excitation energies, couplings and atomic motions were determined. Such correlations have been proposed as possible origin of the long-lived quantum coherences in the energy transport but found to be very small.

Contents

1. Introduction

The elementary process of photosynthesis, that is, the conversion of light energy into chemical energy in form of adenosine triphosphate (ATP), evolved already about 3.5 billion years ago [1]. At first there were photosynthetic organisms which operated the so-called anoxygenic photosynthesis, i.e., a photosynthetic process without the production of oxygen. Hereby, the captured light energy is used to oxidize inorganic compounds, like hydrogen sulfide, sulfur compounds, hydrogen or ferrous iron [2]. Anoxygenic green and purple bacteria often live under extreme conditions with low-light environments, such as at the ground of the Pacific ocean next to hot springs and at depths of more than 3000 m. The process of oxygenic photosynthesis has been evolved about one billion years later than that of the anaerobic photosynthesis [3]. In contrast to anoxygenic photosynthetic organisms, oxygenic organisms, i.e., plants and cyanobacteria use water as the electron donor. The general reaction equation reads therefore

$$n\,CO_2 + 2n\,H_2X \xrightarrow{\text{light energy}} (CH_2O)_n + 2n\,X\ + n\,H_2O \qquad (1.1)$$
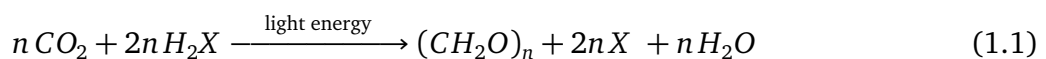
with H_2X representing the reducing agents like H_2O, H_2S, or H_2, and CH_2O symbolizes the biomass, like carbonhydrates [1].

In both, oxygenic and anoxygenic photosynthesis, the initial step consists of the absorption of light energy. This is achieved by pigment molecules. In plants and cyanobacteria, mainly chlorophyll (Chl) is employed to capture the light. Within anaerobic bacteria, a structurally similar pigment molecule, bacteriochlorophyll (BChl) is utilized. The pigments are arranged within proteins, the so-called light-harvesting (LH) complexes. These pigment-protein complexes are either embedded into the photosynthetic membrane or associated with it [4–7]. Some of the LH com-

plexes contain a so-called reaction center[1] (RC) to which the absorbed light energy is transferred. There, the absorbed energy induces a charge separation, i.e., one of the above mentioned electron donors is oxidized, and initiates a cascade of steps towards the production of ATP and finally of biomass.

Efficient production of enough "green" energy, i.e., without using fossil raw materials, is one of the biggest challenges these days (cf. Fig. 1.1). The photosynthesis in oxygenic and anoxygenic organism operate with nearly 100 % quantum efficiency, that is, almost each captured photon is engaged

Figure 1.1.: *Solar thermal field* (picture adopted from [8]).

in the process of energy conversion [4]. Such high efficiency in energy migration could not be achieved by man-made assemblies of pigments so far. During the last two billion years these fascinating and optimized LH complexes has been generated by evolution. More recently, quantum coherence phenomena in the energy transport across different LH systems were observed which are supposed to facilitate the energy transport [9–12]. So far, this quantum effect, especially at the molecular level, is not completely understood and introduced the new research field of "quantum biology" [13, 14]. A big step towards understanding the structure-function relations was achieved by resolving the X-ray crystal structure of the LH complexes. The first structure of a pigment-protein complex was resolved by Fenna and Matthews in 1975 [15]. In 1984 the arrangement of pigments and proteins of the RC belonging to the purple bacteria *Rhodopseudomonas viridis* became available [16, 17]. For this achievement Deisenhofer, Huber and Michel were honored with the Nobel Prize in 1988. The three-dimensional X-ray structures enable detailed modeling and calculation of intrinsic properties to gain insight into the structure-function relation and a better interpretation of experimental measured data of LH complexes. The main aim of the present thesis is a parameter-free description of optical properties and excited state dynamics of LH systems based on a multi-scale approach using classical MD with subsequently applied electronic structure calculations. Understanding the evolved mechanisms of the optimized biological LH complexes might create new ideas about the construction of artificial LH systems.

---

[1]Aerobic organisms contain two of types LH complexes including the RC, the photosystem (PS) I and II. The RC containing complex in purple bacteria is called LH1.

2. Photosynthesis at the Nanometer Scale

Efficient harvesting of light energy is a crucial process for plants and some types of bacteria to supply their cells with chemical energy in the form of ATP. Evolution has formed a large variety of pigment–protein complexes due to possible light limitations and stress conditions. Fig. 2.1 shows a collection of some LH complexes of plants and bacteria. Most LH complexes are embedded in a photosynthetic membrane[1] and are surrounded by others, like the LH1 and LH2 complexes of purple bacteria [4–7, 18, 19], the LH complexes (LHC) I and II of plants, and the photosystems (PS) I and II in plants, algae and cyanobacteria [4, 20–22]. Some complexes, e.g., the Fenna–Matthews–Olsen (FMO) complex [15, 23] and phycobilisomes [24], are water soluble and are attached to a LH complex which is embedded in the membrane.

The light is absorbed by pigment molecules like the well known chlorophyll molecules which are mostly embedded in a protein environment. The absorption of a photon of appropriate energy induces an excitation in one pigment. This excitation energy delocalizes and spreads over several pigments due to electronic couplings between the pigments. As a consequence the energy is transferred on the pigments within the complex and further to pigments of neighboring LH complexes until it reaches the reaction center (RC). There the excitation induces a charge separation which finally leads to a proton gradient across the membrane. This gradient drives the synthesis of ADP to ATP, which is the "fuel of the cells". The single steps of energy conversion are sketched in Fig. 2.2, for simplicity, on the example of a photosynthetic membrane of purple bacteria. The main principle of the LH process

---

[1]In the case of plants and cyanobacteria the LH complexes can be found in the thylakoid membrane. The LH complexes of purple bacteria are located in the cytoplasmic membrane.
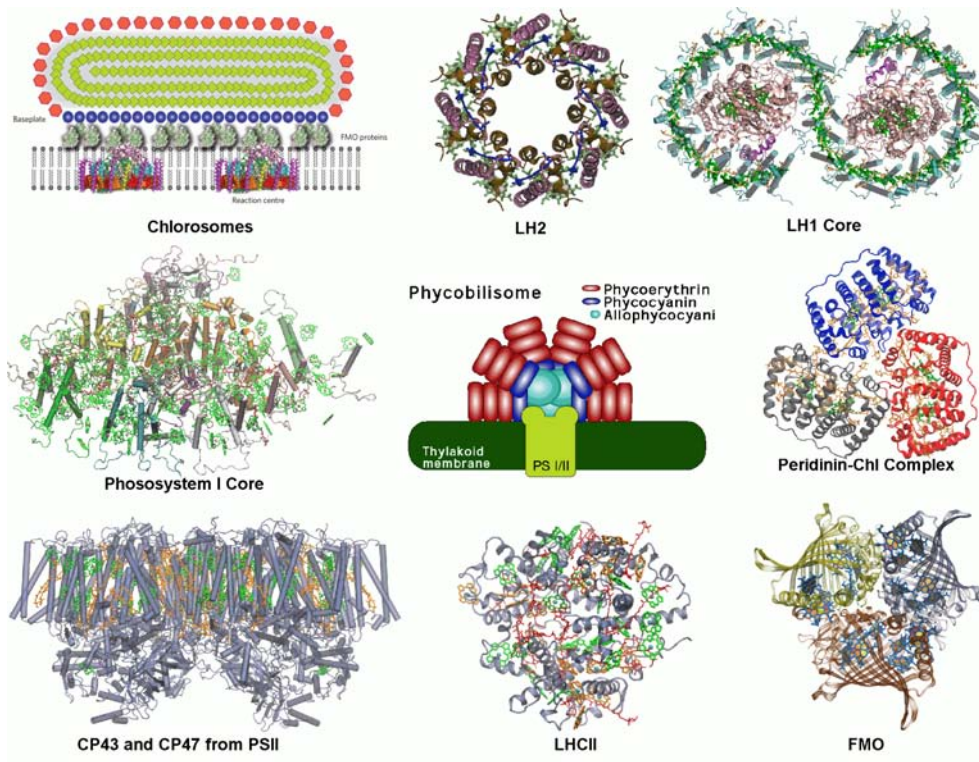
Figure 2.1.: Collection of various LH systems from plants as well as from bacteria. (Sketch of the chlorosome is adopted with permissions from [25].)
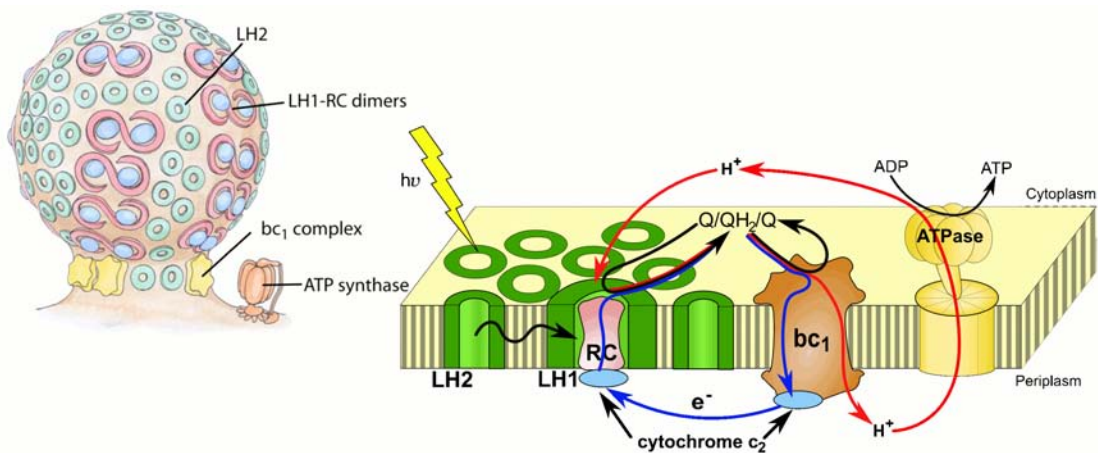
Figure 2.2.: Sketch of a photosynthetic membrane of purple bacteria *Rhodobacter sphaeroides*[2]. The arrangement of the LH2 and LH1 complexes with the RC is shown on left. The lower part shows the single steps of energy conversion from light absorption over transfer of excitation energy to the RC including charge separation and inducing the proton gradient. The latter one drives the ATPase which transforms ADP to ATP and stores the original light energy in form of chemical energy. (Sketch of the vesical is adopted with permissions from [26].)

of plants, cyanobacteria and green-sulfur bacteria is the same as for purple bacteria. However, different kinds of LH systems and other types of proteins complexes are involved in the different LH organisms. The RCs act like sinks for the excitation. In that way the excitation energy is channeled energetically down to the lowest absorption energy [27]. Thereby the excitation can be shared by a number of pigments, i.e., the ratio between the individual transition energy of the pigments and the electronic coupling between them causes the excitation energy either to be localized at one or spread over several pigments [18].

The aforementioned first revelation of the crystal structure of a pigment-protein complex by Fenna and Matthews, the structure of the Fenna-Matthews-Olsen (FMO) complex [15] of green–sulfur bacteria, in 1975 was an important step towards the understanding of relations between structure and function of LH complexes. Some years later the first structure of a RC became available [16]. Since that a large number of various structures of different organisms have been resolved, e.g., [21, 22, 28–33]. These "frozen" structures of atomic resolution, which are not necessarily equilibrium structures, opened the gate for modeling the energy transfer within and between such LH complexes. There has been a lot of research combining theoretical approaches using parameters fitted to experimentally obtained data. However, it is still challenging starting from the crystal structure of a LH complex and obtaining a trajectory of consecutive structures, which enables the calculation of time-dependent excitation energies of the pigments and furthermore the dynamical as well as optical properties. This complex of problems will be investigated in the present thesis.

In the following sections the basic components of LH complexes are briefly described. Furthermore, the LH2 as well as the FMO complex, which are the two investigated LH complexes in the present thesis, are characterized in more detail. The main concepts and methods, which were applied to gain insight into the electronic relaxation in the LH2 complex (see publications in the chapter 5) and the FMO complex (see publications in the chapter 6), are described in the chapter 3. Chapter 4 gives a summary of the obtained results and the resulting publications in the chapters 5 and 6.

---

[2]The photosynthetic membrane of other bacteria than *Rhodobacter sphaeroides* are commonly stacks of flat lamellar folds.
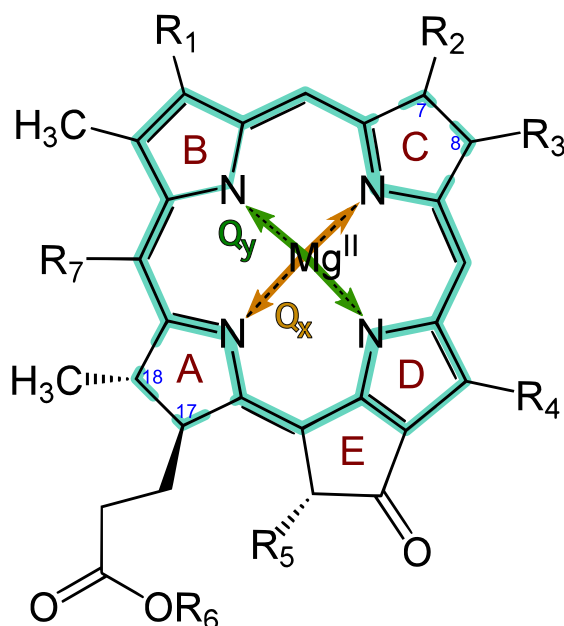
Figure 2.3.: Structure of (bacterio-)chlorophylls. The various types of (bacterio-)chlorophylls differ in the side chains R_1-R_7. The light blue lines indicate the delocalized π electron system. Only BChl$a$ and BChl$b$ have a single bond between the seventh and eighth carbon and Chl$c$ a double bond between 17th and 18th carbon. The green and orange arrows sketch the directions of the TDMs of the Q_y and Q_x excited states, respectively.

2.1. Pigments

The initial step in photosynthesis is the absorption of solar energy by pigment molecules. Although the different classes of photosynthetic pigments vary in their overall structure, they share the common property of a conjugated π electron system. It is formed by compounds with alternating single and double bonds which result in a overlap of p orbitals[3], bridging the interjacent single bonds. This allows a delocalization of the π electrons. The excitation of such π electrons to the π^* state is one of the important transitions, the so-called $\pi \rightarrow \pi^*$ transition, in photosynthetic pigments.

The most important types of pigments in photosynthesis are chlorophyll a (Chl$a$) molecules, which can be found in green plants, aerobic algae, as well as cyanobacteria. Furthermore, bacteriochlorophyll a (BChl$a$) molecules are present in anaerobic bacteria like green and purple bacteria. The complete configuration and structure of chlorophyll was resolved by Fleming in 1967 [34]. During the evolution, differ-

---

[3]In heavier atoms d orbitals can be involved as well.

ent subclasses of (B)Chls have been developed: Chl a, b, c_1, c_2, d, f and BChl $a, b,$ c, c_s, d, e, g. The general structure for Chl and BChl is quite similar and shown in Fig. 2.3. The differences of the various subclasses of Chls and BChls are in the side chains R_1-R_7. In case of BChl$a$, which occurs in all LH complexes investigated in the present work, the side chains are R_1: –CO–CH$_3$, R_2: –CH$_3$, R_3: –CH$_2$CH$_3$, R_4: –CH$_3$, R_5: –CO–O–CH$_3$, R_6: –phytyl, and R_7: –H.

The absorption wavelengths of Chl and BChl are in the range of 700-900 nm and around 400 nm. The specific values depend on the subclass of Chl or BChl, and the organism or solvent [35, 36]. The absorption at 700-900 nm is predominated by the conjugated π–electron system (see Fig. 2.3, light blue lines). There are two main absorbing states, called Q_x and Q_y. The latter one is characterized by a transition dipole moment (TDM) along the y axis, which is aligned to the connection between the opposite pyrrol rings B and D (cf. Fig. 2.3). The Q_x state has a TDM perpendicular to the one of the Q_y state along the x axis between the pyrrol rings A and C. The Q_y state is energetically the lowest and all higher states will quickly relax into it. Hence, it is the most important donor state for the excitation transfer.

Beside Chls and BChls, most LH complexes contain carotenoids, which are basically a chain of alternating single and double bonds, i.e., there exists a conjugated π electron system. Some carotenoids are terminated by rings as in the case of β–carotene. The lengths of the conjugated π electron systems determine the absorption properties [37]. In general, carotenoids mainly absorb in the wavelength range of 400-500 nm. Additionally, carotenoids act as photochemical quencher, i.e., they prevent the formation of destructive singlet oxygen [38, 39].

A further kind of pigments are bilins [40–42] of which a large variety exist. However, in general, bilins consist of a linear arrangement of four pyrrol rings and can be found in the water soluble phycobiliproteins of so-called cryptophytes, cyanobacteria, and red algae. Bilins enhance the amount and the spectral window of light absorption due to their absorption within 400 and 600 nm.

2.2. Protein Environment

Proteins are fundamental components of cells. The genetic code defines the sequence of amino acids which defines the structure and function of the particular protein. LH complexes are formed by the composition of specific proteins and pigments (cf. Fig. 2.1). The RCs together with the associated LH complexes are called photosynthetic units (PSU). The orientations and positions of the pigments relative to each other as determined by the protein matrix, which is often called scaffold, strongly influence the spectral properties of the PSU as a whole For example, in the case of BChl$a$, the central Mg^{2+} ion is five coordinate[4] and can link to different ligands, like histidine, aspartate and water [28, 43, 44]. The ligands can cause small shifts in the Q_y absorption [45]. Furthermore, a polar environment and especially close-by charged amino acids can induce shifts of the absorption. The direction of the shift depends on the sign of the surrounding charges [46–48]. Moreover, due to protein side chains, the pigment can be forced to get slightly distorted [44] which also shifts the position of the Q_y absorption line [49]. Additionally, the torsion angle of certain side groups of, e.g., BChl$a$, can induce a shift of up to 30 nm in the position of the absorption [18, 50]. Related to this, in the LH2 complex a loss of hydrogen bonds, which might have stabilized the orientation of the side group, reduces the position of the Q_y state from 850 nm to 820 nm [18, 45]. If the pigments are closely packed, i.e., strongly coupled like in the LH2 complex, the individual absorbing states, the so-called site energies, mix and form delocalized excitonic states over the coupled pigments. This mixing leads to a red shift in the absorption energies of the excitonic states compared to the site energies [18, 45, 51].

The chapters 5 and 6 focus on the LH2 and the FMO complexes. To this end, those two complexes are described in more detail in the following two subsections.

2.2.1. The Light-Harvesting Complex 2 of Purple Bacteria

The LH2 complex is part of the PSU of purple bacteria, like *Rhodospirillum (Rs.) molischianum* [28] and *Rhodopseudomonas (Rps.) acidophila* [52]. The overall structure of the different LH2 complexes is very similar and the structure of both

---

[4]The Mg^{2+} ion is already linked to the four nitrogen atoms in (B)Chl molecules (cf. Fig. 2.3).
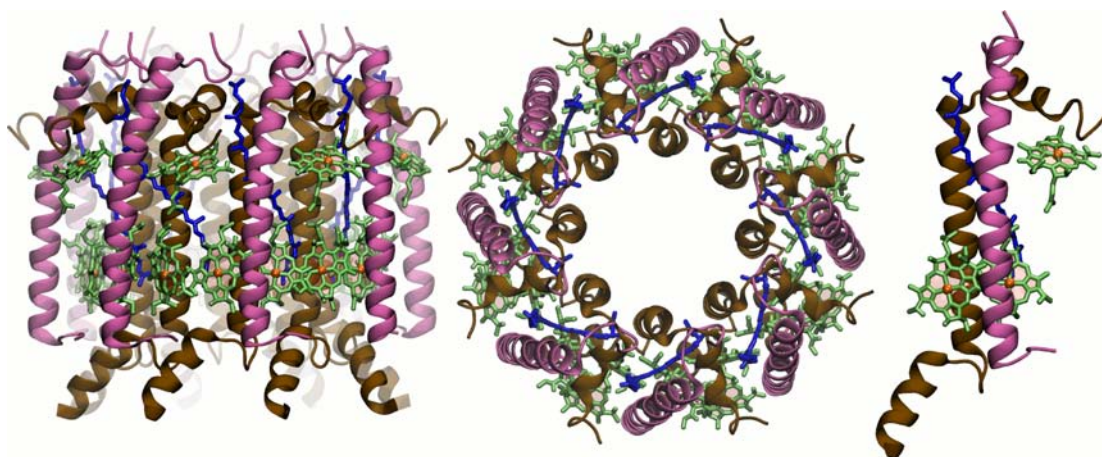
Figure 2.4.: LH2 complex of *Rs. molischianum*: front view (left), top view (middle), single subunit (right); BChl*a* molecules are shown in green (without phytyl tail), lycopens in blue, α-apoproteins in brown, and β-apoproteins in purple.

complexes have been determined by X-ray crystallography to an atomic resolution of 2.4 Å [28] and 2.0 Å [33], respectively. The structure of *Rhodobacter (Rb.) spharodies* has not been resolved yet, but the associate gene sequence shows large analogy to the one of *Rps. acidophila* [19]. As depicted in Figs. 2.1 and 2.2, the LH2 complexes exhibit a circular shape and surrounds the LH1 complex including the RC. The LH2 as well as the LH1 complexes are embedded into the photosynthetic membrane, i.e., the intracytoplasmic membrane [7]. These complexes are responsible for the initial absorption of light energy, and the excitation energy transport to the RC where the charge separation takes place. The structure of the LH2 complex of *Rs. molischianum* is shown in Fig. 2.4. It consists of eight subunits whereas *Rps. acidophila* is a nonamer. Each subunit includes one α- and one β-apoprotein spanning the membrane. Three BChl*a* and one carotenoid are noncovalently bound to the two apoproteins of each subunit. Papiz *et al.* [33] found an additional carotenoid per subunit for *Rps. acidophila* when refining an older structure . There are two different kinds of carotenoids in the two bacteria. Lycopen is found in *Rs. molischianum* whereas *Rps. acidophila* contains rhodopin glucoside.

LH2 complexes enclose two rings of BChl*a* molecules. In case of *Rs. molischianum*, the two rings are denoted B800 and the B850 according to their absorption maxima at 800 and 850 nm, respectively. The BChls in the B850 ring are in close contact which is one of the main reasons of the different absorption wave length compared to the BChls in the B800 ring. Due to the subunit structure, the two BChls of

the B850 ring form a dimer. The intradimer distance between the central Mg^{2+} ions is 9.2 Å, and the interdimer distance measures 8.9 Å [28]. The BChls in the B800 ring are almost perpendicular orientated towards the BChls in the B850 ring. Additionally, the environment is mainly hydrophilic whereas the binding pockets of the BChls in the B850 ring are hydrophobic [28].

The PSU of a purple bacteria contains a number of LH2 complexes which surround a LH1 complex including the RC. The single steps of excitation energy transfer down to the RC in purple bacteria have been reviewed in, e.g, [51, 53, 54]. The transfer times of the cascade [B800→B800, B800→B850, B850→B850, LH2→LH1 ring, LH1 ring→RC] have been found to be [∼1.5 ps, ∼0.9 ps, ∼ 50 fs, 2-5 ps, 20-50 ps] as reviewed in [18].

The LH2 complex of *Rs. molischianum* has been studied by a combined molecular-mechanics/quantum-mechanics approach in the chapter 5. From this, the site energies and couplings of the BChl*a* molecules and the exciton dynamics as well as optical properties could be explored.

2.2.2. The Fenna–Matthews–Olsen Complex

Green sulfur bacteria contain the Fenna–Matthews–Olsen (FMO) LH complexes. The water soluble FMO complex pipes the excitation energy harvested by the main LH complex of green sulfur bacteria, the so-called chlorosome, to the RC, which is embedded into the membrane. See on the left-hand side of Fig. 2.5 for an illustration. In 1975 Fenna and Matthews for the first time succeeded in crystalizing a pigment–protein complex [15], the FMO complex, which consequently became one of the most extensively studied LH complexes [55]. Nowadays, the crystal structures for *Pelodictyon phaeum*, *Prosthecochloris aestuarii*, and *Chlorobaculum tepidum* are available at resolutions of up to 1.3 Å [31, 56]. The native complex has a trimeric structure, whereas each monomer contains eight BChl*a* molecules numbered as depicted in Fig. 2.5. The eighth one is located between two monomers (see Fig. 2.5, middle and right). Its presence had been overlooked for a long time and it has been crystallized within the complex only recently [56]. However, most of the interpretations of experimental observations and theoretical models considered only seven BChls per monomer so far, e.g, [48, 57, 58]. Since the FMO complex
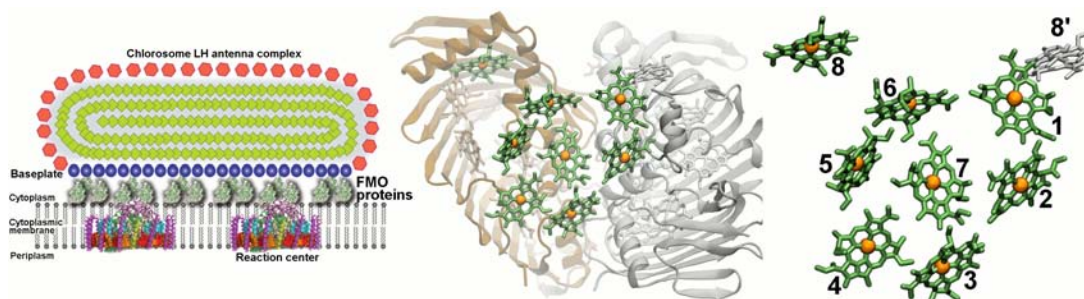
Figure 2.5.: *left*: The FMO complex funnels the light energy harvested by the chlorosome to the RC. The picture is adopted with permissions from Ref. [25]. *middle*: Structure of the FMO trimer (the protein structure of the monomer in the front is not shown): Each monomer contains eight BChl*a* molecules shown in green (the phytyl tail is omitted). *right*: Numbering of the BChls. The eighth BChls are located between the monomers. BChl 8' belongs to the neighboring monomer.

channels the excitation energy, the latter enters at BChl 1 and 6 from the chlorosome and exits at BChl 3, which is in close contact to the RC [23, 59]. The solvent exposed parts of the protein scaffold, which enclose the BChl*a* molecules, consists of 15 strands formed by β-sheets. The contact area of the monomers is mainly composed of four α-helices. On average the BChls within a monomer are approximately 13 Å apart from each other (center-center distance). Not taking BChl 8 into account[5], the minimum inter-monomer distance is about 23 Å. The FMO complex is one of the simplest pigment–protein complexes with known high-resolution structure. For this reason, it has been studied intensely as test object. See, e.g., the review by Milder *et al.* [55].

Some years ago, two-dimensional correlation spectroscopy experiments have been performed by the Fleming group. They observed unexpected coherent energy transfer in the FMO complex of up to 1 ps at cryogenic temperature [9, 10]. This has caused a lot of theoretical and experimental investigations towards the origin of this observed long coherence times [12, 60–71]. Similar observations have been made for other LH systems as well such as for phycobilisoms [11] and conjugated polymers [72]. It is thought that such long-lived quantum coherences facilitate the excitation energy transport across LH complexes and thereby counteract the weak coupling due to separation of the pigments [10–12]. Different suggestions for the origins of the observed quantum coherences were proposed. Some of them will

---

[5]The shortest distance of a BChl and BChl 8 within the monomer is about 23 Å and around 13 Å to a neighboring monomer.
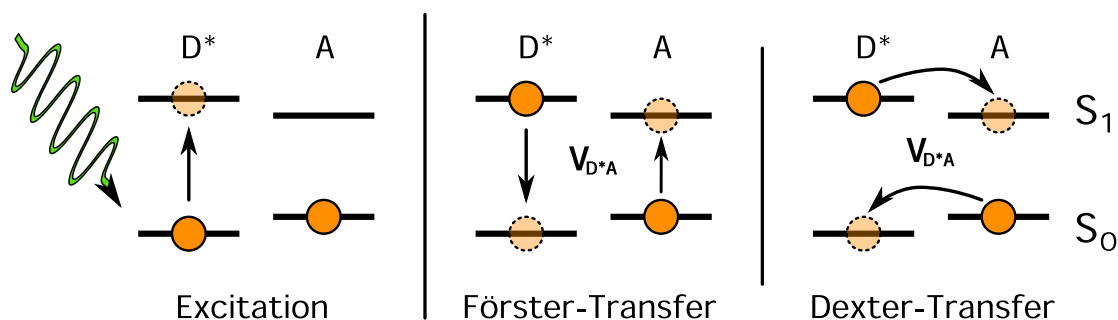
Figure 2.6.: Scheme of the Förster (*middle*) and Dexter (*right*) excitation energy transfer after initial excitation (*left*).

be examined in the chapter 6 for the FMO complex of *Chlorobaculum tepidum*. To this end, we used a QM/MM approach and investigated the temporal motions and fluctuations of the site energies and couplings as well as time-resolved spectra.

2.3. Excitation Energy Transfer Mechanisms

The excitation energy needs to be transferred from the initially excited pigment to the RC where it can induce a charge separation. This energy transfer usually happens radiationless, i.e., without fluorescence and re-absorption. The radiationless transfer from one initially excited pigment, denoted as donor D^*, to the acceptor A (cf. Fig. 2.6, left) can be described via two possible mechanisms: the Förster transfer [73] and the Dexter transfer [74]. Within the Förster transfer, the excitation is transferred via an intermediate virtual photon, i.e., without any particle exchange, such that the donor relaxes back to the ground state and the acceptor becomes excited (see Fig. 2.6, middle). The transfer efficiency depends mainly on the Coulomb coupling between the donor and the acceptor and decays with one over distance to the power of six. In contrast to the Förster transfer, the Dexter transfer involves the exchange of two electrons between the donor and the acceptor (see Fig. 2.6, right). Therefore, an overlap of the electronic wavefunctions is necessary, and due to an exponential dependence of the electron exchange interaction to the distance, a short distance between the donor and the acceptor is required [75]. However, the electronic coupling of the transition densities of the two pigments mainly influences the transfer efficiency.

Due to the short distance between the donor and the acceptor in the RC, the Dexter transfer needs to be considered for the description of charge transfer processes [76]. For larger distances, i.e., larger than the molecular extension like in the FMO complex, the Förster transfer applies and the contribution from the Dexter transfer vanishes.

3. Calculation of Key Quantities

During evolution nature has formed an enormous variety of protein complexes. Each has a special function like collecting solar energy [4], synthesis of ATP [77], reading the genetic code from the DNA [78], removing toxic compounds from the cell [79], etc. To understand the structure-function relationship in detail, it is necessary to have a closer look at the dynamics of the processes at the atomic level. In most cases, the environment cannot be neglected. Plenty of research efforts concerning energy transfer in light-harvesting systems are based on crystal structures, i.e., a single static structure. The included effect of the environment depends usually on fit parameters to experimental data [59, 80]. To gain a complete theoretical picture of the energy dynamics, a full quantum mechanical description, i.e., ab initio calculations of the time evolution, would be computational too expensive. Such QM modeling is only possible for small systems using the Car-Parinello [81] molecular dynamics (MD) method [82]. On the other hand, a pure classical MD simulation following Newton's equation of motion is not sufficient for certain systems which are involved in energy transfer, charge transfer, chemical reactions or if optical properties are important. So one could think about a QM/MM (quantum mechanics/molecular mechanics) approach, that is using QM for a small part of the system only and using the much faster classical molecular mechanics for the rest of the system.

The applied QM/MM approach in the present, see chapters 5 and 6, differs from the previous mentioned QM/MM scheme. In the present thesis, we studied the changes of the molecular structure and subsequent the effect on the excitation energies due to the utilized temperature. To this end, a classical MD simulation was performed to obtain a trajectory which sampled the atomic coordinates every second or fifth femtosecond in an initial step. In a second step, along the recorded trajectory, quantum chemistry calculations were carried out for each molecule of interest, i.e.,
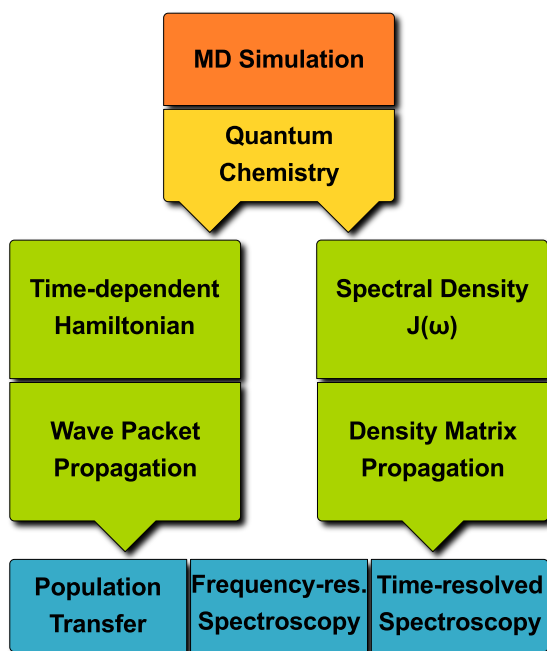
Figure 3.1.: Schematic description of the mixed quantum-classical approach.

BChl*a*. Hereby, the environment of the molecule is taken into account as well. As a result one obtains time-dependent fluctuations of the excited state energies. These energies together with the time-dependent electronic couplings enables one to study the excitation energy transfer across the system of interest. To this end, one can use either wave packet dynamics [83–85], i.e., solving the Schödinger equation for a pure state at each time step, or a density-matrix formalism [83, 86, 87], i.e., evolving a density of mixed states using the Liouville-von Neumann equation over time. Finally, it is possible to calculate certain properties, like transfer times, delocalization lengths of excited states, linear and non-linear spectra, and time-resolved two-dimensional correlation spectrum. Finally, those results allow a comparison with experimental results. Fig. 3.1 depicts a schematic view of this approach.

The necessary key ingredients to perform wave packet or density matrix propagation are the excited state energies of the subsystems, i.e., of the BChl*a* molecules in this study, and the electronic couplings between them. On the one hand, one can construct a time-dependent Hamiltonian followed by ensemble-averaged wave packet calculations, and, on the other hand, a time-averaged Hamiltonian together with a spectral density, which is based on the time-evolution of the site energies,

can be employed using a density matrix approach.

In summary, a parameter-free description of optical properties and excited state dynamics of LH systems based on a multi-scale approach using classical ground state MD with subsequently applied electronic structure calculations, is the main aim this study.

The following sections of this chapter will give an introduction to the methods and concepts to derive the key ingredients for the subsequently applied methods to calculate dynamical and spectroscopy properties.

3.1. Molecular Dynamics Simulations

The analysis of the time-dependent nature of molecular systems and their properties has been one of the main aims for the present thesis. Classical molecular dynamics (MD) simulation is one of the most powerful tools to study protein folding, ion transport through pores, DNA unzipping, RNA hairpin formation, protein complex interaction, stretching of muscle fibres, motion of molecular motors, etc. at the atomic level [88–96]. Classical MD simulation for a N particle system is based on Newton's second law of motion

$$m_i \frac{d^2}{dt^2}\mathbf{x}_i(t) = \mathbf{F}_i(t) = -\nabla V(\mathbf{R}) \,, \tag{3.1}$$

with the mass m_i of particle i at its position $\mathbf{x}_i(t)$ and the acting force $\mathbf{F}_i(t)$ at a time t. This differential equation has to be solved, in the present case numerically, to obtain successive configurations of the system. The acting force on the particle is actually a result of the spatial derivative of the potential energy landscape $V(\mathbf{R})$ depending on the set of positions of the particles $\mathbf{R}$. This energy landscape can be a superposition of different kinds of potentials, like Coulomb, or van der Waals or intermolecular interactions like bond stretching and angle bond angle rotation.

Here, the focus is on all-atom MD simulations, i.e, each particle represents a single atom in the following such that the complete system is set up in atomic resolution. The timescales in biological systems range from femtoseconds for bond vibrations

over nanoseconds for diffusion of water to milliseconds and longer for protein fold-ing processes. Usual MD simulation times are 10-100 ns. However, for small sys-tems simulations of up 10 μs are performed [97]. To achieve this long running simulations with much bigger systems, one can use coarse-grained MD [98], that is, representing groups of atoms as single particles.

The initial coordinates of the molecular system can be generated by molecular "drawing" programs, which is useful for chemical compounds, or from X-ray or nuclear magnetic resonance crystallography data, which is usually the case for pro-tein systems. Furthermore, artificial positioning of the atoms is possible, as well. The initial velocities of the atoms is usually chosen according to the temperature dependent Maxwell–Boltzmann distribution. Once the molecular system has been set up, the integration of the equation of motion (3.1) and calculating the forces acting on the atoms is a deterministic process. Nevertheless, keeping the pressure constant, e.g., by rescaling the simulation volume, or controlling the temperature of the system, e.g., via additional friction forces or rescaling the velocities, can cause random effects. The velocity Verlet [99] or the Leap Frog scheme [100] is usually applied to calculate the motion of the atoms.

The acting forces on the atoms are described via so-called force fields like CHARMM [101], GAFF [102] , OPLS [103]. Each force field is based on a certain functional forms of the energy terms which is specified via a set of parameters to describe the interaction between certain types of atoms. The parametrization of the force fields is performed with the help of quantum calculations or by fitting to experimental values and is usually carried out on fractions of whole molecules like single amino acids of a protein. The forces are calculated with respect to the spatial derivatives of the potential energy. This can be written as sum of so-called bonded and non-bonded interactions, i.e.,

$$V(\mathbf{R}) = V^{\text{non-bonded}}(\mathbf{R}) + V^{\text{bonded}}(\mathbf{R}).$$ (3.2)

Fig. 3.2 shows a schematic representation of the commonly treated interactions in all-atom MD simulations. The first term in Eq. 3.2 is described by the electrostatic and the van der Waals potentials. The van der Waals potential is usually approxi-mated by the Lennard-Johns (6,12) potential. The total non-bonded potential for
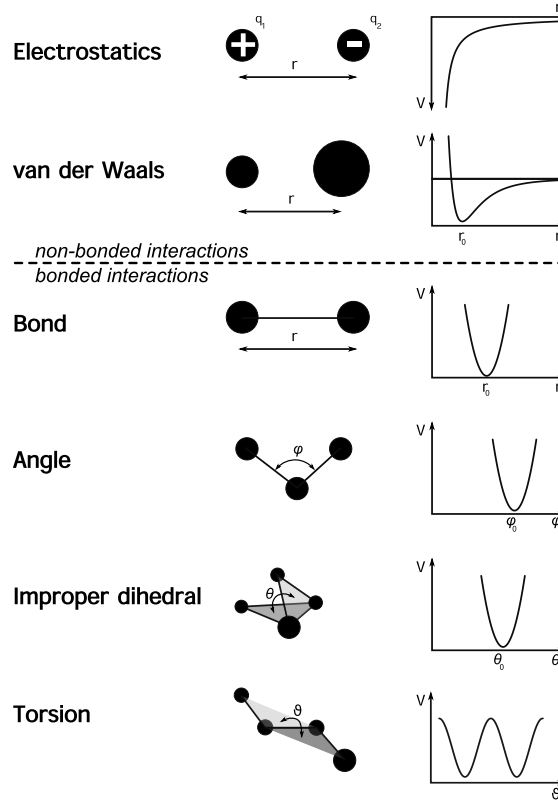
Figure 3.2.: Schematic representation of bonded and non-bonded interactions in all-atom MD simulations.

N atoms reads

$$V^{\text{non-bonded}}(\mathbf{R}) = \sum_{i,j=1,i\neq j}^{N} \left(\frac{1}{4\pi\varepsilon_0} \frac{q_i\,q_j}{r_{ij}} + 4\varepsilon_{ij} \left[\left(\frac{\sigma_{ij}}{r_{ij}}\right)^{12} - \left(\frac{\sigma_{ij}}{r_{ij}}\right)^6 \right] \right), \quad (3.3)$$

with the charges q_i and q_j and the distance r_{ij} between atom i and j. ε_0 is the dielectric constant of the vacuum and ε_{ij} and σ_{ij} are the Lennard-Johns parameters. Both parts of the non-bonded potential are long range. Especially the electrostatic interaction decreases with $\frac{1}{r}$ which might influence more distant atoms. Computationally this is very time consuming because for each possible considered atom pair the interaction has to be calculated. To this end, certain approximations are applied, e.g., a cut-off distance is used, usually in combination with a switching function to avoid any discontinuities in the potential and force calculations. The switching function damps the interaction strength smoothly for distances smaller than the cut-off distance. Additionally to the cut-off distance, the electrostatic in-

teractions is calculated using the Particle Mesh Ewald (PME) formalism. The idea in this algorithm is to split the electrostatic energies in two parts: short- and long-range interactions. The short-range component is calculated directly and the long-range component is evaluated on a discrete lattice in Fourier space. This formalism reduces the number of calculations from $O(N^2)$ to $O(N \log N)$ with N beeing the number of atoms.

While $V^{\text{non-bonded}}$ describes the interaction of one atom with all other atoms, in principle, the second term in Eq. 3.2, i.e., V^{bonded}, characterizes short-range interactions between covalently bonded atoms and defines the overall structure of the molecules. As already depicted in Fig. 3.2, four different types are considered: bond terms, angular terms, improper-dihedral angle terms and terms describing the torsion angles. A common representation of these bonded terms reads

$$V^{\text{bonded}}(\mathbf{R}) = \sum_{\text{bonds}} \frac{k_b}{2}(r - r_0)^2 + \sum_{\text{angles}} \frac{k_a}{2}(\varphi - \varphi_0)^2$$
$$+ \sum_{\text{impr.}} \frac{k_{i\text{-}d}}{2}(\theta - \theta_0)^2 + \sum_{\text{torsions}} \frac{k_t}{2}(1 + \cos(n\vartheta + \delta)), \quad (3.4)$$

with reference values r_0, φ_0, and θ_0 for the bond length r, the angle bending φ, and improper-dihedral angle θ, respectively. The shape of potential belonging to the torsion angle is described by cosine functions including the phase factor δ and the so-called multiplicity n. The width of the harmonic potentials, or in the case of the torsion angle the height of the barrier, is assigned by the factor k_α with $\alpha \epsilon \{b, a, i\text{-}d, t\}$.

Some force fields imply additional cross terms, that is, the interactions between bond lengths and angles, between pairs of angles, etc. Others are taking polarizability effects into account or treating the formation of hydrogen bonds explicitly.

Due to the parametrization of the potential for the interatomic interactions, one can apply MD simulations to a larger variety of atomic systems. Even systems with more than a million atoms can be computed nowadays [104]. Nevertheless, in some cases classical MD simulations are not able to describe certain systems properly. For example, chemical reactions or proton transfer, i.e., forming or breaking chemical bonds, or structural changes of a molecule due to excitation by incident light, is not possible to simulate using classical MD. To this end, QM/MM approaches, need

to be used as described above. In the present study the focus is on calculations of optical properties, i.e, bond breaking and big changes in charges are not expected during the temporal development. Hence, QM calculations are applied to molecular subsystems after the classical MD calculations was finished.

3.2. Electronic Structure Calculations

The absence of electrons in classical MD simulations and consequently the lack of related properties like excited state energies requires an additional treatment to achieve those. One of the basic approximations in the theory of molecular physics is the Born-Oppenheimer approximation. Due to the mass difference of the nucleus and the much lighter and faster electrons, one can separate the electronic problem from the motions of the nuclei. This approximation has been used already in classical MD, where the motion of the nuclei is described independently from any electrons by the Newton's law of motion along a potential energy surface. Some effects of the electrons, like bonded and non-bonded interactions between the atoms, are represented via parameters to some extent. Vice versa, the electronic problem can be described in the context of fixed nuclei.

The fundamental equation for an electronic system is the (time-independent[1]) Schrödinger equation

$$\hat{H}_{total}\Psi_{total}(\mathbf{R}, \mathbf{r}) = E_{total}\Psi_{total}(\mathbf{R}, \mathbf{r}) \,, \tag{3.5}$$

with $\mathbf{R}$ and $\mathbf{r}$ being the nuclear and the electron coordinates, respectively, Ψ_{total} the wave function, $\hat{H}_{total}$ the total Hamilton operator of the system, and E_{total} the total energy. Implying to the Born-Oppenheimer approximation one can make the ansatz

$$\hat{H}_{total} = \hat{H}_e + \hat{T}_n + \hat{V}_{nn} \,,$$
$$\hat{H}_e = \hat{T}_e + \hat{V}_{ne} + \hat{V}_{ee} \,, \tag{3.6}$$
$$\Psi_{total}(\mathbf{R}, \mathbf{r}) = \Psi_n(\mathbf{R})\Psi_e(\mathbf{R}, \mathbf{r}) \,,$$

---

[1]In the case of a time-independent potential energy operator the time-independent Schrödinger equation is used, otherwise the time-dependent Schrödinger equation $\hat{H}(t)\Psi(t) = i\hbar\frac{\partial \Psi(t)}{\partial t}$ needs to be employed.

with the kinetic energy operator $\hat{\mathbf{T}}$, the interaction potential operators $\hat{\mathbf{V}}$, and the subscripts n for the nuclear, e for electron, and ne for the interaction of both. From this follows the electronic Schrödinger equation

$$\hat{\mathbf{H}}_e \Psi_e(\mathbf{R}, \mathbf{r}) = E_e(\mathbf{R})\Psi_e(\mathbf{R}, \mathbf{r}) \,. \tag{3.7}$$

Once the electronic Schrödinger equation has been solved for many molecular geometries, a potential energy surface can be constructed which forms the basis to calculate the motion of the nuclei either classically (see section 3.1) or quantum mechanically by solving the nuclear Schrödinger equation

$$(\hat{\mathbf{T}}_n + \hat{\mathbf{V}}_{nn} + E_e(\mathbf{R}))\Psi_n(\mathbf{R}) = E_{total}\Psi_n(\mathbf{R}) \,. \tag{3.8}$$

Apart from the Born-Oppenheimer approximation, the independent-electron approximation is another simplification to solve the electronic Schrödinger equation and introduces the effective Hamiltonian $\hat{\mathbf{H}}_e = \sum_i \hat{\mathbf{H}}_i^{eff}$. This approximation assumes that there is a separate Schrödinger equation for each electron including a mean field of the other electrons. The resulting wave function Ψ_i for the i-th electron is called molecular orbital with its orbital energy ε_i. Each orbital can be occupied by two electrons according to the Pauli principal. The molecular orbitals are usually characterized by a linear combination of atomic orbitals Φ_ν (LCAO approximation), that is

$$\Psi_i = \sum_\nu \mathbf{C}_{\nu i}\Phi_\nu \,, \tag{3.9}$$

where $\mathbf{C}$ is the expansion-coefficient matrix. Two types of basis functions are typically used: the Slater type [105], i.e., exponential dependence on the radius, and the Gaussian type [106]. The functional form of the orbitals enables one to calculate the matrix elements of a matrix $\mathbf{H}_{\mu\nu} = \int d\mathbf{r}\,\Phi_\mu \hat{\mathbf{H}}^{eff}\Phi_\nu$ and the overlap matrix between two atomic orbitals $\mathbf{S}_{\mu\nu} = \int d\mathbf{r}\,\Phi_\mu\Phi_\nu$. From this follows the matrix notation of Eq. 3.7

$$\mathbf{HC} = \mathbf{SC}\varepsilon \,, \tag{3.10}$$

with ε being the diagonal matrix of the orbital energies $\varepsilon_{ij} = \varepsilon_i\delta_{ij}$.

Ignoring the interaction between all the electrons, taking only valence orbitals into account, and using empirical ionization potentials energies for $\mathbf{H}_{\mu\nu}$, Eq. 3.10 can be easily solved. This simple semiempirical approach is called the extended Hückel theory (EHT) [107].

Hartree-Fock Method The Hartree-Fock (HF) method, which applies the Roothaan-Hall equations [108, 109], introduces the Fock matrix $\mathbf{F}$ in place of the effective one-electron Hamiltonian in Eq. 3.10. $\mathbf{F}$ includes the kinetic energy and the interaction of a single electron with the nuclei and a mean field potential formed by the other electrons. The matrix elements of the restricted[2] Fock matrix reads

$$\mathbf{F}_{\mu\nu} = \mathbf{H}_{\mu\nu} + \sum_{\lambda\sigma} \mathbf{P}_{\lambda\sigma} \left[(\mu\nu|\lambda\sigma) - \frac{1}{2}(\mu\lambda|\nu\sigma) \right],$$ (3.11)

with the density matrix for all occupied orbitals

$$\mathbf{P}_{\mu\nu} = \sum_{i}^{occ.} \mathbf{C}_{\mu i} \mathbf{C}_{\nu i},$$ (3.12)

and the one-electron Hamiltonian $\mathbf{H}_{\mu\nu}$ as a sum of kinetic energy and the interaction with all nuclei A

$$\mathbf{H}_{\mu\nu} = \mathbf{T}_{\mu\nu} + \sum_{A} \mathbf{V}_{A,\mu\nu}$$

$$\mathbf{T}_{\mu\nu} = \int d\mathbf{r}_1 \, \Phi_{\mu}(\mathbf{r}_1) \left(-\frac{1}{2}\nabla^2 \right) \Phi_{\nu}(\mathbf{r}_1)$$ (3.13)

$$\mathbf{V}_{A,\mu\nu} = \int d\mathbf{r}_1 \, \Phi_{\mu}(\mathbf{r}_1) \left(-\frac{Z_A}{|\mathbf{r}_1-\mathbf{r}_A|} \right) \Phi_{\nu}(\mathbf{r}_1).$$

$(\mu\nu|\lambda\sigma)$ denotes the multi center two-electron integral

$$(\mu\nu|\lambda\sigma) = \int d\mathbf{r}_1 d\mathbf{r}_2 \Phi_{\mu}^{A}(\mathbf{r}_1)\Phi_{\nu}^{B}(\mathbf{r}_1)\frac{1}{|\mathbf{r}_1-\mathbf{r}_2|}\Phi_{\lambda}^{C}(\mathbf{r}_2)\Phi_{\sigma}^{D}(\mathbf{r}_2)$$ (3.14)

---

[2]In the restricted Hartree-Fock method each molecular orbital is occupied by two electrons, one with spin up and one with spin down. The Pople-Nesbest unrestricted equations are a generalization of the Roothaan-Hall equations for each spin direction [110].
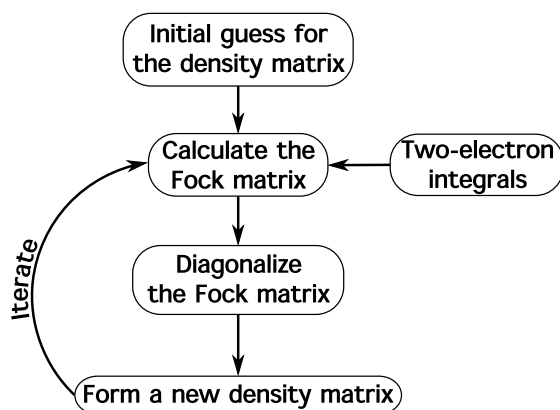
Figure 3.3.: The self-consistent field method.

with the atomic orbital Φ_μ^A centered at atom A. Depending on the specific atomic center and orbital assignment of μ, ν, λ, and σ, the two terms in the summation in Eq. 3.11 describe different properties. The first term in the sum of Eq. 3.11 represents the Coulomb interaction, that is, the electron-electron repulsion, and is commonly denoted as **J**. The second term in the sum refers to the electron exchange interaction which is commonly denoted as **K**.

Self-consistent Field Approach The Fock matrix (Eq. 3.11) depends implicitly on the solution of the Schrödinger equation (Eq. 3.7), i.e., the density matrix **P** depends on the expansion coefficients of the wave function. For this reason, one needs to apply an iterative scheme, which successively converges to the final solution. This procedure is called self-consistent field (SCF) method. The short[3] version of the SCF procedure is sketched in Fig. 3.3 and briefly described in the following. First, the Fock matrix needs to be constructed, that is, one has to make an initial guess for the density matrix, **P**, which can be an empty matrix or one calculates it via a computational cheep approach like the semiempirical EHT method [107]. In a second step, **F** needs to be diagonalised which leads to new expansion coefficients, **C**, to construct new densities and Fock matrices. This needs to be repeated until, e.g., the Fock matrix does not change significantly.

---

[3]See [88] for a more detailed described SCF procedure.

24

Semiempirical Methods Because the computational effort for solving the Schrödinger equation for the electronic degrees of freedom using the HF approach is formally proportional to the M^4, M being the number of basis functions, and therefore also proportional to the system size, it becomes unfeasible to handle large molecular systems. This unfavorable scaling behavior has its main origin in the number of necessary two-electron integrals like in Eq. 3.14 [89, 111, 112]. Therefore one needs to introduce certain approximations which lead to so-called semiempirical methods. Basically, all semiempirical methods imply the following four basic features. First, only valence electrons are treated explicitly. The electron-nuclei repulsion potential is typically modified such that it includes the repulsion of the core electrons in an effective way. Furthermore, the valence orbitals are described by a minimal basis set only. Especially the calculation of multi-center integrals (see Eq. 3.14) are computational expensive. Hence, three- and four-center integrals are neglected. This limit the number of possible combinations drastically and one could express the Coulomb repulsion based on Eq. 3.14 as $(\mu\mu'|\nu\nu')$. μ, μ' and ν, ν' are orbitals centered at atoms A and B, respectively. This is called zero differential overlap (ZDO) approximation[4] and the overlap matrix becomes diagonal, i.e., $S_{\mu\nu} = \delta_{\mu\nu}$. The fourth approximation makes use of parameters for the two-center integrals. The utilization of parameters, usually stemming from fits to experiments or to high-level electronic structure calculations is the reason of this class of methods, i.e., semiemprical.

Besides EHT, one can group all other semiempirical methods in three types: complete neglect of differential overlap (CNDO) [113, 114], intermediate neglect of differential overlap (INDO) [115] and neglect of diatomic differential overlap (NDDO) [113]. No further approximations to the above mentioned ones are performed in order to obtain the NDDO type methods. Representatives of the modified neglect of diatomic orbitals (MNDO) methods [116] are, orthogonalization model 1 and 2 (OM 1/2) [117, 118], Austin model 1 (AM1) [119], parametric model 3 and 5 (PM 3/5) [120, 120]. The main differences lies in the treatment of the core-core repulsion and the parametrization [89].

The CNDO type methods, like the Pariser-Poeple-Parr (PPP) method [121–123], substitute all two-electron integrals by parameters [88]. However, in contrast to the EHT, basis functions are used to construct a density matrix and a Fock matrix

---

[4]All electron-electron interactions are represented by parameters in the EHT method [107]

(see Eq. 3.11) which needs to be solved self-consistently. In summary, the electron repulsion in different orbitals depends only on the involved atom types and not on the specific orbital [124], i.e., the electrons only feel an average repulsion. Due to neglecting almost all exchange integrals, multiplicity is not taken into account.

The INDO type methods are an improvement in accuracy of the CNDO methods. The exchange integrals for electrons on the same atom depend on the implied orbitals which leads to a significant improvement of the results comparing to CNDO. In contrast to NDDO, two-center integrals for electrons on different atoms are neglected. For the INDO methods, a version called INDO/1 for geometry optimisation exists and a version INDO/S which was designed for calculating UV spectra but gives poor ground-state energies. Especially Prof. Michael Zerner has pushed forward the development of the INDO implementation and parametrization for transition metals like Mg [125, 126]. For the parametrization, experimental data like the ionization potentials has been used to extract the Slater-Condon factors F and G [127]. The spectroscopic version INDO/S was calibrated to reproduce the excited state energies of higher order ab initio calculations to structures taken directly from the experiment [112]. The INDO versions which make use of the improvements and parameters made by Prof. Zerner are commonly denoted as ZINDO/1 and ZINDO/S, respectively. In context of the present thesis, it is worth to note, that the ZINDO was parametrized and tested for Chlorophyll and related structures by Prof. Zerner [128–130].

Semiempirical methods have advantages and disadvantages. Due to the employed approximations those methods are computational quite efficient and enable one to study large molecules of up to 1000 atoms or to perform quantum chemistry calculations along trajectories of structural fluctuations. The latter is one of the essential parts of the present work, for this see chapter 5 and 6. The drawback of the semiempirical methods is the parametrization. Usually, the parametrization has been performed only for a selection of atom types and can only be as good as the available data for comparison. Electron correlation is included only implicitly due to parameter fits to experimental data [88, 89]. Recently M. R. Silva-Junior found that ZINDO/S performs quite good for calculations of excited states in comparison with other semiempirical methods like OM2 and AM1[131].

Treatment of Environment   The surrounding environment of the quantum system influences the electronic properties like charge distribution and ground as well as excited state energies [132, 133]. There are mainly two types of treatments: either individual solvent molecules are described or a continuum model for the solvent is used, i.e., embedding the QM system in a suitably shaped hole in a medium of mostly constant dielectric constant [89]. In the present work we used an approach which is known as "electrostatic embedding" [134]. To this end, the environment is represented in atomic resolution within a certain distance around the QM system via point charges taken from the classical MD force field. Such procedures are denoted as mixed models, that is, part of the full system is treated as a fixed classical region and the quantum region is affected by, e.g., polarization effects. An overview about the implementation for different electronic structure calculation methods is given in [124, 134, 135].

Electron Correlation and Excited States   Due to the replacement of the electron-electron interaction by an average interaction in the HF framework, which partially applies to semiempirical methods as well, one can achieve anomalous results when describing chemical phenomena. Although, the correlation energy accounts for only roughly 1% of the total energy for large enough basis sets, it is essential for dissociation processes and calculations of excited states. Configuration Interaction (CI), Many-Body Pertubation Theory (MBPT) and Couple Cluster (CC) are the three main theories for the calculation of electron correlation. The CI method is used in the present work together with the ZINDO/S method to determine the excitation energies of BChl$a$ molecules. This method mixes the already obtained ground state wavefunction Ψ_0 with excited-state wavefunctions $\Psi_{i>0}$ in a linear combination: $\Psi = c_0\Psi_0 + c_1\Psi_1 + \cdots$. The excited-state wavefunctions are constructed on the basis of the ground state wavefunction by moving one or more electrons from an occupied orbitals to unoccupied orbitals. Afterwards, the total energy of the system needs to be minimized. It is named CIS (CI singles), if only one electron is moved to another orbital, CID (CI double) if two electrons are substituted, or CISD (CI single and double) if the latter two types are combined.

The TDM μ_{mn} and the oscillator strength $f_{mn} \propto \mu_{mn}^2$ are two measures to quantity

the electronic transition from state m to state n. The TDM is given by

$$\mu_{mn} = \int d\mathbf{r}\, \Psi_n^* \left(e \sum_j \mathbf{r}_j \right) \Psi_m \,. \qquad (3.15)$$

The TDMs as calculated by CIS methods, tend to be overestimated by a factor of about two [89].

Density Functional Theory Beside the HF method and the various semiempirical methods, Density Functional Theory (DFT) can be used to describe the electronic structure of molecules. The DFT method is related to the HF method but instead of solving the complete Schrödinger equation, the system can be described in principle exactly by the density matrix. The idea that the electronic energy of system is directly related to the electron density $E = E[\rho]$ has been proven by Hohnberg and Kohn [136]. Describing the system just with an electron density, reduces the degrees of freedom for a N electron system from 3N [5] to 3 spatial coordinates independent of the number of electrons. Because the details of the N electron system are averaged out, one has to describe the electron correlation with an estimated functional. If this functional is exact, the electronic system is described exactly [89, 124]. A large variety of functionals have been developed. But so far, none of them is able to describe all properties of different systems correctly. Some functionals, like the popular B3LYP [137], even benefit from the calculation of the HF exchange energies and mix them to a certain fraction with correlation energy using empirical parameter. For DFT one can use basically the same techniques as for HF. So thus the SCF procedure applies to DFT to find the ground state of the system. A detailed description of the DFT method itself, functionals, properties and drawbacks are presented, for example, in [88, 89]. Excited states can be calculated by Time-Dependent DFT (TDDFT) based on the Runge-Gross theorem [138]. This extension to DFT makes use of a time-dependent external perturbation which leads consequently to poles at the excitation energies in the solution of the linear response function.

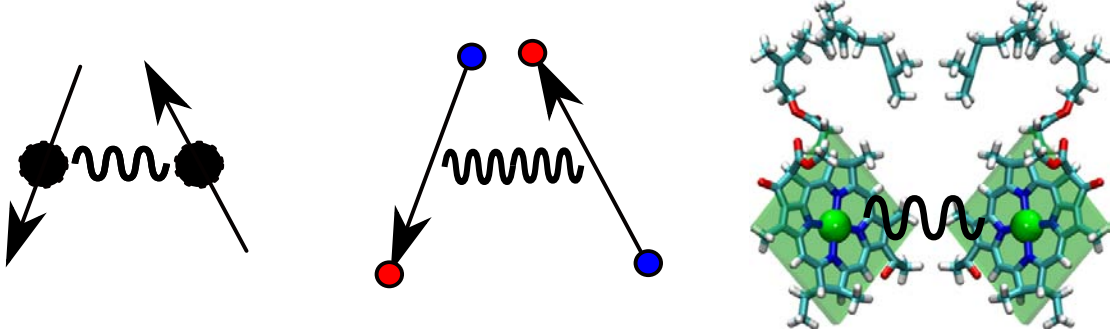[5] 4N if taking the spin into account.

Figure 3.4.: Schemes of pigment-pigment interactions: (*left*) point-dipole approximation, (*middle*) extended-dipole approximation, (*right*) representation for TrEsp, and the dimer approximation

3.3. Pigment-Pigment Interactions

The interaction or coupling strength between the pigments in LH complexes is the second key quantity besides the excitation energies. As already mentioned in the section 2.3, both excitation energy transfer mechanisms, as introduced by Förster and Dexter, require a quantity which describes how well the excitation can be transferred from a donor to an acceptor. Due to the coupling, the excited states, localized on the individual pigments, become delocalized excitonic states which might have occupations on several pigments. This effect is related to the so-called Davydov splitting.

Förster introduced the so-called point dipole interaction (PDA) [73]

$$
V_{ij}^{\text{PDA}} = \frac{f}{4\pi\varepsilon_0} \left(\frac{\mu_{\mathbf{i}}\mu_{\mathbf{j}}}{r_{ij}^3} - 3\frac{(\mu_{\mathbf{i}}\mathbf{r}_{ij})(\mu_{\mathbf{j}}\mathbf{r}_{ij})}{r_{ij}^5} \right).
\tag{3.16}
$$

Thereby, each site (donor or acceptor) i is represented by a TDM μ_i located at the postion $\mathbf{r}_i$ (see Fig. 3.4, left). Those TDMs are vectors with a certain length and can be achieved by electronic structure calculations. The coupling V_{ij} depends on the relative orientation and distance $r_{ij} = |\mathbf{r}_i - \mathbf{r}_j|$ of the pigments to each other. The prefactor f scales the coupling due to solvent-screening effects and will be discussed later. For short distances the PDA is known to lead to poor results [139–142].

A somewhat enhanced coupling method is the extended dipole approximation (EDA)

[141, 143]:

$$V_{ij}^{\text{EDA}} = \frac{f\,|q_i^T|\,|q_j^T|}{4\pi\varepsilon_0} \left[\frac{1}{|\mathbf{r}_i^+ - \mathbf{r}_j^+|} + \frac{1}{|\mathbf{r}_i^- - \mathbf{r}_j^-|} - \frac{1}{|\mathbf{r}_i^+ - \mathbf{r}_j^-|} - \frac{1}{|\mathbf{r}_i^- - \mathbf{r}_j^+|} \right] . \qquad (3.17)$$

Hereby, each molecule i is represented via a TDM (see Fig. 3.4, middle), which is determined by two transition charges q_i^T of equal absolute value but opposite sign, denoted by the superscripts "+" and "-" at the position vectors. The positions and the values of the two charges reflect a calculated transition density to some extent[6].

Assigning to each atom of the molecule a transition charge, in such a way that the resulting electrostatic potential fits to the corresponding transition density, accounts for the molecular structure in much more detail than within PDA or EDA. This method is named TrEsp (Transition charges from electrostatic potential) [141, 144]. The TrEsp interaction has the same form as the Coulomb interaction

$$V_{ij}^{TrEsp} = \frac{f}{4\pi\epsilon_0} \sum_{\substack{m\in i \\ n\in j}} \frac{q_m^T q_n^T}{|\mathbf{r}_m - \mathbf{r}_n|} . \qquad (3.18)$$

This method is computationally very efficient and reflects the interaction of the full molecular structures (see Fig. 3.4, right).

Instead of fitting an electrostatic potential, which is formed by transition charges, to a transition density, one can use these directly to calculate the exact Coulomb interaction. Thereby, the transition densities are mapped to a three-dimensional grid with volume elements, i.e., cubes of the size $V = \delta x \delta y \delta z$. This transition density cube (TDC) method has been developed by Krueger *et al.* [145]. The expression for the transition density M within this formulation reads

$$M(x, y, z) = \int_z^{z+\delta z} \int_y^{y+\delta y} \int_x^{x+\delta x} \int_s \mathrm{d}s\,\mathrm{d}x\,\mathrm{d}y\,\mathrm{d}z\; \Psi_{\text{ground}}^* \Psi_{\text{excited}} ,$$

$$V_{ij}^{\text{TDC}} = \frac{f\,V_i V_j}{4\pi\epsilon_0} \sum_{mn} \frac{M_m^i M_n^j}{|\mathbf{r}_m - \mathbf{r}_n|} , \qquad (3.19)$$

in which s represents the spin variables. Although one can get the transition den-

---

[6]Usually it is necessary to scale the transition charges in such a way, that the resulting dipole strength matches an experimental measured dipole strength, due to over- or underestimating the transition dipoles in the electronic structure calculations.

sities from electronic structure calculations, the summation to calculate the TDC couplings is computationally quite expensive.

The electronic coupling can also be calculated from an interacting dimer of pigments. For this purpose, the excitation energies of the two individual monomers, E_i and E_j, and the corresponding two excitation energies of the dimer calculation, ε_1 and ε_2, are necessary [133, 146, 147]. This kind of interaction is expressed as

$$V_{ij}^{\mathrm{dimer}} = \frac{f}{2} \sqrt{(\varepsilon_1 - \varepsilon_2)^2 - (E_i - E_j)^2} \, . \tag{3.20}$$

The quality of the calculated coupling depends on three electronic structure calculations and the employed method. Especially, due to the mixing of the excited states it might be difficult to select the correct states. Furthermore, depending on the electronic structure methods numerical demands, this method might cause much more effort than the previous ones.

To account for solvent-screening effects, in all previously described methods the prefactor f is used. In the Förster or Onsager theory f is given as $f = 1/n^2$ or $f = 3/(2n^2 + 1)$, respectively, with n denoting the refractive index[7] of the solvent. But other effective pre-factores are used in literature to reproduce the energy level splitting [146, 148, 149]. Scholes *et al.* developed a distance dependent screening factor with exponential decay [150]:

$$f(r_{ij}) = A\exp(-Br_{ij}) + f_0 \quad \text{with } A = 2.68, \ B = 0.27, \ f_0 = 0.54 \, . \tag{3.21}$$

The latter approach has been applied in all of our studies, see chapters 5 and 6.

3.4. Time-Dependent Hamiltonian

The extracted excitation energies ε_i from the electronic structure calculations, also referred to as site energies, (see section 3.2) can be combined together with the calculated electronic couplings V_{ij} between all the individual sites (see the previous section 3.3) to a Hamiltonian H. If the electronic structure calculations as well as the coupling calculations are performed on a trajectory of consecutive molecular

---

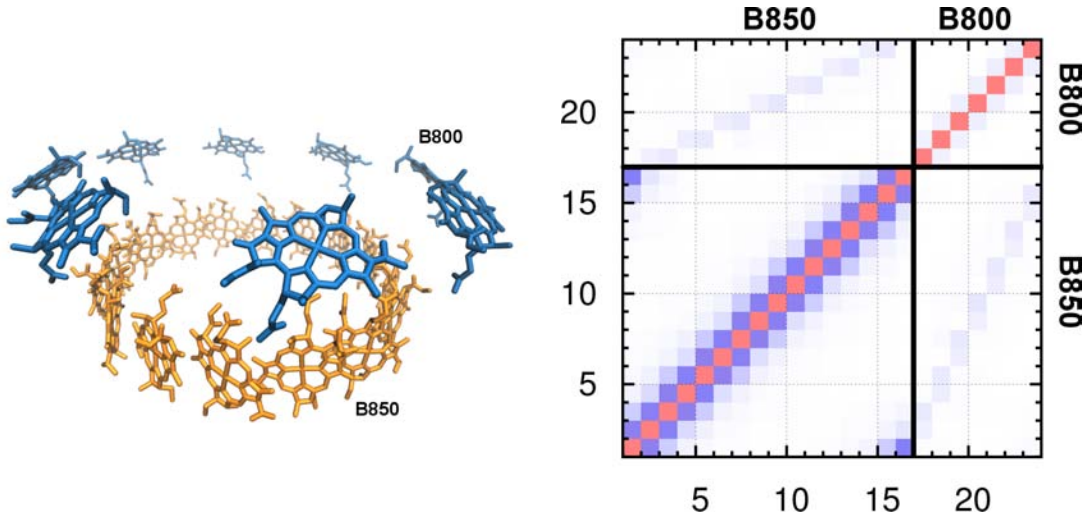[7]Commonly, $n^2 = 2$ is used for a protein environment.

Figure 3.5.: Visual representation of the matrix elements of the Hamiltonian (*right*) for the LH2 system of *Rs. molischianum* (*left*) The BChl*a* molecules from the B850 ring are shown in orange and the ones from B800 ring in blue. The diagonal elements of the Hamiltonian are the site energies (red) and the off-diagonal elements represent the coupling strength between the sites (blue). The upper left and the lower right parts of the Hamiltonian represent the couplings between the two rings.

conformations, which might come from MD simulations, the site energies and couplings become time-dependent quantities. Consequently, the Hamiltonian becomes time-dependent as well. For a system with N sites, the Hamiltonian reads

$$H(t) = \sum_i^N \varepsilon_i(t) \left|i\right\rangle \left\langle i\right| + \sum_{i \neq j}^N V_{ij}(t) \left|i\right\rangle \left\langle j\right| . \tag{3.22}$$

Fig. 3.5 shows a visual representation of the matrix elements of the Hamiltonian at a certain time together with the corresponding the LH2 system *Rs. molischianum*. The diagonal elements represent the site energies, which seem to be quite similar using this color scale. In blue and light-blue, one can identify the nearest and next-nearest neighbor couplings within and between the two rings of BChl*a* molecules.

Although the time-dependent Hamiltonian represents a coarse grained version of the actual molecular complex, it contains all necessary information to describe the dynamics of excitation energy transfer in this complex system. Propagation of wave packets along the given Hamiltonian in Eq. 3.22 by numerical integration of the time-dependent Schrödinger equation can yield insight into the energy transfer.

Optical properties can be calculated as well. The drawback of this method is the implicit high-temperature limit leading to equal populations of all sites in the long time limit, i.e., it does not account for the Boltzman distribution of the population for a given temperature. Another ansatz to calculate properties of the system is the density matrix formalism. To this end, the time-dependent Hamiltonian is averaged over time and one needs to couple an the system to a collection of external vibrations which interact with the system. The quantity, which describes the coupling between the system and the external vibrations at energy $\hbar\omega$ including the density of the vibrations, is the spectral density $J(\omega)$ and will be discussed in the following section.

3.5. Spectral Density

The spectral density is one of the necessary quantities for calculations on dissipative quantum systems. It describes the frequency-dependent coupling between the excitonic sub-system, e.g., a BChl molecule, and its thermal environment. In other words, the spectral density represents the spectral distribution of the system–bath coupling constants [151]. Experimentally, there are mainly two approaches to extract information about the spectral density: *fluorescence stoke shift* and *photon echo spectroscopy* measurements [152].

The spectral density $J(\omega)$ in terms of coupling constant $c_{n\xi}$ between the pigment n and a certain bath-frequency ω_ξ is given as [153]

$$J_n(\omega) = \frac{\pi}{\hbar} \sum_\xi |c_{n\xi}|^2 \delta(\omega - \omega_\xi)\,. \tag{3.23}$$

Different proposed functional forms have been fitted to either experimental data or to model calculations and are shown in Fig. 3.6. All three shapes of the spectral density decay exponentially at higher energies and do not show any molecular vibrational modes, e.g., signals at typical bond-stretching vibrations.

The environmental influence is commonly modeled as a "bath" of independent harmonic oscillators. Within the assumption of a linear system–bath coupling, the spectral density is temperature independent.
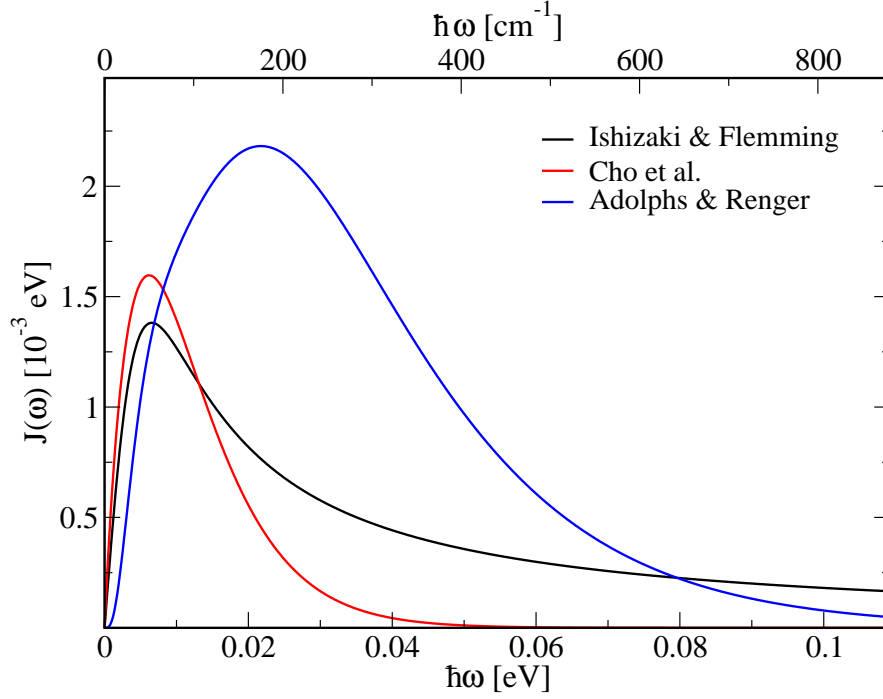
Figure 3.6.: Proposed spectral densities of other studies by Adolphs and Renger [59], Cho *et al.* [154] and Isishaki and Fleming [57].

According to the fluctuation-dissipation theorem [155–157], for a system in thermal equilibrium, it is possible to relate time-dependent fluctuations of a system, e.g., of the site energy, and its response[8] to a applied perturbation. In the context of light-harvesting complexes, i.e., pigments embedded into a protein scaffold, the fluctuations of the energy due to the thermal motion and surrounding environment contain the information about the so-called *system-bath interaction*, i.e., spectral density. To calculate the spectral density out of the trajectory of site energies, e.g., based on a MD simulation, one needs to evaluate the autocorrelation function $C_{nn}(t)$ of fluctuations around the time average of site n [9]:

$$C_{nn}(t) = \left\langle \delta E_n(t)\, \delta E_n(0) \right\rangle, \tag{3.24}$$

where $\langle \cdots \rangle$ denotes a sample average and $\delta E_n(t) = E_n(t) - \left\langle E_n \right\rangle$ the deviation from

---

[8]in the context of the linear response theory
[9]in general, it is possible to calculate a correlation C_{mn} which correlates the quantities from different sites

the mean value. The discrete version, i.e., the numerical realisation reads

$$C_{nn}^w(t_i) = \frac{1}{N_t - i} \sum_k^{N_t - i} \delta E_n^w(t_i + t_k) \, \delta E_n^w(t_k) \,. \tag{3.25}$$

Hereby, the full trajectory is divided in N_w sections of the length N_t. $C_{nn}(t)$ is calculated for each section independently and subsequently averaged:

$$C_{nn}(t_i) = \frac{1}{N_w} \sum_w^{N_w} C_{nn}^w(t_i) \tag{3.26}$$

To this end, it is possible that the sections might overlap after the correlation has decayed. Fig. 3.7 shows a schematic picture of Eq. 3.25.
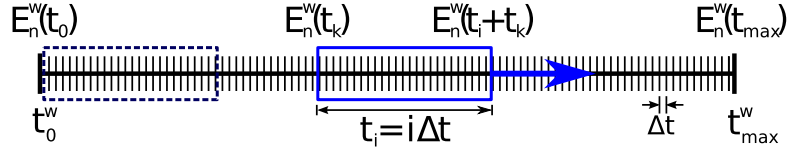
Figure 3.7.: Calculation of an autocorrelation function along a trajectory of site energies of site n for a specific section w.

Finally, the spectral density $J_n(\omega)$ of site n can be obtained through an inverse cosine transformation of $C_{nn}(t)$ [148, 158]

$$J_n(\omega) = \frac{2}{\pi\hbar} \tanh(\beta\hbar\omega/2) \int_0^T \mathrm{d}t \, C_{nn}(t) \cos(\omega t) \,. \tag{3.27}$$

A formal derivation of the spectral density is described in Ref. [86]. The quantum correction factor $\tanh(\beta\hbar\omega/2)$ ensures the detailed balance relation between the transition from the classical bath–correlation function to the quantum nature of the spectral density [157]. Different factors have been proposed as well, but there was no overall satisfactory version for all the considered models [159, 160].

Since MD trajectories have a finite length, the upper integration limit in Eq. 3.27 is finite, i.e., $T \neq \infty$. Reliable results can be obtained using $T = N_t \Delta t / 2$, i.e., half of the autocorrelation length. Nevertheless, the shape of the resulting spectral density strongly depends on the choice of N_t, as shown in Fig. 3.8 although one would expect to achieve a more defined shape of $J_n(\omega)$ for longer integration times. Un-
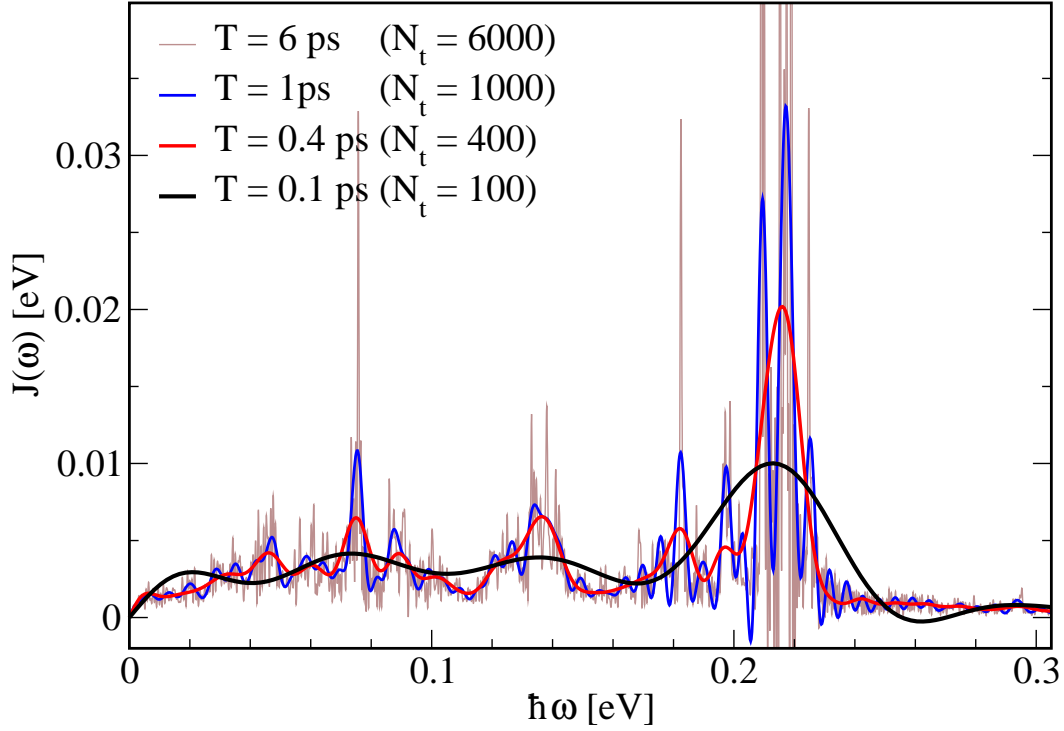
Figure 3.8.: Spectral densities based autocorrelation functions of different lengths.

fortunately, the calculated autocorrelation functions are not vanishing completely. Even for larger times, they show oscillatory behavior, which might be numerical noise and leads to the very structured functions and may even cause negative values of $J_n(\omega)$ as shown in Fig. 3.8.

Due to the mentioned uncertainty about the proper final structure and to obtain an analytic expression for $J_n(\omega)$, we have fitted the calculated autocorrelation functions from the MD simulations [161, 162]. This can be done via different functions. An obvious choice is a combination of exponential functions and damped oscillating, i.e., sine or cosine, functions. This choice has also the advantage of an analytic solution of the spectral densities. On the left-hand side of Fig. 3.9 an example of a fitted function to the autocorrelation function of the site energies is shown. Here, a combination of three exponential functions with 13 damped cosine functions have been used for the fit. The agreement of the fit function with the original data and the resulting spectral density is quite good. Additionally, it is clearly visible that the transformation of the numerical data includes a lot of artificial noise which depends on the lengths of the autocorrelation, the averaging procedure and a possible

Figure 3.9.: Comparison of simulation data (black) and a corresponding fit (red) for the autocorrelation function of the site energies (*left*) and the resulting spectral density (*right*). The insets show an enlarged cut-out.
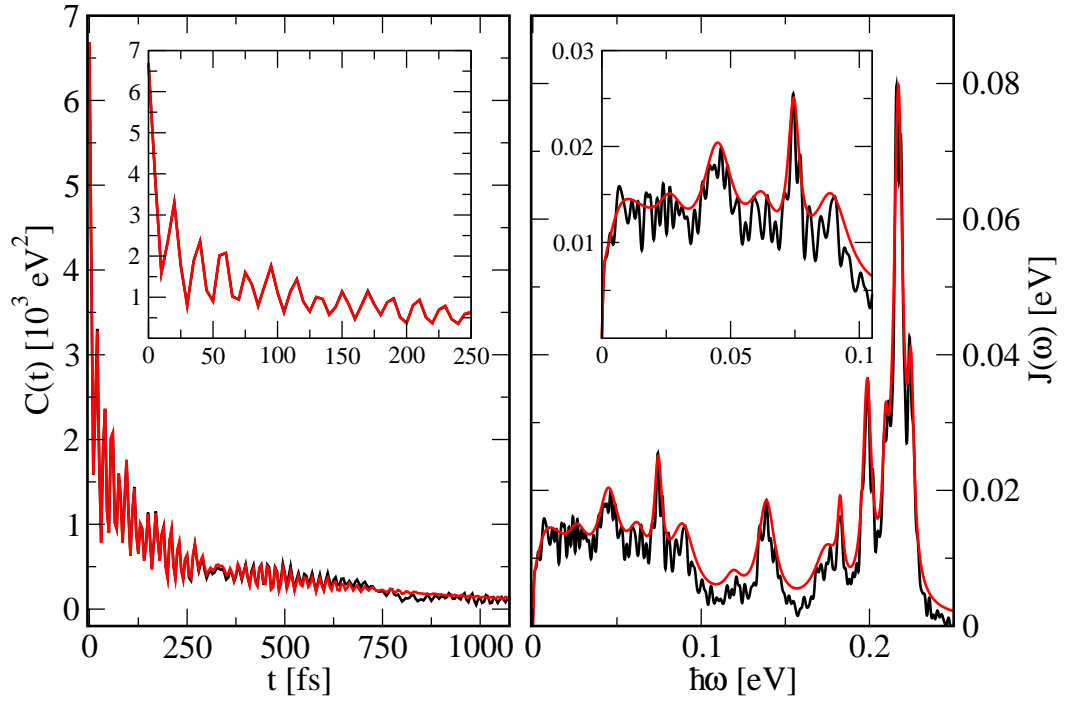
smooth cut-off at the end of the autocorrelation function. We applied this fitting procedure to LH2 complex of *Rhodospirillum molischianum* (see section 5.1) and the *FMO* complex (see section 6.3).

4. Summary of Results

The light-harvesting (LH) process in plants and photosynthetic bacteria is determined by pigment molecules, the arrangement of the pigments to each other, the surrounding protein scaffold, the solvent, and the time-dependent character. This together affects the shape of the linear and non-linear spectra, and the efficiency of the energy transfer. Especially, at ambient temperature, at which most LH organisms live, thermal fluctuations have a big influence on the dynamical properties, i.e., on the transfer and subsequent on optical properties.

In the present work, we performed classical molecular dynamics (MD) simulations on the LH2 complex of *Rhodospirillum molischianum* and on the Fenna–Matthews–Olson (FMO) complex of *Chlorobaculum tepedium*. Each LH complex was embedded in its native environment. For simplicity, both complexes will be denoted in the following as LH2 and FMO, respectively. From the subsequently applied electronic structure calculations along the MD trajectory for each bacteriochlorophyll *a* (BChl*a*) molecule we achieved time-dependent fluctuations of the energy gaps between ground an the first excited state, also referred to as site energies. Due to the very large number of necessary electronic structure calculations, we mainly used the semiempirical ZINDO/S method in combination with the CIS approach.

Initial Investigations on the LH2 Complex   First we analyzed a 12 ps long trajectory of the LH2 complex with respect to the influence of the surrounding environment on the energy gap fluctuations. For this see section 5.1. The environment is represented as classical point charges around the quantum mechanical treated BChl*a* molecule and acts as a polarizing medium. As a first consequence, the surrounding leads to a shift of the energy distributions to lower energies. Furthermore, the high-energy wing of the distribution becomes more pronounced, especially for the BChls in the B800 ring. Additionally, a charge radius of 20 Å around the BChl

molecule was shown to be a good compromise of convergence. We investigated different active orbital spaces for the CIS calculations (data is not shown in the publication), that is, which of the highest occupied and lowest unoccupied orbitals are taken into account. A larger active space leads to a further red shift of the site energies. But slightly broader distributions for larger active spaces could be observed as well. Because the original parametrization procedure had been used only a small active space [163] and others found good agreement for implying the ten highest occupied and 10 lowest unoccupied orbitals [35, 164], we restricted our calculations to ZINDO/S-CIS(10,10) in the studies in the chapters 5 and 6. In an earlier work [148], a much shorter MD trajectory of the same LH2 complex was used for HF/CIS calculations of the BChl molecules. To this end, the STO-3G basis set was used. In section 5.1, we also performed HF/CIS and TDDFT calculations with STO-3G basis set along a part of the full trajectory. Besides the larger average excitation energy for the latter methods, the fluctuations of the site energies stemming from the HF/CIS calculations are by two to three times larger than the one from the ZINDO/S-CIS or TDDFT. The width of the fluctuations of the latter two methods are comparable. The computationally most efficient method is by far ZINDO/S-CIS with less than 10 s per calculation compared to 16 min and 30 min for TDDFT and HF/CIS, respectively.

Evaluation of the Electronic Couplings   Electronic couplings between the BChl*a* molecules are the driving forces for the energy transfer in the LH complexes. To this end, in section 5.1 we compared four approximative methods for the LH2 complex: point-dipole approximation (PDA) [73], extended-dipole approximation (EDA) [141], transition charges from electrostatic potential (TrEsp) [141], and the dimer approach [133, 146, 147]. Additionally, a distant dependent solvent screening factor was used to account for effect of the environment to the couplings [150]. Although PDA is widely used in the literature, it is known to give poor results for short distances between the pigments. Due to the dimeric arrangements of the BChls in the LH2 complex, a dimerization of the distribution of the couplings is expected. PDA do not show distinguishable distributions for interdimer and intradimer couplings, whereas EDA overestimates this classification. The results of the dimer approach show very broad distributions and strongly depend on the outcome of the employed electronic structure calculations. Especially for the analysis

along a trajectory, this method is computationally expensive and therefore not favorable. The obtained results of the TrEsp couplings show a dimerization and the average couplings are in good agreement with couplings calculated with the computational expensive transition density cube method based on the crystal structure [28, 145]. Due to the coarse-grain character of the PDA, partially much broader distributions are obtained. The achieved distributions of some couplings in the FMO complex can be up to factor of four broader compared to that calculated by the TrEsp method.

Spatial Correlations Some years ago, unexpected long coherent energy transfer of up to 1 ps has been observed in the FMO complex at cryogenic temperatures by the Fleming group [9, 10]. It was suggested, that correlated motion tuned by the protein scaffold [165–167], or correlations in the site energies [10, 11, 60, 61, 165, 166, 168, 169] and/or couplings [170] cause the long-living coherences. To gain some insight in the underlying mechanism, we investigated this question and looked for correlated motions of the BChl molecules, correlations of the site energies and couplings in the LH2 complex (see section 5.1) as well as in the FMO complex (see section 6.1). The spatial arrangement of the BChls are very different for the two complexes. Nevertheless, for both complexes no significant correlation in the atomic motion of different BChls could be observed, even not for nearest neighbors in the LH2 complex. Only intramolecular correlated motion was detected. For DNA nucleobases, a correlation in the site energies was found [168] which enhances the charge transfer. Nevertheless, neither in the LH2 nor in the FMO complex correlations could be found between the site energies. The correlation between site energies and TrEsp couplings are negligible small as well. Because the transition dipole moments (TDMs) are directly related to the site energies, there is a correlation between the site energy and the PDA couplings, but only for those BChls which are involved in the coupling. Furthermore, some correlations between the couplings could be found. Especially, if two BChls share a common partner, like the couplings 4-5 and 5-7, the correlation between those couplings is relatively large. This is induced by the motion of the common partner, that is BChl 5 in the previous example. This motion influences both couplings and results in a correlation among them. Furthermore, if one of the two correlated couplings is small, the obtained correlation might be unimportant, because the absolute values of cou-

plings are not taken into account. Usually, small couplings have small fluctuations as well. Those couplings are rather unimportant for dynamical and spectroscopic properties of the LH complexes.

Time-dependent Hamiltonian The time-dependent site energies together with the time-dependent electronic couplings can be used to form a time-dependent Hamiltonian. This was done for the LH2 complex (see section 5.2) and the FMO complex (see section 6.2). In the case of the LH2 complex, a combined Hamiltonian for the B850 and B800 ring from a 12 ps long trajectory was constituted. The linear absorption spectra was calculated by binning the excitonic energies and weighting them with excitonic dipole strength for the particular state. The calculated absorption peak of the B800 ring is very low compared to that of the B850 ring. Because the excitonic levels at around 800 nm do not show significant absorption strength, which can be found only the first four excitonic level. Furthermore, the site energies of the B800 ring needed to be shifted by 44 meV. This shift was introduced, since the calculated average site energies of the B850 ring and the B800 ring was too similar, that is, the ZINDO/S calculations did not fully account for the differences in the environment of the two rings. In case of the second LH complex, that is, the FMO complex, two time-dependent Hamiltonians were created (see section 6.2): a 200 ps long from a FMO trimer MD simulation with 24 sites, and a second one using a 300 ps long FMO monomer MD simulation with seven sites only. The eighth BChl detached from the structure during the equilibration of the single FMO monomer complex, which might explain that it was resolved in the crystal structure just recently [56]. Whereas the FMO trimer complex structure keep close to the original crystal structure, the single FMO monomer complex is more flexible, which has some impact on the distributions of site energies and couplings. Especially, the coupling between BChl 1 and 2 is only half as strong as in the trimer simulation. The two finally achieved time-dependent Hamiltonians were used to compute exciton dynamics and optical properties. To this end, the time-dependent Schrödinger equation was solved numerically [85, 171–174] along the fluctuating Hamiltonian. Overall, the excitation transfer across a single FMO[1] in the trimer structure is faster than in a individual monomer structure. Two

---

[1]In vivo, the excitation might enter at BChl 1 or 6 from the chlorosome and will be transferred to BChl 3 or 4 which connects to the reaction center.

distinct pathways within a monomer are available: BChl $1 \to 2 \to 3$ and BChl $6 \to (5, 7) \to 4$. The latter one is the faster. The excitation transfer from the eighth BChl to other BChls is the slowest. It might therefore assist the excitation transfer between the FMO monomers within the trimer complex and does not acts as an input channel for excitation energy from the chlorosome. Furthermore, the excitation transfer dynamics can be studied by two-dimensional correlation spectroscopy (2D CS) [9, 10], here in context with a time-dependent Hamiltonian based on MD simulations at 300 K. 2D CS is a technique which is related to photon echo peak shift measurements, pump–probe spectroscopy and two-dimensional NMR COSY technique [175]. The resulting 2D CS spectra obtained at room temperature for the FMO monomer and the FMO trimer using different waiting times do not reveal distinct features like the experimentally measured spectra at 277 K [60]. The off-diagonal signal, taken at 150 cm^{-1} below peak, shows small oscillations which might be connected to the experimental observed ones at lower temperatures and hence to the observed coherent energy transfer. Due to smaller thermal fluctuations and hence smaller environmental effects at much lower temperatures, e.g., at 77 K, the experimental 2D CS spectra show much more details. One would have to repeat the MD simulations at those low temperatures to establish a clearer connection between experiment and simulation. Nevertheless, such low temperatures are slightly problematic for the MD simulations. It should be noted, however, that there would be almost no excitation transfer in LH complexes if no environmental effects were present [62, 176]. It is an open question if the environmental coupling in LH systems is optimized in such a manner to yield the most efficient transfer rates. The calculated linear absorption spectra of the FMO complexes in section 6.2 show a good agreement with the experimental ones, though static disorder is not yet included in the present approach. This results in a narrower absorption line shape of about 15%. The skewness of experimental spectra is also well reproduced originating from the non-Gaussian distributions of the site energies of the individual BChls. The peak position is slightly off the experimental one. Although only little coherent population transfer between the sites and almost no spatial correlation can be detected from our simulations of the FMO complex at room temperature the overall excitation transfer across the complex is very efficient with transfer times of less than 100 fs.

Evaluation of Spectral Densities   Instead of describing exciton dynamics using a time-dependent Hamiltonians for LH2 and FMO as discussed above, one can use a density matrix approach based on a time-independent Hamiltonian, e.g., a time-averaged one, in combination with the frequency-dependent system-environment coupling, the so-called spectral density. A brief comparison of the wave packet dynamics approach and the density matrix method has been reported very recently [177]. Using spectral densities, different approximate or numerically exact reduced density matrix theories have been used to calculate dynamics and spectra, e.g., [62–68, 178–180]. Spectral densities were obtained for LH2 (see sections 5.1) and FMO (see section 6.3). To this end, the autocorrelation functions of the site energy fluctuations were fitted either to two exponential only or a combination of exponential functions with damped cosine functions [161, 162]. The fitting provides a parametrized analytic form of spectral densities and it reduces a lot of artificial noise compared to direct, i.e., without fitting, transformation of the autocorrelation functions to the spectral densities. The double exponential fitting of the autocorrelation function results to a smooth profile. This yields already a good approximation without any peak structure. The latter is induced by including the damped oscillations to the fitting. Most likely, the spectral densities based on the fit with two exponentials describe the background, whereas the peaks in the spectral densities are caused by intramolecular modes. Especially, a very prominent oscillation of about 20 fs in period is present in all the site energies as well as the autocorrelation functions. This leads to strong signals at around 1600 cm^{-1}. Such fast oscillations are related to vibrational modes of double bonds in the BChl. Even if there was no precise assignment yet, an association with C=C or C=O stretch vibrations is very likely [148, 181, 182].

For the FMO monomer and trimer complex, parametrized spectral densities are presented for all BChl*a* molecules[2] (see section 6.3). Because all individual spectral densities show an akin peak structure and BChls 1 to 6 have a similar mean height, an averaged spectral densities for BChls 1 to 6 of the trimer is presented as well. The variance in the spectral densities, especially in the low energy region, are most likely originated from the differences in the surrounding environment and mainly via its electrostatic interaction to the BChls. Spectral density from previous approximations to the by Adolphs Renger and by the Flemming group (see Fig. 3.6) have a

---

[2]In the case of the FMO trimer complex the spectral densities for each BChl in a monomer were averaged over the three monomers.

lower height and do not show peaks due to intramolecular vibrations [57, 59, 154]. Latter spectral densities were obtained through fits to experimental observations at very low temperatures. Recently, Nalbach *et al.* included a rather broad vibrational mode which did not lead to large differences in the exciton dynamics [58]. Comparing the aforementioned approximations to the spectral densities for BChl 1 to 6 stemming from our room temperature MD simulations, the latter one is by a factor of 2 to 3 larger and extends to higher energies which is in agreement to proposed Huang–Rhys for Chl*a* [183, 184].

In the case of the LH2 complex with its B850 and B800 rings, only two spectral densities were calculated due to symmetry reasons (see sections 5.1). The peak structure for both is quite similar to the ones of FMO but differ in the amplitudes due to different environments. The amplitude of spectral density of the B800 ring is almost twice as large of the B850 ring and comparable to the one obtained for BChl 1 to 6 of the FMO trimer complex. The calculated linear absorption spectrum in the framework of the so-called polaron model, yielded too narrow spectral peaks for the two rings due to omitting static disorder. Furthermore, dynamic disorder due to high frequency modes in the site energies reduces the width of the spectrum.

Conclusion The current thesis presents a multi-scale approach based on classical MD simulations capturing the atomic motions of LH systems to obtain parameter-free calculations of optical properties and excited state dynamics. Subsequent to the MD simulations, electronic structure calculations were utilized to molecular subsystems, i.e., the BChl*a* molecules, along extensive trajectories, which were much longer than in earlier studies [148, 172, 182, 185–193]. The essential quantities like site energies and electronic couplings were determined in a time-dependent manner which enables the study of optical properties as well as electronic phenomena with different approaches without employing additional parameters. Furthermore, investigations to spatial correlations are presented which were suggested as possible origin of the observed quantum coherent energy transfer. Alltogether, the present thesis demonstrates, that it is also possible to gain insight into the time-dependent electronic relaxations of LH systems in atomic resolution by using the here applied QM/MM scheme.

Outlook   In the future, other LH systems of interested can be studied as well using the reported approach or improved versions thereof. Especially sub-complexes of phycobilisomes such as PE 545 and PC 645 including bilins are interesting candidates for modeling. Those complexes have shown long-lived coherence times like that observed in the FMO complex but at room temperature [11]. To this end, it is also necessary to extent the QM/MM calculations to much longer times to cover a broad range of conformations in order to model static disorder. Additionally, there is still room for improvements on the technical side, like covering polarization effects already during the MD simulations, include nearby protein side chains into the electronic structure calculations, or even using a high-level ab intio method to overcome the limitations of the semi-empirical ZINDO/S method. Furthermore, instead of performing a ground-state classical path MD simulation, there are methods which allow a excited-state path dynamics for a QM subsystem.

Bibliography

[1] J. Olson. *Photosynthesis in the Archean Era*. Photosynth. Res. **88** (2006) 109.

[2] D. A. Bryant and N.-U. Frigaard. *Prokaryotic photosynthesis and phototrophy illuminated*. Trends Microbiol. **14** (2006) 488 .

[3] R. Buick. *When did oxygenic photosynthesis evolve?* Phil. Trans. R. Soc. B **363** (2008) 2731.

[4] N. Nelson and A. Ben-Shem. *The complex architecture of oxygenic photosynthesis*. Nat. Rev. Mol. Cell Biol. **5** (2004) 971.

[5] R. Kouril, J. P. Dekker and E. J. Boekema. *Supramolecular organization of photosystem II in green plants*. Biochim. Biophys. Acta, Bioenerg. (2011) . In Press, DOI: 10.1016/j.bbabio.2011.05.024.

[6] R. Blankenship, M. Madigan and C. Bauer. *Anoxygenic photosynthetic bacteria*. Advances in photosynthesis (Kluwer Academic Publishers, 1995).

[7] X. Hu, T. Ritz, A. Damjanović, F. Autenrieth and K. Schulten. *Photosynthetic apparatus of purple bacteria*. Q. Rev. Biophys. **35** (2002) 1.

[8] National Renewable Energy Laboratory. *Wikipedia: Solar Two experimental solar power plant*.
http://upload.wikimedia.org/wikipedia/commons/b/b6/Solar_two.jpg.

[9] T. Brixner, J. Stenger, H. M. Vaswani, M. Cho, R. E. Blankenship and G. R. Fleming. *Two-dimensional spectroscopy of electronic couplings in photosynthesis*. Nature **434** (2005) 625.

[10] G. S. Engel, T. R. Calhoun, E. L. Read, T. K. Ahn, T. Mancal, Y. C. Cheng, R. E. Blankenship and G. R. Fleming. *Evidence for wavelike energy transfer through quantum coherence in photosynthetic systems*. Nature **446** (2007) 782.

[11] E. Collini, C. Y. Wong, K. E. Wilk, P. M. Curmi, P. Brumer and G. D. Scholes. *Coherently wired light-harvesting in photosynthetic marine algae at ambient temperature*. Nature **463** (2010) 644.

[12] G. D. Scholes. *Quantum-Coherent Electronic Energy Transfer: Did Nature Think of It First?* J. Phys. Chem. Lett. **1** (2010) 2.

[13] P. Ball. *Physics of life: The dawn of quantum biology*. Nature **474** (2011) 272.

[14] G. D. Scholes. *Quantum biology: Coherence in photosynthesis*. Nat Phys **7** (2011) 448.

[15] R. E. Fenna and B. W. Matthews. *Chlorophyll arrangement in a bacteriochlorophyll protein from Chlorobium limicola*. Nature **258** (1975) 573.

[16] H. Michel. *Three-dimensional crystals of a membrane protein complex : The photosynthetic reaction centre from Rhodopseudomonas viridis*. J. Mol. Biol. **158** (1982) 567 .

[17] J. Deisenhofer, O. Epp, K. Miki, R. Huber and H. Michel. *X-ray structure analysis of a membrane protein complex: Electron density map at 3 Å resolution and a model of the chromophores of the photosynthetic reaction center from Rhodopseudomonas viridis*. J. Mol. Biol. **180** (1984) 385 .

[18] R. J. Cogdell, A. Gall and J. Köhler. *The architecture and function of the light-harvesting apparatus of purple bacteria: From single molecules to in vivo membranes*. Q. Rev. Biophys. **39** (2006) 227.

[19] K. Schulten. *Simplicity and complexity in proteins and nucleic acids* (Dahlem University Press, Berlin, 1999).

[20] X. Hu, A. Damjanović, T. Ritz and K. Schulten. *Architecture and function of the light-harvesting apparatus of purple bacteria*. Proc. Natl. Acad. Sci. USA **95** (1998) 5935.

[21] A. Amunts, O. Drory and N. Nelson. *The structure of a plant photosystem I supercomplex at 3.4 Å resolution*. Nature **447** (2007) 58.

[22] A. Ben-Shem, F. Frolow and N. Nelson. *Crystal structure of plant photosystem I*. Nature **426** (2003) 630.

[23] H.-W. Rémigy, G. Hauska, S. Müller and G. Tsiotis. *The reaction centre from green sulphur bacteria: Progress towards structural elucidation*. Photosynth. Res. **71** (2002) 91.

[24] C. Mullineaux. *Phycobilisome-reaction centre interaction in cyanobacteria*. Photosynth. Res. **95** (2008) 175.

[25] G. D. Scholes. *Biophysics: Green quantum computers*. Nat. Phys. **6** (2010) 402.

[26] D. E. Chandler, J. Hsin, C. B. Harrison, J. Gumbart and K. Schulten. *Intrinsic curvature properties of photosynthetic proteins in chromatophores*. Biophys. J. **95** (2008) 2822 .

[27] R. J. Cogdell, N. W. Isaacs, T. D. Howard, K. McLuskey, N. J. Fraser and S. M. Prince. *How photosynthetic bacteria harvest solar energy*. J. Bacteriol. **181** (1999) 3869.

[28] J. Koepke, X. Hu, C. Muenke, K. Schulten and H. Michel. *The crystal structure of the light harvesting complex II (B800-850) from Rhodospirillum molischianum.* Structure **4** (1996) 581.

[29] A. B. Doust, C. N. Marai, S. J. Harrop, K. E. Wilk, P. M. Curmi and G. D. Scholes. *Developing a structure-function model for the cryptophyte phycoerythrin 545 using ultrahigh resolution crystallography and ultrafast laser spectroscopy.* J. Mol. Biol. **344** (2004) 135.

[30] N. Kamiya and J.-R. Shen. *Crystal structure of oxygen-evolving photosystem II from Thermosynechococcus vulcanus at 3.7-angstrom resolution.* Proc. Natl. Acad. Sci. USA **100** (2003) 98.

[31] C. Larson, C. Seng, L. Lauman, H. Matthies, J. Wen, R. Blankenship and J. Allen. *The three-dimensional structure of the FMO protein from Pelodictyon phaeum and the implications for energy transfer.* Photosynth. Res. **107** (2011) 139.

[32] J. Linnanto, J. Martiskainen, V. Lehtovuori, J. Ihalainen, R. Kananavicius, R. Barbato and J. Korppi-Tommola. *Excitation energy transfer in the LHC-II trimer: a model based on the new 2.72 Å structure.* Photosynth. Res. **87** (2006) 267.

[33] M. Z. Papiz, S. M. Prince, T. Howard, R. J. Cogdell and N. W. Isaacs. *The structure and thermal motion of the B800-850 LH2 complex from Rps. acidophila at 2.0 Å resolution and 100 K: New structural features and functionally relevant motions.* J. Mol. Biol. **326** (2003) 1523 .

[34] I. Fleming. *Absolute configuration and the structure of chlorophyll.* Nature **216** (1967) 151.

[35] J. Linnanto and J. Korppi-Tommola. *Spectroscopic properties of Mg-chlorin, Mg-porphin and chlorophylls a, b, c_1, c_2, c_3 and d studied by semi-empirical and ab initio MO/CI methods.* Phys. Chem. Chem. Phys. **2** (2000) 4962.

[36] J. Linnanto and J. Korppi-Tommola. *Spectroscopic properties of Mg-Chlorin, Mg-bacteriochlorin, and bacteriochlorophylls a, b, c, d, e, f, g, and h studied by semiempirical and ab initio MO/CI methods.* J. Phys. Chem. A **105** (2001) 3855.

[37] D. Niedzwiedzki, J. F. Koscielecki, H. Cong, J. O. Sullivan, G. N. Gibson, R. R. Birge and H. A. Frank. *Ultrafast dynamics and excited state spectra of open-chain carotenoids at room and low temperatures.* J. Phys. Chem. B **111** (2007) 5984.

[38] H. A. Frank and R. J. Cogdell. *Carotenoids in photosynthesis.* Photochem. Photobiol. **63** (1996) 257.

[39] Y. Koyama, M. Kuki, P. O. Andersson and T. Gillbro. *Singlet excited states and the light-harvesting function of carotenoids in bacterial photosynthesis*. Photochem. Photobiol. **63** (1996) 243.

[40] H. Hanzawa, T. Shinomura, K. Inomata, T. Kakiuchi, H. Kinoshita, K. Wada and M. Furuya. *Structural requirement of bilin chromophore for the photosensory specificity of phytochromes A and B*. Proc. Natl. Acad. Sci. U. S. A. **99** (2002) 4725.

[41] C. L. Colyer, C. S. Kinkade, P. J. Viskari and J. P. Landers. *Analysis of cyanobacterial pigments and proteins by electrophoretic and chromatographic methods*. Analytical and Bioanalytical Chemistry **382** (2005) 559.

[42] A. B. Doust, K. E. Wilk, P. M. Curmi and G. D. Scholes. *The photophysics of cryptophyte light-harvesting*. J. Photochem. Photobiol. A: Chem. **184** (2006) 1 .

[43] D. E. Tronrud, M. F. Schmid and B. W. Matthews. *Structure and X-ray amino acid sequence of a bacteriochlorophyll a protein from Prosthecochloris aestuarii refined at 1.9 Å resolution*. J. Mol. Biol. **188** (1986) 443.

[44] S. M. Prince, M. Z. Papiz, A. A. Freer, G. McDermott, A. M. Hawthornthwaite-Lawless, R. J. Cogdell and N. W. Isaacs. *Apoprotein structure in the LH2 complex from Rhodopseudomonas acidophila strain 10050: Modular assembly and protein pigment interactions*. J. Mol. Biol. **268** (1997) 412 .

[45] R. Cogdell, T. Howard, N. Isaacs, K. McLuskey and A. Gardiner. *Structural factors which control the position of the Q(y) absorption band of bacteriochlorophyll a in purple bacterial antenna complexes*. Photosynth. Res. **74** (2002) 135.

[46] J. Eccles and B. Honig. *Charged amino acids as spectroscopic determinants for chlorophyll in vivo*. Proc. Natl. Acad. Sci. U. S. A. **80** (1983) 4959.

[47] M. Cho. *Vibrational solvatochromism and electrochromism: Coarse-grained models and their relationships*. J. Chem. Phys. **130** (2009) 094505.

[48] J. Adolphs, F. Müh, M. E. Madjet and T. Renger. *Calculation of pigment transition energies in the FMO protein: From simplicity to complexity and back*. Photosynth. Res. **95** (2008) 197.

[49] S. Gentemann, N. Y. Nelson, L. Jaquinod, D. J. Nurco, S. H. Leung, C. J. Medforth, K. M. Smith, J. Fajer and D. Holten. *Variations and temperature dependence of the excited state properties of conformationally and electronically perturbed zinc and free base porphyrins*. J. Phys. Chem. B **101** (1997) 1247.

[50] E. Gudowska-Nowak, M. D. Newton and J. Fajer. *Conformational and environmental effects on bacteriochlorophyll optical spectra: Correlations of calculated spectra with structural results*. J. Phys. Chem. **94** (1990) 5795.

[51] B. Robert, R. J. Cogdell and R. van Grondelle. *The light-harvesting system of purple bacteria*. In B. B. Green and W. W. Parson (Eds.), *Light-harvesting antennas in photosynthesis*, volume 13 of *Advances in Photosynthesis* (Kluwer Academic Publishers, Dordrecht, 2003), pages 169–194.

[52] G. McDermott, S. M. Prince, A. A. Freer, A. M. Hawthornthwaite-Lawless, M. Z. Papiz, R. J. Cogdell and N. W. Isaacs. *Crystal structure of an integral membrane light-harvesting complex from photosynthetic bacteria*. Nature **374** (1995) 517.

[53] V. Sundström, T. Pullerits and R. van Grondelle. *Photosynthetic light-arvesting: Reconciling dynamics and structure of purple bacterial LH2 reveals function of photosynthetic unit*. J. Phys. Chem. B **103** (1999) 2327.

[54] T. Pullerits and V. Sundström. *Photosynthetic light-harvesting pigment-protein complexes: Toward understanding how and why*. Acc. Chem. Res. **29** (1996) 381.

[55] M. T. Milder, B. Brüggemann, R. van Grondelle and J. L. Herek. *Revisiting the optical properties of the FMO protein*. Photosynth. Res. **104** (2010) 257.

[56] D. E. Tronrud, J. Wen, L. Gay and R. E. Blankenship. *The structural basis for the difference in absorbance spectra for the FMO antenna protein from various green sulfur bacteria*. Photosynth. Res. **100** (2009) 79.

[57] A. Ishizaki and G. R. Fleming. *Theoretical examination of quantum coherence in a photosynthetic system at physiological temperature*. Proc. Natl. Acad. Sci. USA **106** (2009) 17255.

[58] P. Nalbach, D. Braun and M. Thorwart. *How "quantum" is the exciton dynamics in the Fenna-Matthews-Olson complex?* (2011). ArXiv:1104.2031v1.

[59] J. Adolphs and T. Renger. *How proteins trigger excitation energy transfer in the FMO complex of green sulfur bacteria*. Biophys. J. **91** (2006) 2778.

[60] G. Panitchayangkoon, D. Hayes, K. A. Fransted, J. R. Caram, E. Harel, J. Wen, R. E. Blankenship and G. S. Engel. *Long-lived quantum coherence in photosynthetic complexes at physiological temperature*. Proc. Natl. Acad. Sci. USA **107** (2010) 12766.

[61] P. G. Wolynes. *Some quantum weirdness in physiology*. Proc. Natl. Acad. Sci. USA **106** (2009) 17247.

[62] F. Caruso, A. W. Chin, A. Datta, S. F. Huelga and M. B. Plenio. *Highly efficient energy excitation transfer in light-harvesting complexes: The fundamental role of noise-assisted transport*. J. Chem. Phys. **131** (2009) 105106.

[63] P. Rebentrost, M. Mohseni and A. Aspuru-Guzik. *Role of Quantum Coherence and Environmental Fluctuations in Chromophoric Energy Transport*. J. Phys. Chem. B **113** (2009) 9942.

[64] A. Nazir. *Correlation-Dependent Coherent to Incoherent Transitions in Resonant Energy Transfer Dynamics*. Phys. Rev. Lett. **103** (2009) 146404.

[65] F. Fassioli, A. Nazir and A. Olaya-Castro. *Quantum State Tuning of Energy Transfer in a Correlated Environment*. J. Phys. Chem. Lett. **1** (2010) 2139.

[66] P. Nalbach, J. Eckel and M. Thorwart. *Quantum coherent biomolecular energy transfer with spatially correlated fluctuations*. New J. Phys. **12** (2010) 065043.

[67] J. Strümpfer and K. Schulten. *The Effect of Correlated Bath Fluctuations on Exciton Transfer*. J. Chem. Phys. **134** (2011) 095102.

[68] G. R. Fleming, S. Huelga and M. Plenio. *Focus on Quantum Effects and Noise in Biomolecules*. New J. Phys. **12** (2010) 065002.

[69] D. Abramavicius and S. Mukamel. *Quantum oscillatory exciton migration in photosynthetic reaction centers*. J. Chem. Phys. **133** (2010) 064510.

[70] A. G. Dijkstra, T. L. C. Jansen and J. Knoester. *Localization and coherent dynamics of excitons in the two-dimensional optical spectrum of molecular J-aggregates*. J. Chem. Phys. **128** (2008) 164511.

[71] J. S. Briggs and A. Eisfeld. *Equivalence of quantum and classical coherence in electronic energy transfer*. Phys. Rev. E **83** (2011) 051911.

[72] E. Collini and G. D. Scholes. *Coherent intrachain energy migration in a conjugated polymer at room temperature*. Science **323** (2009) 369.

[73] T. Förster. *Zwischenmolekulare Energiewanderung und Fluoreszenz*. Annalen der Physik **437** (1948) 55.

[74] D. L. Dexter. *A theory of sensitized luminescence in solids*. J. Chem. Phys. **21** (1953) 836.

[75] A. Olaya-Castro and G. D. Scholes. *Energy transfer from Förste-Dexter theory to quantum coherent light-harvesting*. International Reviews in Physical Chemistry **30** (2011) 49.

[76] G. D. Scholes. *Long-range resonance energy transfer in molecular systems*. Annu. Rev. Phys. Chem. **54** (2003) 57.

[77] S. Steigmiller, P. Turina and P. Gräber. *The thermodynamic H+/ATP ratios of the H+-ATPsynthases from chloroplasts and Escherichia coli*. Proc. Natl. Acad. Sci. U. S. A. **105** (2008) 3745.

[78] A. Korostelev, S. Trakhanov, M. Laurberg and H. F. Noller. *Crystal structure of a 70S ribosome-tRNA complex reveals functional interactions and rearrangements.* Cell **126** (2006) 1065.

[79] K. Poole. *Efflux pumps as antimicrobial resistance mechanisms.* Annals of Medicine **39** (2007) 162.

[80] M. Schmidt am Busch, F. Mühh, M. El-Amine Madjet and T. Renger. *The eighth bacteriochlorophyll completes the excitation energy funnel in the FMO protein.* J. Phys. Chem. Lett. **2** (2011) 93.

[81] R. Car and M. Parrinello. *Unified approach for molecular dynamics and density-functional theory.* Phys. Rev. Lett. **55** (1985) 2471.

[82] Y. Yan and O. Kühn. *Geometric correlations and infrared spectrum of adenine-uracil hydrogen bonds in CDCl3 solution.* Phys. Chem. Chem. Phys. **12** (2010) 15695.

[83] D. J. Tannor. *Introduction to quantum mechanics: A time-dependent perspective* (University Science Press, Sausalito, 2007).

[84] P. R. Holland. *The quantum theory of motion* (Cambridge University Press, 1995).

[85] T. L. C. Jansen and J. Knoester. *Waiting Time Dynamics in Two-Dimensional Infrared Spectroscopy.* Acc. Chem. Res. **42** (2009) 1405.

[86] V. May and O. Kühn. *Charge and energy transfer in molecular systems* (Wiley–VCH, Berlin, 2004), 2 edition.

[87] E. Bittner. *Quantum dynamics: Aplications in biological and materials systems* (CRC Press, 2010).

[88] A. R. Leach. *Molecular modelling, principles and applications* (Pearson, Harlow, 2001), 2nd edition.

[89] F. Jensen. *Introduction to computational chemistry* (Wiley, Chichester, 2007), 2nd edition.

[90] P. L. Freddolino, C. B. Harrison, Y. Liu and K. Schulten. *Challenges in protein folding simulations: Timescale, representation, and analysis.* Nature Physics **6** (2010) 751.

[91] H. Grubmüller and K. Schulten. *Special issue: Advances in molecular dynamics simulations.* J. Struct. Biol. **157** (2007) 443.

[92] F. Khalili-Araghi, J. Gumbart, P. C. Wen, M. Sotomayor, E. Tajkhorshid and K. Schulten. *Molecular dynamics simulations of membrane channels and transporters.* Curr. Opin. Struct. Biol. **19** (2009) 128.

[93] N. Koga and S. Takada. *Folding-based molecular simulations reveal mechanisms of the rotary motor F_1-ATPase*. Proc. Natl. Acad. Sci. USA **103** (2006) 5367.

[94] S. Pezeshki, C. Chimerel, A. Bessenov, M. Winterhalter and U. Kleinekathöfer. *Understanding ion conductance on a molecular level: An all-atom modeling of the bacterial porin OmpF*. Biophys. J. **97** (2009) 1898.

[95] U. Kleinekathöfer, B. Isralewitz, M. Dittrich and K. Schulten. *Domain motion of individual F_1-ATPase β-subunits during unbiased molecular dynamics simulations*. J. Phys. Chem. A **115** (2011) 7267.

[96] R. Schulz, A. V. Vargiu, F. Collu, U. Kleinekathöfer and P. Ruggerone. *Functional rotation of the transporter AcrB: Insights into drug extrusion from simulations*. PLoS Comput. Biol. **6** (2010) e1000806.

[97] P. L. Freddolino, F. Liu, M. Gruebele and K. Schulten. *Ten-microsecond molecular dynamics simulation of a fast-folding WW domain*. Biophys. J. **94** (2008) L75 .

[98] J. C. Shelley, M. Y. Shelley, R. C. Reeder, S. Bandyopadhyay and M. L. Klein. *A coarse grain model for phospholipid simulations*. J. Phys. Chem. B **105** (2001) 4464.

[99] L. Verlet. *Computer "Experiments" on Classical Fluids. I. Thermodynamical Properties of Lennard-Jones Molecules*. Phys. Rev. **159** (1967) 98.

[100] E. Hairer, C. Lubich and G. Wanner. *Geometric numerical integration illustrated by the Störmer?Verlet method*. Acta Numerica **12** (2003) 399.

[101] A. D. MacKerell, N. Banavali and N. Foloppe. *Development and current status of the CHARMM force field for nucleic acids*. Biopolymers **56** (2000) 257.

[102] J. Wang, R. M. Wolf, J. W. Caldwell, P. A. Kollman and D. A. Case. *Development and testing of a general amber force field*. J. Comput. Chem. **25** (2004) 1157.

[103] G. A. Kaminski, R. A. Friesner, J. Tirado-Rives and W. L. Jorgensen. *Evaluation and reparametrization of the OPLS-AA force field for proteins via comparison with accurate quantum chemical calculations on peptides*. J. Phys. Chem. B **105** (2001) 6474.

[104] P. L. Freddolino, A. S. Arkhipov, S. B. Larson, A. McPherson and K. Schulten. *Molecular dynamics simulations of the complete satellite tobacco mosaic virus*. Structure **14** (2006) 437 .

[105] J. C. Slater. *Atomic shielding constants*. Phys. Rev. **36** (1930) 57.

[106] E. R. Davidson and D. Feller. *Basis set selection for molecular calculations*. Chemical Reviews **86** (1986) 681.

[107] R. Hoffmann. *An extended Hückel theory. I. Hydrocarbons*. J. Chem. Phys. **39** (1963) 1397.

[108] C. C. J. Roothaan. *New developments in molecular orbital theory*. Rev. Mod. Phys. **23** (1951) 69.

[109] G. G. Hall. *The molecular orbital theory of chemical valency. VIII. A method of calculating ionization potentials*. Proc. R. Soc. A **205** (1951) 541.

[110] J. A. Pople and R. K. Nesbet. *Self-consistent orbitals for radicals*. J. Chem. Phys. **22** (1954) 571.

[111] M. C. Zerner. *Semiempirical molecular orbital methods*, volume 2 of *Reviews in Computational Chemistry*, chapter 8 (VCH, New York, 1991), pages 313–365.

[112] T. Bredow and K. Jug. *Theory and range of modern semiempirical molecular orbital methods*. Theor. Chem. Acc. **113** (2005) 1.

[113] J. A. Pople, D. P. Santry and G. A. Segal. *Approximate self-consistent molecular orbital theory. I. invariant procedures*. J. Chem. Phys. **43** (1965) S129.

[114] J. A. Pople and G. A. Segal. *Approximate self-consistent molecular orbital theory. III. CNDO results for AB[sub 2] and AB[sub 3] systems*. J. Chem. Phys. **44** (1966) 3289.

[115] J. A. Pople, D. L. Beveridge and P. A. Dobosh. *Approximate self-consistent molecular-orbital theory. V. intermediate neglect of differential overlap*. J. Chem. Phys. **47** (1967) 2026.

[116] M. J. S. Dewar and W. Thiel. *Ground states of molecules. 38. The MNDO method. Approximations and parameters*. J. Am. Chem. Soc. **99** (1977) 4899.

[117] M. Kolb and W. Thiel. *Beyond the MNDO model: Methodical considerations and numerical results*. J. Comput. Chem. **14** (1993) 775.

[118] W. Weber and W. Thiel. *Orthogonalization corrections for semiempirical methods*. Theor. Chem. Acc. **103** (2000) 495.

[119] M. J. S. Dewar, E. G. Zoebisch, E. F. Healy and J. J. P. Stewart. *Development and use of quantum mechanical molecular models. 76. AM1: A new general purpose quantum mechanical molecular model*. J. Am. Chem. Soc. **107** (1985) 3902.

[120] J. J. P. Stewart. *Optimization of parameters for semiempirical methods I. Method*. J. Comput. Chem. **10** (1989) 209.

[121] J. A. Pople. *Electron interaction in unsaturated hydrocarbons*. Trans. Faraday Soc. **49** (1953) 1375.

[122] R. Pariser and R. G. Parr. *A semi-empirical theory of the electronic spectra and electronic structure of complex unsaturated molecules. I.* J. Chem. Phys. **21** (1953) 466.

[123] R. Pariser and R. G. Parr. *A semi-empirical theory of the electronic spectra and electronic structure of complex unsaturated molecules. II*. J. Chem. Phys. **21** (1953) 767.

[124] Hypercube, Inc. *HyperChem® Release 7 Manual* (2002).

[125] J. Ridley and M. C. Zerner. *An intermediate neglect of differential overlap technique for spectroscopy: Pyrrole and the azines*. Theor. Chim. Acta **32** (1973) 111.

[126] M. C. Zerner, G. H. Loew, R. F. Kirchner and U. T. Mueller-Westerhoff. *An intermediate neglect of differential overlap technique for spectroscopy of transition-metal complexes. Ferrocene*. J. Am. Chem. Soc. **102** (1980) 589.

[127] A. D. Bacon and M. C. Zerner. *An intermediate neglect of differential overlap theory for transition metal complexes: Fe, Co and Cu chlorides*. Theor. Chem. Acc. **53** (1979) 21.

[128] W. D. Edwards, J. D. Head and M. C. Zerner. *On the electronic excited states of model chlorophyll*. J. Am. Chem. Soc. **104** (1982) 5833.

[129] W. D. Edwards and M. C. Zerner. *Electronic structure of model chlorophyll systems*. Int. J. Quantum Chem. **23** (1983) 1407.

[130] M. A. Thompson, M. C. Zerner and J. Fajer. *Electronic structure of bacteriochlorophyll dimers. 1. Bacteriochlorin models*. J. Phys. Chem. **94** (1990) 3820.

[131] M. R. Silva-Junior and W. Thiel. *Benchmark of electronically excited states for semiempirical methods: MNDO, AM1, PM3, OM1, OM2, OM3, INDO/S, and INDO/S2*. J. Chem. Theory Comput. **6** (2010) 1546.

[132] B. Mennucci and C. Curutchet. *The role of the environment in electronic energy transfer: a molecular modeling perspective*. Phys. Chem. Chem. Phys. **13** (2011) 11538.

[133] J. Neugebauer. *Subsystem-based theoretical spectroscopy of biomolecules and biomolecular assemblies*. ChemPhysChem **10** (2009) 3148.

[134] H. M. Senn and W. Thiel. *QM/MM Methods for Biomolecular Systems*. Angew. Chem., Int. Ed. **48** (2009) 1198.

[135] S. F. Alberti and J. Echave. *Theoretical study of the solvatochromism of a merocyanine dye*. Chem. Phys. **223** (1997) 183 .

[136] P. Hohenberg and W. Kohn. *Inhomogeneous electron gas*. Phys. Rev. **136** (1964) B864.

[137] J. P. Perdew, M. Ernzerhof and K. Burke. *Rationale for mixing exact exchange with density functional approximations*. J. Chem. Phys. **105** (1996) 9982.

[138] E. Runge and E. K. U. Gross. *Density-functional theory for time-dependent systems*. Phys. Rev. Lett. **52** (1984) 997.

[139] I. A. Howard, F. Zutterman, G. Deroover, D. Lamoen and C. V. Alsenoy. *Approaches to calculation of exciton interaction energies for a molecular dimer*. J. Phys. Chem. B **108** (2004) 19155.

[140] J. Linnanto, J. E. I. Korppi-Tommola and V. Helenius. *Electronic States, Absorption Spectrum and Circular Dichroism Spectrum of the Photosynthetic Bacterial LH2 Antenna of Rhodopseudomonas acidophila as Predicted by Exciton Theory and Semiempirical Calculations*. J. Phys. Chem. B **103** (1999) 8739.

[141] M. E. Madjet, A. Abdurahman and T. Renger. *Intermolecular coulomb couplings from ab initio electrostatic potentials: application to optical transitions of strongly coupled pigments in photosynthetic antennae and reaction centers*. J. Phys. Chem. B **110** (2006) 17268.

[142] D. Beljonne, C. Curutchet, G. D. Scholes and R. J. Silbey. *Beyond Förster resonance energy transfer in biological and nanoscale systems*. J. Phys. Chem. B **113** (2009) 6583.

[143] V. Czikklely, H. D. Forsterling and H. Kuhn. *Extended dipole model for aggregates of dye molecules*. Chem. Phys. Lett. **6** (1970) 207 .

[144] T. Renger. *Theory of excitation energy transfer: From structure to function*. Photosynth. Res. **102** (2009) 471.

[145] B. Krueger, G. Scholes and G. Fleming. *Calculation of couplings and energy transfer pathways between the pigments of LH2 by the ab initio transition density cube method*. J. Phys. Chem. B **102** (1998) 5378.

[146] A. Damjanović, H. M. Vaswani, P. Fromme and G. R. Fleming. *Chlorophyll excitations in photosystem I of Synechococcus elongatus*. J. Phys. Chem. B **106** (2002) 10251.

[147] C. Curutchet, A. Muñoz Losa, S. Monti, J. Kongsted, G. D. Scholes and B. Mennucci. *Electronic Energy Transfer in Condensed Phase Studied by a Polarizable QM/MM Model*. J. Chem. Theory Comput. **5** (2009) 1838.

[148] A. Damjanović, I. Kosztin, U. Kleinekathöfer and K. Schulten. *Excitons in a Photosynthetic Light-Harvesting System: A Combined Molecular Dynamics, Quantum Chemistry and Polaron Model Study*. Phys. Rev. E **65** (2002) 031919.

[149] T. Ritz, A. Damjanović, K. Schulten, J.-P. Zhang and Y. Koyama. *Efficient light harvesting through carotenoids*. Photosynth. Res. **66** (2000) 125.

[150] G. D. Scholes, C. Curutchet, B. Mennucci, R. Cammi and J.Tomasi. *How Solvent Controls Electronic Energy Transfer and Light Harvesting*. J. Phys. Chem. B **111** (2007) 6978.

[151] G. R. Fleming and M. Cho. *Chromophore-solvent dynamics*. Annu. Rev. Phys. Chem. **47** (1996) 109.

[152] M. Cho. *Coherent Two-Dimensional Optical Spectroscopy*. Chem. Rev. **108** (2008) 1331.

[153] U. Weiss. *Quantum dissipative systems* (World Scientific, Singapore, 1999), 2nd edition.

[154] M. Cho, H. M. Vaswani, T. Brixner, J. Stenger and G. R. Fleming. *Exciton analysis in 2D electronic spectroscopy*. J. Phys. Chem. B **109** (2005) 10542.

[155] J. Weber. *Fluctuation dissipation theorem*. Phys. Rev. **101** (1956) 1620.

[156] B. U. Felderhof. *On the derivation of the fluctuation-dissipation theorem*. J. Phys. A **11** (1978) 921.

[157] D. Chandler. *Introduction to modern statistical mechanics* (Oxford University Press, 1987).

[158] R. Gutiérrez, R. Caetano, P. B. Woiczikowski, T. Kubař, M. Elstner and G. Cuniberti. *Structural fluctuations and quantum transport through DNA molecular wires: A combined molecular dynamics and model Hamiltonian approach*. New J. Phys. **12** (2010) 023022.

[159] S. A. Egorov, K. F. Everitt and J. L. Skinner. *Quantum dynamics and vibrational relaxation*. J. Phys. Chem. A **103** (1999) 9494.

[160] H. Kim and P. J. Rossky. *Evaluation of quantum correlation functions from classical data*. J. Phys. Chem. B **106** (2002) 8240.

[161] T. Joo, Y. Jia, J.-Y. Yu, M. J. Lang and G. R. Fleming. *Third-order nonlinear time domain probes of solvation dynamics*. J. Chem. Phys. **104** (1996) 6089.

[162] M. Yang, R. Agarwal and G. R. Fleming. *The Mechanism of Energy Transfer in the Antenna of Photosynthetic Purple Bacteria*. J. Photochem. Photobiol. A **142** (2001) 107.

[163] J. Li, B. Williams, C. J. Cramer and D. G. Truhlar. *A class IV charge model for molecular excited states*. J. Chem. Phys. **110** (1999) 724.

[164] J. Linnanto and J. Korppi-Tommola. *Quantum chemical simulation of excited states of chlorophylls, bacteriochlorophylls and their complexes*. Phys. Chem. Chem. Phys. **8** (2006) 663.

[165] J. M. Womick and A. M. Moran. *Exciton Coherence and Energy Transport in the Light-Harvesting Dimers of Allophycocyanin*. J. Phys. Chem. B **113** (2009) 15747.

[166] J. M. Womick, S. A. Miller and A. M. Moran. *Toward the origin of exciton electronic structure in phycobiliproteins*. J. Chem. Phys. **133** (2010) 024507.

[167] A. G. Dijkstra and Y. Tanimura. *Correlated fluctuations in the exciton dynamics and spectroscopy of DNA*. New J. Phys. **12** (2010) 055005.

[168] T. Kubař, U. Kleinekathöfer and M. Elstner. *Solvent fluctuations drive the hole transfer in DNA: A mixed quantum-classical study*. J. Phys. Chem. B **113** (2009) 13107.

[169] Y. C. Cheng and G. R. Fleming. *Dynamics of light harvesting in photosynthesis*. Annu. Rev. Phys. Chem. **60** (2009) 241.

[170] X. Chen and R. J. Silbey. *Effect of correlation of local fluctuations on exciton coherence*. J. Chem. Phys. **132** (2010) 204503.

[171] T. L. C. Jansen and J. Knoester. *Nonadiabatic effects in the two-dimensional infrared spectra of peptides*. J. Phys. Chem. B **110** (2006) 22910.

[172] M. Kobus, R. D. Gorbunov, P. Nguyen and G. Stock. *Nonadiabatic vibrational dynamics and spectroscopy of peptides: A quantum-classical description*. Chem. Phys. **347** (2008) 208.

[173] H. Zhu, V. May, B. Röder and T. Renger. *Linear absorbance of the pheophorbide-a butanediamine dendrimer P-4 in solution: Computational studies using a mixed quantum classical methodology*. J. Chem. Phys. **128** (2008) 154905.

[174] H. Zhu, B. Röder and V. May. *Time and Frequency Resolved Spontaneous Emission from Supramolecular Pheophorbide-a Complexes: A Mixed Quantum Classical Computation*. Chem. Phys. **362** (2009) 19.

[175] R. R. Ernst, G. Bodenhausen and A. Wokaun. *Principles of nuclear magnetic resonance in one and two dimensions* (Oxford University Press, New York, 1995).

[176] P. Rebentrost, M. Mohseni, I. Kassal, S. Lloyd and A. Aspuru-Guzik. *Environment-assisted quantum transport*. New J. Phys. **11** (2009) 033003.

[177] A. Ishizaki and G. R. Fleming. *On the Interpretation of Quantum Coherent Beats Observed in Two-Dimensional Electronic Spectra of Photosynthetic Light Harvesting Complexes*. J. Phys. Chem. B **115** (2011) 6227.

[178] M. Schröder, U. Kleinekathöfer and M. Schreiber. *Calculation of absorption spectra for light-harvesting systems using non-Markovian approaches as well as modified Redfield theory*. J. Chem. Phys. **124** (2006) 084903.

[179] L. Z. Sharp, D. Egorova and W. Domcke. *Efficient and accurate simulations of two-dimensional electronic photon-echo signals: Illustration for a simple model of the Fenna-Matthews-Olson complex*. J. Chem. Phys. **132** (2010) 014501.

[180] R. Martinazzo, K. H. Hughes, F. Martelli and I. Burghardt. *Effective spectral densities for system-environment dynamics at conical intersections: S2-S1 conical intersection in pyrazine*. Chem. Phys. **377** (2010) 21 .

[181] M. Ceccarelli, P. Procacci and M. Marchi. *An ab initio force field for the cofactors of bacterial photosynthesis*. J. Comput. Chem. **24** (2003) 129.

[182] R. C. Walker, I. P. Mercer, I. R. Gould and D. R. Klug. *Comparison of basis set effects and the performance of ab initio and DFT methods for probing equilibrium fluctuations*. J. Comput. Chem. **28** (2007) 478.

[183] G. Zucchelli, R. C. Jennings, F. M. Garlaschi, G. Cinque, R. Bassi and O. Cremonesi. *The calculated in vitro and in vivo chlorophyll a absorption bandshape*. Biophys. J. **82** (2002) 378.

[184] M. Yang, A. Damjanović, H. M. Vaswani and G. R. Fleming. *Energy transfer in photosystem I of cyanobacteria Synechococcus elongatus: Model study with structure-based semi-empirical Hamiltonian and experimental spectral density*. Biophys. J. **85** (2003) 140.

[185] M. C. Zwier, J. M. Shorb and B. P. Krueger. *Hybrid molecular dynamics-quantum mechanics simulations of solute spectral properties in the condensed phase: Evaluation of simulation parameters*. J. Comput. Chem. **28** (2007) 1572.

[186] L. Janosi, I. Kosztin and A. Damjanović. *Theoretical prediction of spectral and optical properties of bacteriochlorophylls in thermally disordered LH2 antenna complexes*. J. Chem. Phys. **125** (2006) 014903.

[187] I. Kosztin and K. Schulten. *Molecular dynamics methods for bioelectronic systems in photosynthesis*. In T. Aartsma and J. Matysik (Eds.), *Biophysical Techniques in Photosynthesis II*, volume 26 of *Advances in photosynthesis and respiration* (Springer, Dordrecht, 2008), pages 445–464.

[188] J. S. Kwon, C. M. Choi, H. J. Kim, N. J. Kim, J. Jang and M. Yang. *Combined theoretical modeling of photoexcitation spectrum of an isolated protonated tyrosine*. J. Phys. Chem. A **113** (2009) 2715.

[189] I. P. Mercer, I. R. Gould and D. R. Klug. *Optical properties of solvated molecules calculated by a QMMM methods: Chlorophyll a and Bacteriochlorophyll a*. Faraday Discuss. **108** (1997) 51.

[190] I. P. Mercer, I. R. Gould and D. R. Klug. *A Quantum Mechanical/Molecular Mechanical Approach to Relaxation Dynamics: Calculation of the Optical Properties of Solvated Bacteriochlorophyll-a*. J. Phys. Chem. B **103** (1999) 7720.

[191] S. Vasil'ev and D. Bruce. *A protein dynamics study of photosystem II: The effects of protein conformation on reaction center function*. Biophys. J. **90** (2006) 3062.

[192] H. Fujisaki and G. Stock. *Dynamic treatment of vibrational energy relaxation in heterogeneous and fluctuating environment*. J. Chem. Phys. **129** (2008) 134110.

[193] J. Jiang, D. Abramavicius, B. M. Bulheller, J. D. Hirst and S. Mukamel. *Ultraviolet spectroscopy of protein backbone transitions in aqueous solution: Combined QM and MM simulations*. J. Phys. Chem. B **114** (2010) 8270.

5. Publications Concerning the LH2 Complex

I have started my research on LH systems with the LH2 complex of the purple bacteria *Rhodospirillum molischianum*. This complex is circular shaped and contains 24 BChl*a* molecules distributed in two rings with 16 and eight BChls, respectively. An introduction to this complex is given in the section 2.2.1. During the preparation of the system for the MD simulations[1], special attention was drawn to the interface between protein structures and the surrounding membrane to ensure that water molecules were not penetrating. After equilibrium of the system had been achieved, each single MD step was recorded, i.e., a trajectory of different conformations of the BChl*a* molecules with 1 fs resolution in time was gained, with a total length of 12 ps. Subsequent to this trajectory calculation, different analyses were performed which are presented in the next section 5.1. On the one hand, electronic structure calculation were carried out for each BChl and for each snapshot mainly on the ZINDO/S-CIS level, i.e. 288,000 calculation had to be performed. Furthermore, different radii of the environment, which was represented as classical point charges, were taken into account. Form those quantum chemistry calculations, we gained the site energies and the TDMs for each step in the trajectory. On the other hand, based on the atomic motion, electronic couplings between the BChls along the trajectory were calculated using four different approaches. Due to observed quantum coherences in energy transfer in the FMO complex, correlations in atomic motion and site energies has been proposed as possible origin. For this reason, both correlations were calculated. In the next step the time-dependent quantities site energies and couplings were combined to a time-dependent Hamiltonian. Based on that, the dynamics of the exciton energies were calculated in the section 5.2

---

[1]The LH2 complex is embedded in a membrane and below and above surrounded by water.

and moreover the absorption spectra. The fluctuations of the site energies can be analyzed in terms of an autocorrelation function and furthermore employed to determine the spectral density (see section 5.1). Subsequently, a fitting procedure to the autocorrelation function was developed and applied which in the end provides parameters and an analytic form of the spectral densities of the two rings in the LH2 complex. Lastly, the spectral densities were used to calculate exciton dynamics and the linear absorption spectrum of the complete two-ring system on the basis of a time-averaged Hamiltonian.

5.1. The Journal of Physical Chemistry B (2010): Time-Dependent Atomistic View on The Electronic Relaxation in Light-Harvesting System II

Authors: C. Olbrich and U. Kleinekathöfer

Time-Dependent Atomistic View on the Electronic Relaxation in Light-Harvesting System II

Carsten Olbrich and Ulrich Kleinekathöfer*

School of Engineering and Science, Jacobs University Bremen, Campus Ring 1, 28759 Bremen, Germany

Received: July 14, 2010; Revised Manuscript Received: August 16, 2010

Aiming at a better understanding of the molecular details in light absorption during photosynthesis, spatial and temporal correlation functions as well as spectral densities have been determined. At the focus of the present study are the light-harvesting II complexes of the purple bacterium *Rhodospirillum molischianum*. The calculations are based on a time-dependent combination of molecular dynamics simulations and quantum chemistry methods. Using a 12 ps long trajectory, different quantum chemical methods have been compared to each other. Furthermore, several approaches to determine the couplings between the individual chromophores have been tested. Correlations between energy gap fluctuations of different individual pigments are analyzed but found to be negligible. From the energy gap fluctuations, spectral densities are extracted which serve as input for calculations of optical properties and exciton dynamics. To this end, the spectral densities are tested by determining the linear absorption of the complete two-ring system. One important difference from earlier studies is given by the severely extended length of the trajectory along which the quantum chemical calculations have been performed. Due to this extension, more accurate and reliable data have been obtained in the low frequency regime which is important in the dynamics of electronic relaxation.

Introduction

The photoexcitation of a chromophore in light-harvesting (LH) systems represents the primary step in photosynthesis. Over the past years and even decades, the absorption properties and energy transfer process in LH systems have been elucidated to quite some detail.[1−5] Recent experiments showed strong evidence that excitonic coherences are protected by the protein environment[6−9] and therefore spurred an even enhanced interest in these systems.[10] The surprising feature of the quantum-coherent energy transfer in these systems is the fact that the coherences survive for several hundreds of femtoseconds in such a complex biological system. Several studies recently investigated in detail the influence of the environment on the quantum coherences in terms of quantum efficiency,[11] noise-assisted transport,[12,13] as well as entanglement and other nonclassical effects.[14]

To date, optical spectra of several LH systems are well characterized experimentally and modeled theoretically.[2,15,16] Nevertheless, most of these models of static as well as transient spectra are not based on calculations on an atomic level. Femtosecond techniques of nonlinear spectroscopy have been used to probe the exciton dynamics, for example, in light-harvesting II (LH2) complexes in detail.[17−23] In addition, single-molecule studies of LH2 complexes have been performed as well,[2,24−28] having the big advantage of resolving spectral features which are hidden otherwise in the ensemble average.

Especially the light-harvesting systems of purple bacteria have been thoroughly studied experimentally as well as theoretically.[1,15,16,29−32] Many computational investigations on the optical properties are based on density-matrix methods with parameters extracted from experiments. Other studies are based on the available crystal structures.[33−37] First, high-resolution structures of a photosynthetic reaction center were resolved in 1985.[38] The light-harvesting I (LH1) complex surrounds the reaction center,

while at the same time most purple bacteria contain the secondary light-harvesting system, LH2, which neighbors LH1.[1] The X-ray structural data of two of these LH2 complexes (*Rhodopseudomonas (Rps.) acidophila*[39,40] and *Rhodospirillum (Rs.) molischianum*[41]) opened the possibility to study their structure−function relationship in atomic detail.[15,29,31]

The present study focuses on the LH2 system of *Rs. molischianum*. The optically active entities in these LH complexes are bacteriochlorophyll a (BChl a) molecules as well as carotenoids. As shown in Figure 1, the BChls are arranged in two rings absorbing at around 850 and 800 nm and therefore are called B850 and B800. The additional carotenoids absorb at lower frequencies but are not in the focus of the present study. Eight $\alpha\beta$ heterodimers form the B850 ring, while the B800 ring consists of eight weakly coupled monomers, leading to an 8-fold symmetry of the whole complex. Not only is the number of chromophores different in the two rings but also their environments. The binding pockets of the BChls in the B850 rings are mainly hydrophobic. In contrast, those of the B800 ring are predominantly hydrophilic.[41] These different environments are in turn responsible for the spectral shifts in the optical properties of the BChls.

Classical molecular dynamics (MD) simulations allow the computational investigation of arrangements, conformational motions, and electronic ground state properties of systems of the size of LH systems or even larger.[43] To obtain the optical properties of LH systems, quantum calculations including excited states are required. To be able to describe excitation energy transport (EET) and optical properties, the site energies of the individual BChls and their electronic couplings need to be determined (see, for example, the review in ref 44). Within the one-exciton model, the site energies of the system are equivalent to the differences between ground and first optically allowed state Q_y.[45] Because of the size of the LH complexes, one usually treats them in a subsystem-based approach; i.e., the individual chromophores are treated separately and then the electronic coupling is added. Furthermore, individual BChls are

* To whom correspondence should be addressed. E-mail: u.kleinekathoefer@jacobs-university.de.
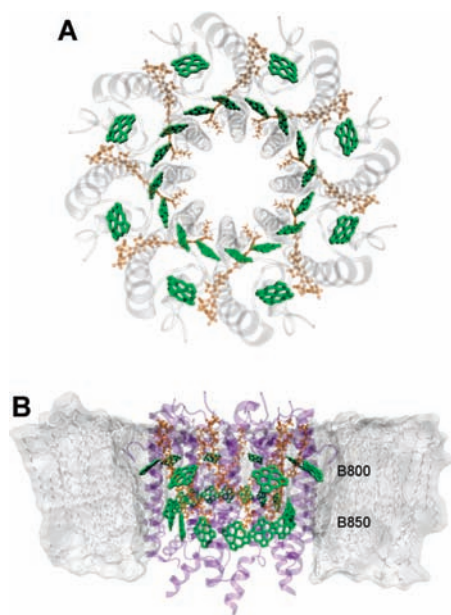
Figure 1. Top and side views of the simulated system. Panel A: (perspective) top view clearly showing the two rings with 8 and 16 BChls (green), i.e., the B800 and B850 rings, respectively. The eight carotenoids are displayed in brown, while the protein structure is indicated in a light gray cartoon representation. Panel B: The same as in the upper panel but as a side view including a cut through the membrane. Figures rendered using VMD.[42]

already complex molecules and thus are often treated on a semiempirical level and a number of times using Zerner's intermediate neglect of differential orbital with parameters for spectroscopic properties (ZINDO/S).[46−48] In this approximation, it is even possible to determine the electronic states of complete LH rings for a few conformations.[30,49] By now, there is quite a list of publications using ZINDO/S or very similar techniques within the subsystem-based approach for LH complexes[30,33−35,50−55] and other systems as well, e.g., refs 56−58. ZINDO/S-CIS is well suited for the calculation of vertical excitation energies when combined with the configuration interaction formalism at the single configuration level (ZINDO/S-CIS). One of the biggest advantages of ZINDO/S-CIS is its computational performance for molecules of the size of BChl. Therefore, it can be employed to calculate the energy gap between the ground and excited state energies along MD trajectories.[52,54,57,58] This kind of combination of MD simulation and quantum chemical techniques is, of course, not limited to a certain type of electronic structure calculations but can be performed with different approaches.[31,59−64] The dynamics of the electronic states along the MD trajectory then allow for the calculation of the spectral density or similar properties which in turn allow for the computation of spectra and EET dynamics.[31,52,54,65] Alternatively, the time-dependent site energies and their couplings can be used in a wave packet calculation directly.[63,66−69]

In addition to the energies of the individual BChls, one needs to calculate the couplings among them. In the Förster formula for EET, the coupling is assumed to be dominated by the Coulomb interaction and is calculated using the point-dipole approximation (PDA). This approximation is well-known to fail for shorter distances.[56,70−72] One alternative is to calculate the

energy of an interacting dimer and then use Davidov's formula to determine the coupling. In the context of LH systems, this supermolecule approach is often combined with the ZINDO/S approach.[33,53] Significant progress has also been achieved in the direct quantum mechanical calculation of the Coulomb interaction between two molecules. At this point, one certainly needs to mention the accurate but numerically expensive ab initio transition density cube method[73] which has also been applied to LH systems.[74] Renger and co-workers developed the method of transition charges from electrostatic potentials (TrEsp)[71,75] which was applied to different light-harvesting systems[37] including the special pair[37] and calculations of the solvatochromic shifts.[76] A simplification of this approach is the so-called extended dipole approximation (EDA) in which the molecular transition charge density distribution is approximated by a dipole consisting of one positive and one negative charge.[56,71] In many studies, the effects of the environment are not taken into account in the calculation of the interaction energy and then it has to be corrected for afterward. This can be done by a constant factor[75] or more accurately using a distance-dependent correction developed by Scholes and co-workers.[72,77]

The present contribution begins with a description of the MD calculations before different electronic structure methods of ground and excited state energy calculations are detailed and tested. Furthermore, the effect of the environment is discussed. This is also an issue while determining the electronic couplings between the individual pigments. In the subsequent section, spatial as well as temporal correlations between the fluctuations of the energy gaps of neighboring BChls are investigated. The temporal correlations are afterward used to determine the so-called spectral density which describes the frequency-dependent coupling of the system modes to the environment. Finally, this spectral density is used to determine the linear absorption spectrum of the studied LH2 system.

Molecular Dynamics

In an initial step of the present multiscale approach, a MD simulation of the LH2 complex embedded in a membrane environment was performed similar to the setup detailed in ref 31. To this end, the missing hydrogen atoms were added to the crystal structure of *Rs. molishianum* (PDB: 1LGH).[41] Thereafter, the pigment−protein complex has been embedded in a POPC lipid bilayer with about 30 Å of water on both sides. By adding 16 $Cl^−$ ions to the bulk water, the system was neutralized. The complete MD system as shown in Figure 1 consists of 114 011 atoms. The MD simulations of the LH2 complex using the CHARMM27 force field[78,79] for lipids, water, and protein were carried out using the NAMD program package.[80] As a water model, the TIP3P water approach was employed, while force field parameters for the BChls and lycopenes have been reported in ref 31.

Subsequent to an energy minimization, the system was equilibrated in several steps at room temperature (300 K) and normal pressure (1 atm) in a NpT ensemble using periodic boundary conditions. Furthermore, we used the particle mesh Ewald (PME) method and a 2 fs time step together with the SHAKE constraint on all hydrogen atoms. Initially, the complete system was kept fix except the lipid tails which were equilibrated for 2 ns. In the step thereafter, only the LH2 complex was constrained for another 4 ns. During this equilibration step, a repulsive potential has been applied to the water molecules preventing them from penetrating into the protein−membrane interface. These steps were performed in order to permit lipids, water, and ions to adapt to the protein in its crystal form.
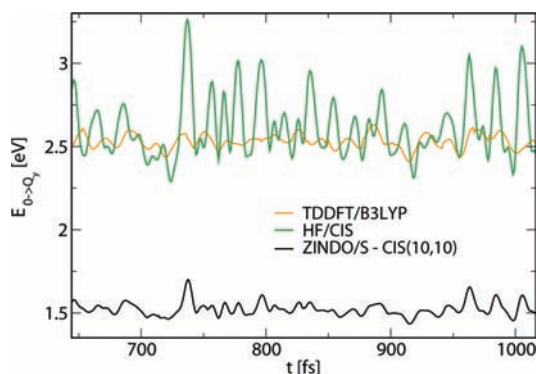
67

Figure 2. Time evolution of the energy gap between ground and Q_y state using different electronic structure methods from HF-based CIS over TDDFT to ZINDO/S-CIS.

Figure 3. Dependence of the site energies on the size of the charge cloud.

Thereafter, another equilibration of 2 ns without any constraints followed. At last, a 12 ps long production run with a time step of 1 fs was carried out. The atomic coordinates were recorded every time step, resulting in 12 000 snapshots which were channeled into the QM calculations afterward. The average center-to-center distance of the BChls of the B850 ring during the final simulation was found to be 9.70 Å within and 8.85 Å between the $\alpha\beta$ heterodimers. The average distance between the centers of the BChl belonging to the B800 ring was measured to be 22.25 Å. These values are close to those reported in ref 31 and differ slightly from the respective crystal structure values of 9.2 and 8.9 Å for the $\alpha\beta$ heterodimers and 22.0 Å for the BChls belonging to the B800 ring.[41]

Site Energies

In subsystem-based approaches, key components are the ground and excited state energies of the individual subsystems. Together with the electronic couplings which will be detailed in the next section, this leads to a time-dependent Hamiltonian. This Hamiltonian can be employed in a subsequent step to either calculate the spectral density and from that the optical properties using a density matrix approach[31,52,54] or to directly use wave packet dynamics on a time-dependent Hamiltonian, e.g., in the Ehrenfest approximations.[66−69]

In order to increase efficiency and since the optical properties of BChls are determined by the cyclic conjugated π-electron system, the quantum system was restricted to a truncated structure of the BChl molecule. To this end, each terminal CH_3 and CH_2CH_3 group as well as the pythyl tails were replaced by hydrogen atoms. Such truncation schemes have been employed previously and were tested during the present investigation, yielding only slight changes in the calculated energy differences.[30,52,60] As in previous studies,[52,54,57,58] the quantum chemical calculations were performed on the semiempirical ZINDO/S-CIS level. Its accuracy for vertical excitation energies has been investigated recently and the method has been found to be quite accurate for low-lying excited states.[81] For each individual BChl out of the B850 ring, the time evolution of the energy gap between the ground and first excited, i.e., Q_y state, is shown in Figure 2 on the ZINDO/S-CIS level with an active space of the 10 highest occupied and the 10 lowest unoccupied states denoted by (10,10) in the following. The active space size of (10,10) agrees well with the size used in the ZINDO/S parametrization.[46,47] Furthermore, earlier studies on gas phase BChl molecules[50,53] found
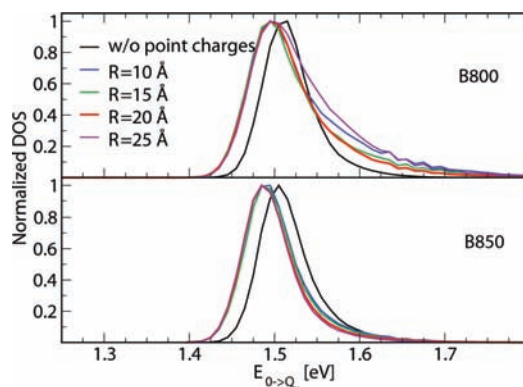
a similar but slightly larger space of (15,15) to agree best with experimental data. In addition, in Figure 2, the energy gap is shown using the time-dependent density functional theory (TDDFT) with the B3LYP functional and using the Hartree−Fock based configuration interaction scheme with single excitations (HF-CIS). In the latter two approaches, the STO-3G basis set was used. Since the peak position of the B850 absorption band is around 1.5 eV, it is clear that the absolute gap energies for the TDDFT and CIS calculations are overestimated by at least 1 eV, while the values based on the ZINDO/S-CIS calculation yield a decent agreement with experiments (see below). The gap fluctuations for the HF-CIS method are certainly larger than those for the TDDFT calculations which are usually superior due to the inclusion of electron interaction effects. The sizes of the fluctuations on the TDDFT and ZINDO/S levels, on the other hand, are quite comparable. Nevertheless, the computational effort is quite different between the latter two approaches. On a 2.5 GHz Xeon processor using the ORCA code (University Bonn, Germany),[82] an energy gap can be calculated using ZINDO/S-CIS (10,10) within 5 s, using TDDFT within 16 min, and using the HF-CIS method within 30 min. This clearly shows that the evaluation along a longer MD trajectory is much less time-consuming using the ZINDO/S-CIS. Nevertheless, the HF-CIS approach has been employed for this purpose in previous studies but on rather short trajectories or smaller systems.[31,60,61]

In a next step, the surrounding partial charges from the MD simulation were taken into account during the electronic structure calculations as well. Figure 3 shows the effect of these external charges as a function of the maximum distance from the chlorophyll molecules, again averaged over the molecules within one ring. The distance R here does not denote the radius of a spherical charge cloud but rather the maximal distance of the charges from any of the BChl atoms. Especially for small values of the distance, this charge cloud has a more elliptical shape because of the shape of the BChl molecules. Concerning the B850 ring, the inclusion of the external charges leads to a red shift of the peak position of about 20 meV and a slightly more pronounced asymmetry of the DOS. Starting with a charge radius of 10 Å, no major differences are visible in the DOS. The situation is slightly different for the B800 ring. The peak position shows a red shift of 15 meV, but the high-energy wing of the DOS is more dependent on the charge radius. In the following, we will use a radius of 20 Å for practical reasons, though there is still some difference for the DOS using a charge radius of 20 and 25 Å. Comparing the peak position of the B850

ring with that of experiment (see below), we conclude that the ZINDO/S-CIS (10,10) calculations do reproduce the experimental data quite reasonably.

Electronic Coupling

In addition to the energies of the individual BChls, one needs to calculate the couplings among them. A collection of different values for the couplings in purple bacteria is, for example, given in ref 2. Several approaches and approximations to calculate the EET coupling were mentioned in the Introduction. Four of these theories are applied in the following to determine the coupling for the present study of the LH2 complex. In the Förster approach, the EET coupling is assumed to be dominated by the Coulomb interaction which is determined using point dipoles, i.e., the PDA. In the present study, a screening factor f is used which will be detailed below. Despite its well-known failure for shorter distances, the PDA has been applied to several LH systems mainly for reasons of simplicity.[56,70–72] In the results shown below, the transition dipole moments have been determined in the ZINDO/S calculations, as detailed in the previous section. Their absolute value has been rescaled by a factor of 0.558 to obtain an average value of 6.3 D which corresponds to the experimentally measured value.[83]

To get an improved description of the spatial arrangement of the charges, one can approximate the transition charge density by a dipole consisting of two partial charges $\pm\delta$ of opposite sign.[56,75,84] The use of extended dipoles corresponds to the EDA which is used here together with a screening factor f. The directions of the dipoles were adopted from the ZINDO/S calculations as in the case of the PDA, while the charges have equal distances from the central Mg atoms belonging to each BChl molecule. Furthermore, the values of 10.2 Å for the dipole length and of 0.13 e (elementary charges) for δ were adapted from the literature.[71]

As already mentioned in the Introduction, Renger and co-workers developed the TrEsp method.[71,75] In this approach, the transition density of pigment m is described using atomic transition charges q_I^T that are localized at the respective pigment, i.e., $\rho(\mathbf{r}) = \sum_I q_I^T \delta(\mathbf{r} - \mathbf{R}_m^I)$, where $\mathbf{R}_m^I$ denotes the coordinates of the Ith atom of BChl m. The coupling between two pigment molecules is then given by

$$V_{nm} = \frac{f}{4\pi\varepsilon_0} \sum_{I,J} \frac{q_I^T \cdot q_J^T}{|\mathbf{R}_m^I - \mathbf{R}_n^J|} \qquad (1)$$

The atomic partial charges can be calculated using different electronic structure methods. In ref 71, these charges are given for BChl a and Chl a molecules in their equilibrium structures calculated using HF-CIS and TDDFT/B3LYP. Used in the present study are the charges calculated by the later method using a scaling factor of 0.732 to match the experimental value of the dipole moment of 6.3 D.[83] This rescaling was already suggested by the developers of the TrEsp method.[71] Furthermore, it is assumed that the charges do not change with varying molecular geometry and we therefore employ the fixed transition charge values for the calculations along the MD trajectory. This approximation is quite plausible, since the molecular geometries in an equilibrium MD simulation should fluctuate around the equilibrium positions. Despite this assumption, the TrEsp method is the most sophisticated among the ones presented here and also among the most accurate ones known in the literature.[71,75]

In an alternative method to calculate the electronic coupling, the supermolecule approach is adopted[44] and here referred to as the dimer method. To this end, two energies of a BChl dimer $\varepsilon_{1,2}$ consisting of monomers m and n are calculated using the ZINDO/S-CIS method without external charges. At the same time, the respective monomer energies $E_{n,m}$ are calculated at the same level of accuracy. The coupling energy V_{nm} can then be calculated according to[44,85]

$$V_{nm} = \frac{f}{2}\sqrt{(\varepsilon_1 - \varepsilon_2)^2 - (E_n - E_m)^2} \qquad (2)$$

Though external point charges could be included in the ZINDO/S calculations for the couplings as well, they would only account for a minor effect on the couplings through changes in the orbital energies. The more important electronic polarization effects would still be neglected due to the use of nonpolarizable point charges. One possible solution would be to couple the ZINDO/S calculations to a polarizable force field, as performed in ref 85. In the present study, we simply estimate the environmental polarization effects by the scaling factor f as done for the other schemes to calculate the EET coupling. The couplings calculated in this manner depend on four estimated energies calculated on the ZINDO/S level assuming that this semiempirical method applies similarly well to the monomer and the dimer energies. Nevertheless, it offers a systematic way of estimating the coupling energies and has been applied a number of times to LH complexes[33,35,53] or similar systems.[56]

In a next step, we focus on the screening factor f. In the Förster theory, this factor is simply given by $f_F = 1/n^2$, where n is the refractive index. Alternatively, in Onsager theory, dipoles are assumed to be in spherical cavities and a screening factor of $f_O = 3/(2n^2 + 1)$ is predicted. Scholes et al.[77] performed a detailed analysis of screening factors and found that, despite the range of sizes, shapes, and orientations of the donor and acceptor molecules, a trend is evident in the solvent screening f. Fitting their results, Scholes et al.[77] found a distance-dependent screening factor

$$f(R_{mn}) = A \exp(-BR_{mn}) + f_0 \qquad (3)$$

with $A = 2.68$, $B = 0.27$ 1/Å, and $f_0 = 0.54$. At large distances ($R_{mn} > 20$ Å), this function reaches the value $f = 0.54$ which is situated in between the values used in the Förster theory f_F and the Onsager value f_O assuming a protein environment with $n^2 = 2$. This distance-dependent solvent-screening factor f is included in all results presented below.

Similar to the results for the site energies, the time dependence of a specific interdimer coupling determined using the PDA, the EDA, the TrEsp method, and the dimer approach along a piece of the MD trajectory is given in Figure 4. The various formalisms differ quite drastically in their average value and the fluctuations around these values. Instead of analyzing this part of the trajectory in detail, we report in Figure 5 the probability of finding a certain B850 coupling value along the studied trajectory. The dimer approach results in the largest coupling values with a splitting into intra- and interdimer couplings. In the case of using the full active space for the ZINDO/S-CIS method, the average values are 0.0358 eV (289 cm^{-1}) and 0.0500 eV (403 cm^{-1}), respectively. A reduced active space would lead to even larger couplings. Already in previous comparisons of coupling values, the dimer approach was reported to yield the largest values.[2] In comparison to this,
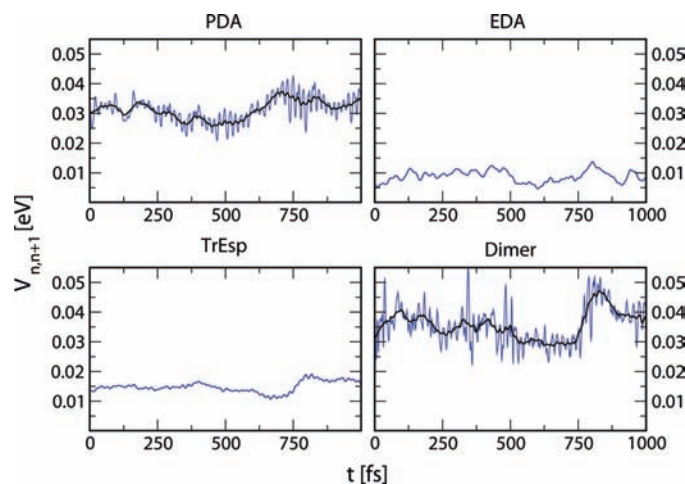
Figure 4. Part of the time evolution belonging to the electronic couplings within the B850 ring for the different methods as detailed in the text for an interdimer example (blue line). The black line represents a running average to guide the eye.
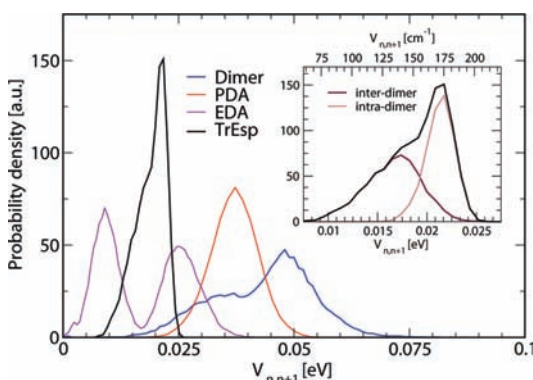

Figure 5. Probability distribution of the electronic couplings in the B850 ring along the MD trajectory in arbitrary units. The inset shows the splitting into intra- and interdimer couplings for the TrEsp method.

the PDA shows a much smaller average coupling value of 0.034 eV (274 cm^{-1}) with a much narrower distribution and without a significant splitting into intra- and interdimer couplings. This changes drastically with the EDA, yielding coupling values of 0.025 eV (202 cm^{-1}) and 0.0091 eV (73 cm^{-1}) for the intra- and interdimer couplings, respectively. For some configurations reported in the literature, the EDA and TrEsp methods yield very similar results.[71] In the present study, this is not the case. The obtained average values are 0.021 eV (173 cm^{-1}) for the intradimer couplings and 0.017 eV (140 cm^{-1}) for the interdimer ones. These values are lower than those reported in the literature. Comparing them to the 238 and 213 cm^{-1} values for the respective properties in *Rps. acidophila* calculated using the sophisticated transition density cube method without environmental screening,[73] the difference appears not so large anymore. If one would scale the values by Krueger et al. using eq 3, they would actually get rather close to those values obtained in the present study.

Let us now turn to the B800 ring which is often treated as a system of uncoupled BChls.[52] In this case, the PDA and EDA yield quite similar values of $(-1.00 \pm 0.19) \times 10^{-3}$ and $(-1.10 \pm 0.15) \times 10^{-3}$ eV, respectively. The coupling values calculated

using the TrEsp method are slightly higher in absolute value $(-1.17 \pm 0.14) \times 10^{-3}$ eV resulting from marginally different dipole orientations in this approach. For a description of the complete system, it is also necessary to determine the coupling values between the B850 and B800 rings. The geometry is such that there are two B850 BChls, one belonging to subunit j and one belonging to $j + 1$ of the double ring system, which are rather close to one B800 BChl belonging to the subunits j. Therefore, $V_{\alpha,j+1}^{B800,j}$ denotes the coupling between the B850-α monomer of subunit $j + 1$ and the B800 BChl of subunit j. Furthermore, $V_{\beta,j}^{B800,j}$ describes the coupling between the B850-β BChl and the B800 BChl within the same subunit. The average distance from the α BChl of subunit $j + 1$ to the B800 BChl in subunit j is 19.2 Å which is a bit smaller than 20.3 Å obtained for the intrasubunit distances. Therefore, the values for $V_{\beta,j}^{B800,j}$ are smaller than the absolute values for $V_{\alpha,j+1}^{B800,j}$. One should note the different signs due to the directions of the dipole moments. Using the PDA, values of $V_{\alpha,j+1}^{B800,j} = (-1.69 \pm 0.20) \times 10^{-3}$ eV and $V_{\beta,j}^{B800,j} = (1.33 \pm 0.16) \times 10^{-3}$ eV are determined, showing rather large fluctuations. If in turn the EDA is employed, the absolute coupling values are somewhat smaller, yielding $V_{\alpha,j+1}^{B800,j} = (-1.57 \pm 0.10) \times 10^{-3}$ eV and $V_{\beta,j}^{B800,j} = (1.26 \pm 0.07) \times 10^{-3}$ eV. The TrEsp method results in rather similar values of $V_{\alpha,j+1}^{B800,j} = (-1.71 \pm 0.11) \times 10^{-3}$ eV and $V_{\alpha,j}^{B800,j} = (1.28 \pm 0.10) \times 10^{-3}$ eV due to the large separations between the pigments.

Spatial and Temporal Correlations of Site Energies

Recently, the question of correlations between the classical and quantum motions as well as between the classical motions of individual pigments in light-harvesting systems became of quite some interest again.[86] To this end, it is important to investigate spatial as well as temporal correlations of the electronic energy gap fluctuations of the individual sites. In a simplified picture, spatial correlations refer to in-phase movements of neighboring sites which in turn would lead to greatly enhanced transfer rates. Using the energy gap ΔE_i of the individual BChl i between the ground and the Q_y state, the correlation coefficients C_{ij}, also called cross-correlation or normalized covariance, are defined as[87,88]

Olbrich and Kleinekathöfer

$$C_{ij} = \frac{\langle (\Delta E_i - \langle \Delta E_i \rangle) \cdot (\Delta E_j - \langle \Delta E_j \rangle) \rangle}{\sqrt{\langle (\Delta E_i - \langle \Delta E_i \rangle)^2 \rangle \cdot \langle (\Delta E_j - \langle \Delta E_j \rangle)^2 \rangle}} \qquad (4)$$

In the case of site energy correlations of individual nucleobases in DNA, for example, a correlation of 0.7 between directly neighboring sites and 0.4 between second neighbors was found.[88] In Figure 6, the results for the present system are shown. The value on the diagonal is by definition equal to 1, while no significant values can be seen for any of the other entries of the correlation matrix. Thus, no correlated movements of the site energies neither in the B850 ring nor in the B800 ring were found.

To emphasize these results, we also studied the correlations of atomic fluctuations between the atoms within individual BChls and between neighboring BChls. The formula for the correlation matrix is the same as that in eq 4 but with atomic positions instead of energy gaps.[87] The correlation coefficients as a function of distance between the two corresponding atoms are shown in Figure 7. Hydrogen atoms were not included in this analysis which was restricted to the cores of the BChl as discussed above. Within one BChl, there are of course correlations between the movements of individual atoms which can be fitted to a Gaussian distance dependence, $\exp(-k_1 x^2)$, with $k_1 = 0.0190$ Å^{-2}. The closest distance of atoms belonging to different BChls is roughly 4 Å. The corresponding curve can be approximated using an exponential dependence, $\exp(-k_2 x)$, with $k_2 = 0.361$ Å^{-1}, as can also be seen in Figure 7. Already at this distance, the correlation between the atoms belonging to different BChls is not much larger than the fluctuations of the correlation coefficients at larger distances. At typical center-to-center distances between neighboring BChls of at least 8 Å, the fluctuations of the correlation coefficients are basically the same as those at much larger distances; i.e., there is no correlation present. Therefore, this finding which can be directly extracted from the MD simulations is in close agreement with the above-described vanishing spatial correlation between the movement of the energy gaps.

After analyzing the spatial correlations, we now focus on temporal correlations. This is also done to be able to calculate the spectral density in a subsequent step. In principle, their is a separate autocorrelation function for each chromophore. Because of symmetry reasons and to get improved statistics, we assume here that all BChls in either the B850 or the B800 ring behave very similar. Therefore, we only define two correlation functions, $C^{B850}(t)$ and $C^{B800}(t)$ belonging to the BChls in the B850 and in the B800 ring, respectively. To be able to determine the correlation function starting with a discrete time series, one needs the energy gaps $\Delta E_j(t_i)$ for BChl j at time steps t_i. Including an average over the equivalent BChls in the same ring, one gets[31]

$$C(t_i) = \frac{1}{M} \sum_{j=1}^{M} \left[\frac{1}{N-i} \sum_{k=1}^{N-i} \Delta E_j(t_i + t_k) \Delta E_j(t_k) \right] \qquad (5)$$

The number M corresponds to 16 for the B850 ring and to 8 for the B800 ring in the present bacterium. As mentioned above, the time step between the individual snapshots in the MD and ZINDO/S calculations is 1 fs. The available time series contains 12.000 points. Since the correlation functions at times longer than 2 ps basically consist of noise or correlations which are very hard to distinguish from noise, 4 ps long windows were used to determine correlation functions of 2 ps length. The
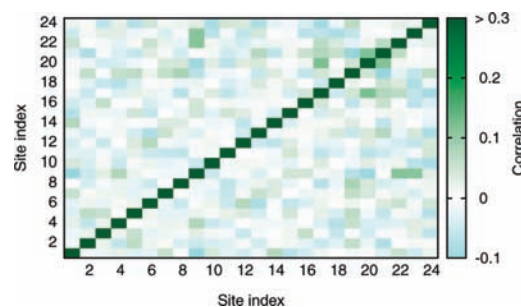

Figure 6. Spatial correlations of the site energies of the individual BChls. The numbers 1−16 correspond to BChls in the B850 ring, while the numbers 17−24, to those of the B800 ring.
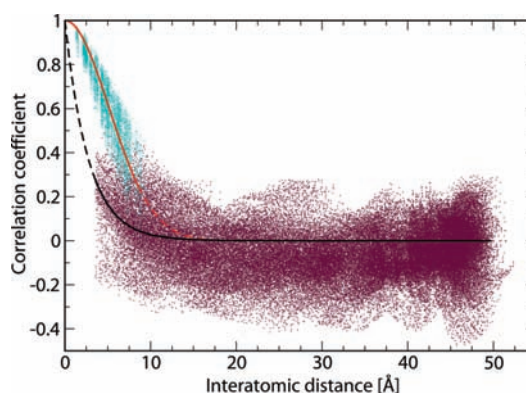

Figure 7. Spatial correlations of the individual atoms of BChls belonging to the B850 ring. The intra- and intermolecular correlations and their fits are shown in cyan/red and maroon/black, respectively.
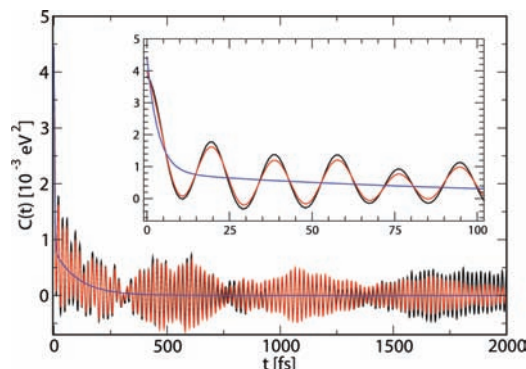

Figure 8. Correlation function (black) and its fit (red) for the B850 ring. The inset shows a closeup of the first 100 fs.

resulting $C(t)$ is then calculated by averaging over the nine available correlation functions obtained by shifting the starting point of the correlation by 1 ps. The average correlation functions are displayed in Figures 8 and 9 for the B850 and B800 rings, respectively. As, for example, also done for echo peak shift experiments,[89,90] we furthermore fitted the correlation functions to an analytical form. These fits have the advantage to enable an approximate separation of the decay of the correlation functions and the superimposed fast oscillations. The fast oscillations are usually attributed to vibrational motions

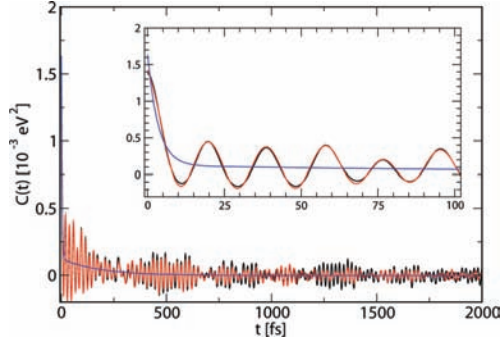Electronic Relaxation in Light-Harvesting System II

Figure 9. Correlation function (black) and its fit (red) for the B800 ring.

TABLE 1: Fitting Parameters for the Correlation Function of the B850 Ring

exponential	η_i (10^{-5} eV^2)		$1/\gamma_i$ (fs)
1	65.7		7.05
2	13.8		165.8
oscillation	$\tilde{\eta}_i$ (10^{-5} eV^2)	$2\pi/\tilde{\omega}_i$ (fs)	$1/\tilde{\gamma}_i$ (fs)
1	2.26	18.4	1765.5
2	22.8	19.0	279.5
3	8.64	19.7	1244.2
4	4.03	20.9	448.6
5	2.97	22.6	2036.6
6	2.92	23.5	156.7
7	11.3	30.4	109.2
8	2.76	46.7	218.4
9	3.24	54.6	1512.8
10	2.23	88.6	294.2

including double bonds, though an exact assignment is difficult due to the complex environment, and are not at the focus of the present study.[31,59,62] Nevertheless, an involvement of C=C or C=O stretch vibrations is highly likely. Since these oscillations are in the high-frequency range, they are actually rather unimportant for the electronic relaxation of excitonic processes. The problem is that these fast oscillations mask the important slower relaxation components and make a separation of signal and noise complicated. Therefore, fits of all components in the correlation functions are in order. The correlation functions can be fitted decently by a combination of exponentials and damped oscillations[89,90]

$$C(t) \approx \sum_{i=1,N_e} \eta_i e^{-\gamma_i t} + \sum_{i=1,N_o} \tilde{\eta}_i \cos(\tilde{\omega}_i t) e^{-\tilde{\gamma}_i t} \quad (6)$$

using $N_e = 2$ and $N_o = 10$. The corresponding fitting parameters are given in Tables 1 and 2. The initial fast decays have decay times $\tau_i = 1/\gamma_i$ of about 7 and 5 fs for the B850 and B800 rings, respectively. These are followed by slower decay times of about 160 fs (B850) and 88 fs (B800). For some of the fast oscillations, the decay times are much longer.

Spectral Densities

In order to describe the exciton dynamics in and between the B850 and B800 rings, one often applies theories for open quantum systems. A key quantity for these theories is the so-called spectral density $J(\omega)$ describing the frequency-dependent coupling between the excitonic subsystem and its thermal

TABLE 2: Same as in Table 1 but for the B800 Ring

exponential	η_i (10^{-5} eV^2)		$1/\gamma_i$ (fs)
1	129.3		4.77
2	100.2		87.53
oscillation	$\tilde{\eta}_i$ (10^{-5} eV^2)	$2\pi/\tilde{\omega}_i$ (fs)	$1/\tilde{\gamma}_i$ (fs)
1	15.5	18.4	1414.5
2	48.6	19.0	2238.3
3	10.3	19.7	2520.5
4	21.4	20.9	602.5
5	6.50	22.6	1703.1
6	7.70	23.9	216.1
7	20.8	29.9	112.1
8	4.88	46.3	729.2
9	13.4	55.2	383.2
10	18.6	90.7	182.7

environment. Starting with a classical autocorrelation, the spectral density $J(\omega)$ can be determined using[31,45]

$$J(\omega) = \frac{2}{\pi\hbar} \tanh(\beta\hbar\omega/2) \int_0^\infty dt\, C(t) \cos(\omega t) \quad (7)$$

where $\beta = 1/(k_B T)$ denotes the inverse temperature. The thermal correction factor in front of the integral ensures the validity of the detailed balance relation. Equation 7 is the key relation for combining the results from the MD and quantum chemistry studies with the theory of open quantum systems.

In the present case in which the autocorrelation function is fitted to the functional form eq 6, the integration can be performed analytically, yielding

$$J(\omega) = \frac{2}{\pi\hbar} \tanh(\beta\hbar\omega/2)\left[\sum_{i=1,N_e} \frac{\eta_i \gamma_i}{\gamma_i^2 + \omega^2} + \sum_{i=1,N_o} \frac{\tilde{\eta}_i \tilde{\gamma}_i}{2(\tilde{\gamma}_i^2 + (\omega - \tilde{\omega}_i)^2)} \right] \quad (8)$$

In principle, the integration of eq 7 yields additional terms. These terms are equivalent to the last term in eq 8 but with $(\omega + \tilde{\omega}_i)^2$ instead of $(\omega - \tilde{\omega}_i)^2$ in the denominator. Because of the relative large values of ω_i and since they would only create peaks at negative nonphysical frequencies, these additional terms can be dropped without influencing the values of the spectral density. In most applications concerning electronic relaxation, one is only interested in the low energy range and therefore almost all terms yielding peaks in the spectral density can actually be dropped. The overall structures of the spectral densities for the B850 and B800 are very similar, which is not astonishing, since both consist of the same pigment molecules. For energies above 0.05 eV, the spectral density for the B800 ring is approximately a factor of 2 larger than that of the B850 ring. For the important energy range below 0.05 eV, this factor is even larger because of the steep rise of the spectral density in the case of the B800 ring. The reason for the larger spectral density of the BChls belonging to the B800 ring is their larger site energy fluctuation which in turn is a result of their more polar environment compared to that of the BChls in the B850 ring.[41,52] Furthermore, the spectral densities basically consist of two contributions: those intramolecular modes which are not taken into account explicitly and environmental modes. Most likely, the background resulting from the two exponentials in the fitted correlation functions is based on environmental modes, while the peaks belong to

intramolecular modes. This also explains the very similar peak structure for BChls belonging to the different rings, though their environments vary.

A comment is in order concerning the comparison between the spectral densities obtained in earlier studies and those in this study. In ref 31, a 400 fs long correlation function was obtained using the HF-CIS method for the energy gap calculations. As discussed earlier, this method leads to larger site energy fluctuations as compared to those using ZINDO/S but also to those using TDDFT calculations. These larger fluctuations in turn result in larger amplitudes for the spectral density. The same is true when using the present HF-CIS results to obtain spectral densities. Since the fluctuations of ZINDO/S-CIS and TDDFT are similar, similar spectral densities based on the present TDDFT results with the rather small basis set are to be expected. A further restriction of the study in ref 31 was the limited length of the trajectory for which the energy gap was calculated, as also in ref 52. As can be seen in the present study, the autocorrelation functions do not decay to zero after 400 fs. Furthermore, we found it to be quite problematic to calculate eq 6 directly using fast Fourier transform (FFT) techniques. In that case, the obtained spectral densities depend significantly on the length of the correlation function and on the damping introduced at the end of the correlation function to avoid FFT artifacts. Therefore, we refrained from this direct use of FFTs and first fitted the correlation function to an analytical form as described above. This procedure gave much more robust results, though small uncertainties in the spectral density resulting from ambiguities in the fitting procedure still exist. It is important to note that the low-frequency range is basically determined by the purely exponential terms in the fit, as can also be seen from the simplified spectral density function including only two exponentially decaying functions. Actually, the problem of obtaining spectral densities and the fit to simplified spectral densities has been discussed much earlier already,[91] though in that case a very simplified form of the spectral density was used.

To avoid confusion, we want to emphasize once more that for electronic relaxation processes in the present systems only the low-frequency part of the obtained spectral densities is needed and only very few of the peaks play a role if any. Furthermore, the spectral densities discussed so far are spectral densities in the site representation, i.e., local spectral densities. Either one observes this fact in the theories using these spectral densities, as for example in refs 31, 52, and 54, or one has to transform the spectral densities into the energy representation, i.e., the exciton picture. Denoting the unitary transformation matrix between the site and the exciton representation by U, the states in the site presentation (Latin characters) are given in terms of the excitonic states (Greek characters) by

$$|k\rangle = \sum_\mu U_{k\mu}|\mu\rangle \qquad (9)$$

In principle, one can define spectral densities for each individual site $J_k(\omega) = J_{k,k}(\omega)$ or even for the transition between the site $J_{k,l}(\omega)$. Above, we assumed that all proteins see the same environment and did not introduce intersite spectral densities which would involve the fluctuations of the electronic couplings. Therefore, just one $J(\omega)$ was obtained. On one hand, going back to the definition of spectral density,[92] it is given in terms of coupling constants $c_{k,\xi}$ between the system mode at site k and the bath modes ξ

$$J_k(\omega) = \frac{\pi}{\hbar} \sum_\xi |c_{k,\xi}|^2 \delta(\omega - \omega_\xi) \qquad (10)$$

On the other hand, the spectral density between excitonic states μ and ν is given by[45,93,94]

$$\begin{aligned} J_{\mu\nu}(\omega) &= \frac{\pi}{\hbar} \sum_\xi |c_{\mu\nu,\xi}|^2 \delta(\omega - \omega_\xi) \\ &= \frac{\pi}{\hbar} \sum_\xi \sum_{k,i} U_{k\mu} U_{k\nu}^* U_{i\mu}^* U_{i\nu} c_{k,\xi} c_{i,\xi}^* f(R_{i,k}) \delta(\omega - \omega_\xi) \end{aligned} \qquad (11)$$

where we introduced the additional correlation function $f(R_{i,k})$.[93] This function describes the spatial correlation function between the pigments, as shown in Figure 7. Above, it was discussed that for usual distances in the present systems no spatial correlations are found. Therefore, we can safely assume that $f(R_{i,k}) = \delta_{i,k}$. This assumption is often performed in this context, but here we actually substantiate it through numerical calculations. The substitution of f by the δ function leads to

$$\begin{aligned} J_{\mu\nu}(\omega) &= \frac{\pi}{\hbar} \sum_k |U_{k\mu}|^2 |U_{k\nu}|^2 \sum_\xi |c_{k,\xi}|^2 \delta(\omega - \omega_\xi) \\ &= \sum_k |U_{k\mu}|^2 |U_{k\nu}|^2 J_k(\omega) \\ &= J(\omega) \sum_k |U_{k\mu}|^2 |U_{k\nu}|^2 \end{aligned} \qquad (12)$$

In the last equality, we assumed that the spectral densities at all sites are the same. For an ideal ring structure, many of the sums (depending on μ and ν) are equal to or close to $1/M$, with M being the number of pigments. Moreover, one has to keep in mind that $J_{\mu\nu}$ describes the coupling from one excitonic state to one of the other $M - 1$ states, whereas there is no extra summation concerning $J(\omega)$ in the site representation. Spectral densities of the type described in eq 12 can then be employed directly in theories using an excitonic basis.[23,94−96]

Absorption

Knowing the spectral density of the systems allows one to determine a whole manifold of different transport and linear as well as nonlinear optical properties. At this point, we restrict ourselves to a first test, i.e., the calculation of the linear absorption spectrum. Because of the weak coupling between the B850 and B800 rings, we do assume that the spectrum can be determined as the sum of the absorption spectra of the individual rings.

In principle, one can calculate the absorption spectrum using the Fourier transform of the dipole−dipole correlation function, as has been done for the present system.[97] Here, we actually employ a formulation derived in ref 31. Thus, the reader is referred to this reference for further details. Within a second-order cumulant expansion, the line-shape function is given by

$$I(\omega) \propto \sum_\mu |d_\mu|^2 \int_0^\infty \mathrm{d}t \, \exp[-\Phi'_\mu(t)] \cos[(\omega - \omega_\mu)t + \Phi''_\mu(t)] \qquad (13)$$

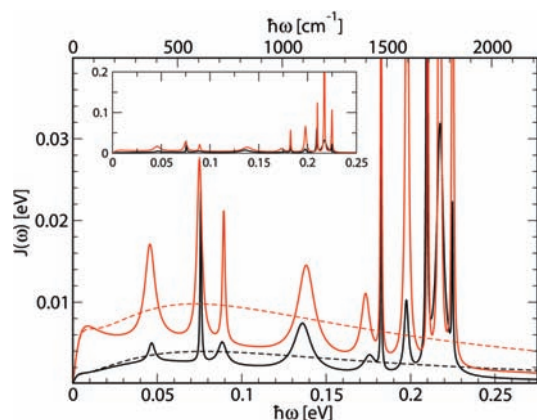Electronic Relaxation in Light-Harvesting System II

Figure 10. Spectral densities of the two rings based on the fitted correlation functions. The black lines show the results for the B850 and the red ones for the B800 ring. The dashed lines indicate the results when fitting the autocorrelation function with two exponentials only. The inset shows the same data with an enlarged scale on the ordinate.

with $|d_\mu|$ being the magnitude of the transition dipole moment connecting the ground electronic state and the excitonic state $|\mu\rangle$ with energy $\hbar\omega_\mu$. The time-dependent functions $\Phi'_\mu(t)$ and $\Phi''_\mu(t)$ directly resulting from the cumulant expansion are given by

$$\Phi'_\mu(t) = \int_0^t d\tau (t - \tau)[C(\tau)\mathrm{Re}\{F_\mu(\tau)\} - D(\tau)\mathrm{Im}\{F_\mu(\tau)\}] \tag{14}$$

and

$$\Phi''_\mu(t) = \int_0^t d\tau (t - \tau)[D(\tau)\mathrm{Re}\{F_\mu(\tau)\} + C(\tau)\mathrm{Im}\{F_\mu(\tau)\}] \tag{15}$$

In these expressions, the state-independent function $D(t)$ is given by an integral over the spectral density

$$D(t) = \int_0^\infty d\omega\, J(\omega) \sin \omega t \tag{16}$$

while the excitonic coupling factor $F_\mu(t)$, which is responsible for the so-called exchange narrowing, contains a sum over all excitonic states of the corresponding ring

$$F_\mu(t) = \frac{1}{M} \sum_\nu \exp[i(\varepsilon_\mu - \varepsilon_{\mu-\nu})t] \tag{17}$$

For weakly coupled BChls like in the B800 ring, the excitonic coupling almost vanishes and this results in $F(t) \approx 1$. Together with the correlation function derived above, all input parameters for the linear absorption spectrum are determined in the present study from a microscopic model. The result is given in Figure 11 together with an experimental result for comparison.[98] As discussed above, first the individual absorption spectra are calculated and shown in Figure 11 together with their sum. There is no need for a shift in the peak position for the B850 ring, but the peak of the B800 ring has been shifted by 44 meV to account
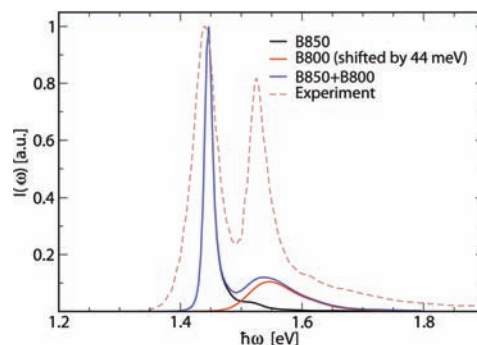

Figure 11. Absorption spectrum as calculated using the present theory (solid, orange) compared to an experimental spectrum (dashed blue). Additionally, the spectra of the individual rings are shown (black, B850 ring; red, B800 ring).

for the same splitting of the absorption peaks as observed in experiment. Due to the excitonic couplings in the B850 ring, the absorption is slightly shifted to the red. This shows that the ZINDO/S method is accurately parametrized for the BChls in the B850 ring but has problems reproducing the shift of the lines due to the more polar environment in the B800 ring. The B850 peak is too narrow, which is not surprising, since the present model does not include any static disorder usually introduced to represent very slow dynamics. In the present study, we refrain from adding Gaussian static disorder to obtain more accurate peak widths, but this would be possible in a straight-forward manner. It has to be mentioned as well that in the present representation of the results both the experimental as well as the theoretical peaks were normalized to a maximum value of 1. Other normalizations would lead to quite different graphs. Furthermore, the ratios of peak heights between the B850 and B800 rings in experiments and theory are different. This indicates that probably the calculations of the dipole moments need some refinement.

Conclusion

In this contribution, several methods to calculate the site energies of individual BChls and the coupling between them have been compared along a MD trajectory. As in previous publications,[57] the semiempirical ZINDO/S-CIS method showed a good compromise between accuracy and numerical performance. The size of the level fluctuations between the ZINDO/S-CIS and the TDDFT was shown to be similar, while the HF-based calculations showed much larger fluctuations in the energy gaps. For the ZINDO/S-CIS (10,10) approach, even the absolute size of the energy gap between the ground and the Q_y state is in good agreement with experiment. Some care has to be taken concerning the size of the active space used in the ZINDO/S-CIS simulations. As in earlier investigations,[50,53] it was shown here that small sizes of active spaces of about (10,10) yield quite accurate results which are in agreement with the original parametrization procedure using only small active spaces.[48] Especially for the pigments within the B800 ring, the effects of the external partial charges are important to obtain the correct energy distribution.

Likewise, for the electronic couplings, different methods were contrasted and a large spread of results along the MD trajectory was observed. Performing calculations for BChl dimers in the scope of a supermolecule approach and extracting the couplings most likely yielded too large couplings in the present case.

Olbrich and Kleinekathöfer

Furthermore, the results for the extended dipole approximation should be superior to those of the point-dipole approximation. As the most elaborate formalism, the TrEsp method was combined with a distance-dependent solvent screening factor. This procedure resulted in couplings at the lower limit of those published so far for the present (or similar) system. In a list reported in ref 2, the transition density cube approach (without screening factor) resulted in the smallest coupling values. The TrEsp method is very similar but numerically superior to the transition density cube method. Taking into account the additional environmental screening factor employed here, the obtained results are actually quite reasonable.

Most interestingly in the context of the recent experimental findings of long-lived coherences in LH systems,[6-9] spatial correlations have not been observed between the site energy fluctuations at different BChls. The temporal correlation functions were found to quickly decay with superimposed fast oscillations. Fitting these correlation functions to exponential decaying functions and damped oscillations, it was possible to extract the spectral densities of the coupling between the system of coupled two-level systems and the environment, i.e., the excluded internal modes as well as protein, membrane, and water motions. These spectral densities now open up the possibility to combine the present results with a whole variety of different techniques and phenomena from the area of dissipative quantum dynamics. Several simulations on LH2 systems in this direction have been performed in the past, while most of them relied on parameters estimated from experiments of similar sources.[23,94-96,99,100] A first test of the spectral density was realized at the end of the present study in the form of a calculation of the linear absorption spectrum. This yielded too narrow spectral peaks, which is not surprising, since static disorder is not included in the present model and would have to be added to the present model.

Earlier studies of the same complex[31,52,54] relied on the HF-based CIS calculations of the energy gap fluctuations and the PDA of the electronic couplings. Here, several methods for determining the site energies and coupling have been tested. As a result, we conclude that an energy calculation using ZINDO/S-CIS and coupling calculations using TrEsp with DFT-based transition charges yield a reasonable compromise between accuracy and numerical efficiency.

To conclude, the present study shows the current possibilities and limitations of determining a time-dependent Hamiltonian based on atomic-level calculations. Such a Hamiltonian can be employed to study optical and other electronic phenomena in large multichromophoric complexes such as light-harvesting complexes. Fast, reliable calculations of electronic structures and couplings are still a limiting factor, though progress has been made in both aspects. Expertise is being gained in studies such as the present one combining classical MD with electronic structure calculations, finally enabling the determination of quantum properties in large molecular aggregates.[31,52,54,57-65]

References and Notes

(1) Hu, X.; Ritz, T.; Damjanović, A.; Autenrieth, F.; Schulten, K. *Q. Rev. Biophys.* **2002**, *35*, 1–62.
(2) Cogdell, R. J.; Gall, A.; Köhler, J. *Q. Rev. Biophys.* **2006**, *39*, 227–324.
(3) Sundström, V. *Annu. Rev. Phys. Chem.* **2008**, *59*, 53–77.
(4) Cheng, Y. C.; Fleming, G. R. *Annu. Rev. Phys. Chem.* **2009**, *60*, 241–242.
(5) Novoderezhkin, V. I.; van Grondelle, R. *Phys. Chem. Chem. Phys.* **2010**, *12*, 7352–7365.
(6) Engel, G. S.; Calhoun, T. R.; Read, E. L.; Ahn, T. K.; Mancal, T.; Cheng, Y. C.; Blankenship, R. E.; Fleming, G. R. *Nature* **2007**, *446*, 782–786.
(7) Ginsberg, N. S.; Cheng, Y. C.; Fleming, G. R. *Acc. Chem. Res.* **2009**, *42*, 1352–1353.
(8) Collini, E.; Wong, C. Y.; Wilk, K. E.; Curmi, P. M.; Brumer, P.; Scholes, G. D. *Nature* **2010**, *463*, 644–647.
(9) Ishizaki, A.; Calhoun, T. R.; Schlau-Cohen, G. S.; Fleming, G. R. *Phys. Chem. Chem. Phys.* **2010**, *12*, 7319–7337.
(10) Scholes, G. D. *J. Phys. Chem. Lett.* **2010**, *1*, 2–8.
(11) Olaya-Castro, A.; Lee, C. F.; Olsen, F. F.; Johnson, N. F. *Phys. Rev. B* **2008**, *78*, 085115.
(12) Caruso, F.; Chin, A. W.; Datta, A.; Huelga, S. F.; Plenio, M. B. *J. Chem. Phys.* **2009**, *131*, 105106.
(13) Rebentrost, P.; Mohseni, M.; Aspuru-Guzik, A. *J. Phys. Chem. B* **2009**, *113*, 9942–9947.
(14) Arndt, M.; Juffmann, T.; Vedral, V. *HFSP J.* **2009**, *3*, 386–400.
(15) van Amerongen, H.; Valkunas, L.; van Grondelle, R. *Photosynthetic Excitons*; World Scientific: Singapore, 2000.
(16) Georgakopoulou, S.; Frese, R. N.; Jonson, E.; Koolhaas, C.; Cogdell, R. J.; van Grondelle, R.; van der Zwan, G. *Biophys. J.* **2002**, *82*, 2184–2197.
(17) Pullerits, T.; Chachisvillis, M.; Sundström, V. *J. Phys. Chem.* **1996**, *100*, 10787–10792.
(18) Kennis, J. T. M.; Streltsov, A. M.; Permentier, H.; Aartsma, T. J.; Amesz, J. *J. Phys. Chem. B* **1997**, *101*, 8369–8374.
(19) Renger, T.; Marcus, R. A. *J. Chem. Phys.* **2002**, *116*, 9997–10019.
(20) Agarwal, R.; Rizvi, A. H.; Prall, B. S.; Olsen, J. D.; Hunter, C. N.; Fleming, G. R. *J. Phys. Chem. A* **2002**, *106*, 7573–7578.
(21) Novoderezhkin, V.; Wendling, M.; van Grondelle, R. *J. Phys. Chem. B* **2003**, *107*, 11534–11548.
(22) Georgakopoulou, S.; van Grondelle, R.; van der Zwan, G. *Biophys. J.* **2004**, *87*, 3010–3022.
(23) Abramavicius, D.; Palmieri, B.; Voronine, D. V.; Sanda, F.; Mukamel, S. *Chem. Rev.* **2009**, *109*, 2350–2358.
(24) Tietz, C.; Chekhlov, O.; Dräbenstedt, A.; Schuster, J.; Wrachtrup, J. *J. Phys. Chem. B* **1999**, *103*, 6328–6333.
(25) Matsushita, M.; Ketelaars, M.; van Ojien, A. M.; Köhler, J.; Aartsma, T. J.; Schmidt, J. *Biophys. J.* **2001**, *80*, 1591–1603.
(26) Hofmann, C.; Ketelaars, M.; Matsushita, M.; Aartsma, T. J.; Köhler, J. *Phys. Rev. Lett.* **2003**, *90*, 013004.
(27) Hofmann, C.; Michel, H.; van Heel, M.; Köhler, J. *Phys. Rev. Lett.* **2005**, *94*, 195501.
(28) Rutkauskas, D.; Novoderezhkin, V.; Cogdell, R. J.; van Grondelle, R. *Biophys. J.* **2005**, *88*, 422–435.
(29) Hu, X.; Damjanović, A.; Ritz, T.; Schulten, K. *Proc. Natl. Acad. Sci. U.S.A.* **1998**, *95*, 5935–5941.
(30) Cory, M. G.; Zerner, M. C.; Hu, X.; Schulten, K. *J. Phys. Chem. B* **1998**, *102*, 7640–7650.
(31) Damjanović, A.; Kosztin, I; Kleinekathöfer, U.; Schulten, K. *Phys. Rev. E* **2002**, *65*, 031919.
(32) Sener, M. K.; Lu, D.; Ritz, T.; Park, S.; Fromme, P.; Schulten, K. *J. Phys. Chem. B* **2002**, *106*, 7948–7960.
(33) Tretiak, S.; Middleton, C.; Chernyak, V.; Mukamel, S. *J. Phys. Chem. B* **2000**, *104*, 4519–4528.
(34) Tretiak, S.; Middleton, C.; Chernyak, V.; Mukamel, S. *J. Phys. Chem. B* **2000**, *104*, 9540–9553.
(35) Damjanović, A.; Vaswani, H. M.; Fromme, P.; Fleming, G. R. *J. Phys. Chem. B* **2002**, *106*, 10251–10262.
(36) Yang, M.; Damjanović, A.; Vaswani, H. M.; Fleming, G. R. *Biophys. J.* **2003**, *85*, 140–148.
(37) Madjet, M. E.; Müh, F.; Renger, T. *J. Phys. Chem. B* **2009**, *113*, 12603–14.
(38) Deisenhofer, J.; Epp, O.; Miki, K.; Huber, R.; Michel, H. *Nature* **1985**, *318*, 618–624.
(39) McDermott, G.; Prince, S. M.; Freer, A. A.; Hawthornthwaite-Lawless, A. M.; Papiz, M. Z.; Cogdell, R. J.; Isaacs, N. W. *Nature* **1995**, *374*, 517–521.
(40) Cogdell, R. J.; Isaacs, N. W.; Freer, A. A.; Howard, T.; Gardiner, A. T.; Prince, S. M.; Papiz, M. Z. *FEBS Lett.* **2003**, *5555*, 35–39.
(41) Koepke, J.; Hu, X.; Muenke, C.; Schulten, K.; Michel, H. *Structure* **1996**, *4*, 581–597.
(42) Humphrey, W. F.; Dalke, A.; Schulten, K. *J. Mol. Graphics* **1996**, *14*, 33–38.
(43) Sener, M. K.; Strümpfer, J.; Timney, J. A.; Freiberg, A.; Hunter, C. N.; Schulten, K. *Biophys. J.* **2010**, *99*, 67–75.
(44) Neugebauer, J. *ChemPhysChem* **2009**, *10*, 3148–3153.

75

(45) May, V.; Kühn, O. *Charge and Energy Transfer in Molecular Systems*; Wiley-VCH: Berlin, 2000.

(46) Ridley, J.; Zerner, M. C. *Theor. Chim. Acta* **1973**, *32*, 111–134.

(47) Zerner, M. C.; Loew, G. H.; Kirchner, R. F.; Mueller-Westerhoff, U. T. *J. Am. Chem. Soc.* **1980**, *102*, 589–599.

(48) Li, J.; Williams, B.; Cramer, C. J.; Truhlar, D. G. *J. Chem. Phys.* **1999**, *110*, 724–733.

(49) Zhao, Y.; Ng, M.-F.; Chen, G. *Phys. Rev. E* **2004**, *69*, 032902.

(50) Linnanto, J.; Korppi-Tommola, J. *Phys. Chem. Chem. Phys.* **2000**, *2*, 4962–4970.

(51) Linnanto, J.; Korppi-Tommola, J. *Phys. Chem. Chem. Phys.* **2002**, *2*, 3453–3460.

(52) Janosi, L.; Kosztin, I.; Damjanović, A. *J. Chem. Phys.* **2006**, *125*, 014903.

(53) Linnanto, J.; Korppi-Tommola, J. *Phys. Chem. Chem. Phys.* **2006**, *8*, 663–667.

(54) Kosztin, I.; Schulten, K. Molecular dynamics methods for bio-electronic systems in photosynthesis. *Biophysical Techniques in Photosynthesis II*; Springer: Dordrecht, The Netherlands, 2008; pp 445−464.

(55) Linnanto, J.; Korppi-Tommola, J. *Chem. Phys.* **2009**, *357*, 171–180.

(56) Howard, I. A.; Zutterman, F.; Deroover, G.; Lamoen, D.; Alsenoy, C. V. *J. Phys. Chem. B* **2004**, *108*, 19155–19162.

(57) Zwier, M. C.; Shorb, J. M.; Krueger, B. P. *J. Comput. Chem.* **2007**, *28*, 1572–1581.

(58) Kwon, J. S.; Choi, C. M.; Kim, H. J.; Kim, N. J.; Jang, J.; Yang, M. *J. Phys. Chem. A* **2009**, *113*, 2715–2723.

(59) Mercer, I. P.; Gould, I. R.; Klug, D. R. *Faraday Discuss.* **1997**, *108*, 51–62.

(60) Mercer, I. P.; Gould, I. R.; Klug, D. R. *J. Phys. Chem. B* **1999**, *103*, 7720–7727.

(61) Vasil'ev, S.; Bruce, D. *Biophys. J.* **2006**, *90*, 3062–3063.

(62) Walker, R. C.; Mercer, I. P.; Gould, I. R.; Klug, D. R. *J. Comput. Chem.* **2007**, *28*, 478–480.

(63) Kobus, M.; Gorbunov, R. D.; Nguyen, P.; Stock, G. *Chem. Phys.* **2008**, *347*, 208–217.

(64) Jiang, J.; Abramavicius, D.; Bulheller, B. M.; Hirst, J. D.; Mukamel, S. *J. Phys. Chem. B* **2010**, *114*, 8270–8277.

(65) Fujisaki, H.; Stock, G. *J. Chem. Phys.* **2008**, *129*, 134110.

(66) Jansen, T. L. C.; Knoester, J. *J. Phys. Chem. B* **2006**, *110*, 22910–22916.

(67) Jansen, T. L. C.; Knoester, J. *Acc. Chem. Res.* **2009**, *42*, 1405–1411.

(68) Zhu, H.; May, V.; Röder, B.; Renger, T. *J. Chem. Phys.* **2008**, *128*, 154905.

(69) Zhu, H.; Röder, B.; May, V. *Chem. Phys.* **2009**, *362*, 19–26.

(70) Linnanto, J.; Korppi-Tommola, J. E. I.; Helenius, V. *J. Phys. Chem. B* **1999**, *103*, 8739–8750.

(71) Madjet, M. E.; Abdurahman, A.; Renger, T. *J. Phys. Chem. B* **2006**, *110*, 17268–81.

(72) Beljonne, D.; Curutchet, C.; Scholes, G. D.; Silbey, R. J. *J. Phys. Chem. B* **2009**, *113*, 6583–6599.

(73) Krueger, B.; Scholes, G.; Fleming, G. *J. Phys. Chem. B* **1998**, *102*, 5378–5386.

(74) Frähmcke, J. S.; Walla, P. J. *Chem. Phys. Lett.* **2006**, *430*, 397–403.

(75) Renger, T. *Photosynth. Res.* **2009**, *102*, 471–485.

(76) Renger, T.; Grundkötter, B.; Madjet, M. E.; Müh, F. *Proc. Natl. Acad. Sci. U.S.A.* **2008**, *105*, 13235–40.

(77) Scholes, G. D.; Curutchet, C.; Mennucci, B.; Cammi, R.; Tomasi, J. *J. Phys. Chem. B* **2007**, *111*, 6978–6982.

(78) Foloppe, N.; MacKerell, A. D., Jr. *J. Comput. Chem.* **2000**, *21*, 86–104.

(79) MacKerell, A.; et al. *J. Phys. Chem. B* **1998**, *102*, 3586–3616.

(80) Phillips, J. C.; Braun, R.; Wang, W.; Gumbart, J.; Tajkhorshid, E.; Villa, E.; Chipot, C.; Skeel, R. D.; Kale, L.; Schulten, K. *J. Comput. Chem.* **2005**, *26*, 1781–1802.

(81) Silva-Junior, M. R.; Thiel, W. *J. Chem. Theory Comput.* **2010**, *6*, 1546–1564.

(82) Petrenko, T.; Neese, F. *J. Chem. Phys.* **2007**, *127*, 164319.

(83) Alden, R. G.; Johnson, E.; Nagarajan, V.; Law, W. W. P. J.; Cogdell, R. G. *J. Phys. Chem. B* **1997**, *101*, 4667–4680.

(84) Czikklely, V.; Försterling, H. D.; Kuhn, H. *Chem. Phys. Lett.* **1970**, *6*, 207–210.

(85) Curutchet, C.; Muñoz Losa, A.; Monti, S.; Kongsted, J.; Scholes, G. D.; Mennucci, B. *J. Chem. Theory Comput.* **2009**, *5*, 1838–1848.

(86) Wolynes, P. G. *Proc. Natl. Acad. Sci. U.S.A.* **2009**, *106*, 17247–17248.

(87) Hünenberger, P. H.; Mark, A. E.; van Gunsteren, W. F. *J. Mol. Biol.* **1995**, *252*, 492–503.

(88) Kubař, T.; Kleinekathöfer, U.; Elstner, M. *J. Phys. Chem. B* **2009**, *113*, 13107–13117.

(89) Joo, T.; Jia, Y.; Yu, J.-Y.; Lang, M. J.; Fleming, G. R. *J. Chem. Phys.* **1996**, *104*, 6089–6108.

(90) Yang, M.; Agarwal, R.; Fleming, G. R. *J. Photochem. Photobiol., A* **2001**, *142*, 107–119.

(91) Makri, N.; Sim, E.; Makarov, D.; Topaler, M. *Proc. Natl. Acad. Sci. U.S.A.* **1996**, *93*, 3926–3931.

(92) Weiss, U. *Quantum Dissipative Systems*, 2nd ed.; World Scientific: Singapore, 1999.

(93) Renger, T.; May, V.; Kühn, O. *Phys. Rep.* **2001**, *343*, 137–254.

(94) Cho, M. *Chem. Rev.* **2008**, *108*, 1331–1418.

(95) Kleinekathöfer, U.; Barvík, I.; Heřman, P.; Kondov, I.; Schreiber, M. *J. Phys. Chem. B* **2003**, *107*, 14094–14102.

(96) Strümpfer, J.; Schulten, K. *J. Chem. Phys.* **2009**, *131*, 225101.

(97) Schröder, M.; Kleinekathöfer, U.; Schreiber, M. *J. Chem. Phys.* **2006**, *124*, 084903−1−14.

(98) Zhang, J.-P.; Fujii, R.; Qian, P.; Inaba, T.; Mizoguchi, T.; Koyama, Y. *J. Phys. Chem. B* **2000**, *104*, 3683–3691.

(99) Heřman, P.; Kleinekathöfer, U.; Barvík, I.; Schreiber, M. *J. Lumin.* **2001**, *94&95*, 447–450.

(100) Heřman, P.; Kleinekathöfer, U.; Barvík, I.; Schreiber, M. *Chem. Phys.* **2002**, *275*, 1–13.

JP106542V

5.2. physica status solidi (b) (2011)
Modeling of Light-Harvesting in Purple Bacteria Using a Time-Dependent Hamiltonian Approach

Authors: C. Olbrich, J. Liebers, and U. Kleinekathöfer

Modeling of light-harvesting in purple bacteria using a time-dependent Hamiltonian approach

Carsten Olbrich, Jörg Liebers, and Ulrich Kleinekathöfer*

School of Engineering and Science, Jacobs University Bremen, Campus Ring 1, 28759 Bremen, Germany

* Corresponding author: e-mail u.kleinekathoefer@jacobs-university.de, Phone: +49-421-200-3523, Fax: +49-421-200-493523

The photosynthetic light-harvesting system II (LH2) of *Rhodospirillum molischianum* is investigated using a time-dependent combination of molecular dynamics simulations and semiempirical ZINDO/S electronic structure calculations. The classical simulations are performed on the available crystal structure of the LH2 complex. Snapshots of the atomic fluctuations along this 12 ps long trajectory serve as input for the calculation of the excitation energies of the individual bacteriochlorophylls embedded in the LH2 complex. Furthermore, the couplings between the bacteriochlorophylls are computed using the method of transition charges from electrostatic potentials and for comparison also using the point-dipole approximation. With these quantities the excitonic energies of the complete system as well as the linear absorption spectra are calculated and compared to experimental findings.

1 Introduction Since photosynthesis is one of the most important biological processes on earth, it has been at the focus of many investigations. Many details of the molecular properties have been unraveled by a combination of experimental and theoretical studies [1–5]. Optical spectra have been investigated in experiment and theory especially also for the light-harvesting (LH) systems of purple bacteria [2, 6, 7]. In the last decades several high resolution crystal structures became available and opened the opportunity to study the structure–function relationship in atomic detail [6, 8–15]. Here, the light-harvesting system II (LH2) system of *Rhodospirillum* (*Rs.*) *molischianum* is in the focus of interest. This LH complex, as depicted in Fig. 1, consists of two rings with 16 and 8 bacteriochlorophyll a (BChl a) molecules, respectively. These two rings with eightfold symmetry are named B850 and B800 based on their respective absorption maxima at 850 and 800 nm. The difference in the absorption profile of the two rings is on the one hand caused by the strong coupling of the BChls in the B850 ring [35] and on the other hand by unlike environments around the chromophores. For the B800 ring its surrounding is hydrophilic while for the B850 ring it is rather hydrophobic [17]. In addition to the 24 BChls eight light-absorbing carotenoids are embedded into the protein matrix of the LH complex.

Classical molecular dynamics (MD) simulations provide an insight into the ground state properties of molecular complexes especially into their conformational changes. In order to describe optical properties one needs to apply quantum calculations providing the site energies of the system. Because of the size of the BChls these are often treated on a semiempirical level using, e.g., the ZINDO/S approach [18–20]. Over the last years this technique became rather popular and was applied to LH complexes [10–12, 15, 21–26] and other systems as well, e.g., Refs. [27–29]. Due to its low computational costs compared to *ab initio* methods, the semiempirical ZINDO/S method is quite suitable for performing excited state calculations along MD trajectories [24, 28, 29]. This in turn allows to determine the so-called spectral density. This spectral density can be used to calculate optical spectra, excitation energy transfer (EET) dynamics, and similar properties [9, 15, 24].

Another quantity which is necessary to describe electronic properties of the LH system are the electronic couplings between the individual sites (see, e.g., the review in Ref. [30]). Often it is assumed that for EET the coupling is dominated by the Coulomb interaction. A quite commonly used approach to that is the point-dipole approximation (PDA) which is known to be problematic at short distances
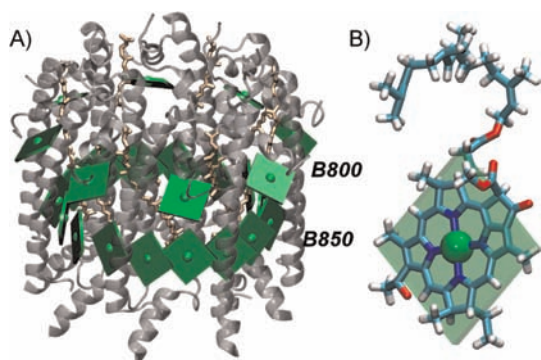
Figure 1 (online color at: www.pss-b.com) Panel A: LH2 complex of *Rs. molishianum*. In gray, the protein structure is shown while the carotenoids are depicted in light yellow. Furthermore, the BChl molecules are represented as green squares with the central Mg atom as a sphere. Panel B: A green square as used in panel A overlaying a single BChl a molecule. (Figure rendered using VMD [16].)

[27, 31–33]. Alternatively, one can calculate the interaction energy by a supermolecule approach of two chromophores [10, 25]. Another accurate but numerically expensive techniques which calculates the Coulomb interaction in an *ab initio* manner is the transition density cube method [34]. Renger and co-workers developed the method of transition charges from electrostatic potentials (TrEsp) [32, 35]. In this approach, atomic centered partial transition charges are fitted to the electrostatic potential of the transition density belonging to the corresponding molecule. A simplification of that method is the so-called extended dipole method [27, 32]. In this case two charges, representing the dipole, are fitted to reproduce the transition charge density distribution. To account for a solvent screening effect on the couplings one can either use a constant factor [35] or, in an alternative approach, a distance-dependent correction developed by Scholes and co-workers [33, 36]. In a subsequent step, one can combine the obtained energies and couplings to construct a time-dependent Hamiltonian. This Hamiltonian can be used to evaluate optical properties and transfer rates from wave packet calculation directly [37–40] or using alternative approaches [15].

The present contribution starts with a description of the MD simulations before a semiempirical electronic structure methods for the ground and excited state energy calculations is detailed. A comparison is furthermore performed for the electronic couplings between the individual pigments. Preceding the conclusions, a time-dependent Hamiltonian is constructed to determine the time evolution of the electronic states and dipole strengths as well as the average linear absorption spectrum of the LH2 system under investigation.

2 Molecular dynamics simulations The MD simulations are based on the crystal structure of *Rs. molishianum*

(PDB:1LGH) [17]. After adding the missing hydrogen atoms, the pigment–protein complex was embedded into a POPC lipid bilayer with about 30 Å of water on both sides. To neutralize the system, 16 Cl^- ions were added to the bulk water. In total the system contained about 114,000 atoms with a dimension of $115 \times 115 \times 96 \, \text{Å}^3$. The simulations were carried out using the NAMD program package [41] with the CHARMM27 force field parameter for lipids, protein and the TIP3P water model. The same parameters as reported in [9] were employed for BChls and lycopenes.

Subsequent to an energy minimization the system was equilibrated in several steps at room temperature (300 K) and normal pressure (1 atm) in a NpT ensemble using periodic boundary conditions, the particle mesh Ewald method and a 2 fs time step using the SHAKE algorithm. In a first step, only the lipid tails were equilibrated for 2 ns while everything else was kept fixed. In the next step the constraints were limited to the LH2 complex for another 4 ns followed by a 2 ns equilibration without constrains. Finally a 12 ps production run with a time step of 1 fs was carried out. The atomic coordinates were recorded at every time step, resulting in 12,000 snapshots which were subsequently used in the QM calculations.

3 Quantum chemistry calculations Based on the MD simulations, we used the ORCA code (University Bonn, Germany) [42] in order to calculate the site energies for all 24 BChls in the complex at each of the 12,000 snapshots. So in total 288,000 single-point calculations were performed. Due to the large number of calculations to be performed and because the optical properties of BChls are determined by the cyclic conjugated π-electron system, we restricted the quantum system to a truncated structure of the BChl molecule. Each terminal CH_3 and CH_2CH_3 group as well as the pythyl tail were replaced by H atoms. Such truncation schemes have been employed previously [21, 24, 43]. Because of its accuracy [44] and the low computational cost we used the semiempirical ZINDO/S-CIS(10,10) method using the 10 highest occupied and the 10 lowest unoccupied states. This technique was also used in Refs. [24, 28, 29] for similar systems. To account for the effect of the surrounding environment, point charges from the MD simulations, from within a cutoff radius of 20 Å around the truncated BChl molecule, were included in the ZINDO/S-CIS calculations. The energy gap between the ground and the first excited, i.e., the Q_y, state and the corresponding density of state (DOS) is shown in Fig. 2 for several individual BChls. In this figure, the coupling between the BChls is neglected. Clearly a fluctuation of the energy gap around an average value is visible.

4 Electronic coupling In order to be able to construct the time-dependent Hamiltonian, one needs the coupling between the individual BChls in addition to the site energies. As already mentioned in Section 1, there exists several approaches to calculate the EET coupling. For purple bacteria a wide range of values were reported and a recent overview is, for example, given in Ref. [2].
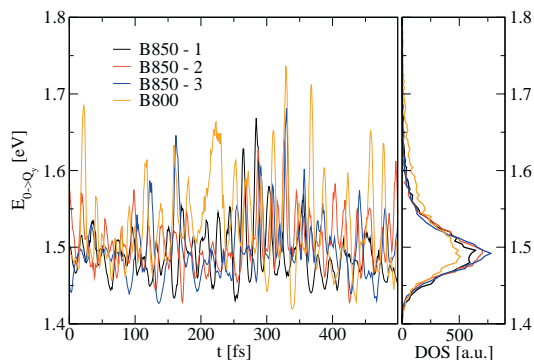
79

Figure 2 (online color at: www.pss-b.com) Site energy fluctuations and corresponding DOS exemplified using three individual BChls from the B850 ring and of one BChl from the B800 ring. The coupling between the BChls is not taken into account in this figure.

In the Förster approach to exciton dynamics the coupling is assumed to be dominated by the Coulomb interaction and calculated using the PDA. Including a screening factor f which will be detailed below, the PDA is given by

$$V_{nm} = \frac{f}{4\pi\varepsilon_0} \left(\frac{\mathbf{d}_m \mathbf{d}_n}{R_{mn}^3} - 3 \frac{(\mathbf{d}_m \mathbf{R}_{mn})(\mathbf{d}_n \mathbf{R}_{mn})}{R_{mn}^5} \right), \quad (1)$$

where the vector $\mathbf{d}_m$ denotes the optical transition dipole moments, which were rescaled by 0.558 to match the experimental measured value of 6.3 D [45] on average. $\mathbf{R}_{mn}$ connects the center of the BChls m and n and R_{mn} denotes the corresponding distance. The PDA has been applied in many studies, e.g., Refs. [27, 31–33], for reasons of simplicity although its problematic behavior for short distances is well known.

To get an improved description of the spatial arrangement of the charges, Renger and co-workers developed the TrEsp method [32, 35]. In this approach, the transition density of pigment m is described using atomic transition charges q_I^T that are localized at the respective pigment, i.e., $\rho(\mathbf{r}) = \sum_I q_I^T \delta(\mathbf{r} - \mathbf{R}_m^I)$ where $\mathbf{R}_m^I$ denotes the coordinates of the Ith atom of BChl m. The coupling between two pigment molecules is then given by

$$V_{nm} = \frac{f}{4\pi\varepsilon_0} \sum_{I,J} \frac{q_I^T \cdot q_J^T}{|\mathbf{R}_m^I - \mathbf{R}_n^J|}. \quad (2)$$

In Ref. [32] these charges were calculated on the level of HF-CIS and TDDFT/B3LYP. In the following, the corresponding couplings will be denoted as TrEsp(HF) and TrEsp(DFT), respectively.

In addition, to include solvent effects to the couplings, the results for the PDA and TrEsp need to be scaled. To this end, two approaches are commonly used: while in the Förster theory the screening factor is given by $f_F = 1/n^2$, in the Onsager theory cavities around the dipole are assumed and

the factors is determined to be $f_O = 3/(2n^2 + 1)$. In these expressions n denotes the refractive index. After a detailed analysis on protein environments, Scholes et al. [36] fitted a distance-dependent screening factor to their results

$$f(R_{mn}) = A\exp(-BR_{mn}) + f_O, \quad (3)$$

with $A = 2.68$, $B = 0.27$ 1/Å, and $f_O = 0.54$. At large distances $(R_{mn} > 20\,\text{Å})$ this function reaches the value $f = 0.54$ which lies in between the values used in Förster theory f_F and the Onsager value f_O for $n^2 = 2$, i.e., a protein environment. In the following calculations, this distance-dependent solvent-screening factor f is applied to all results, i.e., to the PDA, TrEsp(HF), as well as TrEsp(DFT) approaches.

The probability densities to find certain coupling values in the B850 ring along the MD trajectory are shown Fig. 3 for the three different methods detailed above. In comparison, the PDA method yields larger average coupling values of 0.035 eV (282 cm^{-1}) and the broadest distribution. Also the distribution does not show any splitting into intra- and inter-dimer couplings.

When using the TrEsp methods a splitting into couplings between the BChls within the heterodimer and couplings between the heterodimers can be observed. The charges used in the TrEsp method resulting from the TDDFT and the HF/CIS calculations are rather similar after rescaling them in order to obtain realistic transition dipole moments. The observed variations result from different treatments of electron interaction in the two electronic structure theories. The couplings within and between the dimers calculated using TrEsp(HF) are on average 0.024 eV (195 cm^{-1}) and 0.021 eV (166 cm^{-1}), respectively. The average values for TrEsp(DFT) are 0.021 eV (172 cm^{-1}) and for the intra-dimer couplings 0.017 eV (138 cm^{-1}). Furthermore, the couplings between the individual BChls within the B800 ring are much lower than those in the B850 ring due to their average
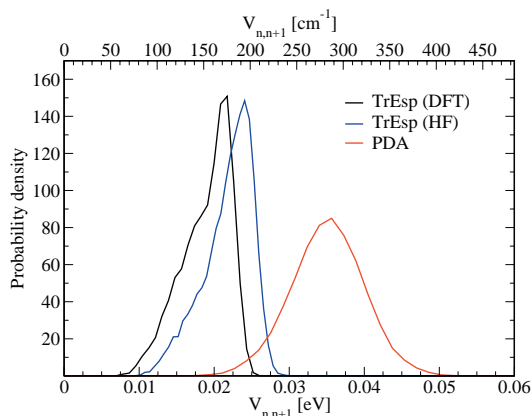

Figure 3 (online color at: www.pss-b.com) Probability density of the electronic couplings in the B850 ring using three different approaches.

distance of about 22.25 Å. For the PDA, we get an average value of -1.00×10^{-3} eV $(-8.06 \, \text{cm}^{-1})$. The average coupling strength for TrEsp(HF) and TrEsp(DFT) are -1.07×10^{-3} eV $(-8.63 \, \text{cm}^{-1})$ and $-1.17 \; 10^{-3}$ eV $(-9.43 \, \text{cm}^{-1})$, respectively.

5 Excitonic states and linear absorption The excitonic states of the complete system can be determined from the site energies and the electronic couplings gained from the quantum chemical calculations. To achieve this, a Hamiltonian for the LH2 composed of the two BChl rings is constructed. This Hamiltonian includes the excitation energies of the sites and the couplings $V_{nm}(t)$ between them

$$H(t) = \sum_n |n\rangle \varepsilon_n(t) \langle n| + \sum_{n,m} |n\rangle V_{nm}(t) \langle m|. \tag{4}$$

Here the states $|n\rangle$ represent the singly excited BChl states and the energies $\varepsilon_n(t)$ correspond to the energy difference between the ground and excited state of BChl n. The indices n and m run over all 24 sites. In addition, the site energies of the eight BChls belonging to the B800 ring where shifted by an energy of 44 meV. This was necessary since the absolute value of the individual site energies is not reproduced exactly by the ZINDO approach. In order to calculate the energies of the excitonic states the system Hamiltonian needs to be diagonalized. Since the values of the site energies and the couplings vary along the MD trajectory this diagonalization has to be carried out at every time step resulting in time-dependent exciton energies. The upper panel of Fig. 4 shows the time evolution of these excitonic state energies. The energies lie within a range of 1.4–2 eV. It is evident that the energies of the higher exciton states oscillate notably stronger then those belonging to the low energy states. This becomes more obvious in the DOS of the individual states which is shown in the middle panel of Fig. 4. As can be seen there, the width of the distribution increases for increasing energies. The lower panel of Fig. 4 depicts the average excitonic energies over the 12 ps long MD trajectory with error bars corresponding to the variance of the DOS of the individual states.

The spectrum of linear absorbance is calculated to be able to compare the simulated results with experiments. To compute this experimentally accessible observable the excitonic transition dipole moments are needed in addition to the excitonic energies. They can be calculated from the expansion coefficients C_ν^n of the excitonic states in the site representation and the transition dipole moments $\mathbf{d}_n$ from the ZINDO/S calculations

$$\mathbf{d}_\nu = \sum_n C_\nu^n \mathbf{d}_n. \tag{5}$$

The dipole strength for an excitonic state ν can then be given as

$$D_\nu = |\mathbf{d}_\nu|^2 = \sum_n \sum_m C_\nu^n C_\nu^{*m} \times (\mathbf{d}_n \mathbf{d}_m). \tag{6}$$
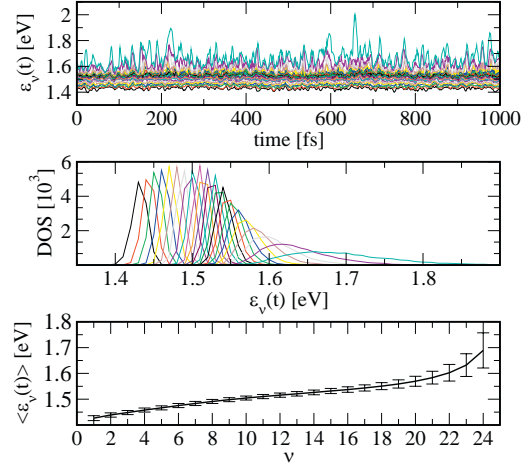

Figure 4 (online color at: www.pss-b.com) Excitonic energies of the complete LH2 system as calculated using the TrEsp(DFT) couplings. The individual excitonic states are distinguished by different colors. Upper panel: Time evolution of the exciton energies, every line belongs to one excitonic state. Middle panel: Distribution of the exciton energies along the MD trajectory. Lower panel: Average exciton energies with error bars corresponding to the variance of the distribution.

Figure 5 (online color at: www.pss-b.com) Excitonic dipole strengths in units of the average monomeric dipole strength of 6.3 D as calculated using TrEsp(DFT) couplings. The various states are distinguished by different colors. Upper panel: Time evolution of the dipole strengths, every line belongs to one excitonic state. Middle panel: Distribution of the dipole strengths along the MD trajectory. Lower panel: Average dipole strength with error bars corresponding to the variance of the distribution.
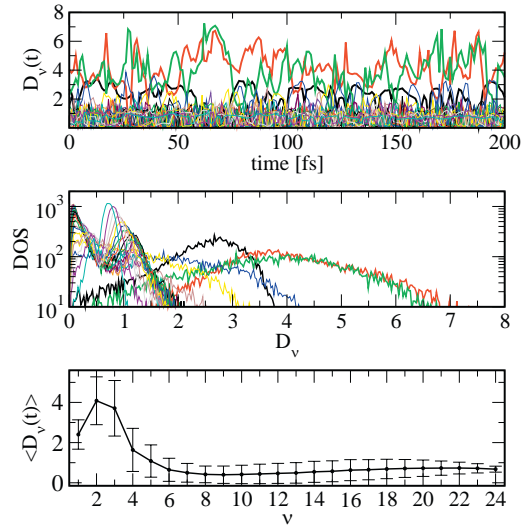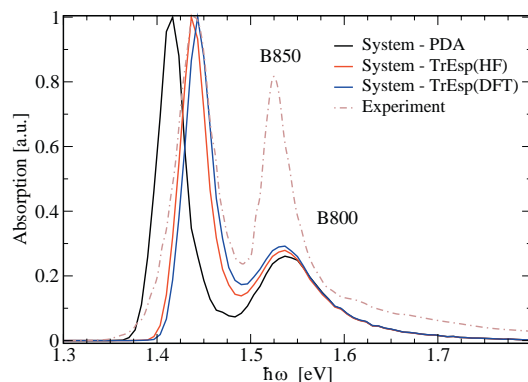
Figure 6 (online color at: www.pss-b.com) Absorption spectrum evaluated from the DOS weighted with the dipole strengths for TrEsp and PDA calculations compared to the experimentally obtained spectrum [47].

Shown in Fig. 5 are the obtained values. The upper panel displays the time evolution of the dipole strength for each excitonic state. The distribution of the individual dipole strengths within the MD trajectory is shown in the middle panel and the average dipole strength with corresponding variance of the distribution in the lower one.

If a δ-like absorption line shape is assumed, the linear absorption spectrum is comparable to the sum over all DOSs of the individual excitonic levels weighted by their dipole strengths. To estimate the spectrum the frequency axis is divided into an equidistant grid with spacing $\Delta\omega$ (binning). The value of the spectrum at grid point ω_j is then evaluated by adding up all dipole strengths of those excitonic levels which lie in the energy range of $\omega_j \pm \frac{1}{2}\Delta\omega$ [24, 39, 46]. The absorption spectrum for the three different calculated couplings is shown in Fig. 6 together with an experimentally obtained spectrum [47]. All three employed methods produce spectra which show the same basic features as the experimental one. Using the PDA the absorption peak of the B850 ring lies at a notably lower frequency than the peaks in the spectra obtained from TrEsp couplings. Both TrEsp couplings produce spectra with a good agreement to the experiment.

6 Conclusions Based on the trajectory of the MD simulation the energy gap fluctuations between ground and excited state were calculated on the semiempirical ZINDO/S level. From the absorption spectrum it can be deferred that a good agreement of the site energies and the experimental data were obtained. Only the energies for the B800 ring had to be slightly shifted (44 meV) due to an insufficient red shift in the ZINDO calculations. An important quantity beside the site energies is the coupling. To this end the commonly used PDA was compared to the TrEsp method using two different sets of transition charges from either HF-CIS or TDDFT/ B3LYP calculations. In addition a distance-dependent

solvent screening factor was used. We were able to show that the TrEsp methods show an obvious splitting of couplings due to the eightfold symmetry of the system. The TrEsp approach yields rather accurate coupling values due to the more realistic representation of the transition densities of the whole molecules. Especially for short distances this is certainly superior to the PDA. The site energies together with the couplings were used in a time-depend Hamiltonian approach for the complete system of the B850 and B800 rings. Especially the obtained excitonic energies of the higher levels show strong fluctuations. Opposite to this, the dipole strengths of the lower excitonic levels have a broad distribution. The first four levels on average carry the largest dipole strengths leading to a peak of the B850 ring in the absorption spectra. The dipole strength for the excitonic level with energy around the B800 peak (1.55 eV) is rather low. This might be the reason for the smaller absorption strength of the B800 ring in the simulations compared to experiment. This discrepancy might also be caused by an insufficient sampling of the relevant energies and dipole strengths. The three different kinds of couplings, PDA and TrEsp(HF) and TrEsp(DFT), do not have a large influence on the peak position of the B800 ring due to the low coupling between the BChls in all three cases. The larger couplings of the PDA compared to TrEsp approaches for the BChls in the B850 ring lead to a red shift of the calculated B850 peak and a larger splitting between the two peaks of the complex. Due to the quite similar average coupling values of TrEsp(DFT) and TrEsp(HF) methods for the BChls within the B850 ring the spectra does but differ remarkable. The spectra are in good agreement with the experimental one.

In the present contribution the time-dependent Hamiltonian was analyzed in terms of the time dependence of the excitonic states and the resulting absorption. In Ref. [15] it is shown how the data can be used to obtain the so-called spectral density. This function is a key ingredient in the theory of open quantum systems and can also be used to determine exciton dynamics and optical properties [48–51].

References

[1] X. Hu, T. Ritz, A. Damjanović, F. Autenrieth, and K. Schulten, Q. Rev. Biophys. **35**, 1–62 (2002).
[2] R. J. Cogdell, A. Gall, and J. Köhler, Q. Rev. Biophys. **39**, 227–324 (2006).
[3] V. Sundström, Annu. Rev. Phys. Chem. **59**, 53–77 (2008).
[4] Y. C. Cheng and G. R. Fleming, Annu. Rev. Phys. Chem. **60**, 241–242 (2009).
[5] V. I. Novoderezhkin and R. van Grondelle, Phys. Chem. Chem. Phys. **12**, 7352–7365 (2010).
[6] H. van Amerongen, L. Valkunas, and R. van Grondelle, Photosynthetic Excitons (World Scientific, Singapore, 2000).

[7] S. Georgakopoulou, R. N. Frese, E. Jonson, C. Koolhaas, R. J. Cogdell, R. van Grondelle, and G. van der Zwan, Biophys. J. **82**, 2184–2197 (2002).

[8] X. Hu, A. Damjanović, T. Ritz, and K. Schulten, Proc. Natl. Acad. Sci. USA **95**, 5935–5941 (1998).

[9] A. Damjanović, I. Kosztin, U. Kleinekathöfer, and K. Schulten, Phys. Rev. E **65**, 031919 (2002).

[10] S. Tretiak, C. Middleton, V. Chernyak, and S. Mukamel, J. Phys. Chem. B **104**, 4519–4528 (2000).

[11] S. Tretiak, C. Middleton, V. Chernyak, and S. Mukamel, J. Phys. Chem. B **104**, 9540–9553 (2000).

[12] A. Damjanović, H. M. Vaswani, P. Fromme, and G. R. Fleming, J. Phys. Chem. B **106**, 10251–10262 (2002).

[13] M. Yang, A. Damjanović, H. M. Vaswani, and G. R. Fleming, Biophys. J. **85**, 140–148 (2003).

[14] M. E. Madjet, F. Müh, and T. Renger, J. Phys. Chem. B **113**, 12603–12614 (2009).

[15] C. Olbrich and U. Kleinekathöfer, J. Phys. Chem. B **114**, 12427–12437 (2010).

[16] W. F. Humphrey, A. Dalke, and K. Schulten, J. Mol. Graph. **14**, 33–38 (1996).

[17] J. Koepke, X. Hu, C. Muenke, K. Schulten, and H. Michel, Structure **4**, 581–597 (1996).

[18] J. Ridley and M. C. Zerner, Theor. Chim. Acta **32**, 111–134 (1973).

[19] M. C. Zerner, G. H. Loew, R. F. Kirchner, and U. T. Mueller-Westerhoff, J. Am. Chem. Soc. **102**, 589–599 (1980).

[20] J. Li, B. Williams, C. J. Cramer, and D. G. Truhlar, J. Chem. Phys. **110**, 724–733 (1999).

[21] M. G. Cory, M. C. Zerner, X. Hu, and K. Schulten, J. Phys. Chem. B **102**, 7640–7650 (1998).

[22] J. Linnanto and J. Korppi-Tommola, Phys. Chem. Chem. Phys. **2**, 4962–4970 (2000).

[23] J. Linnanto and J. Korppi-Tommola, Phys. Chem. Chem. Phys. **2**, 3453–3460 (2002).

[24] L. Janosi, I. Kosztin, and A. Damjanović, J. Chem. Phys. **125**, 014903 (2006).

[25] J. Linnanto and J. Korppi-Tommola, Phys. Chem. Chem. Phys. **8**, 663–667 (2006).

[26] J. Linnanto and J. Korppi-Tommola, Chem. Phys. **357**, 171–180 (2009).

[27] I. A. Howard, F. Zutterman, G. Deroover, D. Lamoen, and C. V. Alsenoy, J. Phys. Chem. B **108**, 19155–19162 (2004).

[28] M. C. Zwier, J. M. Shorb, and B. P. Krueger, J. Comput. Chem. **28**, 1572–1581 (2007).

[29] J. S. Kwon, C. M. Choi, H. J. Kim, N. J. Kim, J. Jang, and M. Yang, J. Phys. Chem. A **113**, 2715–2723 (2009).

[30] J. Neugebauer, Chemphyschem **10**, 3148–3153 (2009).

[31] J. Linnanto, J. E. I. Korppi-Tommola, and V. Helenius, J. Phys. Chem. B **103**, 8739–8750 (1999).

[32] M. E. Madjet, A. Abdurahman, and T. Renger, J. Phys. Chem. B **110**, 17268–17281 (2006).

[33] D. Beljonne, C. Curutchet, G. D. Scholes, and R. J. Silbey, J. Phys. Chem. B **113**, 6583–6599 (2009).

[34] B. Krueger, G. Scholes, and G. Fleming, J. Phys. Chem. B **102**, 5378–5386 (1998).

[35] T. Renger, Photosynth. Res. **102**, 471–485 (2009).

[36] G. D. Scholes, C. Curutchet, B. Mennucci, R. Cammi, and J. Tomasi, J. Phys. Chem. B **111**, 6978–6982 (2007).

[37] T. L. C. Jansen and J. Knoester, J. Phys. Chem. B **110**, 22910–22916 (2006).

[38] T. L. C. Jansen and J. Knoester, Acc. Chem. Res. **42**, 1405–1411 (2009).

[39] H. Zhu, V. May, B. Röder, and T. Renger, J. Chem. Phys. **128**, 154905 (2008).

[40] H. Zhu, B. Röder, and V. May, Chem. Phys. **362**, 19–26 (2009).

[41] J. C. Phillips, R. Braun, W. Wang, J. Gumbart, E. Tajkhorshid, E. Villa, C. Chipot, R. D. Skeel, L. Kale, and K. Schulten, J. Comput. Chem. **26**, 1781–1802 (2005).

[42] T. Petrenko and F. Neese, J. Chem. Phys. **127**, 164319 (2007).

[43] I. P. Mercer, I. R. Gould, and D. R. Klug, J. Phys. Chem. B **103**, 7720–7727 (1999).

[44] M. R. Silva-Junior and W. Thiel, J. Chem. Theor. Comput. **6**, 1546–1564 (2010).

[45] R. G. Alden, E. Johnson, V. Nagarajan, W. W. P. J. Law, and R. G. Cogdell, J. Phys. Chem. B **101**, 4667–4680 (1997).

[46] H. Zhu, V. May, B. Röder, M. E. Madjet, and T. Renger, Chem. Phys. Lett. **444**, 118–124 (2007).

[47] J. P. Zhang, R. Fujii, P. Qian, T. Inaba, T. Mizoguchi, and Y. Koyama, J. Phys. Chem. B **104**, 3683–3691 (2000).

[48] P. Heřman, U. Kleinekathöfer, I. Barvík, and M. Schreiber, J. Lumin. **94/95**, 447–450 (2001).

[49] P. Heřman, U. Kleinekathöfer, I. Barvík, and M. Schreiber, Chem. Phys. **275**, 1–13 (2002).

[50] U. Kleinekathöfer, I. Barvík, P. Heřman, I. Kondov, and M. Schreiber, J. Phys. Chem. B **107**, 14094–14102 (2003).

[51] J. Strümpfer and K. Schulten, J. Chem. Phys. **131**, 225101 (2009).

6. Publication Concerning the FMO Complex

The FMO complex in general and here in particular of the green sulfur bacteria *Chlorobaculum tepidum* has been an object of many investigations. Nevertheless, the observation of unexpected long-lived quantum coherences in the excitation energy transfer in this complex have caused some attention. Due to the experiences we have gained in our investigations on the LH2 complex (see the previous chapter 5) in modeling LH systems, we started to study the electronic relaxation in the FMO complex too. All the presented investigations in this chapter relay on the equilibrated MD system setups of the full trimeric complex and the one of a singe monomer. An introduction to the FMO complex is given in the section 2.2.2. However, the two setups for the MD simulations were prepared by Johan Strümpfer (Urbana-Champaign, USA). Already during the equilibration of the FMO monomer system a detaching of the eighth BChl*a* molecule was observed. Based on this two equilibrated MD setups additional MD simulations were performed by me with recording the trajectories of systems every fifth femtosecond. In the case of the monomer complex the total trajectory last 300 ps whereas the trajectory of the trimer complex covers 200 ps. The following procedure is quite similar to the investigations with the LH2 complex: the site energies were calculated with the semiempirical ZINDO/S-CIS method for each BChl*a* molecule and snapshot, i.e., 960,000 and 420,000 electronic structure calculations were performed for the trimer and the monomer complexes, respectively. All necessary quantities, such as the site energies, TDMs and electronic couplings, were calculated.

In our first analysis (see next section 6.1) we focused on possible correlations in the system which were proposed to play a role in the observed long-lived quantum coherences in the excitation energy transfer. Only weakly correlated motions to

neighboring BChls were observed. Furthermore, the site energies are uncorrelated which agrees with the often-employed uncorrelated bath approximation in open quantum systems. However, to some extent correlations between the couplings are present but most of them turned out to be insignificant.

In the next step (see section 6.2) we combined the time-dependent site energies and couplings to a time-dependent Hamiltonian. Wave packet calculations, i.e., numerical integration of the Schrödinger equation, for this Hamiltonian were performed by Thomas la Cour Jansen, Jörg Liebers, and Mortaza Aghtar and excitation energy population dynamics were achieved. Furthermore, Thomas la Cour Jansen determined the linear absorption spectra and the time-resolved two-dimensional spectra. The experimentally observed quantum coherences have been detected in such a kind of spectra before.

Many research groups employ approaches of open quantum systems to investigate the electronic relaxation dynamics. To this end, spectral densities are employed. In section 6.3 spectral densities for each BChl and groups of BChls for the FMO monomer and trimer complex is presented. Like in the investigations on the LH2 complex in the chapter 5, we provide the parameters for the analytic form of the obtained spectral densities based on the site energy fluctuations.

6.1. The Journal of Physical Chemistry B (2011): The Quest for Spatially Correlated Fluctuations in the FMO Light-Harvesting Complex

Authors: C. Olbrich, J. Strümpfer, K. Schulten, and U. Kleinekathöefer

Quest for Spatially Correlated Fluctuations in the FMO Light-Harvesting Complex

Carsten Olbrich,[†] Johan Strümpfer,[‡] Klaus Schulten,[‡] and Ulrich Kleinekathöfer*,[†]

School of Engineering and Science, Jacobs University Bremen, Campus Ring 1, 28759 Bremen, Germany, and Center for Biophysics and Computational Biology and Beckman Institute, University of Illinois at Urbana-Champaign, Urbana, Illinois 61801, United States

Received: October 17, 2010; Revised Manuscript Received: November 19, 2010

The light absorption in light-harvesting complexes is performed by molecules such as chlorophyll, carotenoid, or bilin. Recent experimental findings in some of these complexes suggest the existence of long-lived coherences between the individual pigments at low temperatures. In this context, the question arises if the bath-induced fluctuations at different chromophores are spatially correlated or not. Here we investigate this question for the Fenna−Matthews−Olson (FMO) complex of *Chlorobaculum tepidum* by a combination of atomistic theories, i.e., classical molecular dynamics simulations and semiempirical quantum chemistry calculations. In these investigations at ambient temperatures, only weak correlations between the movements of the chromophores can be detected at the atomic level and none at the more coarse-grained level of site energies. The often-employed uncorrelated bath approximations indeed seem to be valid. Nevertheless, correlations between fluctuations in the electronic couplings between the pigments can be found. Depending on the level of theory employed, also correlations between the fluctuations of site energies and the fluctuations in electronic couplings are discernible.

Introduction

Photosynthesis certainly is one of the key processes of energy transformations on earth. Light is absorbed by individual pigments and its energy is converted into chemical energy. Most photosynthetic systems contain so-called light-harvesting (LH) complexes which collect light and funnel it to the reaction centers.[1] Over the past years and even decades, the dynamics of light-harvesting systems has been elucidated in detail.[2−4] Already in 1985, high-resolution structures of a photosynthetic reaction center became available.[5] Examples of further available crystal structures include LH2[6,7] and LH1[8] complexes of purple bacteria, LHCII of higher plants,[9] and several others (see, e.g., ref 4). All these structures show that the chromophores are held fixed at their positions by a protein scaffold and reveal many details underlying the absorption and transfer processes in these aggregates. Nevertheless, how and to what extent the very efficient energy transfer is characterized by the structures of the LH complexes and their motions is still an open discussion.

Recent experiments suggest that excitonic coherence is protected by the protein environment[3,10−13] and enhance interest in these systems even further.[4,14] The surprising feature of the quantum coherent energy transfer is that coherence survives for several hundreds of femtoseconds in a complex biological system. By now several studies have investigated in detail the effect of the environment on quantum coherence in terms of quantum efficiency,[15] noise-assisted transport,[16,17] entanglement,[18] and other nonclassical effects.[19] It has been suggested that long-lived coherence is due to correlations of the fluctuations of the site energies.[20] Recently, Womick et al. suggested that, e.g., for allophycocyanin, long-lived electronic coherence requires tuning of the protein environment.[21,22]

In DNA, spatial site correlation has been shown to have a drastic effect on transport properties.[23,24] The effect of such correlation on 2D spectra has been studied earlier already, e.g., in refs 25 and 26. In multichromophore complexes such as the Fenna−Matthews−Olson (FMO) light-harvesting complex, strong correlation between protein-induced fluctuations in the site energies has been suggested as the source of the experimentally observed coherence beatings.[3,10,11,13,20−22] Alternative explanations, namely that the long-lived coherence originates from interference of different quantum pathways, have been put forward recently.[27] Concerning correlated fluctuations, Nazir[28] investigated the influence of correlations on a donor−acceptor system for strong system−bath coupling. Using a Lindblad approach, the influence of correlation on the trapping probability in ring systems was investigated by Fassioli et al.[29] It was found that correlation might play a role in tuning the trapping probability. Surprising effects of correlation in the site energy fluctuations were also shown in a study by Nalbach et al.[30] on a toy model. Furthermore, it has been shown that, in a light-harvesting complex of purple bacteria, LH2, spatial correlations would modify the optical and transport properties significantly.[31] Because of all these possible implications of spatial correlation, we investigate in the present study if such correlation can be observed in simulations at physiological, i.e., ambient, temperatures. This might offer insight into whether spatial correlations are actually important for the biological function of light-harvesting systems.

The specific system under investigation here is the FMO complex of the green sulfur bacterium *Chlorobaculum tepidum*.[32] The optical active entities are bacteriochlorophyll *a* (BChl *a*) molecules. In green sulfur bacteria, the chlorosomes are the main light-harvesting antennae. The excitation transfer between these chlorosomes and the membrane-embedded reaction center is mediated by the FMO trimer, i.e., the system of interest here. Milder et al.[33] have recently reviewed the optical properties of

* To whom correspondence should be addressed. E-mail: u.kleinekathoefer@jacobs-university.de.
[†] Jacobs University Bremen.
[‡] University of Illinois at Urbana-Champaign.

6.1. The Quest for Spatially Correlated Fluctuations in the FMO Light-Harvesting Complex

TABLE 1: Summary of Simulated Systems

FMO monomer	
box size	$100.7 \times 72.5 \times 84.1$ Å^3
no. of atoms	57377
no. of Na$^+$	15
no. of Cl$^-$	16
FMO trimer	
box size	$119.7 \times 115.4 \times 102.4$ Å^3
no. of atoms	133604
no. of Na$^+$	34
no. of Cl$^-$	37

FMO complexes together with the experimental and theoretical approaches comprehensively.[33]

Arrangements, conformational motions, and electronic ground-state properties of whole light-harvesting systems or even complexes thereof can be simulated using classical molecular dynamics (MD).[34] To obtain optical properties, these classical simulation have to be coupled to electronic structure calculations.[35−40] In a subsystem-based approach, the individual chromophores are usually treated separately. The electronic coupling between the subsystems is determined subsequently. Because of the size of the BChl molecules and the large number of vertical transition energy calculations required along an MD trajectory to capture the quantum mechanical behavior, one often employs the semiempirical Zerner's intermediate neglect of differential orbital method with parameters for spectroscopic properties (ZINDO/S).[38−43] We recently tested this method for a LH2 system[39] together with the TrEsp approach for the electronic couplings. TrEsp is the abbreviation for the method of transition charges from electrostatic potentials[44,45] which was applied to different light-harvesting systems[46] before.

Molecular Dynamics

As preparation for the MD simulations, both the monomer and trimer FMO systems, consisting of the pigment−protein complexes, ions, and water, were constructed from the crystal structure of *Chlorobaculum tedium* (PDB code 3ENI).[32] After hydrogens were added to the crystal structures, each pigment−protein complex was embedded in a TIP3P[48] water box. The water boxes were sized such that there was a 15 Å distance from the boundaries of each pigment−protein complex to the edge of the water box. Sodium and chloride ions were added to each water box to bring the total ionic concentrations for each system to 0.1 mol/L. System size, atom counts, and number of ions are summarized in Table 1. In the monomer calculations, the eighth BChl was not associated well and started separating from the structure. Therefore, these simulations were only performed with seven BChls.

MD simulations were carried out using NAMD2[49] with the CHARMM27 force field.[50,51] BChl parameters used were those reported in ref 35. TIP3P water hydrogens were constrained using the SHAKE algorithm.[52] Periodic boundary conditions were employed in the simulation together with the particle mesh Ewald (PME) method[53,54] for electrostatic summations. Subsequent to an energy minimization, each system was equilibrated for 10 ns at 300 K and 1 atm pressure as an NPT ensemble using 1 fs time steps. Thereafter, a production run was carried out with 1 fs time steps for 300 ps. The atomic coordinates from every 5 fs of the 300 ps production run were used for the subsequent QM calculations.

Site Energy and Electronic Coupling Calculations

In subsystem-based quantum approaches, one calculates the ground- and excited-state energies of the individual subsystems.

Together with electronic couplings (see below), these lead to a time-dependent Hamiltonian. The energy differences which are referred to here as site energies were calculated as reported in ref 39 for LH2 of *Rhodospirillum (Rs.) molischianum*. The ORCA code (University of Bonn, Germany)[55] was employed in order to calculate the energy gap between ground and first excited, i.e., the Q_y, state for all BChls in the complex at each snapshot. To make the calculations efficient and because the optical properties of BChls are determined by a cyclic conjugated π-electron system, we restricted the quantum system to a truncated structure of the BChl molecule. To this end, each terminal CH$_3$ and CH$_2$CH$_3$ group as well as the phytyl tail were replaced by H atoms.[38,56] As a compromise between accuracy and computational efficiency, the semiempirical ZINDO/S-CIS(10,10) method was employed using the 10 highest occupied and the 10 lowest unoccupied states in the configuration interaction description. For a similar system, this approach was employed before.[37,38] Point charges stemming from the MD simulations within a cutoff radius of 20 Å around the truncated BChl molecule were included in the ZINDO/S-CIS calculations. In this way, one can account for the main effects of surrounding environments on orbital energies.

In addition to describing the electronic excitations of the individual BChls, one needs to determine the coupling among excitations. In this regard, we followed ref 39. In the TrEsp approach,[44,45] the transition density of pigment m is described using atomic transition charges q_I^T that are localized at the respective pigment, i.e., it is described through $\rho(\mathbf{r}) = \sum_I q_I^T \delta(\mathbf{r} - \mathbf{R}_m^I)$ where $\mathbf{R}_m^I$ denotes the coordinates of the Ith atom of BChl m. The coupling between two pigment molecules is then given by

$$V_{nm} = \frac{f}{4\pi\varepsilon_0} \sum_{I,J} \frac{q_I^T \cdot q_J^T}{|\mathbf{R}_m^I - \mathbf{R}_n^J|} \qquad (1)$$

The atomic partial charges can be calculated using different electronic structure methods. In ref 44 these charges are given for BChl a and Chl a molecules in their planar structures calculated using HF-CIS and TDDFT/B3LYP. The charges calculated by the latter method are used in the present study with a scaling factor of 0.732 to match the size of the experimental dipole moment of 6.3 D.[57] Furthermore, it is assumed that the charges do not change with varying molecular geometry and, therefore, we employ them for the calculation along the MD trajectory. This approximation is quite plausible since the molecular geometries in an equilibrium MD simulation should fluctuate around the equilibrium positions. To account for solvent effects on the electronic couplings, a distance-dependent screening factor f is introduced.[39,58]

Correlations of Atomic Motions

In the present study, we aim at analyzing the role of correlated atomic fluctuations. The established method to quantify the respective correlations from MD simulation is an extension of the Pearson coefficient to the multidimensional case.[59−61] For simplicity, we will denote, in the following, this extension as simply the Pearson coefficient. In this approach, one considers the positional fluctuations, i.e., the deviation from the respective mean values, $\mathbf{x} = \mathbf{r} - \langle \mathbf{r} \rangle$. The multidimensional variant of the Pearson coefficient is then defined as the normalized covariance matrix of the fluctuations $C_{ij}^P = \langle \mathbf{x}_i \cdot \mathbf{x}_j \rangle / [\langle \mathbf{x}_i^2 \rangle \langle \mathbf{x}_j^2 \rangle]^{1/2}$. This coefficient varies between ± 1, i.e., between maximally positive
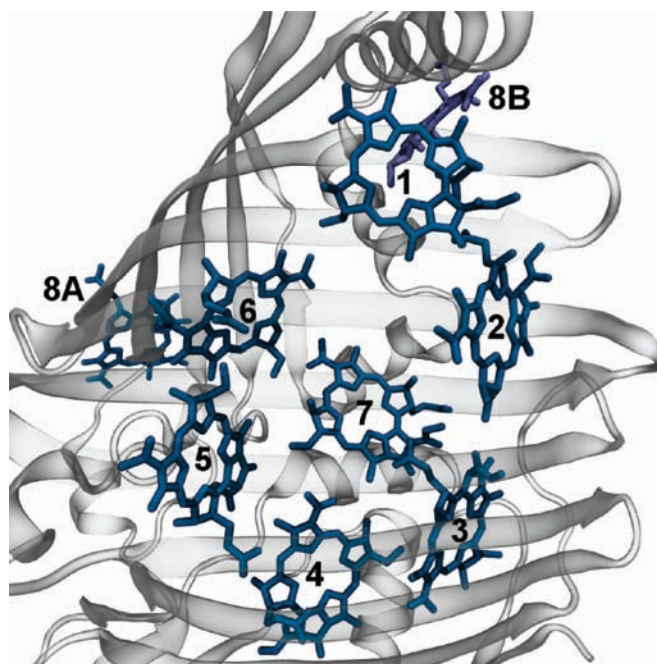
Olbrich et al.

Figure 1. Monomer of the FMO trimer. Shown are the eight BChls of one monomer together with nearby BChl 8B of a neighboring monomer. The protein structure is shown in cartoon representation. Figure drawn using VMD.[47]
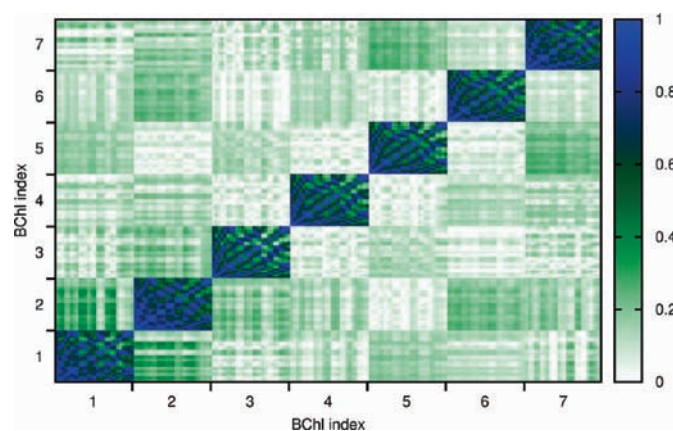

Figure 2. Correlation of atomic motion between the different BChls with 27 atoms per BChl determined using the absolute value of the Pearson coefficient.

and negative correlated motions. Though often employed, this correlation measure has several drawbacks.[61] The Pearson coefficient is based on the assumption of collinear motion with unit variance and an underlying Gaussian distribution. Furthermore, it only detects linear correlation since it is a measure for the quality of the best linear fit.

In contrast to the Pearson coefficient, the generalized correlation coefficient C^{MI}, developed by Lange and Grubmüller,[61] is based on the mutual information between atomic fluctuations. This measure has, for example, been applied to analyze correlations for the transporter BtuB.[62] The generalized correlation is able to detect correlated motion regardless of the relative orientation and includes nonlinear contributions. C^{MI}

captures also the correlation between two atoms fluctuating sinusoidally, but out of phase. For the calculation of the generalized correlation coefficient C^{MI}, the g_correlation software developed by Lange and Grubmüller with a density estimator nearest-neighbor parameter $k = 6$ was employed.[61] Furthermore, the linearized version of C^{MI} is computed below which is restricted to linear correlations like the Pearson coefficient, but is not based on collinear motions.

Correlation analysis using the different measures was performed on 300 ps equilibrium trajectories for the FMO monomer and 200 ps trajectories for the trimer. Saving frames every 5 fs, 60 000 and 40 000 states were taken into account for the FMO monomer and trimer, respectively. To remove all rota-

6.1. The Quest for Spatially Correlated Fluctuations in the FMO Light-Harvesting Complex
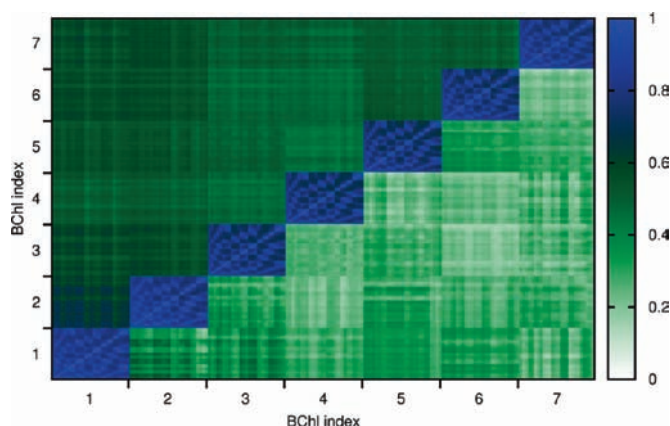
FMO Light-Harvesting Complex

J. Phys. Chem. B, Vol. 115, No. 4, 2011 **761**

Figure 3. Correlation of atomic motion between different sites with 27 atoms per BChl using the generalized correlation coefficient r_{MI} (upper triangle) as well as its linear approximation (lower triangle).

tional and translational motions, the conformation of the protein in each frame was aligned to that of the initial frame. Furthermore, to ensure that correlation values are converged and do not show spurious effects,[63] calculations were performed for trajectory lengths of 100 and 200 ps, and for the monomer also for 300 ps. No significant differences for the correlations were observed for the different trajectory lengths. All figures shown below were obtained using the longest available trajectory length. Hydrogen atoms were not included in this analysis which was restricted to the cores of the BChls as discussed above.

Figure 2 shows the absolute value of the Pearson coefficients for the FMO monomer. The seven blocks on the diagonal show the atomic correlations within each BChl. As mentioned above, only a core BChl has been treated including 27 non-hydrogen atoms. Within each BChl strong correlations are visible. Between the different BChls the atomic correlation is maximally 0.4 with the apparently largest values for correlations between atoms in BChls 1 and 2. Figure S1 in the Supporting Information shows the same property for the simulation of the trimer with very similar results.

As discussed above, the multidimensional Pearson coefficient has several deficiencies. Therefore, we also use the generalized correlation coefficient to analyze atomic correlations in FMO. In Figure 3 the generalized correlation coefficient is shown together with its linear approximation. Naturally, strong correlations within the individual BChls can be seen. At the same time, the minimal values of the correlations, for both the generalized coefficient and its linearized version, are much higher than for the absolute value of the Pearson coefficient. Again, somewhat higher correlations are seen for atoms in BChls 1 and 2. The trimer version of these results is shown in Figure S2 in the Supporting Information, being very similar to the monomer case.

To understand why the generalized correlation C^{MI} coefficients seem to show larger correlations than the C^P even for distant atoms, we plot in Figure 4 the same data as before, not using atom indices, but atom pair distances. This time the Pearson coefficient is shown including its sign. For distances above 10 Å mainly fluctuations around zero arise. For the generalized correlation coefficient the situation is slightly different. This coefficient is larger than or equal to zero by definition; i.e., fluctuations around zero are impossible. Furthermore, this measure has been defined by rescaling an information theoretical measure, which varies between zero and
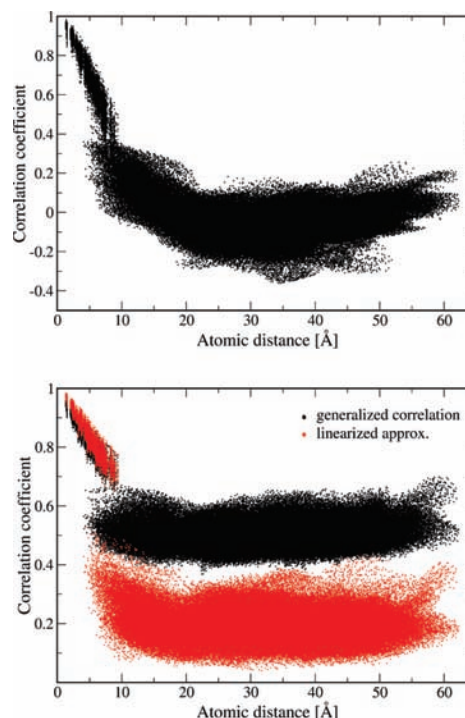

Figure 4. Correlation of atomic motions between different BChls determined using the Pearson approach (top), the generalized correlation coefficient and its linearized approximation (bottom).

infinity, to vary between zero and one; the rescaling is achieved by using the highly nonlinear exponential function which in this case very much overemphasizes small correlations. The data shown in Figure 4 belong to the trimer simulations. The results for the monomer are shown in Figure S3 in the Supporting Information. Neither the generalized coefficient nor its linearization shows much change in the range from 10 to 60 Å. At these latter distances, it can safely be assumed that no important correlations are present. From this we conclude that there is also no correlation at 10 Å as well. Though the nonlinear correlation coefficient shows values of about 0.5, these values
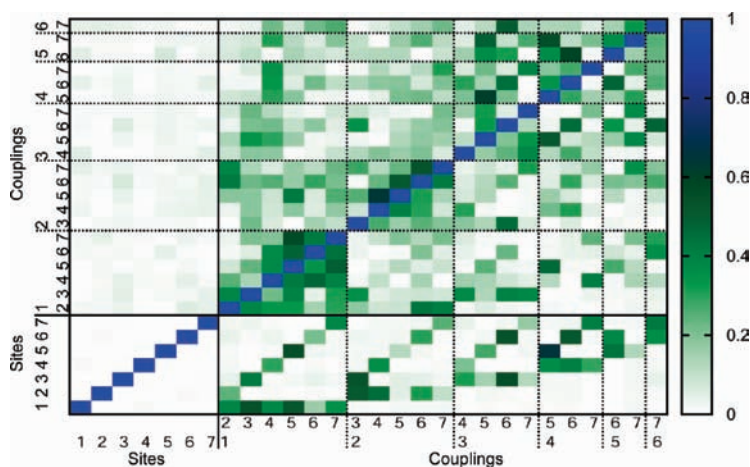
Olbrich et al.

Figure 5. Absolute value of the Pearson coefficient for correlations between site energies and couplings of the monomer system. The lower left corner shows correlations between site energies. The lower triangle of the whole matrix corresponds to couplings determined using the point dipole approximation while the upper triangle is based on TrEsp calculations. The numbers 1 to 7 correspond to the BChls in the FMO monomer.

do not indicate large correlations between atoms, but are merely artifacts of the positive-definiteness and the highly nonlinear scaling in the definition of these generalized coefficients. For an improved generalized coefficient, the "background" correlation would have to be taken into account. Nevertheless, the generalized coefficients also show enhanced correlations between atoms in BChl 1 and 2.

Correlations of Site Energies and Couplings

To see if correlations might explain the observed long-lived coherence in the 2D spectra,[20] we need to investigate the electronic system, namely site energies and couplings. In direct analogy to the formulas used for atomic correlations, correlations between site energies, between electronic couplings, and between site energies and couplings can be determined using the Pearson coefficient, the generalized correlation coefficient, and its linearized variant. Since the latter two do not yield new information in the present case, we only show below the results for the one-dimensional Pearson coefficient. As one example of site energy correlations, in the case of individual nucleobases in DNA, a correlation of 0.7 between neighbors and 0.4 between second neighbors was found.[23] In Figure 5 the results for the present monomer system are shown in the lower left corner. The values on the diagonal are by definition equal to one. Significant correlation cannot be discerned for in the correlation matrix for BChls 1 and 2, though some of the atom pairs between these BChls showed enlarged correlation coefficients. Apparently the observed atomic correlation is not strong enough to show correlation between the electronic properties. The results for the trimer in Figure S4 (in the Supporting Information) look similar; naturally, the number of combinations is much larger in this case.

Despite the observed lack of correlation between site energies, there is still the possibility of correlation between the corresponding electronic couplings. As given in eq 1, the electronic coupling depends on positions of individual atoms and, therefore, atomic correlations can lead to spatial correlation in the electronic couplings. Corresponding results are given in Figure 5 for the monomer and in Figure S4 (in the Supporting Information) for the trimer. The couplings have been determined using either the point dipole approximation or the TrEsp

approach. In either approach, correlations are discernible. The actual degree of correlation depends on the method applied.

It was recently proposed that mixed correlations between fluctuations in site energies and fluctuations in couplings may enhance electronic coherences as seen, for example, in 2D spectra.[64] Such mixed correlations are seen in Figure 5. While couplings from the point dipole approximation are substantial for some pairs, couplings based on TrEsp are negligble. The largest correlations between couplings appear for cases in which the two BChl pairs share a common partner. For example, there is a rather large correlation between couplings 4−5 and 5−7 for the TrEsp results; i.e., if pigment 5 is moving, this imposes a change in the coupling between pigments 4 and 7 and, therefore, causes a correlation between the two couplings. Though there appear to be areas of larger correlations in the correlation matrix, these represent rather local correlations. Large correlations appear for movements of BChl 5 since there are, in addition to the just mentioned pair, correlations between the coupling pair 3−5 and 4−5. Also the movement of pigment 2 leads to correlations in the coupling pairs 2−4 and 2−5, 2−5 and 2−6, and 2−6 and 2−7.

One has to keep in mind that the correlation matrix does not reveal the absolute values of the couplings involved; i.e., many of the correlations might be unimportant since one of the two couplings might be very small. Furthermore, the size of fluctuations might be rather small and unimportant for dynamical and spectroscopic properties. For example, there is a rather large correlation between the couplings 4−5 and 5−6 for the TrEsp results. This correlation is also very prominent in the weighted correlation matrix Figure S5 (in the Supporting Information). If pigment 5 is moving, this imposes a change in the couplings to pigments 4 and 6 at the same time. Therefore, a correlation between both couplings is present. Figure S5 shows the correlation of the couplings as in Figure 5 but weighted by the widths of the two corresponding coupling distributions. This weighting factor is indicative of their importance. A more detailed analysis is needed in order to clarify if the correlations described here can explain long-lived coherences as observed in experiment. Work in this direction is in progress.

6.1. The Quest for Spatially Correlated Fluctuations in the FMO Light-Harvesting Complex

FMO Light-Harvesting Complex

J. Phys. Chem. B, Vol. 115, No. 4, 2011 **763**

Conclusions

This study focused on spatial correlations in geometrical and electronic properties of the FMO complex based on atomistic simulations. It was motivated by experimental evidence for excitonic coherences in the system.[3,10−12] It had been suggested that the observed long-lived coherence is due to correlation between fluctuations of the site energies.[20] However, we found only weak atomic correlations in our present study. Only BChls 1 and 2 exhibit somewhat significant correlation in their atomic motion, but not in the fluctuation of their site energies.

The present study was performed at room temperature while the initial experiments finding of long-lived coherence were performed at 77 K.[10] Recently, experiments have been extended to temperatures of 125, 150, and 277 K;[13] beating signals were seen at all the temperatures.[13] The comparison between present results and the reported experimental findings is difficult. It seems to be clear, though, that site correlations do not play a role at physiological conditions and that the biological function of the FMO complex is not affected by spatial site energy correlations. A similar conclusion has already been drawn for the light-harvesting II complex of *Rhodospirillum molischianum* in a similar study.[39] Whether correlations in the couplings or whether an alternative mechanisms[27] are responsible for the long-lived coherences is unknown so far.

In our approach we first performed a classical equilibrium MD simulation and then carried out electronic structure calculations employing the trajectory data; i.e., we never really do simulations involving excited states of BChls. The excitation process leads to a redistribution of charges and to dipole moment changes of the excited BChls which has influence on the movements of nuclei, i.e., the MD part. However, in contrast to the case of charge transport, e.g., in DNA,[23,24] the charge state of the BChls stays the same. Therefore, the present results should not be significantly influenced by the missing back-reaction of the electronic onto the nuclear part of our description.

The present combination of MD and quantum chemistry can also be used to derive the so-called spectral density.[35,39] The latter quantity is a crucial input parameter for theories of dissipative quantum dynamics. Many such calculations have been performed for light-harvesting systems; see, e.g., refs 12, 15−17, 31, and 65−68. Calculations such as the one presented here help to make a direct connection between atomistic simulations and models of dissipative excitation dynamics.

Supporting Information Available: Atomic and site-energy/coupling correlation matrices of the trimer simulation and weighted correlation matrix of couplings for FMO monomer. This material is available free of charge via the Internet at http://pubs.acs.org.

References and Notes

(1) Hu, X.; Ritz, T.; Damjanović, A.; Autenrieth, F.; Schulten, K. Photosynthetic apparatus of purple bacteria. *Q. Rev. Biophys.* **2002**, *35*, 1–62.

(2) Cogdell, R. J.; Gall, A.; Köhler, J. The architecture and function of the light-harvesting apparatus of purple bacteria: from single molecules to in vivo membranes. *Q. Rev. Biophys.* **2006**, *39*, 227–324.

(3) Cheng, Y. C.; Fleming, G. R. Dynamics of light harvesting in photosynthesis. *Annu. Rev. Phys. Chem.* **2009**, *60*, 241–242.

(4) Novoderezhkin, V. I.; van Grondelle, R. Physical origins and models of energy transfer in photosynthetic light-harvesting. *Phys. Chem. Chem. Phys.* **2010**, *12*, 7352–7365.

(5) Deisenhofer, J.; Epp, O.; Miki, K.; Huber, R.; Michel, H. Structure of the protein subunits in the photosynthetic reaction centre of Rhodopseudomonas viridis at 3 Å resolution. *Nature* **1985**, *318*, 618–624.

(6) McDermott, G.; Prince, S. M.; Freer, A. A.; Hawthornthwaite-Lawless, A. M.; Papiz, M. Z.; Cogdell, R. J.; Isaacs, N. W. Crystal structure of an integral membrane light-harvesting complex from photosynthetic bacteria. *Nature* **1995**, *374*, 517–521.

(7) Koepke, J.; Hu, X.; Muenke, C.; Schulten, K.; Michel, H. The crystal structure of the light harvesting complex II (B800−850) from *Rhodospirillum molischianum. Structure* **1996**, *4*, 581–597.

(8) Roszak, A. W.; Howard, T. D.; Southall, J.; Gardiner, A. T.; Law, C. J.; Isaacs, N. W.; Cogdell, R. J. Crystal structure of the RC-LH1 core complex from Rhodopseudomonas palustris. *Science* **2003**, *302*, 1969–1972.

(9) Kuhlbrandt, W.; Wang, D. N.; Fujiyoshi, Y. Atomic model of plant light-harvesting complex by electron crystallography. *Nature* **1994**, *367*, 614–621.

(10) Engel, G. S.; Calhoun, T. R.; Read, E. L.; Ahn, T. K.; Mancal, T.; Cheng, Y. C.; Blankenship, R. E.; Fleming, G. R. Evidence for wavelike energy transfer through quantum coherence in photosynthetic systems. *Nature* **2007**, *446*, 782–786.

(11) Collini, E.; Wong, C. Y.; Wilk, K. E.; Curmi, P. M.; Brumer, P.; Scholes, G. D. Coherently wired light-harvesting in photosynthetic marine algae at ambient temperature. *Nature* **2010**, *463*, 644–647.

(12) Ishizaki, A.; Calhoun, T. R.; Schlau-Cohen, G. S.; Fleming, G. R. Quantum coherence and its interplay with protein environments in photosynthetic electronic energy transfer. *Phys. Chem. Chem. Phys.* **2010**, *12*, 7319–7337.

(13) Panitchayangkoon, G.; Hayes, D.; Fransted, K. A.; Caram, J. R.; Harel, E.; Wen, J.; Blankenship, R. E.; Engel, G. S. Long-lived quantum coherence in photosynthetic complexes at physiological temperature. *Proc. Natl. Acad. Sci. U.S.A.* **2010**, *107*, 12766–12770.

(14) Scholes, G. D. Quantum-Coherent Electronic Energy Transfer: Did Nature Think of It First. *J. Phys. Chem. Lett.* **2010**, *1*, 2–8.

(15) Olaya-Castro, A.; Lee, C. F.; Olsen, F. F.; Johnson, N. F. Efficiency of energy transfer in a light-harvesting system under quantum coherence. *Phys. Rev. B* **2008**, *78*, 085115.

(16) Caruso, F.; Chin, A. W.; Datta, A.; Huelga, S. F.; Plenio, M. B. Highly efficient energy excitation transfer in light-harvesting complexes: The fundamental role of noise-assisted transport. *J. Chem. Phys.* **2009**, *131*, 105106.

(17) Rebentrost, P.; Mohseni, M.; Aspuru-Guzik, A. Role of Quantum Coherence and Environmental Fluctuations in Chromophoric Energy Transport. *J. Phys. Chem. B* **2009**, *113*, 9942–9947.

(18) Sarovar, M.; Ishizaki, A.; Fleming, G. R.; Whaley, K. B. Quantum entanglement in photosynthetic light-harvesting complexes. *Nature Phys.* **2010**, *6*, 462–467.

(19) Fleming, G. R.; Huelga, S.; Plenio, M. Focus on Quantum Effects and Noise in Biomolecules. *New J. Phys.* **2010**, *12*, 065002.

(20) Wolynes, P. G. Some quantum weirdness in physiology. *Proc. Natl. Acad. Sci. U.S.A.* **2009**, *106*, 17247–17248.

(21) Womick, J. M.; Moran, A. M. Exciton Coherence and Energy Transport in the Light-Harvesting Dimers of Allophycocyanin. *J. Phys. Chem. B* **2009**, *113*, 15747–15759.

(22) Womick, J. M.; Miller, S. A.; Moran, A. M. Toward the origin of exciton electronic structure in phycobiliproteins. *J. Chem. Phys.* **2010**, *133*, 024507.

(23) Kubař, T.; Kleinekathöfer, U.; Elstner, M. Solvent Fluctuations Drive the Hole Transfer in DNA: a Mixed Quantum-Classical Study. *J. Phys. Chem. B* **2009**, *113*, 13107–13117.

(24) Dijkstra, A. G.; Tanimura, Y. Correlated fluctuations in the exciton dynamics and spectroscopy of DNA. *New J. Phys.* **2010**, *12*, 055005.

(25) Venkatramani, R.; Mukamel, S. Correlated line broadening in multidimensional vibrational spectroscopy. *J. Chem. Phys.* **2002**, *117*, 11089–11101.

(26) Ishizaki, A.; Tanimura, Y. Dynamics of a multimode system coupled to multiple heat baths probed by two-dimensional infrared spectroscopy. *J. Phys. Chem. A* **2007**, *111*, 9269–9276.

(27) Abramavicius, D.; Mukamel, S. Quantum oscillatory exciton migration in photosynthetic reaction centers. *J. Chem. Phys.* **2010**, *133*, 064510.

(28) Nazir, A. Correlation-Dependent Coherent to Incoherent Transitions in Resonant Energy Transfer Dynamics. *Phys. Rev. Lett.* **2009**, *103*, 146404.

(29) Fassioli, F.; Nazir, A.; Olaya-Castro, A. Quantum State Tuning of Energy Transfer in a Correlated Environment. *J. Phys. Chem. Lett.* **2010**, *1*, 2139–2143.

(30) Nalbach, P.; Eckel, J.; Thorwart, M. Quantum coherent biomolecular energy transfer with spatially correlated fluctuations. *New J. Phys.* **2010**, *12*, 065043.

(31) Strümpfer, J.; Schulten, K. The Effect of Correlated Bath Fluctuations on Exciton Transfer. Submitted for publication, 2010.

(32) Tronrud, D. E.; Wen, J.; Gay, L.; Blankenship, R. E. The structural basis for the difference in absorbance spectra for the FMO antenna protein from various green sulfur bacteria. *Photosynth. Res.* **2009**, *100*, 79–87.

(33) Milder, M. T.; Brüggemann, B.; van Grondelle, R.; Herek, J. L. Revisiting the optical properties of the FMO protein. *Photosynth. Res.* **2010**, *104*, 257–264.

(34) Sener, M. K.; Strümpfer, J.; Timney, J. A.; Freiberg, A.; Hunter, C. N.; Schulten, K. Photosynthetic Vesicle Architecture and Constraints on Efficient Energy Harvesting. *Biophys. J.* **2010**, *99*, 67–75.

(35) Damjanović, A.; Kosztin, I.; Kleinekathöfer, U.; Schulten, K. Excitons in a Photosynthetic Light-Harvesting System: A Combined Molecular Dynamics, Quantum Chemistry and Polaron Model Study. *Phys. Rev. E* **2002**, *65*, 031919.

(36) Walker, R. C.; Mercer, I. P.; Gould, I. R.; Klug, D. R. Comparison of basis set effects and the performance of ab initio and DFT methods for probing equilibrium fluctuations. *J. Comput. Chem.* **2007**, *28*, 478–480.

(37) Zwier, M. C.; Shorb, J. M.; Krueger, B. P. Hybrid molecular dynamics-quantum mechanics simulations of solute spectral properties in the condensed phase: evaluation of simulation parameters. *J. Comput. Chem.* **2007**, *28*, 1572–1581.

(38) Janosi, L.; Kosztin, I.; Damjanović, A. Theoretical prediction of spectral and optical properties of bacteriochlorophylls in thermally disordered LH2 antenna complexes. *J. Chem. Phys.* **2006**, *125*, 014903.

(39) Olbrich, C.; Kleinekathöfer, U. Time-dependent atomistic view on the electronic relaxation in light-harvesting system II. *J. Phys. Chem. B* **2010**, *114*, 12427–12437.

(40) Olbrich, C.; Liebers, J.; Kleinekathöfer, U. Modeling of light-harvesting in purple bacteria using a time-dependent Hamiltonian approach. *Phys. Status Solidi B* **2010**, DOI: 10.1002/pssb.201000651.

(41) Ridley, J.; Zerner, M. C. An intermediate neglect of differential overlap technique for spectroscopy: Pyrrole and the azines. *Theor. Chim. Acta* **1973**, *32*, 111–134.

(42) Damjanović, A.; Vaswani, H. M.; Fromme, P.; Fleming, G. R. Chlorophyll Excitations in Photosystem I of Synechococcus elongatus. *J. Phys. Chem. B* **2002**, *106*, 10251–10262.

(43) Linnanto, J.; Korppi-Tommola, J. Quantum chemical simulation of excited states of chlorophylls, bacteriochlorophylls and their complexes. *Phys. Chem. Chem. Phys.* **2006**, *8*, 663–667.

(44) Madjet, M. E.; Abdurahman, A.; Renger, T. Intermolecular coulomb couplings from ab initio electrostatic potentials: application to optical transitions of strongly coupled pigments in photosynthetic antennae and reaction centers. *J. Phys. Chem. B* **2006**, *110*, 17268–81.

(45) Renger, T. Theory of excitation energy transfer: from structure to function. *Photosynth. Res.* **2009**, *102*, 471–485.

(46) Madjet, M. E.; Müh, F.; Renger, T. Deciphering the influence of short-range electronic couplings on optical properties of molecular dimers: application to "special pairs" in photosynthesis. *J. Phys. Chem. B* **2009**, *113*, 12603–14.

(47) Humphrey, W. F.; Dalke, A.; Schulten, K. VMD—Visual Molecular Dynamics. *J. Mol. Graph.* **1996**, *14*, 33–38.

(48) Jorgensen, W. L.; Chandrasekhar, J.; Madura, J. D.; Impey, R. W.; Klein, M. L. Comparison of simple potential functions for simulating liquid water. *J. Chem. Phys.* **1983**, *79*, 926–935.

(49) Phillips, J. C.; Braun, R.; Wang, W.; Gumbart, J.; Tajkhorshid, E.; Villa, E.; Chipot, C.; Skeel, R. D.; Kale, L.; Schulten, K. Scalable molecular dynamics with NAMD. *J. Comput. Chem.* **2005**, *26*, 1781–1802.

(50) Foloppe, N.; MacKerell, A. D., Jr. All-Atom Empirical Force Field for Nucleic Acids: 2) Parameter Optimization Based on Small Molecule and Condensed Phase Macromolecular Target Data. *J. Comput. Chem.* **2000**, *21*, 86–104.

(51) MacKerell, A.; et al. All-Atom Empirical Potential for Molecular Modeling and Dynamics Studies of Proteins. *J. Phys. Chem. B* **1998**, *102*, 3586–3616.

(52) Ryckaert, J.-P.; Ciccotti, G.; Berendsen, H. J. C. Numerical integration of the cartesian equations of motion of a system with constraints: molecular dynamics of n-alkanes. *J. Comput. Phys.* **1977**, *23*, 327–341.

(53) Ewald, P. P. Die Berechnung optischer und elektrostatischer Gitterpotentiale. *Ann. Phys. (Berlin)* **1921**, *369*, 253–287.

(54) Darden, T.; Perera, L.; Li, L.; Pedersen, L. New tricks for modelers from the crystallography toolkit: the particle mesh Ewald algorithm and its use in nucleic acid simulations. *Structure* **1999**, 55–60.

(55) Petrenko, T.; Neese, F. Analysis and prediction of absorption band shapes, fluorescence band shapes, resonance Raman intensities, and excitation profiles using the time-dependent theory of electronic spectroscopy. *J. Chem. Phys.* **2007**, *127*, 164319.

(56) Cory, M. G.; Zerner, M. C.; Hu, X.; Schulten, K. Electronic excitations in aggregates of bacteriochlorophylls. *J. Phys. Chem. B* **1998**, *102*, 7640–7650.

(57) Alden, R. G.; Johnson, E.; Nagarajan, V.; Law, W. W. P. J.; Cogdell, R. G. Calculations of Spectroscopic Properties of the LH2 Bacteriochlorophyll: Protein Antenna Complex from Rhodopseudomonas acidophila. *J. Phys. Chem. B* **1997**, *101*, 4667–4680.

(58) Scholes, G. D.; Curutchet, C.; Mennucci, B.; Cammi, R.; Tomasi, J. How Solvent Controls Electronic Energy Transfer and Light Harvesting. *J. Phys. Chem. B* **2007**, *111*, 6978–6982.

(59) Ichiye, T.; Karplus, M. Collective motions in proteins: a covariance analysis of atomic fluctuations in molecular dynamics and normal mode simulations. *Proteins* **1991**, *11*, 205–207.

(60) Hünenberger, P. H.; Mark, A. E.; van Gunsteren, W. F. Fluctuation and cross-correlation analysis of protein motions observed in nanosecond molecular dynamics simulations. *J. Mol. Biol.* **1995**, *252*, 492–503.

(61) Lange, O. F.; Grubmüller, H. Generalized correlation for biomolecular dynamics. *Proteins* **2006**, *62*, 1053–1061.

(62) Luan, B.; Carr, R.; Caffrey, M.; Aksimentiev, A. The effect of calcium on the conformation of cobalamin transporter BtuB. *Proteins* **2010**, *78*, 1153–1162.

(63) Meinhold, L.; Smith, J. C. Fluctuations and correlations in crystalline protein dynamics: a simulation analysis of staphylococcal nuclease. *Biophys. J.* **2005**, *88*, 2554–2563.

(64) Chen, X.; Silbey, R. J. Effect of correlation of local fluctuations on exciton coherence. *J. Chem. Phys.* **2010**, *132*, 204503.

(65) Heřman, P.; Kleinekathöfer, U.; Barvík, I.; Schreiber, M. Exciton scattering in light-harvesting systems of purple bacteria. *J. Lumin.* **2001**, *94&95*, 447–450.

(66) Heřman, P.; Kleinekathöfer, U.; Barvík, I.; Schreiber, M. Influence of Static and Dynamic Disorder on the Anisotropy of Emission in the Ring Antenna Subunits of Purple Bacteria Photosynthetic Systems. *Chem. Phys.* **2002**, *275*, 1–13.

(67) Kleinekathöfer, U.; Barvík, I.; Heřman, P.; Kondov, I.; Schreiber, M. Memory effects in the fluorescence depolarization dynamics studied within the B850 ring of purple bacteria. *J. Phys. Chem. B* **2003**, *107*, 14094–14102.

(68) Strümpfer, J.; Schulten, K. Light harvesting complex II B850 excitation dynamics. *J. Chem. Phys.* **2009**, *131*, 225101.

JP1099514

SUPPLEMENTARY FIGURES

The quest for spatially correlated fluctuations in the

FMO light-harvesting complex

Carsten Olbrich,[†] Johan Strümpfer,[‡] Klaus Schulten,[‡] and Ulrich Kleinekathöfer[∗,†]

School of Engineering and Science, Jacobs University Bremen, Campus Ring 1, 28759 Bremen, Germany, and Center for Biophysics and Computational Biology and Beckman Institute, University of Illinois at Urbana-Champaign, Urbana, Illinois 61801, USA

E-mail: u.kleinekathoefer@jacobs-university.de

─────────────────────────
[∗]To whom correspondence should be addressed

[†]School of Engineering and Science, Jacobs University Bremen, Campus Ring 1, 28759 Bremen, Germany

[‡]Center for Biophysics and Computational Biology and Beckman Institute, University of Illinois at Urbana-Champaign, Urbana, Illinois 61801, USA
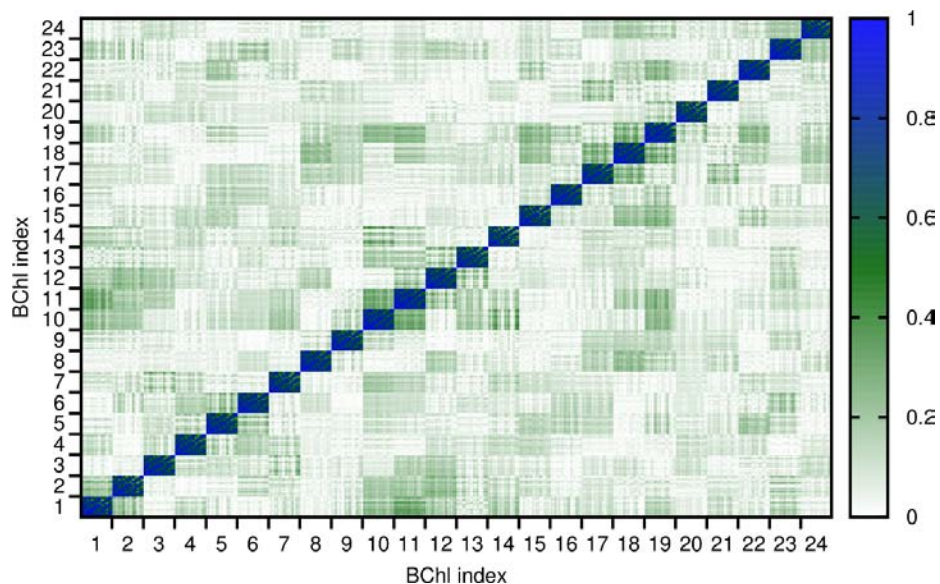
1

Figure S1: Correlation of atomic motion between different BChls determined using the absolute value of the Pearson approach for the FMO trimer.

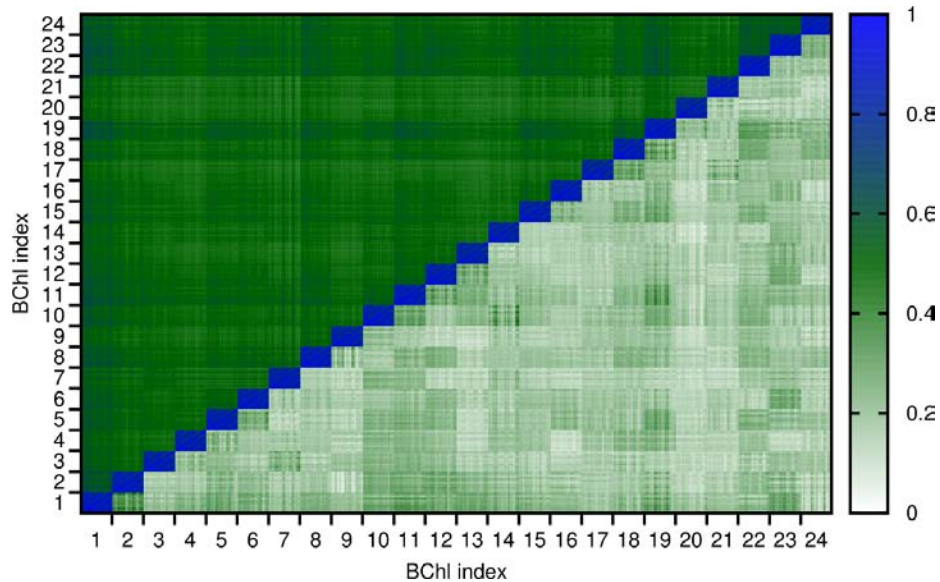Figure S2: Correlation of atomic motion between different sites in the FMO trimer using the generalized correlation coefficient r_{MI} (upper triangle) as well as its linear approximation (lower triangle).

2
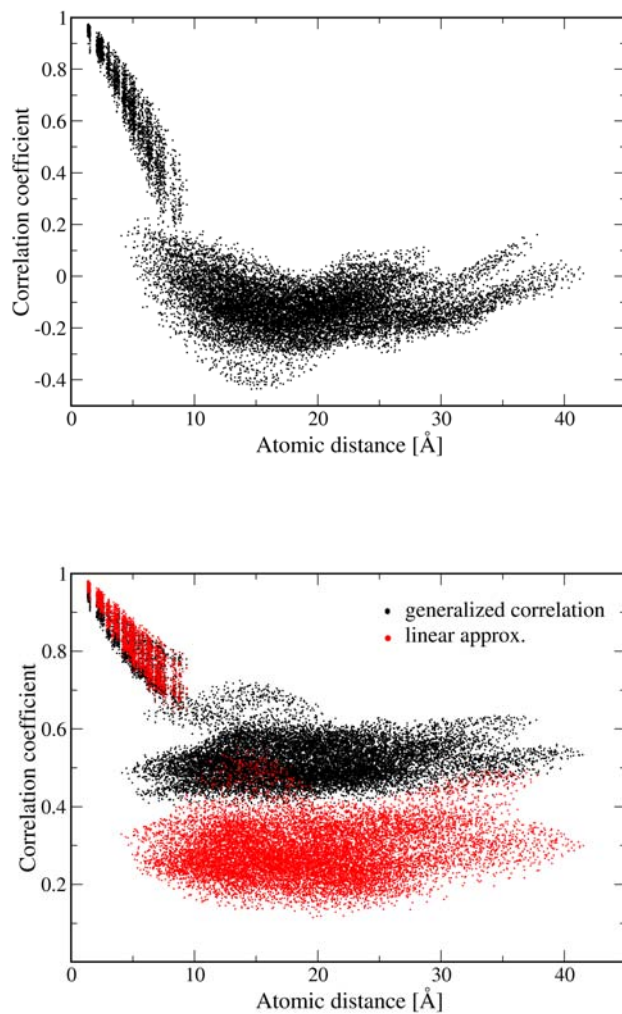
Figure S3: Correlation of atomic motion for FMO monomer between different BChls determined using the Pearson approach (top), the generalized correlation coefficient and its linear approximation (bottom).

3
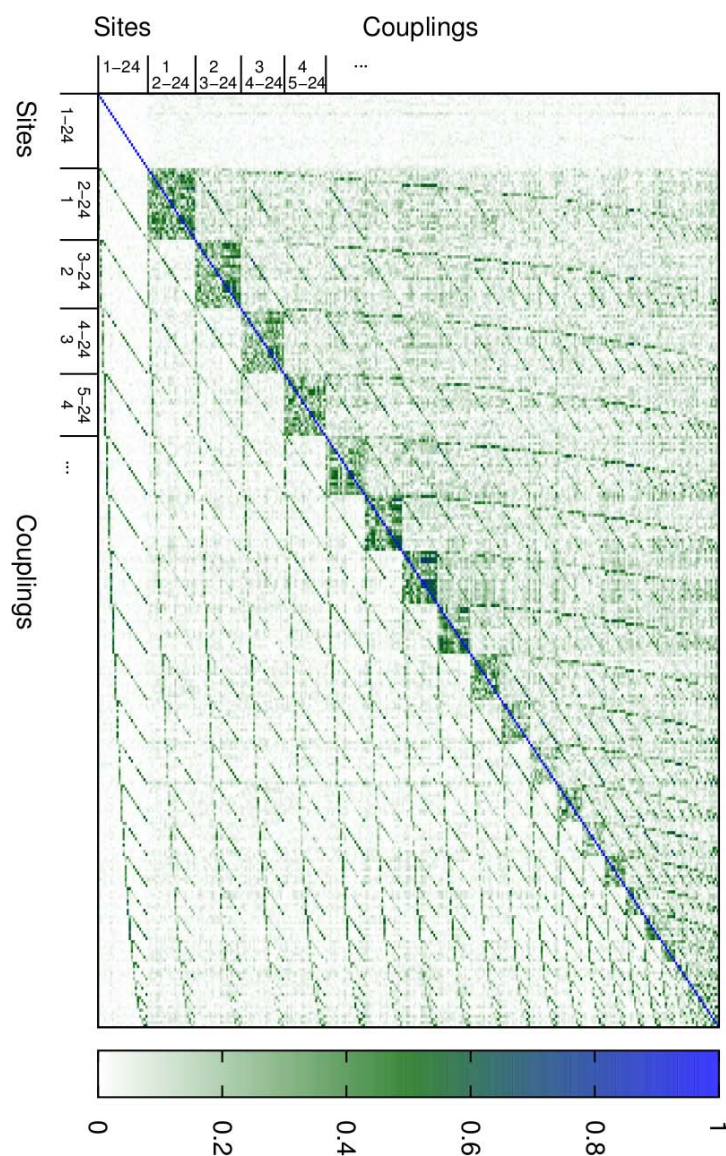
Figure S4: Absolute value of the Pearson coefficient for correlations between site energies and couplings of the trimer system. The lower left corner shows correlations between site energies. The lower triangle of the whole matrix corresponds to couplings determined using the point dipole approximation while the upper triangle is based on TrEsp calculations. The numbers 1 to 24 correspond to the BChls in the FMO trimer.

4
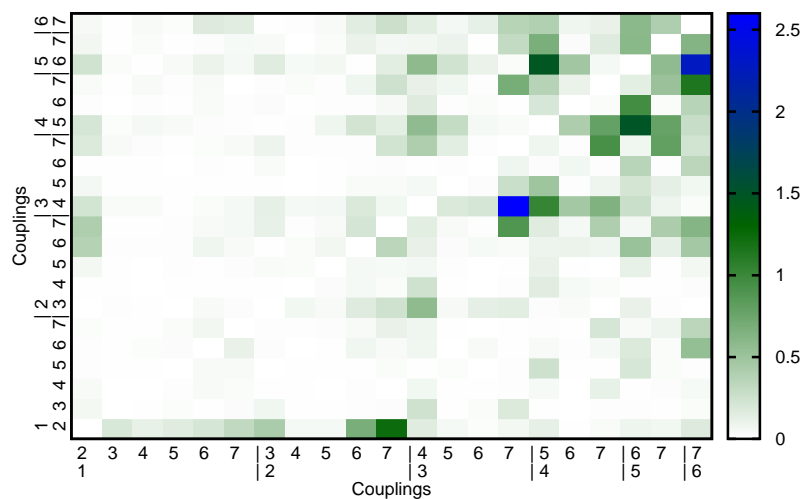
Figure S5: Absolute value of the Pearson coefficient for correlations between couplings of the monomer system weighted by the widths of the two corresponding coupling distributions. The color code is in units of meV^2. The lower triangle of the whole matrix corresponds to couplings determined using the point dipole approximation while the upper triangle is based on TrEsp calculations. To ease the interpretation, the diagonal elements have been set to zero.

5

6.2. The Journal of Physical Chemistry B (2011): From Atomistic Modelling to Excitation Transfer and Two-Dimensional Spectra of the FMO Light-Harvesting Complex

Authors: C. Olbrich, T. C. Jansen, J. Liebers, M. Aghtar, J. Strümpfer, K. Schulten, J. Knoester, and U. Kleinekathöefer

From Atomistic Modeling to Excitation Transfer and Two-Dimensional Spectra of the FMO Light-Harvesting Complex

Carsten Olbrich,[†] Thomas L. C. Jansen,[‡] Jörg Liebers,[†] Mortaza Aghtar,[†] Johan Strümpfer,[§] Klaus Schulten,[§] Jasper Knoester,[‡] and Ulrich Kleinekathöfer[*,†]

[†]School of Engineering and Science, Jacobs University Bremen, Campus Ring 1, 28759 Bremen, Germany

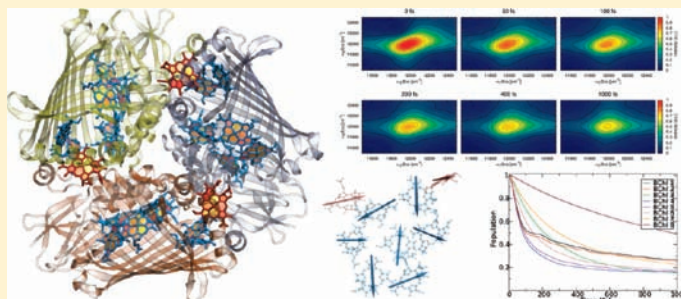[‡]Zernike Institute for Advanced Materials, University of Groningen, Nijenborgh 4, 9747 AG Groningen, The Netherlands

[§]Center for Biophysics and Computational Biology and Beckman Institute, University of Illinois at Urbana—Champaign, Urbana, Illinois 61801, United States

ABSTRACT:

The experimental observation of long-lived quantum coherences in the Fenna—Matthews—Olson (FMO) light-harvesting complex at low temperatures has challenged general intuition in the field of complex molecular systems and provoked considerable theoretical effort in search of explanations. Here we report on room-temperature calculations of the excited-state dynamics in FMO using a combination of molecular dynamics simulations and electronic structure calculations. Thus we obtain trajectories for the Hamiltonian of this system which contains time-dependent vertical excitation energies of the individual bacteriochlorophyll molecules and their mutual electronic couplings. The distribution of energies and couplings is analyzed together with possible spatial correlations. It is found that in contrast to frequent assumptions the site energy distribution is non-Gaussian. In a subsequent step, averaged wave packet dynamics is used to determine the exciton dynamics in the system. Finally, with the time-dependent Hamiltonian, linear and two-dimensional spectra are determined. The thus-obtained linear absorption line shape agrees well with experimental observation and is largely determined by the non-Gaussian site energy distribution. The two-dimensional spectra are in line with what one would expect by extrapolation of the experimental observations at lower temperatures and indicate almost total loss of long-lived coherences.

■ INTRODUCTION

In photosynthesis the energy of sunlight is converted into chemical energy. Light harvesting and charge separation are the primary steps in this process. Specific pigment—protein aggregates, the so-called light-harvesting (LH) complexes, have the function of absorbing light and transporting the energy to the photosynthetic reaction center (RC). Within the RC the excitation is subsequently converted into charge separation.[1] Many of the structural and functional details of these protein complexes have been elucidated already.[2−4]

One of the extensively studied LH systems is the Fenna—Matthews—Olson (FMO) complex of green sulfur bacteria.[5] For the bacterium *Prosthecochloris aestuarii*, the crystal structure was already solved three decades ago,[6] the first time that this was achieved for a pigment—protein complex. Meanwhile the structure

has been characterized at atomic resolution 1.9 Å.[7] Recently, the structure of the FMO complex of *Chlorobaculum tepidum* has been determined as well.[8] Under physiological conditions, the FMO complex forms a homotrimer consisting of eight bacteriochlorophyll-a (BChl a) molecules per monomer. The existence of an eighth BChl molecule in the structure of each monomer has been shown only recently;[8] many earlier studies refer to just seven BChls per monomer. The biological function of the FMO trimer is to transfer excitation energy from the chlorosome, i.e., the main LH antenna system of green sulfur bacteria, to the RC, which is embedded into the membrane.[5] The optical properties of FMO

complexes together with the experimental and theoretical approaches were reviewed recently in great detail.[5] We note that the photophysical investigations published thus far were performed on FMO trimers rather than monomers. Nevertheless, additional studies of the monomeric system as performed here yield insight into properties also of the trimeric arrangement.

A few years ago, using two-dimensional correlation spectroscopy the Fleming group reported evidence for coherent energy-transfer dynamics in FMO.[9,10] Because of the unexpectedly long coherence times of around 700 fs at 77 K, the findings provoked a large number of further studies, both experimental and theoretical ones. By now, similar coherence times have been shown to arise at higher temperatures[11] for the same FMO complex of *Chlorobaculum tepidum*, for a photosynthetic complex of marine algae at ambient temperature[12] as well as in conjugated polymers.[13] It has been suggested that the long-lived coherence is due to correlations of site energies fluctuations.[14] A few publications have investigated the possible effect of correlated motions.[15−22] In earlier simulations for LH systems combined with semiempirical electronic structure calculations, reported by several of the present authors, we did not find spatial correlation in the time dependence of the site energies.[23,24] Alternative suggestions that the long-lived coherences originate from interferences of different quantum pathways have been put forward recently.[25,26]

In this paper, we aim to give a parameter-free calculation of the excited-state dynamics and the linear and two-dimensional spectra for FMO. Our method is based on a combination of classical molecular dynamics (MD) and electronic structure calculations. Using MD one can model complete LH systems.[23,27] Nonetheless, MD simulations are able to describe neither the optical properties of such systems nor the excitation transfer therein. For such description, one has to couple electronic structure calculations to the classical simulations.[23,27−31] Even for semiempirical methods, the determination of the electronic structure of the complete system over time is computationally expensive. Therefore, one usually adopts a subsystem-based approach in which the excitation energy for each individual BChl is calculated separately. In addition to the individual excitation energies, one needs to determine the electronic coupling between the subsystems. To record the effect of the thermal fluctuations on the energy transfer dynamics and optical properties, the quantum chemistry calculations of the excitation energies and the electronic couplings have to be performed along an MD trajectory.[23,27,30−33] To calculate the vertical transition energies of the BChl molecules involved in the LH systems, the semiempirical Zerner Intermediate Neglect of Differential Orbital method with parameters for spectroscopic properties (ZINDO/S) has been shown to be a good compromise between accuracy and computational speed.[29] The ZINDO method is based on the Hartree−Fock framework but two-center electron interaction integrals are neglected. ZINDO/S does not only denote a ground state method but the approach does yield the excited states employing the Configuration Interaction Singles method (also called ZINDO/S-CIS) at the same time. In a recent study for a LH2 system[23] we compared this method combined with the TrEsp approach for the electronic coupling to other commonly used approaches. TrEsp is the abbreviation for the method of transition charges from electrostatic potentials.[34,35] The method has been applied to different light-harvesting systems before.[36]

Nonlinear spectroscopic experiments such as photon echo peak shift[37] and pump−probe spectroscopy permit the study of excitation dynamics. The emergence of two-dimensional correlation spectroscopy (2D CS), first in the infrared[38] and later in the
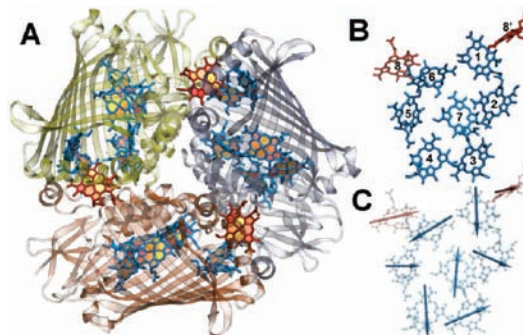

Figure 1. (A) FMO trimer with the protein structure in cartoon representation. (B) Shown are the eight BChls of one monomer together with the close BChl 8′ of the neighboring monomer. (C) The directions of the transition dipole moments between the ground state and the first excited state within each monomer are depicted. Figures drawn using VMD.[46]

visible.[9] made it possible to obtain very detailed information about the excitation dynamics in a system. 2D CS is closely related to the well-known two-dimensional NMR COSY technique[39] and basically relies on correlating the frequencies observed at one time with those that are detected after a time delay. In this way the information is spread in two-dimensions and the technique is particularly sensitive to fluctuations in the eigenfrequencies arising from environmental fluctuations and exciton dynamics. 2D CS is therefore ideally suited for the study of exciton transport in light harvesting systems,[9,10] and as mentioned above, it has been experimentally applied to LH complexes and the FMO system.

We will present simulations of the linear absorption, population transfer, and two-dimensional spectra of the FMO complex in an approach, that combine MD simulations, semiempirical electronic structure calculations, and spectral simulations. The results do depend of course on the MD force field and the semiempirical parametrization, but none of the two were adjusted to obtain agreement with the experiments that we will compare with. Previous studies either used average energies extracted from fits to the spectra at low temperature or obtained from electronic structure calculations of the crystal structure. To account for the environmental dynamics, previous studies typically assumed Gaussian fluctuations of the site energies around the average. We will show that this assumption is not justified.

For the spectral simulations, we will employ the numerical integration of the Schrödinger equation (NISE) scheme.[40,41] The advantage of this scheme is that it allows the calculation of spectra directly from trajectories of the Hamiltonian without assuming the Condon or Gaussian approximations made in most other approaches.[42−44] In contrast to density matrix approaches all time-dependent information is used directly without any prior averaging. For example, transition dipole moment (TDM) changes arising due to non-Condon effects are included as well as their fluctuations over time. These stated changes are usually neglected in density matrix approaches. The largest drawback of our approach is that it can only be applied in the high temperature limit, when the exciton bandwidth is not too large compared to $k_B T$. Recently good results were found for the OH-stretch vibration, where the bandwidth is about $2\ k_B T$.[45]

The present contribution is organized as follows: In the next section the MD simulations and the electronic structure calculations yielding the site energies, couplings, and transition dipole moments are introduced (see Figure 1). The respective results are discussed and compared to literature values. Exciton dynamics is the focus of the third section, whereas linear absorption and two-dimensional spectroscopy is studied in the fourth section. The paper ends with some concluding remarks.

■ SITE ENERGY AND ELECTRONIC COUPLING CALCULATIONS

Methods. Classical all-atom MD simulations were carried out at room temperature on the basis of the trimeric crystal structure of *Chlorobaculum tedium* (PDB code: 3ENI). Starting from this structure, two different simulations were carried out. The first one involved the full trimeric structure with eight BChls per monomer as seen in vivo and in photophysical experiments; the second simulation involved only one monomer to investigate the importance and differences between the monomeric and trimeric complex. In the following these simulations will be denoted as trimer and monomer simulation, respectively. During equilibration of the monomer, the eighth BChl left the complex and, therefore, was removed from the simulation; that is, the analysis in this case is restricted to seven pigments. The weak bond of the eighth BChl in a monomer explains why it was found so late in structural studies. The molecular dynamics simulations explicitly included all atoms of the BChls, the protein scaffold, and the water molecules using the CHARMM force field including the TIP3P water model. The specific setups and simulation protocols are described in detail in ref 24. After equilibration, trajectories were calculated with an integration step size of 1 fs, but frames were recorded only every 5 fs. The total lengths of the trajectories were 300 ps for the monomer and 200 ps for the trimer simulations.

In a subsequent step, the electronic properties of the multichromophore system were calculated for each saved frame of the MD trajectory. The electronic properties thus calculated are the time-dependent site energies (differences between ground and excited state) and transition dipole moments of the individual BChls as well as the electronic couplings between them. The technical details of the calculations can be found in ref 23. To this end, the ORCA code (University Bonn, Germany)[47] was employed in order to calculate the energy gap between ground and first excited state, i.e., the Q_y state, for all BChls in the complex individually. Due to the large number of necessary calculations, we employed the semiempirical ZINDO/S-CIS(10,10) method using the ten highest occupied and the ten lowest unoccupied states, which has been shown to be a good compromise between efficiency and accuracy.[23,29,30] To further increase the efficiency for the QM calculations, each terminal CH_3 and CH_2CH_3 group as well as the pythyl tail were replaced by H atoms.[30,48] This restriction of the quantum system has little influence on the results since the optical properties of BChls are determined by a cyclic conjugated π-electron system. To account for effects of the environment on the orbital energies, the point charges surrounding the truncated BChl molecule stemming from the MD simulations within a cutoff radius of 20 Å were included in the ZINDO/S-CIS calculations which, at the same time, yield the transition dipole moments. In ref 23 the effect of varying the cutoff radius was discussed in more detail.

Since in the FMO complex the minimum interpigment distance is 11 Å, the coupling among the individual BChls is
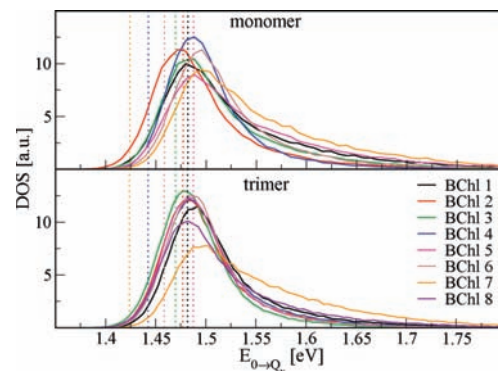

Figure 2. DOS of the energy gaps from monomer and trimer simulations. The vertical lines indicate the energy values obtained for the static crystal structure neglecting environmental effects, i.e., without accounting for the MD point charges of the environment.

Table 1. Peak Postions and Average Energies of the DOS for the Monomer and the Trimer Simulation As Well As for the Crystal Structure

	monomer		trimer		
	peak [eV]	average [eV]	peak [eV]	average [eV]	crystal [eV]
1	1.480	1.532	1.492	1.516	1.483
2	1.472	1.500	1.482	1.503	1.476
3	1.488	1.518	1.477	1.493	1.470
4	1.488	1.506	1.482	1.507	1.442
5	1.488	1.543	1.482	1.501	1.486
6	1.496	1.522	1.487	1.504	1.459
7	1.496	1.558	1.502	1.554	1.423
8			1.482	1.520	1.470

safely approximated by the Coulomb part only and given by

$$V_{nm} = \frac{f}{4\pi\varepsilon_0} \sum_{I,J} \frac{q_I^T \cdot q_J^T}{|\mathbf{R}_m^I - \mathbf{R}_n^J|} \quad (1)$$

In this method, the TrEsp approach,[34,35] one uses atomic transition charges q_I^T which describe the transition density $\rho(\mathbf{r}) = \sum_I q_I^T \delta(\mathbf{r} - \mathbf{R}_m^I)$. The charges are localized at the position $\mathbf{R}_m^I$ of atom I of the mth BChl. Experimentally, a transition dipole moment of 6.3 D[49] for BChl a was estimated. As described in the TrEsp procedure[34,35] and to match the experimental value on average, it is necessary to rescale the transition charges, as extracted from the TDDFT/B3LYP data set in ref 34, by a factor of 0.728. The transition charges are assumed to be constant. Solvent effects on the electronic coupling are taken into account through a distance dependent screening factor f.[50] A comparison of the effect of different approaches can be found in ref 23.

Energies. As summarized in a recent review,[5] there have been several studies aimed at the determination of the site energies of FMO. For *Chlorobaculum tepidum* several attempts have been performed to extract the energies by fitting of the optical spectra.[51−53] In another approach, the shifts of the site energies due to charged amino acids were calculated based on the crystal structure using seven[53] or eight[54] BChls per monomer. Figure 2
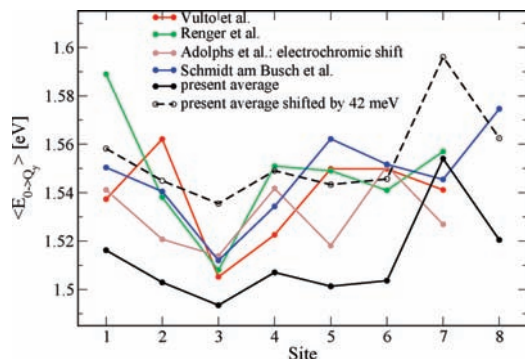
Figure 3. Comparison of averages for individual site energies based on the trimer simulations to the results from Vulto et al.,[51] Renger and May,[52] and electrochromic shift calculations by Adolphs et al.[53] as well as recent results from Schmidt and Busch et al.[54] In addition, a shifted version of the present site energies is shown that reproduces the peak value of the experimental linear absorption spectrum.

Figure 4. Density of couplings based on monomer and trimer simulations calculated using the TrEsp approach. Shown are couplings with an average absolute value above 1 meV. The sticks represent the corresponding values for the crystal structure conformation.

and Table 1 show the results of the present study. In contrast to the earlier investigations, we are not just obtaining a single value per site energy but a whole distribution, i.e., the density of states (DOS) along the MD trajectory. Shown in Figure 2 are both the results based on the monomer and the trimer simulations as calculated from 60 000 and 40 000 snapshots, respectively. For the trimer simulation, the values have been averaged over the three monomers within the trimer. The individual DOSs are broad, non-Gaussian distributions with a tail at the high energy side. As can be easily seen, there are differences for the distributions from monomer and trimer simulations. Obviously, the different environments and the varying flexibility of the complexes show their influence on the site energies. In the monomer simulations one finds more variation among the individual site energy distributions compared to the trimer case, where the site energy distributions largely overlap. An exception is the DOS of BChl 7 and to some extent that of BChl 8. BChl 7, lying in the middle of the FMO monomers, clearly has its DOS extending to the largest energies, which is especially prominent for the trimer simulations and results from the charged environment. BChl 8 shows a DOS that is similar to those of BChls 1 to 6 but slightly biased toward high energies. When looking at the site energies calculated without surrounding point charges, this small bias is retained. This behavior can be explained by a slightly different average conformation of BChl 8 compared to those of pigments 1 to 6. Shown in addition in Figure 2 are the energies based on the static crystal structure neglecting environmental effects. These results have been obtained without accounting for the MD point charges of the environment. In this case, the different energies of the various pigments are solely due to the nonequilibrium geometries of the BChls since only the energy gap for the fixed X-ray structure is calculated without taking environmental effects into account. These effects have been calculated previously by Adolphs et al.[53] using electrochromatic shift calculations.

Since the DOSs are skewed, their peak position is not identical to their average position. In Table 1 we list both, peak and average positions, for monomer and trimer simulations. In addition, the values for the crystal structure are listed. In the latter calculations no environmental effects are included and,
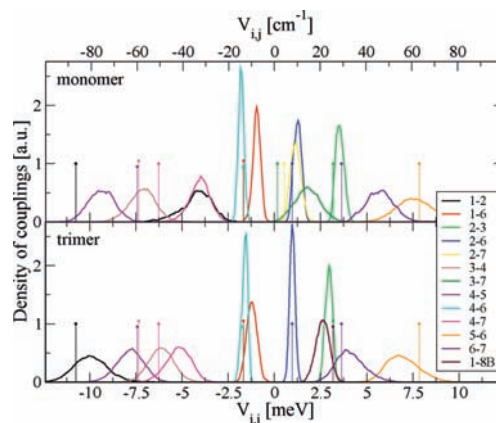
therefore, the spectra lack corresponding shifts. In case of the trimer, the spread of the crystal structure energies is larger than the spread of the peak positions obtained for the dynamic structures; that is, the environment makes some of the BChls more similar with regard to their DOS.

Next, we compare our results with those of previous investigations. To this end, the literature values are shown in Figure 3 together with the averages of the presently calculated DOSs. It can be seen that the present average values are somewhat lower than those calculated in previous studies. This corresponds to a shift in all BChl site energies at the same time. On blue shifting the present results by 42 meV, the peak position of the linear absorption spectrum can be reproduced (see below). This overall underestimate of the site energies results from the semiempirical ZINDO calculations. We note that even computationally expensive high-level quantum chemistry methods do not reproduce the correct energy gap.[33] The site energy differences between BChls 1, 2, 3, and 5 agree quite nicely with the results by Adolphs et al.[53] obtained using electrochromic shift calculations. For BChl 4 the shifted version of the present energy lies in between those obtained in refs 53 and 54. The largest differences are found for BChls 6 and 7. In contrast to the previously discussed data set,[53] we calculated the average site energy of BChl 7 to be larger than that of BChl 6. On comparing the site energy distributions in Figure 2 and Table 1, one finds that the DOS of BChl 7 has a much longer tail than the other DOSs have; the difference between average and peak values is larger than that of all other BChls. The additional pigment, BChl 8, has only been considered in one previous study so far.[54] Furthermore, in Figure 3 two additional energy sets from the literature are shown. As can be seen there is quite a spread in energy for the different sets. Nevertheless, for all sets, BChl 3 shows the lowest energy; that is, excitation starting on any of the pigments should finally end up to some degree at this chromophore.

We note that the difference between the DOS of BChl 7 to the other pigments is larger for the calculations based on the trimer simulations than those based on the monomer simulations. In summary, there is considerable agreement with previous data sets

Table 2. Intramonomer Average Couplings from Monomer Structure in Units of meV[a]

	1	2	3	4	5	6	7
1	–	−10.78	0.47	−0.57	0.60	−1.67	−0.68
2	−4.26	–	3.19	0.75	0.16	0.97	0.54
3	0.61	3.50	–	−7.36	−0.02	−0.85	0.16
4	−0.29	0.76	−7.18	–	−7.44	−1.70	−6.28
5	0.50	0.14	−0.18	−9.40	–	7.87	0.20
6	−0.99	1.21	−0.89	−1.84	7.59	–	3.64
7	−0.79	1.11	1.75	−4.1	0.77	5.68	–

[a] Upper triangle: intra-monomer couplings based on the monomer crystal structure. Lower triangle: based on the monomer MD trajectory (grey background). Couplings with absolute values above 1 meV are highlighted in bold.

Table 3. Average Intramonomer Couplings of the Trimer Structure in Units of meV[a]

	1	2	3	4	5	6	7	8	8B
1	–	−10.78	0.47	−0.57	0.60	−1.67	−0.68	−0.01	3.17
2	−9.96	–	3.19	0.75	0.16	0.97	0.54	0.07	0.46
3	0.44	2.91	–	−7.36	−0.02	−0.85	0.16	0.22	0.08
4	−0.50	0.83	−6.18	–	−7.44	−1.70	−6.28	−0.16	0.15
5	0.56	0.06	−0.18	−7.86	–	7.87	0.20	0.52	0.38
6	−1.26	0.93	−0.81	−1.65	6.92	–	3.64	−0.48	0.93
7	−0.61	0.19	0.15	−5.23	0.58	4.09	–	−0.75	−1.08
8	0.01	0.08	0.18	−0.14	0.50	−0.39	−0.65	–	0.49
8B	2.60	0.41	0.09	−0.15	0.35	−0.90	−1.08	0.45	–

[a] Upper triangle values based on the crystal structure. Lower triangle values based on the MD trajectory.
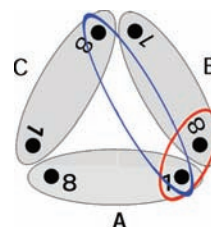

Figure 5. Scheme of the trimer complex and the included intermonomer couplings. The gray ellipses represent the single monomers A−C. There are two different 1−8 couplings between different monomers. The red ellipse describes the coupling between pigment 1 and the closest BChl 8 of a neighboring monomer (also depicted as 8B). Furthermore, the blue ellipse describes the coupling between pigment 1 and the more distant pigment 8 of the third monomer. Because of symmetry there is only one 1−1 coupling.

for the site energies, but there exist also significant differences. One has to keep in mind that in the present study we obtain whole distributions, whereas previous studies were based on fits to spectroscopic data to seven BChls per monomer or on the static crystal structure.

Couplings. The couplings between the pigments shown in Figure 4 have been evaluated based on monomer as well as trimer simulations. The normalized distributions of the various couplings were deduced from the trajectories of the simulations. Let us first focus on the couplings from the monomer simulations including 7 BChls yielding 21 couplings. Shown in Figure 4 are only coupling distributions which on average have an absolute value above 1 meV. The sign of the couplings depends on the charge distribution, i.e., on the dipole moments and their relative orientation in the chromophores under consideration.

The largest absolute values of the couplings are around 10 meV. As can be seen, the widths of the distributions vary; the coupling distributions at larger coupling strength have a width of several meV compared to spreads of less than 1 meV for distributions exhibiting weaker coupling. In contrast to the energy gap distributions, the coupling distributions are more symmetric (albeit not always with a perfect Gaussian shape) and peak and average values are rather close. The average values obtained from the crystal structure and the monomer MD simulations are listed in Table 2.

In contrast to other light-harvesting systems, for example, the LH2 systems of purple bacteria, there is no symmetry in the FMO complex. Nevertheless, the numbering of the BChls in the FMO complex is such that, at least for the average coupling values based on the MD trajectory, the largest couplings are to BChls with neighboring indices. For the crystal structure values, only in the case of BChl 7, which is more or less surrounded by all the other 6 BChls (see Figure 1), the strongest coupling of −6.3 meV is to BChl 4 instead of to BChl 6, which is only 3.6 meV.

For some couplings, the crystal structure value is right in the middle of the distribution from the MD trajectory, e.g., in case of coupling 5−6. For many BChl−BChl pairs the crystallographic structure coupling value is actually at the edge of the respective distribution. This might be an indication that either the crystal structure conformation is not really an equilibrium conformation or that force field inaccuracies are leading to a slightly shifted equilibrium conformation.

In the trimer system with 24 BChls there arise 276 couplings between the pigments. Because of large spatial separations, many of these couplings are very small. The distribution of intramonomer couplings from the trimer simulations are also shown in Figure 4

and average values are listed in Table 3. As in case of the monomer simulation, almost all the couplings with the largest absolute values are on the first secondary diagonal. As can be seen, there are differences in the coupling values between monomer and trimer simulations. The most prominent difference is between the coupling connecting pigments 1 and 2. In case of the monomer simulations its average value is −4 meV while based on the trimer simulations the coupling value is −10 meV. The discrepancy is due to the structural differences in the two simulations and leads to rather different population transfer dynamics (see below). In contrast to the monomer simulation, in the trimer simulation the monomer consist of eight BChls. The absolute value of the coupling strength of the eighth BChl to the other seven pigments within the same monomer is below 1 meV. As already indicated in Figure 1, the eighth chromophore is actually closer to some of the BChls within the neighboring monomers than to those in its own monomer (see also Figure 5). Therefore we also added the coupling values of a close monomer denoted here as BChl 8B. The coupling value of 2.6 meV between BChls 1 and 8B is, for the MD average values, only a factor of 1.5 smaller than that between pigment 6 and 7 and more than four times larger than the largest coupling between BChl 8 and another pigment within the same monomer. Therefore an electronic excitation of a BChl 8 pigment will most likely be transferred to a neighboring monomer rather than within the same monomer.

The average values for the intermonomer couplings extracted along the MD trajectory are given in Table 4 for the two different

Table 4. Intermonomer Couplings Averaged over the MD Trajectory in Units of meV[a]

	1	2	3	4	5	6	7	8
1	0.12	0.04	−0.07	0.08	0.29	0.19	0.11	**2.60**
2	0.18	−0.05	−0.31	−0.19	0.92	0.65	0.18	0.41
3	0.17	0.01	−0.33	0.70	0.57	0.28	0.49	0.09
4	0.04	0.06	0.08	0.24	−0.07	−0.05	0.24	−0.15
5	0.08	0.11	0.13	−0.01	0.22	0.01	−0.08	0.35
6	0.01	0.09	0.10	0.17	−0.17	−0.18	0.20	−0.90
7	0.04	0.03	−0.09	0.60	−0.20	0.01	0.71	**−1.08**
8	0.01	0.090	0.10	−0.10	0.16	−0.12	−0.28	0.45

[a] Upper triangle: couplings of monomer pairs of A−B, B−C, and C−A. Lower triangle: couplings of monomer pairs of A−C, B−A, and C−B.

Table 5. Intermonomer Couplings Based on the Crystal Structure in Units of meV[a]

	1	2	3	4	5	6	7	8
1	0.14	0.06	−0.06	0.08	0.31	0.16	0.13	**3.17**
2	0.21	−0.03	−0.32	−0.23	0.99	0.63	0.28	0.47
3	0.19	0.04	−0.28	0.63	0.61	0.27	0.58	0.08
4	0.04	0.06	0.06	0.26	−0.10	−0.04	0.26	−0.15
5	0.08	0.12	0.15	−0.04	0.24	−0.00	−0.10	0.38
6	0.00	0.09	0.09	0.19	−0.20	−0.18	0.24	−0.93
7	0.04	0.05	−0.09	0.63	−0.22	0.03	0.81	**−1.08**
8	0.00	0.07	0.10	−0.12	0.17	−0.13	−0.31	0.49

[a] Upper triangle: couplings of monomer pairs of A−B, B−C, and C-A. Lower triangle: couplings of monomer pairs of A−C, B−A, and C−B.
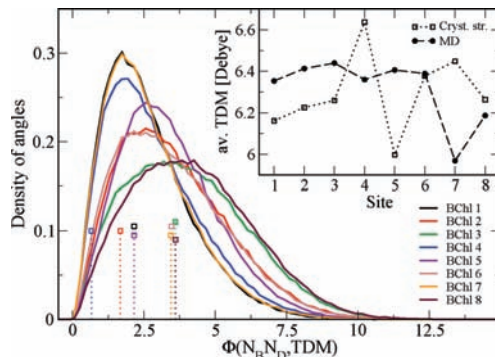

Figure 6. Magnitude and angle distributions of the TDM. The inset shows the magnitude of the transition dipole moment averaged over the trimer trajectory and the three monomers as explained in the text. The main graph shows the corresponding distribution of angles (in degrees) between the TDM and the N_B−N_D axis of the individual BChls (solid lines) together with the values based on the crystal structure (dotted sticks, open squares).

types of intermonomer couplings indicated in Figure 5. The same quantities based on the crystal structure are given in Table 5. Only the mentioned intermonomer coupling between BChl 1 and BChl 8 is larger than 2 meV. Solely one of the couplings between pigments, namely, between 7 and 8, has an average value slightly above 1 meV. All other couplings have absolute average values below 1 meV but there are many of them. As a result, excitations from one monomer will eventually "leak" to the other monomers if not removed from the system beforehand.

The coupling values stated above have all been calculated using the TrEsp approach. A very popular approximation for the coupling calculation is the point dipole approximation (PDA). Recently we tested this latter and other methods to determine coupling values for the LH2 system.[23] With 11 Å the minimum interpigment distance in the FMO complex is even larger than in the B800 ring. Therefore for most couplings the values calculated using the PDA are very similar to the values calculated using the TrEsp approach. The distributions (data not shown) of the couplings are, however, up to twice as broad as in the case of the PDA. Nevertheless, there are some couplings which show a significant difference. As an example we mention the coupling between pigments 5 and 6; the TrEsp method yields an average value of 6.92 meV compared to 9.17 meV obtained from the PDA. Adolphs and Renger also tabulate coupling values calculated using different approaches and based on the crystal structure. Our results for the intramonomer couplings for the crystal structure are rather similar to the values by these authors[53] using the transition monopole approximation with a value for the dielectric constant ε of two and the crystal structure. Actually,

most of the present values are slightly smaller than those reported earlier.[53] As discussed above, the average couplings based on the MD simulations either for the monomer or the trimer system sometimes deviate strongly from those for the crystal structure. In all calculations below, TrEsp coupling values have been used.

Spatial Correlations. As mentioned in the Introduction, spatial correlations in the fluctuations of the site energies have been suggested to underly the experimentally observed long-lived coherence of BChl excitations in FMO. In a previous publication[24] several of us have analyzed these correlations based on the same MD and electronic structure data as employed in the present study. Only weak atomic correlations were found. BChls 1 and 2 exhibit somewhat significant correlation in their atomic motion but not in the fluctuation of their site energies.[24] Some correlation between couplings appear for cases in which two BChl pairs share a common partner. For example, there is a significant correlation between couplings 4−5 and 5−7, i.e., if pigment 5 is moving, this imposes a change in the geometric relationship between pigments 4 and 7 and, therefore, causes a correlation between the two couplings. Nevertheless, only very few couplings showed at the same time correlated fluctuations, large coupling values, and broad distributions. If one of these criteria is not fulfilled, the effect of correlated couplings is negligible. Only if two couplings are relatively large, have large fluctuations and have a non-negligible correlation, will an effect in the dynamics be observed. This is not directly visible from the correlation values since the distributions are normalized.

Transition dipole moments. The transition dipole moments (TDM) of the individual BChls determine the optical properties of the FMO complex. The direction of each BChl's TDM is indicated in Figure 1. The dipole moment of individual BChls are often assumed to be in the direction of the N_B−N_D axis within the molecule.[35] In the present study the transition dipole moments have been determined through ZINDO/S calculations as detailed in Methods. The absolute values of the TDMs have been rescaled by a factor of 0.567 to a value of 6.3 D, when averaged over all BChls, which corresponds to the experimentally measured TDM value.[49] The relative TDM magnitudes of the
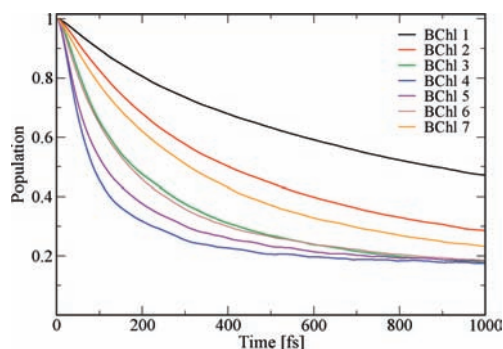
Figure 7. Population dynamics based on the monomer simulation. Shown is the population decay from the respective initially excited chromophore in a monomer, i.e., the decay shown results from calculations with seven different initial conditions.

Figure 8. Same as in Figure 7 based on the trimer simulation. The line style distinguishes the three monomers.

individual BChls after this common rescaling are shown in the inset of Figure 6. Pigments 1−6 have similar magnitudes of their TDM, namely, 6.39 ± 0.41 D. BChl 8 has a slightly smaller value (6.19 ± 0.50 D) as has chromophore 7 (5.97 ± 0.54 D). These are only averages with non-negligible fluctuations as indicated by the standard deviations. We note that there is significant deviation between the average magnitude of the transition dipole moments based on the MD simulations and the corresponding crystal structure data (also rescaled to an average value of 6.3 D).

In addition to the magnitude of the dipole moments, the orientation of the TDM is of importance. The deviation of the TDM direction from the N_B−N_D axis has previously been discussed.[35] As can be seen in Figure 6, the values fluctuate between 0° and 10°. Concerning this property, pigments 1, 4, and 7 behave similarly. Also the pigment triple 2, 5, and 6 and the pigment pair 3 and 8 behave similarly in regard to the distribution of deviation angles. Though high precision calculations of the direction of the TDM are certainly of importance, this example shows that one should not forget in carrying out such calculations that there is quite a spread along a trajectory due to thermal fluctuation.

Supplementary to TDMs stemming from the ZINDO/S calulations, one can compute TDMs using predefined transition charges from the TrEsp approximation (see section about couplings). Compared to the distributions in Figure 6 the deviations of the directions from the N_B−N_D axis are Gaussian distributed between 0° and 5° with a peak maximum at around 2.2° (data not shown). The averaged magnitude is quite similar to that in the inset of Figure 6.

■ EXCITATION DYNAMICS

The dynamics of the electronic properties along the room-temperature MD trajectory can be used to describe the effect of the environment on the exciton dynamics. This is sometimes called a ground-state classical path description since the MD trajectory is a ground state trajectory based on classical dynamics; that is, it does not include the dynamics on excited electronic states. Nevertheless, this procedure is expected to yield a rather useful description for excitation energy transfer processes. For charge transfer scenarios this might be less accurate since a moving charge influences a classical MD simulation much more than a rather localized excitation. For the present purpose one may first determine the spectral
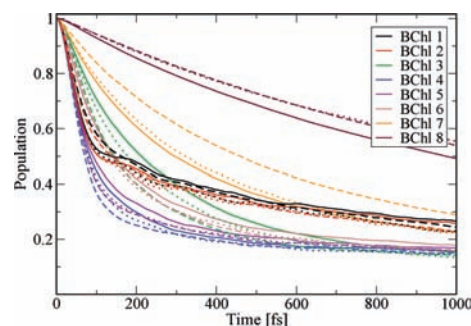
density and then compute exciton dynamics and optical spectra.[23,27] Here we employ an alternative strategy and use the time-dependent site energies of the pigments and their couplings in a wave packet calculation[40,41,55−57] employing the NISE approach. In this approach the evolution of the wave function is calculated by solving the time-dependent Schrödinger equation for the fluctuating Hamiltonian. As this cannot be done directly, time is divided into short time intervals during which the Hamiltonian can be assumed to be constant. The time-independent Schrödinger equation is then solved successively for each time interval providing the solution of the time-dependent Schrödinger equation as long as the short time intervals are brief enough. This implies that the actual fluctuating Hamiltonian is used directly in determining the exciton dynamics and no assumptions on the nature of the spectral density or density of states is made. The averaging of the fluctuations is achieved by averaging over multiple starting configurations along the trajectory. For calculating the exciton dynamics, this was done assuming that the excitation was initially localized on one of the sites. The exciton dynamics was determined using the complete trajectory length available, i.e., 300 ps for the monomer and 200 ps for the trimer simulations with 5 fs time steps between snapshots. The calculations of 1000 fs length were repeated with starting times 100 fs apart in order to average over sufficient starting configurations of the bath. This sample rate is chosen because temporal correlation of the individual site energies is negligible after 50 fs.

Before analyzing the population dynamics in the FMO complex, we want to emphasize once more that the present calculations are based on room-temperature MD simulations. Many previous results for the excitation dynamics in the FMO complex are based on model assumptions for a spectral density and often have been performed at 77 K.[15−19,21,22,25] This lower temperature in previous studies lead to less dephasing in the excitation dynamics compared to the one shown below. To illustrate the resulting population dynamics, we excited individual pigments in the FMO monomer. In Figure 7 the corresponding population decay is shown for the initially excited chromophore. In case that BChl 1 is excited, 50% of the excitation remains at this pigment for 1000 fs while for BChl 4 it remains there only for 100 fs. The time difference agrees with the coupling values resulting from the monomer simulation as seen in Figure 4. The coupling to pigment 1 is small while the largest coupling is found to chromophore 4. Interestingly, the situation changes when performing the same kind of simulations for the trimer, as shown in Figure 8. Of course, in case of the trimer simulations there are
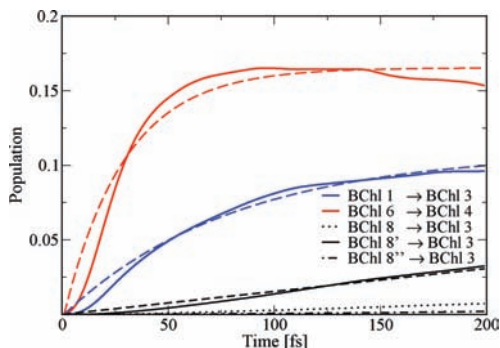
107

Figure 9. Population transfer across the FMO complex trimer over the three monomers. Shown as solid line is the increase of population on sites 3 and 4, respectively. The dashed lines indicate the corresponding fits. BChls 8′ and 8″ belong to neighboring monomers.

Figure 10. Linear absorption spectrum for FMO at room temperature calculated for the trimer (black solid line) and monomer (red solid line) along with the experimental data for the monomer (dashed line) extracted from Freiberg et al.[62]

three different population decays for initially exciting a specific pigment in one of the three monomers. The three respective curves are seen to be similar but not identical. With sufficient sampling, these curves should become identical. In the trimer case the population transfer away from the initially excited pigments 1 or 2 is much faster than in case of the monomer simulations. As can be seen in Figure 8 and discussed above, the coupling between BChl 1 and 2 is lower by a factor of 2.5 in the monomer case leading to slower population transfer from the initially excited BChl 1 to BChl 2 in the same monomer and vice versa. Furthermore, one single coherent oscillation is observed in the population transfer from BChl 1. Initially exciting BChl 8 leads to the slowest transfer to the other pigments. Transfer from the other chromophores proceeds at similar speed in the cases of monomer and trimer. The difference between monomer and trimer simulations is partly due to the different long-time limits imposed by the theory. The wave packet simulations employed here implicitly include a high-temperature limit, i.e., in the thermodynamics limit all sites are equally populated. Since the number of sites in the monomer and trimer case are different in the different simulations, also the long-time populations of the two different simulations are not the same.

In vivo, the FMO complex is supposed to transfer excitation energy from the chlorosomes to the reaction center. This motivates one to take a closer look at energy transfer in this direction. In Figure 9 the population transfer from site 1 to site 3 is shown; that is, in the simulation site 1 was initially excited and the population increase at site 3 was monitored. The same is shown for the transfer from site 6 to 4. The population transfer is fitted with a function assuming direct transfer between the pairs: $P(t) = A(1 - \exp(-t/T_1))$. The transfer times T_1 for the transfer between sites 1 and 3 is 58 fs and between 4 and 6 is 29 fs. The deviation in the initial parts of the fit is due to the actual involvement of intermediate steps. The long-time decay observed for the 6 to 4 transfer arises because the population is first transferred quickly between those sites and only slowly to other sites in the complex. If one knows the number of intermediate steps the transfer can be treated using Poisson statistics.[58] Instead of attempting to construct a complex model for the transfer, we will here simply make the observation that the transfer across several BChls within the FMO complex and involving BChls 1 to 7 is predicted to be very quick within our model with transfer times
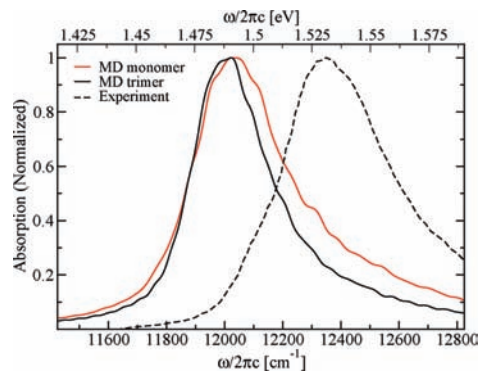
below 100 fs. Though BChl 7 has the largest average energy, it is nevertheless involved in some of the energy transfer pathways. Initially exciting BChl 6, for example, leads to roughly the same excitation on chromophores 5, 6, and 7 after 1 ps. In case BChl 1 is initially excited, basically no excitation energy goes through BChl 7.

In addition to the intramonomer dynamics discussed, transfer from BChl 8 of the three different monomers to BChl 3 in a specific monomer is displayed in Figure 9. The fastest transfer between BChls 8 and 3 does not take place within one monomer, but between different monomers with a transfer time T_1 of about 1.4 ps. As mentioned above, the coupling of this pigment to the other BChls in the same monomer is smaller than that to one of the other two neighboring monomers. This is due to the spatial organization of the BChls in the FMO complex as already indicated in Figure 1. Intermonomer transfer is mainly due to BChl 8; transfer away from BChl 8 in Figure 8 is mainly caused by transfer to a neighboring monomer.

■ SPECTROSCOPY

Linear absorption and two-dimensional spectra were calculated for the FMO trimer using the NISE approach,[41] describing the exciton dynamics in the same way as in the previous section. To calculate the response functions governing the linear and two-dimensional spectra we employed a recently developed sparse matrix algorithm[45] including the split operator propagation scheme for propagating two-exciton states.[59] This sparse scheme was only applied during the coherence times (t_1 and t_3), while the exact one-exciton Hamiltonian was propagated during the waiting time (t_2). This scheme was developed for treating coupled three level systems, i.e., systems where two-exciton states with double excitation on the same site are also allowed. Here, this third level was effectively eliminated by adding a large artificial anharmonicity moving the third level far away from the off-site two-exciton states.[60] The spectra were calculated for 100 ps of the trimer trajectory with 5 fs between the snapshots and for the full 300 ps of the monomer trajectory. The spectral calculation was repeated with starting times 50 fs apart resulting in a total of 1975 samples for the two-dimensional spectra for the trimer. In case of the monomer the calculation was repeated 100 fs apart
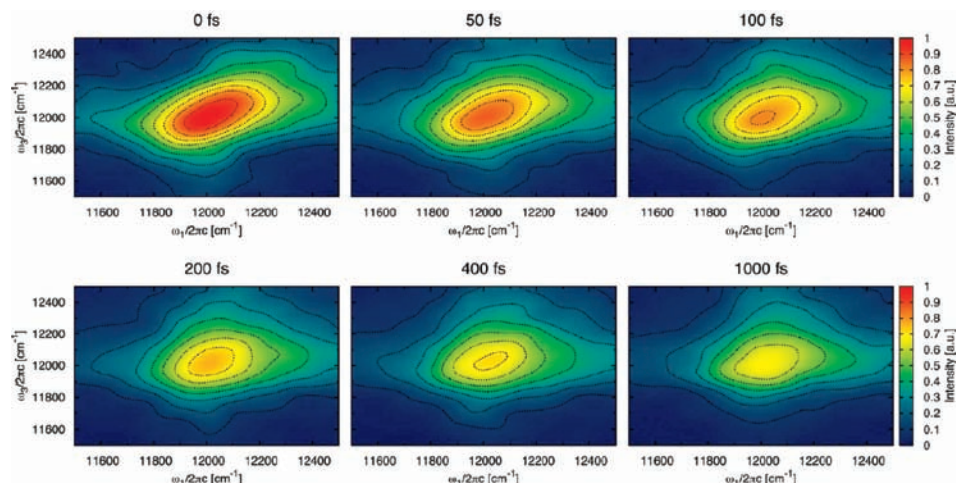
Figure 11. 2D correlation spectroscopy spectrum with parallel polarization and different waiting times of the monomer. To amplify weak features, the contours are plotted at equidistant (10%) intervals of $\mathrm{arcsinh}(10\times S)$, where S is the signal normalized to the peak height for waiting time zero.

resulting in a total of 2988 samples. For the linear absorption the sample times were 5 fs apart resulting in a total of 19 360 samples for the trimer and 59 744 samples for the monomer. The coherence times were sampled using 5 fs intervals up to 640 fs for both monomer and trimer. Furthermore, the waiting time was probed with 25 fs intervals up to 1000 fs. Orientational averaging was performed by averaging over the 21 unique molecular frame polarization directions and adding those up with the proper weight factors to obtain the parallel and perpendicular polarization spectra.[61] Finally, the 2D CS spectra were obtained by a double Fourier transform of the coherence times into the two frequency axes ω_1 and ω_3.

In Figure 10 the linear absorption spectra are shown. The monomer as well as the trimer spectra contain one peak with a long tail stretching to higher frequencies. In both cases the position of this peak is at 12 020 cm^{-1} (1.49 eV), i.e., close to the typical position of the single site energies (see Figure 2). The overall peak shape also resembles the single site DOS. The full-width-half-maximum (fwhm) of the absorption peak is 320 cm^{-1} (40 meV) for the trimer and 391 cm^{-1} (49 meV) for the monomer. For the FMO complex of *Chlorobaculum tepidum* the linear absorption at room temperature was measured by Freiberg et al.[62] The experimental absorption peak is at 12 350 cm^{-1} (1.53 eV) and the fwhm of the spectrum is 448 cm^{-1} (56 meV). As in the calculated spectrum a tail stretching to higher frequencies is observed, which indicates that the non-Gaussian site energy distribution that we find is real. To obtain the same peak position for both, the simulated and the experimental spectra, one could introduce a common shift for all site energies of 42 meV as discussed above. Both the simulated and the experimental widths are smaller than the typical width of the DOS of about 525 cm^{-1} (62 meV). This means that the spectrum is narrowed due to exchange and motional narrowing effects. To analyze this in more detail we calculated the spectra in the static limit, where the effect of motional narrowing is neglected. We found that the linear spectra are comparable in width to the DOS, leading to the conclusion that the narrowing of the spectrum is due to fast fluctuations of the site energies.

This is further supported by the observation that the delocalization length according to the definition of Thouless[63] is only 1.4 for the monomer and 1.6 for the trimer indicating that the excitations are predominantly localized.

The bandwidth in the discussed spectra is about 60 meV, which corresponds to $k_B T$ for a temperature of 700 K. This value implies that one needs to be concerned with finite temperature effects. For the linear spectra temperature effects should not be significant, however, since the spectral dephasing time ($\sim$30 fs) is shorter than the population transfer times. As stated in Introduction, previous simulations of the exciton transfer for the OH-stretch vibration, where the bandwidth is about 2 $k_B T$,[45] found good agreement with experiment.

The 2D CS spectra with parallel polarization of the monomer and trimer are shown in Figure 11 and Figure 12 for a representative subset of waiting times. Since no excited state absorption can be recognized, only one peak is observed, originating from ground state bleach and stimulated emission. Experimentally such peak was detected (also for *Chlorobaculum tepidum*) above the main peak at lower temperatures.[11] The excited state absorption decreases in experiment with increasing temperature and is almost gone at 277 K. The magnitude and position of the ground state bleach and stimulated emission peak is a signature of strong exitonic coupling and delocalization.[26,64] The present spectra thus demonstrate that excitations at 300 K are predominantly localized, in agreement with the delocalization length discussed previously. For the linear absorption, the peak position in the calculated 2D CS spectra is at lower energies than in the experiment,[11] and the line width is a bit narrower. It is noteworthy that the trimer spectrum is narrower than the monomer spectrum demonstrating that the trimer is more ordered. Comparing the shape obtained for the monomer in a 300 K simulation for a waiting time of 400 fs with that observed at the same waiting time but at 277 K, the calculated spectrum has more pronounced wings, which is typical for faster site energy fluctuations. The difference might simply arise since the higher temperature in the simulation results in faster fluctuations or it can be an indication that the fluctuations caused by the dynamics in our molecular dynamics simulations are too fast.
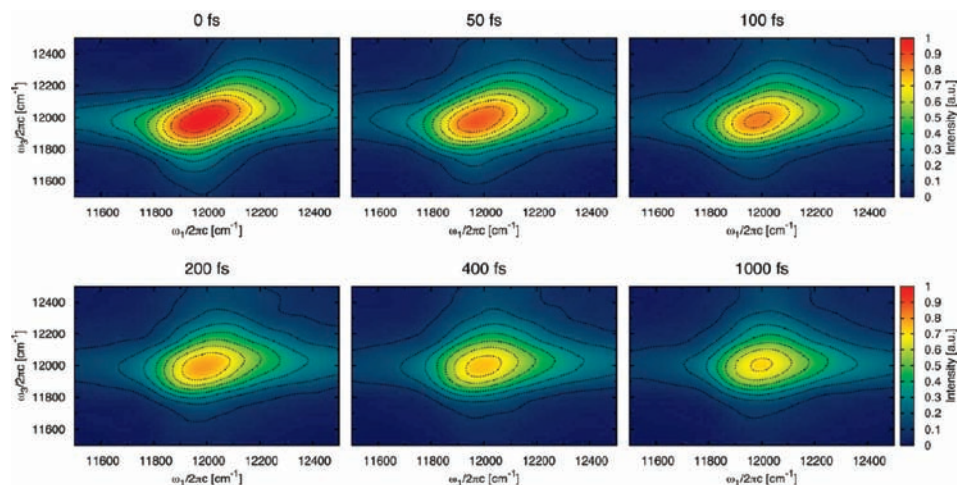
6. Publication Concerning the FMO Complex

Figure 12. 2D correlation spectroscopy spectrum with parallel polarization and different waiting times for the trimer. The contours are plotted as in Figure 11.
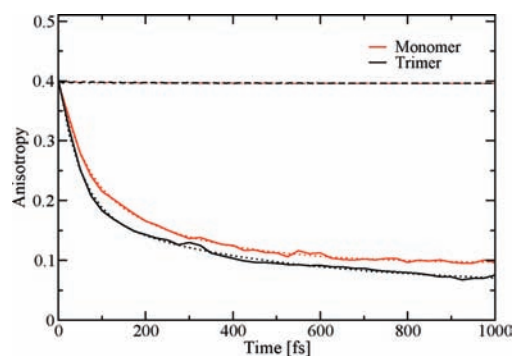

Figure 13. Calculated polarization anisotropy of the peak in the 2D correlation spectroscopy spectra at different waiting times for monomer (red, solid line) and trimer (black, solid line), along with biexponential fits (dotted lines). In addition, the calculated anisotropy from the autocorrelation of the transition dipole moments (dashed lines) is shown.

Figure 14. Diagonal peak intensity of the 2D correlation spectroscopy spectra at different waiting times for the monomer (red) and the trimer (black). The solid lines are biexponential fits with an offset.

We extracted the frequency integrated anisotropy from the 2D CS spectra as shown in Figure 13. This anisotropy is a frequently used measure of the orientational motion or population transfer.[41,65] For the extraction, we fitted the anisotropy to a biexponential function with offset. For the monomer we found decay constants 55 and 240 fs, and for the trimer we found 50 and 420 fs. Apart from a bump at 300 fs for the trimer and at 600 fs for the monomer with heights of these bumps smaller than the error bars in the simulation results, there is no indication of coherent oscillations. The obtained time scales compare well with the time scales typically found in population transfer analysis. The anisotropy decay is completely attributed to exciton transfer between different sites, since the BChls are not reorienting significantly on the subpicosecond time scale. This attribution is also supported by calculating the anisotropy from the autocorrelation of the TDM as given by eq 9 in ref 66. For the trimer
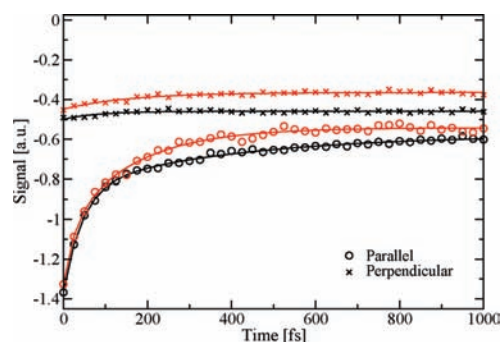
the anisotropy decays to below 0.1 within a picosecond, indicating that the average excitation at this time is delocalized over more than two units. If only two units are involved the anisotropy cannot decay below 0.1, unless the molecules rotate into the third dimension not spanned by their initial transition dipole moment vectors. In contrast, the monomer anisotropy never decays below 0.1. The faster decay in the trimer is a direct reflection of the fact that the population dynamics is faster than in the monomer.

The diagonal peak intensity for the parallel and perpendicular polarization directions is given in Figure 14. The intensities were extracted near the peak maximum at $\omega_1/2\pi c = \omega_3/2\pi c = 12\,000\ cm^{-1}$. The peak for the parallel polarization is particularly sensitive to population transfer. The anisotropy in the perpendicular polarization spectra remains constant on the time scale shown, whereas the anisotropy in the parallel polarization spectra exhibit biexponential decays similar to those observed in the anisotropy decay. Neither of the peaks exhibit signatures of coherent oscillations.
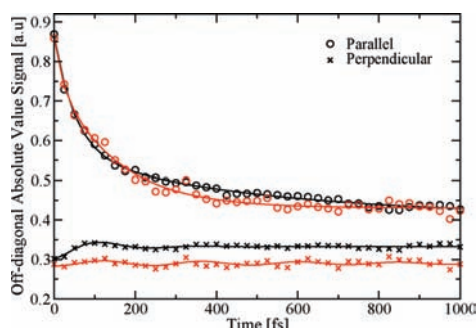
110

Figure 15. Absolute value of the off-diagonal peak intensity of the 2D correlation spectroscopy spectra at different waiting times. Taken at $\omega_1/2\pi c = 12\,000$ cm^{-1} and $\omega_3/2\pi c = 11\,850$ cm^{-1}. The monomer data is given in red and the trimer data in black. The full lines are fits.

Finally, we extracted the absolute value of the off-diagonal intensity taken 150 cm^{-1} below the peak (see Figure 15). This particular point is chosen for comparing with the off-diagonal point examined by Engel et al.[11] At this point no cross peak is resolved at room temperature, but a hidden cross peak between two BChl a chromophores might affect the spectrum. For the parallel polarization no oscillations can be resolved. The decay behavior is again typical for population transfer. For the perpendicular polarization a weak damped oscillation is observed. The oscillation is slightly larger for the trimer, but longer lived for the monomer. Attempts to fit the oscillations reveal that the dominant frequency is 136 cm^{-1} in both cases. In particular for the monomer it is, however, difficult to obtain a unique fit and due to the level of noise we refrain from attributing significance to the oscillations. We do, however, note that the dominant frequency coincides with the 160 cm^{-1} frequency experimentally observed at lower temperature.[11]

■ CONCLUSIONS

In this study we have performed simulations of the exciton dynamics and optical spectra for the FMO complex starting from MD simulations and employing quantum chemistry calculations to generate a time-dependent exciton Hamiltonian. Simulations were performed for both a single FMO monomer and a trimer. Interestingly, in the monomer simulations, an eighth BChl, only recently found in a new crystal structure, did not form a stable complex with the rest of the protein. The main monomer simulations were therefore carried out with only seven BChls. The MD trajectories at room temperature show the thermal fluctuations of the atoms within the protein and the BChl molecules.

In subsequent semiempirical quantum chemical calculations along the MD trajectory, the effect of thermal fluctuations on ground and first excited state of the BChl molecules was calculated. We found that the gaps between first excited state and ground state, denoted as site energies, show similarities and differences with previous studies. The distributions of calculated site energies show rather broad non-Gaussian fluctuations which are much broader than the splitting between individual site energies; the distributions also exhibit pronounced blue tails. The distribution widths of the intramonomer and intermonomer BChl couplings are roughly proportional to the absolute value of

the couplings. In a previous study we already showed that at ambient temperatures no relevant spatial correlation could be found in the site energies or the couplings.[24]

On the basis of the results from the electronic structure calculations, we were able to parametrize a time-dependent model of coupled sites. The solution of the Schrödinger equation in this model revealed the excitation energy transfer within the FMO complex as well as optical properties. Due to the different coupling values in the monomer and trimer results, especially between BChls 1 and 2, the exciton dynamics based on monomer and trimer MD simulations were found to differ significantly. Within the trimer the coupling between the pigments 1 and 2 is so large that faint coherent oscillations are observed despite the fluctuating environment. This observation may be connected to the experimentally observed coherences at 277 K.[11] In general the population transfer between different states was faster in the trimer due to larger couplings and narrower site energy distributions. One can therefore expect coherent oscillations to be larger in the trimer than those already observed in the monomer.

Transfer between individual chromophores, whether directly or indirectly connected by strong couplings, occurs on time scales below 100 fs. Interestingly, although the eighth BChl is situated closest to the chlorosome baseplate,[67] indicating that it could be the first pigment to receive excitation from the chlorosome, it has the slowest transfer rate to any other pigment. The role of the eighth BChl may thus only be to assist excitation transfer between FMO monomers within the trimer and not to directly receive excitation from the chlorosome.

Optical properties of the FMO monomer and trimer complex were determined. For the monomer the simulated peak position of the linear absorption is only about 3% off the experimental value and the width is 15% narrower than the observed width. The skewed shape of the experimental absorption line shape is well reproduced by the simulation. The skewness originates from the non-Gaussian distribution of the individual site energies. The overly narrow line width may be a result in the simulations from inaccuracies in the force field parameters, use of ground-state classical path dynamics, undersampling of protein conformations, neglect of polarization effects, low sensitivity to fluctuations in the environment, errors in site energies based on the semiempirical ZINDO/S method or too fast environmental fluctuations resulting in too much exchange narrowing. Furthermore, the TrEsp couplings are based on fixed transition charges and have been mapped onto dynamical structures which might also change the effect of exchange narrowing. On the positive side we note that the calculated 2D CS spectra show no distinct features just as in the experimental counterparts at 277 K. In the absolute value of the off-diagonal intensity taken 150 cm^{-1} below the peak, very small oscillations are visible, which might be connected to what is seen in experiment at lower temperatures. To establish a clearer connection one would have to repeat simulations at lower temperatures. Here we considered the energy transfer through the FMO complex at room temperature. At lower temperatures the transfer mechanism is surely different as the magnitude and speed of the dynamics of the environmental will be smaller and slower.

From our simulations we find that even though little coherent population transfer between sites is observed in the FMO complex at room temperature the overall excitation transfer is very efficient with transfer times across the complex of only 100 fs. The transfer is predominantly occurring through the individual monomers

which can be thought of as individual energy transfer channels due to small couplings between sites in different monomers. The transfer is more efficient in the naturally ocuring trimer than in the monomer due to smaller energy fluctuations and larger couplings. The reason that the transfer, even though incoherent, can be highly efficient is that the site energy fluctuations are very fast, resulting in nonadiabatic population transfer occurring every time the site energies of coupled sites are close, which happens on a 100 fs time scale.

■ AUTHOR INFORMATION

Corresponding Author
*E-mail: u.kleinekathoefer@jacobs-university.de.

■ ACKNOWLEDGMENT

■ REFERENCES

(1) Hu, X.; Ritz, T.; Damjanović, A.; Autenrieth, F.; Schulten, K. *Q. Rev. Biophys.* **2002**, *35*, 1–62.

(2) Cogdell, R. J.; Gall, A.; Köhler, J. *Q. Rev. Biophys.* **2006**, *39*, 227–324.

(3) Cheng, Y. C.; Fleming, G. R. *Annu. Rev. Phys. Chem.* **2009**, *60*, 241–242.

(4) Novoderezhkin, V. I.; van Grondelle, R. *Phys. Chem. Chem. Phys.* **2010**, *12*, 7352–7365.

(5) Milder, M. T.; Brüggemann, B.; van Grondelle, R.; Herek, J. L. *Photosynth. Res.* **2010**, *104*, 257–264.

(6) Matthews, B. W.; Fenna, R. E.; Bolognesi, M. C.; Schmid, M. F.; Olson, J. M. *J. Mol. Biol.* **1979**, *131*, 259–265.

(7) Tronrud, D. E.; Schmid, M. F.; Matthews, B. W. *J. Mol. Biol.* **1986**, *188*, 443–444.

(8) Tronrud, D. E.; Wen, J.; Gay, L.; Blankenship, R. E. *Photosynth. Res.* **2009**, *100*, 79–87.

(9) Brixner, T.; Stenger, J.; Vaswani, H. M.; Cho, M.; Blankenship, R. E.; Fleming, G. R. *Nature* **2005**, *434*, 625–628.

(10) Engel, G. S.; Calhoun, T. R.; Read, E. L.; Ahn, T. K.; Mancal, T.; Cheng, Y. C.; Blankenship, R. E.; Fleming, G. R. *Nature* **2007**, *446*, 782–786.

(11) Panitchayangkoon, G.; Hayes, D.; Fransted, K. A.; Caram, J. R.; Harel, E.; Wen, J.; Blankenship, R. E.; Engel, G. S. *Proc. Natl. Acad. Sci. U.S.A.* **2010**, *107*, 12766–12770.

(12) Collini, E.; Wong, C. Y.; Wilk, K. E.; Curmi, P. M.; Brumer, P.; Scholes, G. D. *Nature* **2010**, *463*, 644–647.

(13) Collini, E.; Scholes, G. D. *Science* **2009**, *323*, 369–373.

(14) Wolynes, P. G. *Proc. Natl. Acad. Sci. U.S.A.* **2009**, *106*, 17247–17248.

(15) Caruso, F.; Chin, A. W.; Datta, A.; Huelga, S. F.; Plenio, M. B. *J. Chem. Phys.* **2009**, *131*, 105106.

(16) Rebentrost, P.; Mohseni, M.; Aspuru-Guzik, A. *J. Phys. Chem. B* **2009**, *113*, 9942–9947.

(17) Nazir, A. *Phys. Rev. Lett.* **2009**, *103*, 146404.

(18) Fassioli, F.; Nazir, A.; Olaya-Castro, A. *J. Phys. Chem. Lett.* **2010**, *1*, 2139–2143.

(19) Nalbach, P.; Eckel, J.; Thorwart, M. *New J. Phys.* **2010**, *12*, 065043.

(20) Strümpfer, J.; Schulten, K. *J. Chem. Phys.* **2011**, *134*, 095102.

(21) Fleming, G. R.; Huelga, S.; Plenio, M. *New J. Phys.* **2010**, *12*, 065002.

(22) Abramavicius, D.; Mukamel, S. *J. Chem. Phys.* **2011**, *134*, 174504.

(23) Olbrich, C.; Kleinekathöfer, U. *J. Phys. Chem. B* **2010**, *114*, 12427–12437.

(24) Olbrich, C.; Strümpfer, J.; Schulten, K.; Kleinekathöfer, U. *J. Phys. Chem. B* **2011**, *115*, 758–764.

(25) Abramavicius, D.; Mukamel, S. *J. Chem. Phys.* **2010**, *133*, 064510.

(26) Dijkstra, A. G.; Jansen, T. L. C.; Knoester, J. *J. Chem. Phys.* **2008**, *128*, 164511.

(27) Damjanović, A.; Kosztin, I.; Kleinekathöfer, U.; Schulten, K. *Phys. Rev. E* **2002**, *65*, 031919.

(28) Walker, R. C.; Mercer, I. P.; Gould, I. R.; Klug, D. R. *J. Comput. Chem.* **2007**, *28*, 478–480.

(29) Zwier, M. C.; Shorb, J. M.; Krueger, B. P. *J. Comput. Chem.* **2007**, *28*, 1572–1581.

(30) Janosi, L.; Kosztin, I.; Damjanović, A. *J. Chem. Phys.* **2006**, *125*, 014903.

(31) Olbrich, C.; Liebers, J.; Kleinekathöfer, U. *Phys. Status Solidi B* **2011**, *248*, 393–398.

(32) Ridley, J.; Zerner, M. C. *Theor. Chim. Acta* **1973**, *32*, 111–134.

(33) Linnanto, J.; Korppi-Tommola, J. *Phys. Chem. Chem. Phys.* **2006**, *8*, 663–667.

(34) Madjet, M. E.; Abdurahman, A.; Renger, T. *J. Phys. Chem. B* **2006**, *110*, 17268–81.

(35) Renger, T. *Photosynth. Res.* **2009**, *102*, 471–485.

(36) Madjet, M. E.; Müh, F.; Renger, T. *J. Phys. Chem. B* **2009**, *113*, 12603–14.

(37) de Boeij, W. P.; Pshenichnikov, M. S.; Wiersma, D. A. *Chem. Phys. Lett.* **1996**, *253*, 53.

(38) Hamm, P.; Lim, M. H.; Hochstrasser, R. M. *J. Phys. Chem. B* **1998**, *102*, 6123.

(39) Ernst, R. R.; Bodenhausen, G.; Wokaun, A. *Principles of nuclear magnetic resonance in one and two dimensions*; Oxford University Press: New York, 1995.

(40) Jansen, T. L. C.; Knoester, J. *J. Phys. Chem. B* **2006**, *110*, 22910–22916.

(41) Jansen, T. L. C.; Knoester, J. *Acc. Chem. Res.* **2009**, *42*, 1405–1411.

(42) Ishizaki, A.; Fleming, G. R. *J. Chem. Phys.* **2009**, *130*, 234111.

(43) Sharp, L. Z.; Egorova, D.; Domcke, W. *J. Chem. Phys.* **2010**, *132*, 014501.

(44) Palmieri, B.; Abramavicius, D.; Mukamel, S. *Phys. Chem. Chem. Phys.* **2010**, *12*, 108–114.

(45) Jansen, T. L. C.; Auer, B. M.; Yang, M.; Skinner, J. L. *J. Chem. Phys.* **2010**, *132*, 224503.

(46) Humphrey, W. F.; Dalke, A.; Schulten, K. *J. Mol. Graph.* **1996**, *14*, 33–38.

(47) Petrenko, T.; Neese, F. *J. Chem. Phys.* **2007**, *127*, 164319.

(48) Cory, M. G.; Zerner, M. C.; Hu, X.; Schulten, K. *J. Phys. Chem. B* **1998**, *102*, 7640–7650.

(49) Alden, R. G.; Johnson, E.; Nagarajan, V.; Law, W. W. P. J.; Cogdell, R. G. *J. Phys. Chem. B* **1997**, *101*, 4667–4680.

(50) Scholes, G. D.; Curutchet, C.; Mennucci, B.; Cammi, R.; Tomasi, J. *J. Phys. Chem. B* **2007**, *111*, 6978–6982.

(51) Vulto, S. I. E.; de Baat, M. A.; Louwe, R. J. W.; Permentier, H. P.; Neef, T.; Miller, M.; van Amerongen, H.; Aartsma, T. J. *J. Phys. Chem. B* **1998**, *102*, 9577–9582.

(52) Renger, T.; May, V. *J. Phys. Chem. A* **1998**, *102*, 4381–4391.

(53) Adolphs, J.; Renger, T. *Biophys. J.* **2006**, *91*, 2778–2787.

(54) Schmidt am Busch, M.; Müh, F.; Madjet, M. E.; Renger, T. *J. Phys. Chem. Lett.* **2011**, *2*, 93–98.

(55) Kobus, M.; Gorbunov, R. D.; Nguyen, P.; Stock, G. *Chem. Phys.* **2008**, *347*, 208–217.

(56) Zhu, H.; May, V.; Röder, B.; Renger, T. *J. Chem. Phys.* **2008**, *128*, 154905.

(57) Zhu, H.; Röder, B.; May, V. *Chem. Phys.* **2009**, *362*, 19–26.

(58) Deranleau, D. A. *Experientia* **1982**, *38*, 661–662.

(59) Paarmann, A.; Hayashi, T.; Mukamel, S.; Miller, R. J. D. *J. Chem. Phys.* **2009**, *130*, 204110.

(60) Abramavicius, D.; Palmieri, B.; Voronine, D. V.; Sanda, F.; Mukamel, S. *Chem. Rev.* **2009**, *109*, 2350–2358.

(61) Hochstrasser, R. M. *Chem. Phys.* **2001**, *266*, 273–284.

(62) Freiberg, A.; Lin, S.; Timpmann, K.; Blankenship, R. E. *J. Phys. Chem. B* **1997**, *101*, 7211–7220.

(63) Thouless, D. J. *Phys. Rep* **1974**, *13*, 93.

(64) Bakalis, L. D.; Knoester, J. *J. Phys. Chem. B* **1999**, *103*, 6620–6628.

(65) Woutersen, S.; Bakker, H. J. *Nature* **1999**, *402*, 507.

(66) Lin, Y.-S.; Pieniazek, P. A.; Yang, M.; Skinner, J. L. *J. Chem. Phys.* **2010**, *132*, 174505.

(67) Wen, J.; Zhang, H.; Gross, M. L.; Blankenship, R. E. *Proc. Natl. Acad. Sci. U.S.A.* **2009**, *106*, 6134–6139.

8621

dx.doi.org/10.1021/jp202619a |*J. Phys. Chem. B* 2011, 115, 8609–8621

6.3. The Journal of Physical Chemistry Letters (2011):

Theory and Simulation of the Environmental Effects on the FMO Light-Harvesting Complex

Authors: C. Olbrich, J. Strümpfer, K. Schulten, and U. Kleinekathöefer

Theory and Simulation of the Environmental Effects on FMO Electronic Transitions

Carsten Olbrich,[†] Johan Strümpfer,[‡] Klaus Schulten,[‡,¶] and Ulrich Kleinekathöfer*,[‡]

[†]School of Engineering and Science, Jacobs University Bremen, Campus Ring 1, 28759 Bremen, Germany

[‡]Center for Biophysics and Computational Biology and Beckman Institute and [¶]Department of Physics, University of Illinois at Urbana—Champaign, Urbana, Illinois 61801, United States

S *Supporting Information*

ABSTRACT: Long-lived quantum coherence has been experimentally observed in the Fenna—Matthews—Olson (FMO) light-harvesting complex. It is much debated which role thermal effects play and if the observed low-temperature behavior arises also at physiological temperatures. To contribute to this debate, we use molecular dynamics simulations to study the coupling between the protein environment and the vertical excitation energies of individual bacteriochlorophyll molecules in the FMO complex of the green sulfur bacterium *Chlorobaculum tepidum*. The so-called spectral densities, which account for the environmental influence on the excited-state dynamics, are determined from temporal autocorrelation functions of the energy gaps between ground and first excited states of the individual pigments. Although the overall shape of the spectral density is found to be rather similar for all pigments, variations in their magnitude can be seen. Differences between the spectral densities for the pigments of the FMO monomer and FMO trimer are also presented.

SECTION: Biophysical Chemistry
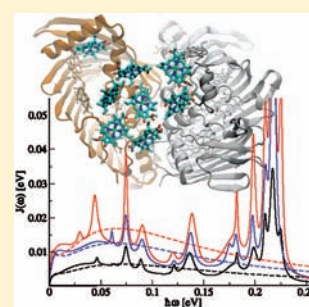
Many plants and bacteria acquire their energy from sunlight through photosynthesis. Light harvesting is arguably thus the most important process of energy acquisition on earth. Green sulfur bacteria and some other phototrophs use large vesicles of pigments, called chlorosomes, as their main antenna for capturing photons. The resulting excitation energy is then transferred across the so-called Fenna—Matthews—Olson (FMO) complex to the reaction center where it is used to establish a charge gradient across the membrane.[1] The crystal structure of the FMO complex from the bacterium *Prosthecochloris aestuarii* was first resolved in 1979.[2] An improved structure at atomic resolution of 1.9 Å was reported later[3] as was a high-resolution structure for *Chlorobaculum tepidum*.[4] The FMO complex forms a homotrimer under physiological conditions, with each monomer containing eight bacteriochlorophyll-a (BChl a) molecules (see Figure 1).

Long-lived coherence effects in time-resolved optical two-dimensional spectra[5−7] spurred a tremendous interest in the FMO complex.[8] In similar experiments, long-lasting coherence beating signals have also been observed for a photosynthetic complex of marine algae at ambient temperatures[9] as well as in conjugated polymers.[10] The obvious and so far open question is how such effects can survive several hundred femtoseconds within a biological environment at low and physiological temperatures. In general, one expects quantum effects to decay within tens of femtoseconds due to the thermal fluctuations inherent in a complex and disordered biological environment. As a result of stated observations, several theoretical studies have

been performed to explore this long-lived coherent beating phenomenon (see, e.g., refs 11−19). It was suggested that long-lived coherent beating arises from correlated fluctuations of the pigment molecules. In DNA, for example, the neighboring entities are close to each other to experience partially the same electrostatic potential of the surrounding, leading to spatial site correlations that have a drastic effect on electronic transport properties.[20] We have recently shown, however, using classical molecular dynamics (MD) simulations and semiempirical electronic structure calculations, that correlations between pigment excitation energy fluctuations most likely do not exist in the FMO complex.[21,22] Interference of different quantum pathways have also been proposed as the origin of the long-lived coherences.[18,23]

The spectral density is the key quantity for all of the theoretical investigations using a density matrix approach to describe the system—environment interaction and, hence, thermal effects.[24,25] For the FMO complex, experimental investigations on the electron—vibrational coupling were reported earlier.[26] The spectral density for light-harvesting complex 2 (LH2) has previously been extracted from a combination of MD and electronic structure calculations.[27−30] Recently, we have used the same approach, that is, MD and quantum chemistry calculations on the ZINDO/S level (Zerner intermediate neglect of
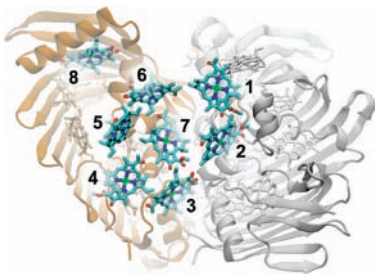
LETTER

Figure 1. The FMO trimer with the protein structure of two monomers shown in cartoon representation. Highlighted are the eight BChls of one monomer.
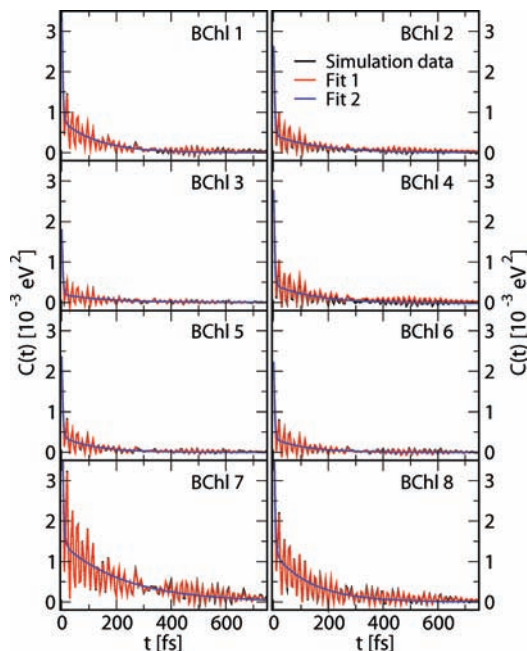

Figure 2. Energy gap autocorrelation functions for the 8 different BChls of the FMO trimer. The simulation data have been averaged over the equivalent BChls in the three monomers. Shown are the data as obtained from the simulations (black), a series of exponential decays and damped oscillations (blue), as well as a double-exponential fit (red, see main text).

differential orbital method with parameters for spectroscopic properties), to construct a time-dependent Hamiltonian for the FMO complex.[21,22] That Hamiltonian was subsequently employed to determine room-temperature exciton population dynamics, linear absorption, and 2D spectra by using it in an ensemble-averaged wavepacket formalism, termed NISE (numerical integration of the Schrödinger equation).[31,32] The drawback of NISE is its implicit assumption of an infinite temperature and that it therefore does not yield the correct thermal equilibrium at finite temperatures. In the present report, the same trajectories of the energy gap fluctuations between the BChl ground and first excited states, that is, the BChl Q_y state, are used to extract the spectral densities of the individual FMO BChls. FMO spectral densities based on the analysis of experimental results have also been proposed by Adolphs and Renger,[33] by Cho and co-workers,[34] as well as by Ishizaki and Fleming.[11] Very recently, another computational study has been reported as well.[35]

For the details of the MD and ZINDO/S calculations, we refer the reader to refs 21 and 22. The MD is a ground-state MD that includes approximations due to the underlying force field. The energy gap fluctuations for BChls of both the FMO trimer and the FMO monomer have been determined using the semiempirical ZINDO/S method, which was parametrized for the BChl molecules. For the trimer, for example, 24 energy gap calculations per snapshot have been performed for 40 000 snapshots, amounting to almost a million ZINDO/S calculations. Though the ZINDO/S method has its limitations, it has been shown to treat environmental effects in chromophores more accurately than, for example, density-functional-based approaches.[36] Because FMO forms a trimer under physiological conditions, the trimer data are described below, while the corresponding monomer data are presented in the Supporting Information.

The first step in the process of obtaining spectral densities is calculating the autocorrelation function of the energy gap between the ground and first excited state. In principle, the autocorrelation functions are different for each pigment. In the case of the trimer simulations, we average over the equivalent pigments in the three monomers. The autocorrelation function is determined using the energy gaps $\Delta E_{j,l}(t_i)$ at time steps t_i for BChl j in monomer l. Including an average over M equivalent BChls, the autocorrelation function $C_j(t_i)$ is given by[27]

$$C_j(t_i) = \frac{1}{M}\sum_{l=1}^{M}\left[\frac{1}{N-i}\sum_{k=1}^{N-i}\Delta E_{j,l}(t_i + t_k)\Delta E_{j,l}(t_k)\right] \quad (1)$$

For the monomer simulations, there are no equivalent BChls, and M therefore equals 1, while for the trimer, its value is 3. The

fastest oscillations in the site energies have periods of around 20 fs, and therefore, we choose a time step of 5 fs between the individual snapshots of the MD and ZINDO/S calculations. For the monomer and trimer simulations, the time series contains 60 000 and 40 000 points. The correlation functions quickly decay within the first 100—200 fs and vanish within 1—2 ps. Therefore, 4-ps-long windows were used to determine correlation functions of 2 ps length. Using a spacing of 1 ps, there are 296 and 196 4-ps-long windows along the trajectories for the trimer and monomer, respectively. The correlation functions were calculated for each window and then averaged. At long times, their values should be 0 by definition. Due to the averaging procedure, the autocorrelation functions sometimes exhibit a small offset, which is discarded in the fitting procedure. The resulting correlation functions for the trimer are shown in Figure 2, and those for the monomer are shown in Figure S1, Supporting Imformation. The correlation functions for BChls 1—6 behave, to some extent, rather similarly with larger deviations for pigments 7 and 8. To keep the number of different functional forms simple, we decided to only use one averaged spectral density for BChls 1—6 but separate ones for BChls 7 and 8. The respective spectral densities for the individual BChls can be found in the Supporting Information.

In the case of LH2,[29] we fitted the correlation functions to an analytical form, that is, a combination of exponentials and damped oscillations

$$C_j(t) \approx \sum_{i=1}^{N_e}\eta_{j,i}e^{-\gamma_{j,i}t} + \sum_{i=1}^{N_o}\tilde{\eta}_{j,i}\cos(\tilde{\omega}_{j,i}t)e^{-\tilde{\gamma}_{j,i}t} \quad (2)$$

Table 1. Parameters of Fit 2 for the Autocorrelation Function Based on the Trimer Simulation Data[a]

	BChl 1	BChl 2	BChl 3	BChl 4	BChl 5	BChl 6	BChl 7	BChl 8	BChls 1–6
η_1	275.20	220.55	161.09	233.66	198.44	189.63	525.25	380.18	213.30
$1/\gamma_1$	4.14	4.18	3.99	3.94	4.10	3.79	4.56	4.54	4.04
η_2	80.16	43.03	20.17	46.09	38.64	33.91	146.42	121.77	43.47
$1/\gamma_2$	131.24	166.76	160.87	154.44	118.44	115.79	227.59	140.78	138.98

[a] The correlation functions are averaged over the equivalent pigments in the three monomers (η_i in $[10^{-5}\ eV^2]$, $1/\gamma_i$ in $[fs]$).
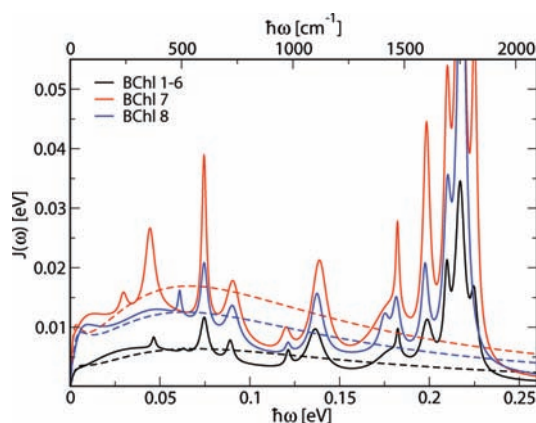

Figure 3. Spectral densities of different BChls in the trimer. The spectral properties of BChls 1–6 are described by an averaged quantity. In addition to results based on Fit 1 (solid lines), approximate spectral densities based on Fit 2 to the correlations functions are shown (dotted lines).

Below, two different fitting functions are used. The first one, called Fit 1, uses two exponentials ($N_e = 2$) and 13 damped oscillations ($N_o = 13$), while a simplified version, called Fit 2, uses two exponentials only ($N_e = 2$, $N_o = 0$). Both fits are shown together with the original correlation functions in Figure 2. The parameters for the simplified fitting form are given in Table 1, while the ones for the more elaborate fits are given in Table S1 (Supporting Information). The corresponding data for the monomer are listed in Tables S2 and S3 (Supporting Information). Looking at the double-exponential fit, the fast initial decay has a decay time $\tau_i = 1/\gamma_i$ of about 4–5 fs for all BChls, while the slower decay time is 140 fs for pigments 1–6 and 8, and it is 230 fs for BChl 7. Beyond these two exponential decays, the correlation function shows strong oscillations with oscillation periods of around 20 fs. These oscillations can be attributed to vibrational motions including C=C and C=O double bonds.[27,29,37–39]

The spectral density $J(\omega)$ describes the frequency-dependent coupling between the excitonic subsystem and the thermal environment. Denoting the inverse temperature by $\beta = 1/(k_B T)$, the spectral density $J_j(\omega)$ of BChl j is given by[27,40,41]

$$J_j(\omega) = \frac{2}{\pi\hbar} \tanh(\beta\hbar\omega/2) \int_0^\infty dt\ C_j(t)\ \cos(\omega t) \qquad (3)$$

which is the key relation for combining the results from the MD and quantum chemistry studies with dissipative exciton dynamics. We note that the spectral density in the Caldeira–Leggett model
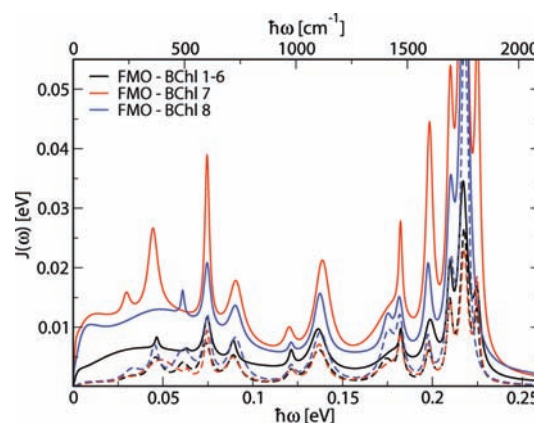

Figure 4. The solid lines show the same spectral densities as those in Figure 3, while the dashed lines show the spectral densities calculated without taking the external charges into account.

$J_{CL,j}(\omega)$ is connected to the present form by $J_{CL,j}(\omega) = (\pi/\hbar)J_j(\omega)$. The thermal correction factor in eq 3 fulfills two functions; it ensures the validity of the detailed balance relation and at the same time (approximately) removes the temperature dependence from the spectral density. The fluctuations in the MD simulations are of course temperature-dependent, but the spectral density is, assuming a harmonic bath, a temperature-independent quantity.

Using the analytic expression for $C(t)$, eq 2, the spectral density is given by

$$J_j(\omega) = \frac{2}{\pi\hbar} \tanh(\beta\hbar\omega/2)$$
$$\times \left[\sum_{i=1}^{N_e} \frac{\eta_{j,i}\gamma_{j,i}}{\gamma_{j,i}^2 + \omega^2} + \sum_{i=1}^{N_o} \frac{\tilde{\eta}_{j,i}\tilde{\gamma}_{j,i}}{2(\tilde{\gamma}_{j,i}^2 + (\omega - \tilde{\omega}_{j,i})^2)} \right] \qquad (4)$$

In this expression, we have neglected terms similar to the last term in eq 4 but with $(\omega + \tilde{\omega}_i)^2$ instead of $(\omega - \tilde{\omega}_i)^2$ in the denominator. Including these terms leads to negligible changes in the values of the spectral density. Furthermore, we note that in most applications concerning electronic relaxation, one is only interested in the low-energy range, and many of the high-energy features of the spectral density might be rather unimportant for these applications.

The resulting spectral densities are displayed in Figure 3. Shown in this figure is the averaged spectral density for BChls 1–6 and the distinctly larger spectral densities for BChls 7 and 8. The forms of all of the spectral densities are very similar; only their amplitudes differ considerably. The biexponential Fit 2 leads to a rather featureless electron–environment coupling.
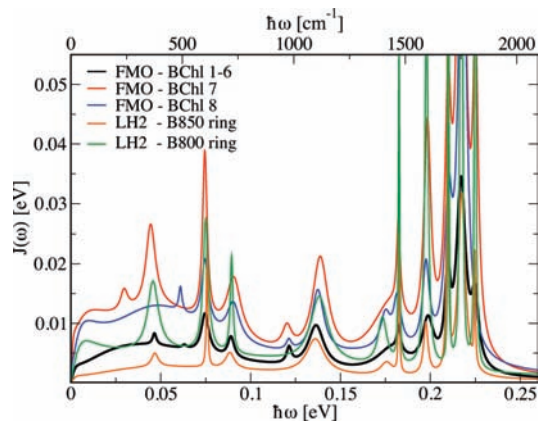
117

Figure 5. The spectral densities for the FMO trimer compared to those of the B800 and B850 rings of the LH2 complex.

Figure 6. Spectral densities for the FMO trimer determined in the present study compared to those of previous studies by Ishizaki and Fleming,[11] Cho et al.,[34] Adolphs and Renger,[33] as well as Nalbach et al.[19] The inset shows an enlarged energy and spectral density range.

The exponential with the long time constant leads to a sharp rise of the spectral density at small frequencies. In the low-energy regime, the difference between spectral densities resulting from Fit 1 and Fit 2 is minor. For many purposes, the simpler spectral density might thus be sufficient. It is no surprise that BChl 8 shows a larger spectral density because it is weakly bound to the complex. In the monomer simulations, BChl 8 even left the complex. BChl 7, on the other hand, seems to have a more fluctuating environment than the other BChls. A detailed analysis including the use of the electrostatic potential, as previously done for DNA in water,[42] is currently underway. Shown in Figure 4 is the comparison between spectral densities calculated using the ZINDO/S with and without taking the charges external to each BChl into account. It becomes clear that the low-energy part of the spectral densities is mainly due to the fluctuations of the environment. Interestingly, basically all peaks in the spectral densities already appear without taking into account the external charges and are therefore internal modes. The fluctuation strengths of these internal modes are influenced by the fluctuating environment.

In a previous study,[29] we analyzed the spectral densities for LH2 of the purple bacterium *Rhodospirillum molischianum*, which were determined using the same approach as that employed in the present investigation. The LH2 system consists of two bacteriochlorophyll systems, the B800 and the B850 rings. The BChl in these two rings experience different environments, leading to two different spectral densities.[29] In Figure 5, the spectral densities for the BChls in the B800 and B850 rings are compared to those from the FMO complex. Again, there is a quite large agreement concerning the functional form but not the amplitude of the different spectral densities. Because the BChl molecules are in different protein environments, the similarities of their spectral densities most likely result from their internal vibrations. For example, it is well-known that BChl molecules have vibrational modes in the region of 1600 cm^{-1}, which are strongly present in Figure 5. The rather featureless background of the spectral densities, especially in the low-energy region, differs between environments and seems to be mainly due to electrostatic interactions with vibrational modes outside of the individual pigment.
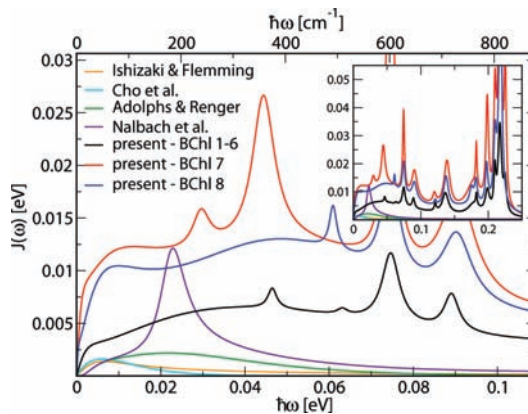
After comparing to spectral densities obtained using the same approach for a different system, we compare, as shown in Figure 6, the present results for the FMO complex with previous approximations for the spectral density, all of them assuming equal properties for all BChls. Adolphs and Renger estimated the electron−environment coupling based on the fluorescence line narrowing spectrum.[33] This spectral density has a maximum at around 0.02 eV and decays exponentially at larger energies. The Fleming group has proposed two other spectral densities[11,34] that do not differ greatly from that of Adolphs and Renger but decay even faster at energies above 0.01 eV. The amplitudes of these spectral densities are considerably smaller than the ones determined in the current work. Recently, Nalbach et al.[19] employed the spectral density of Adolphs and Renger with the addition of a single vibrational mode. Interestingly, the spectral density with this additional broad mode only leads to small differences in the exciton dynamics.[19]

At energies below 0.01 eV, the present system−bath interaction for BChls 1−6 is about a factor of 2−3 larger and extends to higher energies than those reported previously.[11,19,33,34] The present system−bath interaction is, however, in agreement with that of chlorophyll a molecules, which have been proposed in the form of Huang−Rhys factors that also extend to energies of about 0.2 eV.[43,44] Furthermore, it is not surprising that the system−bath interaction is nonvanishing for energies around 0.2 eV because there are several C=O and C=C bonds in chlorophyll and BChl molecules that vibrate with frequencies in this region. In the present approach, internal BChl modes as well as external environmental effects that lead to fluctuations in the energy gap between ground and first excited state are included. The internal modes of BChl based on density functional and force field calculations appear in the same energy range and with a qualitatively similar distribution as that shown in the high-energy region of the present spectral density.[39]

On the basis of the same MD and electronic energy gap calculations as those employed here, we previously presented data on the linear absorption and two-dimensional spectra of FMO at room temperature.[22] Disorder due to large-scale structural changes were, however, not included in those calculations.

These changes are on time scales much longer than those accessible by standard MD simulations and are usually modeled as static disorder. Therefore, spectral features of the linear and 2D spectra showed narrower widths than are observed experimentally. This discrepancy suggests that the time-dependent Hamiltonian, used as the basis for the present results, does not contain, to a sufficient degree, large-amplitude fluctuations. The ensemble-averaged wavepacket dynamics used in ref 22 has the drawback that it includes an implicit high-temperature limit, that is, it leads to incorrect site populations in the long-time limit; some density matrix approaches that could employ the present spectral density usually do not suffer from this drawback. For room-temperature systems, however, we do not expect a significant difference for the linear absorption and two-dimensional spectra and therefore refrain from repeating the calculations using these approaches. Nevertheless, the agreement between the spectra calculated using wavepacket dynamics and experimental spectra indicate that the amplitude of our spectral densities, though larger than previous estimates, are in accordance with experiments.

The present results make it possible to computationally investigate the effects of the experimentally observed long-lived coherence in FMO.[5−7] The impetus to understand these underlying effects has steered many investigations (see, e.g., refs 12−19 and 45) that sometimes assumed rather crude approximations for the system−bath interaction. Other simulations were based on spectral densities by Adolphs and Renger[33] or the Fleming group.[11,34] All of these spectral densities were derived based on specific experimental information, which might not cover the whole energy range, as discussed above. The present spectral densities based on atomistic simulations partially differ for the individual BChls, cover a large frequency range, and make further studies of electronic properties of the FMO complex possible.

■ ASSOCIATED CONTENT

ⓢ Supporting Information. Tables listing the parameters of the autocorrelation function fits and results for the monomer simulations. This material is available free of charge via the Internet at http://pubs.acs.org.

■ AUTHOR INFORMATION

Corresponding Author
*E-mail: u.kleinekathoefer@jacobs-university.de.

■ ACKNOWLEDGMENT

■ REFERENCES

(1) Wen, J.; Zhang, H.; Gross, M. L.; Blankenship, R. E. Membrane Orientation of the FMO Antenna Protein from Chlorobaculum tepidum as determined by Mass Spectrometry-Based Footprinting. *Proc. Natl. Acad. Sci. U.S.A.* **2009**, *106*, 6134–6139.
(2) Matthews, B. W.; Fenna, R. E.; Bolognesi, M. C.; Schmid, M. F.; Olson, J. M. Structure of a Bacteriochlorophyll a-Protein from the Green Photosynthetic Bacterium *Prosthecochloris aestuarii. J. Mol. Biol.* **1979**, *131*, 259–265.
(3) Tronrud, D. E.; Schmid, M. F.; Matthews, B. W. Structure and X-ray Amino Acid Sequence of a Bacteriochlorophyll a Protein from *Prosthecochloris aestuarii* Refined at 1.9 Å Resolution. *J. Mol. Biol.* **1986**, *188*, 443–444.
(4) Tronrud, D. E.; Wen, J.; Gay, L.; Blankenship, R. E. The Structural Basis for the Difference in Absorbance Spectra for the FMO Antenna Protein from Various Green Sulfur Bacteria. *Photosynth. Res.* **2009**, *100*, 79–87.
(5) Brixner, T.; Stenger, J.; Vaswani, H. M.; Cho, M.; Blankenship, R. E.; Fleming, G. R. Two-Dimensional Spectroscopy of Electronic Couplings in Photosynthesis. *Nature* **2005**, *434*, 625–628.
(6) Engel, G. S.; Calhoun, T. R.; Read, E. L.; Ahn, T. K.; Mancal, T.; Cheng, Y. C.; Blankenship, R. E.; Fleming, G. R. Evidence for Wavelike Energy Transfer through Quantum Coherence in Photosynthetic Systems. *Nature* **2007**, *446*, 782–786.
(7) Panitchayangkoon, G.; Hayes, D.; Fransted, K. A.; Caram, J. R.; Harel, E.; Wen, J.; Blankenship, R. E.; Engel, G. S. Long-Lived Quantum Coherence in Photosynthetic Complexes at Physiological Temperature. *Proc. Natl. Acad. Sci. U.S.A.* **2010**, *107*, 12766–12770.
(8) Scholes, G. D. Quantum-Coherent Electronic Energy Transfer: Did Nature Think of It First? *J. Phys. Chem. Lett.* **2010**, *1*, 2–8.
(9) Collini, E.; Wong, C. Y.; Wilk, K. E.; Curmi, P. M.; Brumer, P.; Scholes, G. D. Coherently Wired Light-Harvesting in Photosynthetic Marine Algae at Ambient Temperature. *Nature* **2010**, *463*, 644–647.
(10) Collini, E.; Scholes, G. D. Coherent Intrachain Energy Migration in a Conjugated Polymer at Room Temperature. *Science* **2009**, *323*, 369–373.
(11) Ishizaki, A.; Fleming, G. R. Theoretical Examination of Quantum Coherence in a Photosynthetic System at Physiological Temperature. *Proc. Natl. Acad. Sci. U.S.A.* **2009**, *106*, 17255–17260.
(12) Caruso, F.; Chin, A. W.; Datta, A.; Huelga, S. F.; Plenio, M. B. Highly Efficient Energy Excitation Transfer in Light-Harvesting Complexes: The Fundamental Role of Noise-Assisted Transport. *J. Chem. Phys.* **2009**, *131*, 105106.
(13) Rebentrost, P.; Mohseni, M.; Aspuru-Guzik, A. Role of Quantum Coherence and Environmental Fluctuations in Chromophoric Energy Transport. *J. Phys. Chem. B* **2009**, *113*, 9942–9947.
(14) Nazir, A. Correlation-Dependent Coherent to Incoherent Transitions in Resonant Energy Transfer Dynamics. *Phys. Rev. Lett.* **2009**, *103*, 146404.
(15) Fassioli, F.; Nazir, A.; Olaya-Castro, A. Quantum State Tuning of Energy Transfer in a Correlated Environment. *J. Phys. Chem. Lett.* **2010**, *1*, 2139–2143.
(16) Nalbach, P.; Eckel, J.; Thorwart, M. Quantum Coherent Biomolecular Energy Transfer with Spatially Correlated Fluctuations. *New J. Phys.* **2010**, *12*, 065043.
(17) Fleming, G. R.; Huelga, S.; Plenio, M. Focus on Quantum Effects and Noise in Biomolecules. *New J. Phys.* **2010**, *12*, 065002.
(18) Abramavicius, D.; Mukamel, S. Quantum Oscillatory Exciton Migration in Photosynthetic Reaction Centers. *J. Chem. Phys.* **2010**, *133*, 064510.
(19) Nalbach, P.; Braun, D.; Thorwart, M. How "Quantum" is the Exciton Dynamics in the Fenna-Matthews-Olson Complex? **2011**; arXiv:1104.2031v1.
(20) Kubař, T.; Kleinekathöfer, U.; Elstner, M. Solvent Fluctuations Drive the Hole Transfer in DNA: A Mixed Quantum-Classical Study. *J. Phys. Chem. B* **2009**, *113*, 13107–13117.
(21) Olbrich, C.; Strümpfer, J.; Schulten, K.; Kleinekathöfer, U. Quest for Spatially Correlated Fluctuations in the FMO Light-Harvesting Complex. *J. Phys. Chem. B* **2011**, *115*, 758–764.
(22) Olbrich, C.; Jansen, T. L. C.; Liebers, J.; Aghtar, M.; Strümpfer, J.; Schulten, K.; Knoester, J.; Kleinekathöfer, U. From Atomistic Modeling to Excitation Dynamics and Two-Dimensional Spectra of the FMO Light-Harvesting Complex. *J. Phys. Chem. B* **2011**, *115*, 8609–8621.

LETTER

(23) Dijkstra, A. G.; Jansen, T. L. C.; Knoester, J. Localization and Coherent Dynamics of Excitons in the Two-Dimensional Optical Spectrum of Molecular J-Aggregates. *J. Chem. Phys.* **2008**, *128*, 164511.

(24) Heřman, P.; Kleinekathöfer, U.; Barvk, I.; Schreiber, M. Exciton Scattering in Light-Harvesting Systems of Purple Bacteria. *J. Lumin.* **2001**, *94,95*, 447–450.

(25) Heřman, P.; Kleinekathöfer, U.; Barvk, I.; Schreiber, M. Influence of Static and Dynamic Disorder on the Anisotropy of Emission in the Ring Antenna Subunits of Purple Bacteria Photosynthetic Systems. *Chem. Phys.* **2002**, *275*, 1–13.

(26) Wendling, M.; Pullerits, T.; Przyjalgowski, M. A.; Vulto, S. I. E.; Aartsma, T. J.; Grondelle, R. v.; Amerongen, H. v. Electron-Vibrational Coupling in the Fenna−Matthews−Olson Complex of Prosthecochloris aestuarii Determined by Temperature-Dependent Absorption and Fluorescence Line-Narrowing Measurement. *J. Phys. Chem. B* **2000**, *104*, 5825–5831.

(27) Damjanović, A.; Kosztin, I.; Kleinekathöfer, U.; Schulten, K. Excitons in a Photosynthetic Light-Harvesting System: A Combined Molecular Dynamics, Quantum Chemistry and Polaron Model Study. *Phys. Rev. E* **2002**, *65*, 031919.

(28) Janosi, L.; Kosztin, I.; Damjanović, A. Theoretical Prediction of Spectral and Optical Properties of Bacteriochlorophylls in Thermally Disordered LH2 Antenna Complexes. *J. Chem. Phys.* **2006**, *125*, 014903.

(29) Olbrich, C.; Kleinekathöfer, U. Time-Dependent Atomistic View on the Electronic Relaxation in Light-Harvesting System II. *J. Phys. Chem. B* **2010**, *114*, 12427–12437.

(30) Olbrich, C.; Liebers, J.; Kleinekathöfer, U. Modeling of Light-Harvesting in Purple Bacteria Using a Time-Dependent Hamiltonian Approach. *Phys. Status Solidi B* **2011**, *248*, 393–398.

(31) Jansen, T. L. C.; Knoester, J. Nonadiabatic Effects in the Two-Dimensional Infrared Spectra of Peptides. *J. Phys. Chem. B* **2006**, *110*, 22910–22916.

(32) Jansen, T. L. C.; Knoester, J. Waiting Time Dynamics in Two-Dimensional Infrared Spectroscopy. *Acc. Chem. Res.* **2009**, *42*, 1405–1411.

(33) Adolphs, J.; Renger, T. How Proteins Trigger Excitation Energy Transfer in the FMO Complex of Green Sulfur Bacteria. *Biophys. J.* **2006**, *91*, 2778–2787.

(34) Cho, M.; Vaswani, H. M.; Brixner, T.; Stenger, J.; Fleming, G. R. Exciton Analysis in 2D Electronic Spectroscopy. *J. Phys. Chem. B* **2005**, *109*, 10542–56.

(35) Shim, S.; Rebentrost, P.; Valleau, S.; Aspuru-Guzik, A. Microscopic Origin of the Long-Lived Quantum Coherences in the Fenna−Matthew−Olson Complex. arXiv:1104.2943v1.

(36) Wanko, M.; Hoffmann, M.; Strodel, P.; Koslowski, A.; Thiel, W.; Neese, F.; Frauenheim, T.; Elstner, M. Calculating Absorption Shifts for Retinal Proteins: Computational Challenges. *J. Phys. Chem. B* **2005**, *109*, 3606.

(37) Mercer, I. P.; Gould, I. R.; Klug, D. R. Optical Properties of Solvated Molecules Calculated by QMMM Methods: Chlorophyll a and Bacteriochlorophyll a. *Faraday Discuss.* **1997**, *108*, 51–62.

(38) Walker, R. C.; Mercer, I. P.; Gould, I. R.; Klug, D. R. Comparison of Basis Set Effects and the Performance of Ab Initio and DFT Methods for Probing Equilibrium Fluctuations. *J. Comput. Chem.* **2007**, *28*, 478–480.

(39) Ceccarelli, M.; Procacci, P.; Marchi, M. An ab initio Force Field for the Cofactors of Bacterial Photosynthesis. *J. Comput. Chem.* **2003**, *24*, 129–132.

(40) May, V.; Kühn, O. *Charge and Energy Transfer in Molecular Systems*; Wiley-VCH: Berlin, Germany, 2000.

(41) Gutiérrez, R.; Caetano, R.; Woiczikowski, P. B.; Kubař, T.; Elstner, M.; Cuniberti, G. Structural Fluctuations and Quantum Transport Through DNA Molecular Wires: A Combined Molecular Dynamics and Model Hamiltonian Approach. *New J. Phys.* **2010**, *12*, 023022.

(42) Kubař, T.; Elstner, M. What Governs the Charge Transfer in DNA? The Role of DNA Conformation and Environment. *J. Phys. Chem. B* **2008**, *112*, 8788–8788.

(43) Zucchelli, G.; Jennings, R. C.; Garlaschi, F. M.; Cinque, G.; Bassi, R.; Cremonesi, O. The Calculated In Vitro and In Vivo Chlorophyll a Absorption Bandshape. *Biophys. J.* **2002**, *82*, 378–390.

(44) Yang, M.; Damjanović, A.; Vaswani, H. M.; Fleming, G. R. Energy Transfer in Photosystem I of Cyanobacteria Synechococcus elongatus: Model Study with Structure-Based Semi-Empirical Hamiltonian and Experimental Spectral Density. *Biophys. J.* **2003**, *85*, 140–158.

(45) Strümpfer, J.; Schulten, K. The Effect of Correlated Bath Fluctuations on Exciton Transfer. *J. Chem. Phys.* **2011**, *134*, 095102.

SUPPORTING INFORMATION

Theory and Simulation of the Environmental Effects

on FMO Spectral Transitions

Carsten Olbrich,[†] Johan Strümpfer,[‡] Klaus Schulten,[‡,¶] and Ulrich Kleinekathöfer[*,†]

School of Engineering and Science, Jacobs University Bremen, Campus Ring 1, 28759 Bremen, Germany, and Center for Biophysics and Computational Biology and Beckman Institute, University of Illinois at Urbana-Champaign, Urbana, Illinois 61801, USA

E-mail: u.kleinekathoefer@jacobs-university.de

---

[*]To whom correspondence should be addressed

[†]School of Engineering and Science, Jacobs University Bremen, Campus Ring 1, 28759 Bremen, Germany

[‡]Center for Biophysics and Computational Biology and Beckman Institute, University of Illinois at Urbana-Champaign, Urbana, Illinois 61801, USA

[¶]Department of Physics, University of Illinois at Urbana-Champaign, Urbana, Illinois 61801, USA

1

Table S1: Parameters of Fit 1 for the autocorrelation function based on the trimer simulations. The correlation functions are averaged over the equivalent pigments in the three monomers. (η_i in [10^{-5} eV^2], $1/\gamma_i$ in [fs], $2\pi/\omega_i$ in [fs])

	BChl 1	BChl 2	BChl 3	BChl 4	BChl 5	BChl 6	BChl 7	BChl 8	BChl 1-6
η_1	94.38	56.02	235.21	60.72	46.43	105.05	137.51	137.80	126.99
$1/\gamma_1$	84.41	59.65	13.83	66.59	61.47	9.05	56.58	82.93	11.54
η_2	15.51	15.43	11.45	13.60	8.62	30.25	88.69	28.05	31.70
$1/\gamma_2$	1337.24	560.08	260.99	496.99	545.35	128.39	382.66	1226.80	196.70
$\tilde{\eta}_1$	10.64	11.12	2.56	10.31	6.98	7.24	26.52	58.55	8.25
$2\pi/\tilde{\omega}_1$	18.37	18.41	18.40	18.42	18.38	18.40	18.37	23.14	18.39
$1/\tilde{\gamma}_1$	279.37	276.72	145.48	311.16	268.65	351.68	372.76	12.05	276.25
$\tilde{\eta}_2$	38.82	28.59	22.03	35.53	25.93	25.88	88.40	69.07	30.58
$2\pi/\tilde{\omega}_2$	19.03	19.10	18.99	19.06	19.06	19.05	19.04	18.98	19.05
$1/\tilde{\gamma}_2$	225.46	221.68	200.66	230.93	201.10	241.73	252.88	260.70	211.33
$\tilde{\eta}_3$	10.59	8.18	8.65	8.08	5.41	9.59	23.47	17.90	8.02
$2\pi/\tilde{\omega}_3$	19.70	19.78	19.70	19.73	19.74	19.72	19.71	19.70	19.73
$1/\tilde{\gamma}_3$	340.95	289.97	308.07	443.97	515.83	296.45	323.12	266.56	361.83
$\tilde{\eta}_4$	11.09	7.00	4.23	12.42	10.65	8.04	26.47	10.07	9.57
$2\pi/\tilde{\omega}_4$	20.78	20.84	20.84	20.82	20.84	20.84	20.85	20.93	20.82
$1/\tilde{\gamma}_4$	224.48	301.31	127.66	164.61	116.73	213.25	285.22	287.36	172.38
$\tilde{\eta}_5$	17.52	14.57	8.11	1.59	1.83	1.14	5.28	6.50	1.46
$2\pi/\tilde{\omega}_5$	22.84	22.84	23.01	22.68	22.64	22.65	22.70	22.77	22.67
$1/\tilde{\gamma}_5$	68.00	69.68	117.03	585.27	581.68	670.21	582.01	260.63	573.30
$\tilde{\eta}_6$	86.89	70.10	1.67	13.60	7.76	11.88	42.02	6.02	13.17
$2\pi/\tilde{\omega}_6$	46.29	69.58	28.62	23.29	23.14	22.98	23.24	23.64	23.15
$1/\tilde{\gamma}_6$	5.83	4.87	174.70	69.42	98.78	64.32	50.64	195.86	63.60
$\tilde{\eta}_7$	14.47	13.18	5.14	17.48	8.97	11.02	27.46	13.91	12.19
$2\pi/\tilde{\omega}_7$	30.12	30.38	30.53	30.18	30.48	30.32	29.81	30.10	30.32
$1/\tilde{\gamma}_7$	120.34	112.73	375.16	95.91	132.83	121.96	126.94	160.68	123.11
$\tilde{\eta}_8$	6.27	4.55	1.99	9.58	101.96	2.94	15.49	9.00	2.52
$2\pi/\tilde{\omega}_8$	46.27	46.08	46.83	46.20	76.27	46.40	45.65	45.78	46.43
$1/\tilde{\gamma}_8$	181.92	175.72	254.69	130.69	7.82	208.23	139.43	153.77	305.26
$\tilde{\eta}_9$	12.37	6.51	15.36	10.18	5.06	3.96	14.89	8.80	5.90
$2\pi/\tilde{\omega}_9$	55.93	55.18	56.13	55.73	54.57	55.50	55.50	55.47	55.42
$1/\tilde{\gamma}_9$	193.86	218.00	112.09	208.92	292.51	435.04	435.79	290.50	261.93
$\tilde{\eta}_{10}$	16.67	5.26	-34.13	42.02	4.01	1.14	20.39	140.04	1.06
$2\pi/\tilde{\omega}_{10}$	90.21	88.48	61.37	94.11	92.33	87.71	93.29	94.44	88.97
$1/\tilde{\gamma}_{10}$	118.30	205.43	36.57	41.92	204.55	311.06	204.99	18.33	515.31
$\tilde{\eta}_{11}$	1.77	1.33	0.90	3.52	0.81	1.25	3.70	0.90	1.36
$2\pi/\tilde{\omega}_{11}$	34.22	33.97	34.05	34.20	34.20	33.99	34.40	34.10	34.08
$1/\tilde{\gamma}_{11}$	302.12	313.57	406.85	209.79	507.23	527.23	213.24	389.37	405.65
$\tilde{\eta}_{12}$	3.42	7.86	2.96	39.39	0.28	0.76	142.27	1.67	0.31
$2\pi/\tilde{\omega}_{12}$	66.27	65.04	66.66	0.62	67.31	59.89	87.72	67.87	65.51
$1/\tilde{\gamma}_{12}$	164.24	98.05	225.19	0.20	712.71	559.97	14.82	614.49	433.44
$\tilde{\eta}_{13}$	18.41	13.75	-106.58	0.64	1.31	0.51	5.28	—	—
$2\pi/\tilde{\omega}_{13}$	162.41	1.69	213.20	69.40	146.95	134.29	140.09	—	—
$1/\tilde{\gamma}_{13}$	62.54	45.53	29.19	891.16	398.00	1859.97	267.13	—	—

2

Table S2: Parameters of Fit 1 for the autocorrelation function based on the monomer simulations. (η_i in $[10^{-5}\ \mathrm{eV}^2]$, $1/\gamma_i$ in [fs], $2\pi/\omega_i$ in [fs])

	BChl 1	BChl 2	BChl 3	BChl 4	BChl 5	BChl 6	BChl 7	BChl 1-7
η_1	177.06	104.81	137.08	43.41	200.91	78.49	221.67	148.53
$1/\gamma_1$	78.06	52.41	42.98	61.97	45.28	145.43	74.51	61.39
η_2	76.45	35.92	56.55	17.00	110.40		86.86	51.91
$1/\gamma_2$	745.75	626.10	368.87	282.95	216.72		545.86	459.07
$\tilde{\eta}_1$	18.43	53.89	88.28	14.54	20.88	12.60	13.34	12.94
$2\pi/\tilde{\omega}_1$	18.41	18.86	23.75	18.48	18.39	18.41	18.38	18.39
$1/\tilde{\gamma}_1$	301.02	89.49	10.75	167.74	331.98	320.42	646.60	324.65
$\tilde{\eta}_2$	76.97	6.86	62.73	18.53	90.56	41.95	106.04	62.03
$2\pi/\tilde{\omega}_2$	19.05	19.11	19.00	19.06	19.04	19.06	19.02	19.03
$1/\tilde{\gamma}_2$	199.80	793.56	309.46	314.22	219.29	231.09	244.41	236.43
$\tilde{\eta}_3$	10.23	8.73	17.56	9.66	13.64	11.03	14.94	13.45
$2\pi/\tilde{\omega}_3$	19.74	19.70	19.67	19.71	19.71	19.70	19.70	19.71
$1/\tilde{\gamma}_3$	331.76	280.17	400.44	274.29	401.43	312.99	604.04	351.36
$\tilde{\eta}_4$	29.64	9.16	7.40	10.75	29.21	13.83	18.70	17.45
$2\pi/\tilde{\omega}_4$	20.82	20.80	20.96	20.78	20.86	20.85	20.87	20.84
$1/\tilde{\gamma}_4$	215.80	235.79	426.27	140.93	209.86	222.98	460.86	241.92
$\tilde{\eta}_5$	6.29	9.26	11.84	3.56	3.96	12.50	9.81	23.22
$2\pi/\tilde{\omega}_5$	22.65	22.60	23.05	22.64	22.68	23.04	22.72	22.95
$1/\tilde{\gamma}_5$	363.81	133.40	100.95	379.80	726.48	85.14	243.97	78.20
$\tilde{\eta}_6$	21.74	5.34	0.46	7.78	33.39	3.78	97.48	84.58
$2\pi/\tilde{\omega}_6$	23.68	24.24	24.48	23.50	23.35	30.38	21.98	40.80
$1/\tilde{\gamma}_6$	77.57	110.77	1000.43	75.69	59.65	680.72	19.86	5.91
$\tilde{\eta}_7$	25.34	19.10	9.82	11.14	29.46	0.12	28.09	20.05
$2\pi/\tilde{\omega}_7$	29.81	30.16	30.47	30.32	29.96	43.65	30.05	30.07
$1/\tilde{\gamma}_7$	119.38	89.07	271.44	108.44	99.90	6079.25	124.18	111.36
$\tilde{\eta}_8$	7.55	2.71	21.36	2.50	87.34	4.31	30.36	14.32
$2\pi/\tilde{\omega}_8$	46.13	46.08	45.90	45.81	49.84	54.71	45.63	46.21
$1/\tilde{\gamma}_8$	209.01	367.75	73.61	453.77	25.26	512.15	74.39	104.06
$\tilde{\eta}_9$	8.33	4.99	13.04	12.40	11.30	195.16	13.33	12.42
$2\pi/\tilde{\omega}_9$	55.49	54.70	56.46	55.97	54.83	158.38	54.67	55.08
$1/\tilde{\gamma}_9$	384.95	520.63	199.80	111.83	569.13	8.29	439.30	268.65
$\tilde{\eta}_{10}$	210.62	4.56	21.89	9.34	46.96	3.14	125.58	24.30
$2\pi/\tilde{\omega}_{10}$	94.46	86.93	89.48	89.34	93.42	34.42	100.80	91.03
$1/\tilde{\gamma}_{10}$	15.72	386.51	89.06	133.05	79.03	9.51	34.60	104.30
$\tilde{\eta}_{11}$	1.43	0.29	3.28	2.49	2.79		4.68	2.04
$2\pi/\tilde{\omega}_{11}$	34.16	34.31	33.91	34.13	34.64		34.82	34.30
$1/\tilde{\gamma}_{11}$	472.09	1853.64	278.96	238.44	325.65		130.24	298.10
$\tilde{\eta}_{12}$		95.94	7.28	74.93	0.75		3.21	9.51
$2\pi/\tilde{\omega}_{12}$		65.93	66.84	92.38	67.43		66.34	66.48
$1/\tilde{\gamma}_{12}$		13.46	195.12	5.41	497.02		483.19	111.20
$\tilde{\eta}_{13}$		8.03	7.39	5.64				15.19
$2\pi/\tilde{\omega}_{13}$		116.70	125.06	137.28				136.86
$1/\tilde{\gamma}_{13}$		101.28	191.24	151.85				89.74

3

Table S3: Parameters of Fit 2 for the autocorrelation function based on the monomer simulations. (η_i in [10^{-5} eV^2], 1/γ_i in [fs], $2\pi/\omega_i$ in [fs])

	BChl. 1	BChl. 2	BChl. 3	BChl. 4	BChl. 5	BChl. 6	BChl. 7	BChl. 1-7
η_1	491.64	295.89	364.10	204.54	487.06	287.27	561.58	384.25
$1/\gamma_1$	5.81	5.77	4.72	4.01	4.45	4.07	4.68	4.73
η_2	167.11	70.73	102.17	40.90	205.10	82.87	209.87	126.25
$1/\gamma_2$	234.37	236.39	196.63	149.54	136.57	138.28	201.40	179.56

4
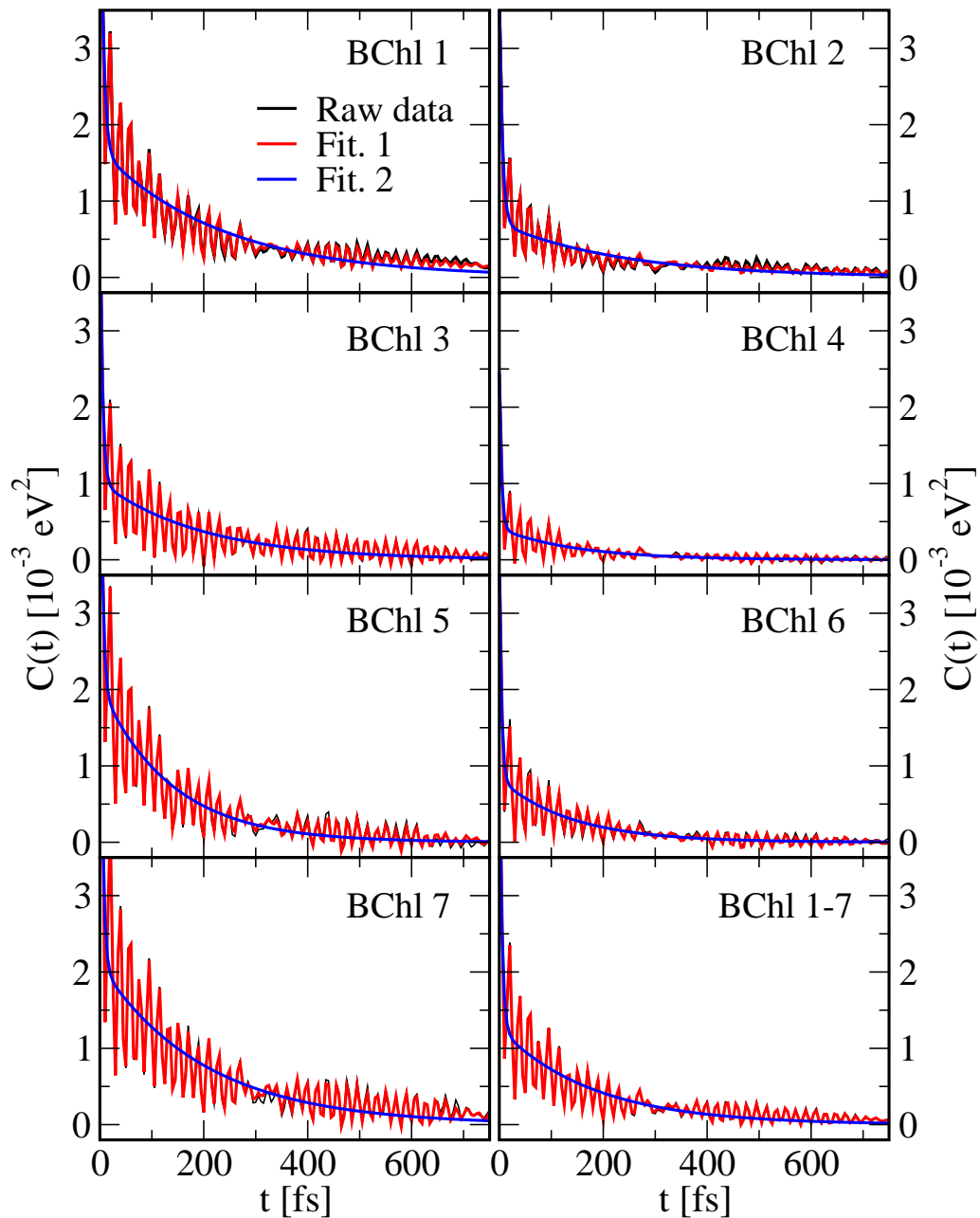
Figure S1: Autocorrelation functions for the FMO monomer complex (simulation results, Fit 1 and Fit 2) for each BChl and an averaged autocorrelation function of all BChls.
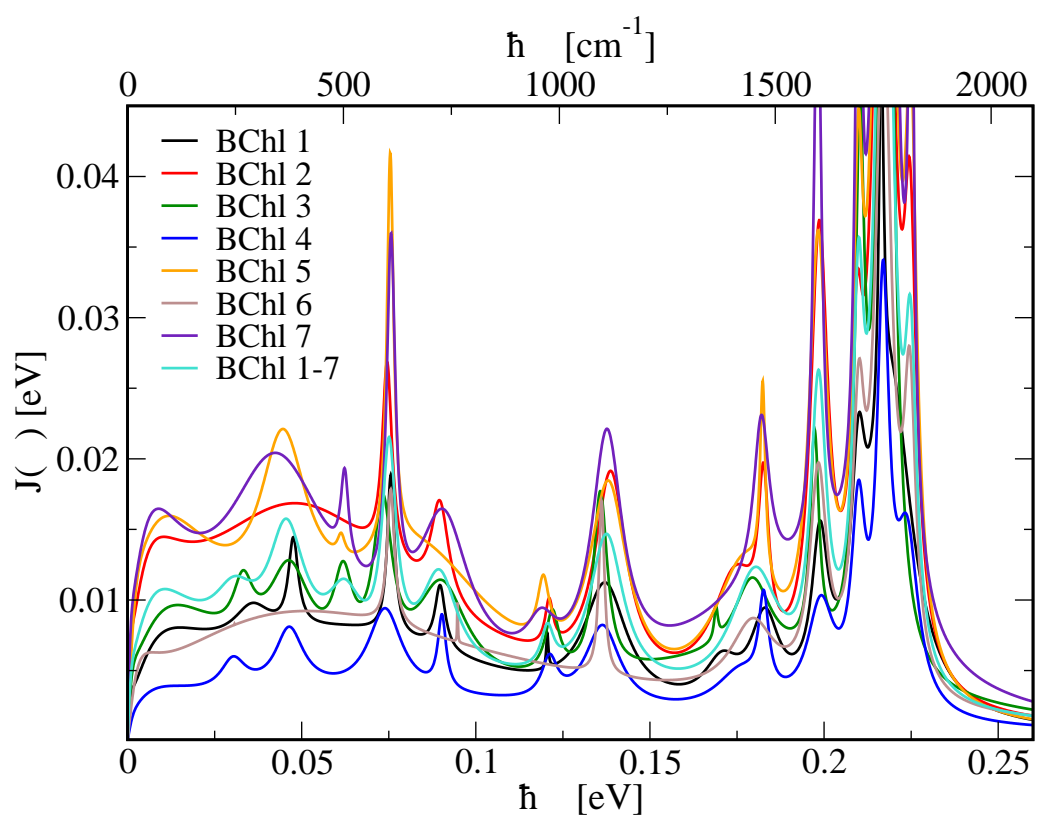
5

Figure S2: Spectral densities belonging to the FMO monomer complex as calculated via Fit 1 for each BChl and an averaged spectral density of all BChls.
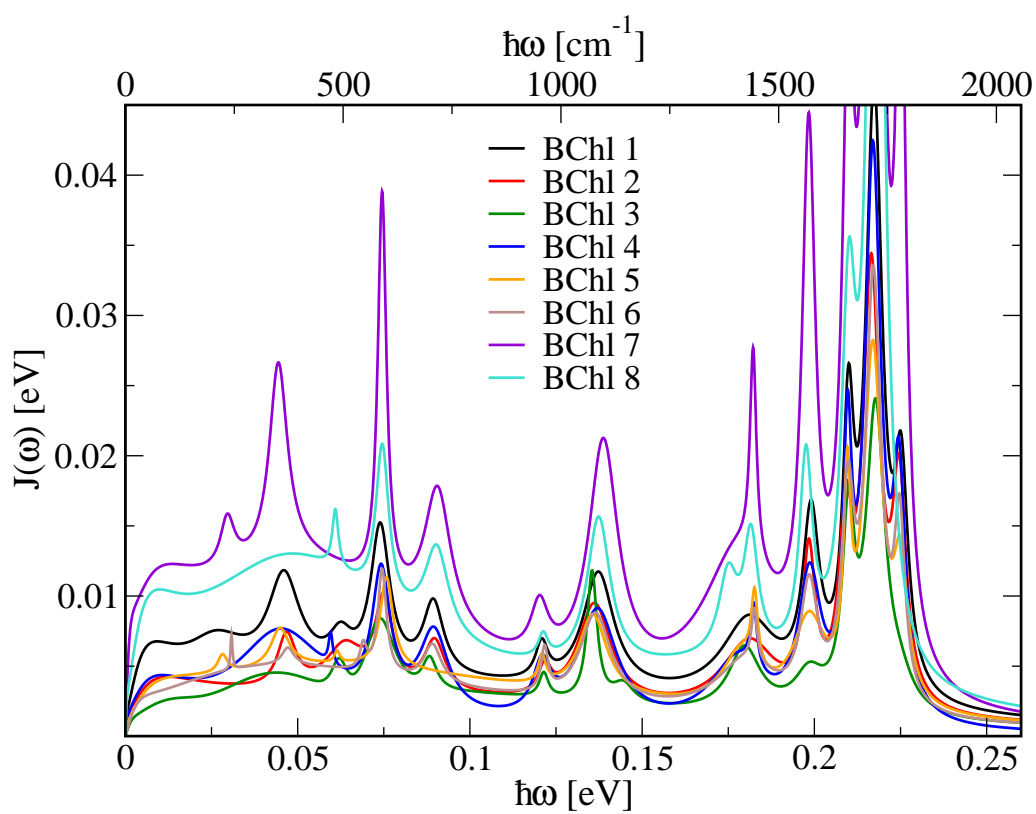
6

Figure S3: Spectral densities as calculated via Fit 1 for each BChl of the FMO trimer complex.

7

A. DNA-Binding Protein TmHU

My studies towards the present thesis were mainly focused on LH systems. However, beside the LH systems and motivated by experimental collaborators we investigated the compaction of DNA by the HU protein from *Thermotoga maritima* (TmHU). The HU proteins are histone-like proteins which can be found in bacteria, bacteriophages, and chloroplasts. Beside their main tasks of DNA condensation and packing, HU proteins play an essential role in the DNA replication, transcription and transposition.

The following publication presents a combined study including experimental methods and theoretical modeling, i.e., classical MD simulations. On the experimental side, the shortening of the end-to-end distance of the DNA was investigated according to the concentration of TmHU proteins and a applied counteracting force. To this end, optical tweezers were employed and two levels of formation of higher structural organization detected. Furthermore, the shape of the condensed TmHU/DNA complexes were analyzed by the atomic force microscope. My contribution to the aforementioned investigations was the modeling of the reverse process, i.e., the unbinding of the DNA from the TmHU protein using MD simulations. The simulations on the unbinding process had been motivated by an earlier work of Mathias Salomon *et al.* (see Ref. 29 in the following publication). Therein, a condensed DNA strand including bound TmHU proteins was stretched using optical tweezers. In contrast to stretching a bare DNA, distinct events in the force measurements were observed which were assigned to the disruption of a single TmHU proteins from the DNA. To this end, the MD simulation setup included a water box containing a 35 base pairs long DNA strand which was wrapped around a single TmHU protein. Subsequent to the equilibration, the termini of the DNA were pulled away from the TmHU protein in opposite directions. Hence, two force-distance dependencies were obtained and both show distinct signals when the respective part

of the DNA disrupts from the TmHU protein. The obtained results from this MD simulation are in good agreement with the aforementioned experimental motivation and match well with the first level of formation belonging to a higher structural organization (see above).

ORIGINAL   PAPER

DNA condensation by TmHU studied by optical tweezers, AFM and molecular dynamics simulations

**Carolin Wagner · Carsten Olbrich · Hergen Brutzer · Mathias Salomo ·
Ulrich Kleinekathöfer · Ulrich F. Keyser · Friedrich Kremer**

Abstract The compaction of DNA by the HU protein from *Thermotoga maritima* (TmHU)
is analysed on a single-molecule level by the usage of an optical tweezers-assisted force
clamp. The condensation reaction is investigated at forces between 2 and 40 pN applied to
the ends of the DNA as well as in dependence on the TmHU concentration. At 2 and 5 pN,
the DNA compaction down to 30% of the initial end-to-end distance takes place in two
regimes. Increasing the force changes the progression of the reaction until almost nothing
is observed at 40 pN. Based on the results of steered molecular dynamics simulations, the
first regime of the length reduction is assigned to a primary level of DNA compaction by
TmHU. The second one is supposed to correspond to the formation of higher levels of
structural organisation. These findings are supported by results obtained by atomic force
microscopy.

C. Wagner · F. Kremer
Experimental Physics 1, University of Leipzig, 04103, Leipzig, Germany

C. Olbrich · U. Kleinekathöfer
School of Engineering and Science, Jacobs University Bremen, 28759, Bremen, Germany

H. Brutzer
Biotechnology Center, TU Dresden, 01307, Dresden, Germany

M. Salomo
c-LEcta GmbH, Leipzig, 04103, Leipzig, Germany

U. F. Keyser
Cavendish Laboratory, Biological and Soft Systems, University of Cambridge, CB3 0HE,
Cambridge, UK

C. Wagner ( )
Molecular Physics, Experimental Physics I, University of Leipzig, Linnéstr. 5, 04103,
Leipzig, Germany
e-mail: Carolin.wagner@physik.uni-leipzig.de

Abbreviations

TmHU   histone-like protein from *Thermotoga maritima*;
bp   basepairs;
Da   Dalton

1 Introduction

The prokaryotic genome is not imbedded in a cellular compartment like the eukaryotic nucleus, but is arranged in a highly compacted way in a particular region of the cytoplasm called the nucleoid. The mechanisms that account for this compaction are DNA super-coiling, macromolecular crowding and the action of nucleoid-associated proteins, but their relative contributions are still unclear [1]. The genome of the hyperthermophilic bacterium *Thermotoga maritima*, which appears as one circular chromosome, amounts to 1,860,725 bp corresponding to a circumference of ∼630 μm [2]. A single *T. maritima* organism has a rod-like shape with an average length of 5 μm [3], implying a micrometre-sized nucleoid. These dimensions underline the importance of powerful mechanisms of compaction that make such a dense packing possible but yet ensure the flexibility to accomplish transcription and replication.

About a dozen proteins, like the histone-like nucleoid structuring protein (H-NS), heat unstable protein (HU), DNA protection during starvation (Dps) and integration host factor (IHF) associate with the nucleoid of the mesophilic bacterium *Escherichia coli* [1]. Similar proteins are believed to play a role in other organisms. However, little is known about the compaction and organisation of the DNA in *T. maritima*, since it does not encode homologs of IHF, Dps or H-NS [4]. The histone-like protein HU, which is nearly ubiquitous in all bacteria, has been found to alter the structure of DNA by introducing kinks and bends [5, 6]. The HU protein of *E. coli* is quite well characterised. It acts on the DNA in an opposed modality: the complex forms stiff filaments without condensation at high protein concentrations whereas at low concentrations the DNA is compacted to 50% of its initial length [7]. Despite the increasing knowledge about DNA compaction in bacteria, it has to be noted that the nature of the contribution of HU proteins to nucleoid structure is still under discussion [8]. Recent reviews by Dame et al. [1] and Luijsterburg et al. [9] describe in detail the current state of knowledge on the contribution of nucleoid-associated proteins to the nucleoid structure. It is supposed that DNA-bending proteins, to which HU proteins belong, do not only play a role in compacting DNA but also have the ability to remodel bacterial chromatin by dislocating the arrangement of loops. However, none of the nucleoid-associated proteins is solely responsible for the organisation of bacterial chromatin. This is corroborated by the fact that bacterial cells that are deficient in one of the nucleoid-associated proteins were usually found to be viable, which suggests that the function of one of those proteins can be taken over by another. Thus, the organisation of bacterial chromatin is rather a matter of an interplay of different proteins that co-operate, compete and also antagonise each other.

Here we concentrate on the role of the HU protein of *T. maritima* (TmHU). In its functional form TmHU is composed of two identical subunits with a molecular weight of 9,994.0 Da each. These form a core part with two protruding beta-ribbon arms [5]. TmHU

has the ability to tightly bind DNA ($K_d = 5.6$ nM) without a detectable sequence specificity [10]. X-ray studies and structure modelling show that the DNA is bent around the protein dimer with an angle of ~160° with the emerging beta-ribbon arms embracing the DNA. The binding leads to a compaction of the double-stranded DNA [5, 11]. Furthermore, TmHU is extraordinarily stable at high temperatures as thermal denaturation of the secondary structure occurs well above 96°C and is nearly completely reversible. One suggested major task of TmHU is to protect the DNA of *T. maritima* against thermal denaturation [5]. With an optimum growth temperature of about 80°C, the organism is adapted to its habitat on the geothermally heated sea floors in Italy and the Azores [3].

Optical tweezers provide an extraordinary technique for the investigation of the interactions between biological macromolecules on a single-molecule level [12] as they allow for positioning a micron-sized particle with nanometre resolution and measuring the forces acting on it with an accuracy of ~50 fN. Using this technique, the elastic properties of double-stranded DNA have been characterised [13–15] as well as their dependence on the ionic conditions [16]. Furthermore, the interaction of DNA molecules with binding partners like transcription factors [17] or intercalating dyes [18] has been studied. Other work investigates antigen–antibody interaction [19], RNA folding [20, 21] and individual steps of single-kinesin motor proteins [22, 23]. Wen et al. observed the translation at a ribosome on the level of single codons [24]. Particularly the investigation of architectural proteins binding to DNA is an ongoing topic of special interest. By stretching single chromatin fibres, histone proteins can be dissociated from the DNA. The force–distance dependence shows a saw-tooth-pattern whose distinct events are interpreted in terms of single DNA/histone complexes being destabilised [25–27]. Dame et al. observed directly the bridging of two DNA duplexes by H-NS employing a quadrupole trap in order to clamp two DNA duplexes [28].

The interaction of TmHU with a single double-stranded DNA molecule has recently been investigated by optical tweezers [29]. We observed a shortening of the contour length accompanied by a steep force increase up to ~30 pN where the reaction was inhibited. Investigating the effects of varying protein concentration yielded information about the kinetics of the reaction [30]. As a further refinement, our set-up is now furnished with a force feedback loop, allowing us to keep the force constant during the experiment. In the present work, the condensation reaction under the action of a constant force is investigated at different force levels, amongst others with regard to the question of whether the final TmHU/DNA complex builds up in different organisational levels. Furthermore, the influence of the protein concentration is analysed. The results are confirmed by measurements with atomic force microscopy (AFM). Finally, steered molecular dynamics (SMD) simulations provide a molecular view of the disassembly of a single TmHU/DNA complex when it is stretched.

2 Materials and methods

2.1 Optical tweezers setup

The force on a single DNA molecule is set and controlled by optical tweezers with video-based force feedback. We create the optical trap with a diode-pumped Nd:YAG laser (1,064 nm, 1 W, LCS-DTL 322; Laser 2000, Wessling, Germany) coupled into a commercial microscope (Axiovert S 100 TV, Carl Zeiss, Jena, Germany). A PID-controller stabilises the

power output of the laser. After passing an optical isolator a quarter-wave plate is employed to produce circular polarised light to exclude effects due to reflection differences between the p and s parts of the laser light. The beam is expanded and coupled into the back aperture of the microscope objective (Plan-Neofluor 100×1.30 Oil, Carl Zeiss, Jena, Germany). Video imaging and optical position detection are accomplished by a charge-coupled device digital camera (Dalsa, Munich, Germany). During the measurements we acquire images with a camera at a frequency of up to 60 frames per second. The microparticle position is extracted on-line from the obtained images via image analysis as described by Otto et al. [31]. The precision in the position determination in the relevant axes x and y is ± 2 nm. In order to hold the force at a constant level during the experiment, a LabView-based PID-control (force clamp) with a regulation frequency of up to 30 Hz is employed. The optical stage can be positioned in three dimensions with nanometre resolution using piezoactuators (P-5173CD, PI; Karlsruhe, Germany). The sample cell with a volume of ~ 300 μl consists of a stainless steel corpus, which is covered at the top and at the bottom by glass coverslips. A custom-made micropipette with an inner diameter at the tip of <1 μm is inserted into the chamber to hold one microparticle by capillary action. Additional inlets and outlets enable flushing the cell with buffer or protein solution using a syringe pump. The whole experimental set-up is situated in a temperature-controlled (± 1 K) room.

2.2 Sample preparation

All measurements are carried out in 10 mM phosphate buffer (pH 7.0) with a sodium chloride concentration of 20 mM. For the experiments, a DNA molecule is immobilised between two polystyrene microparticles (diameter 2.0 μm) via streptavidin/biotin and digoxigenin/anti-digoxigenin (anti-DIG) interaction. The double-stranded 4,000-bp long DNA is amplified from the plasmid pET28a+ via polymerase chain reaction (PCR) and labelled with digoxigenin and biotin, respectively, at their termini via 5′-end modifications of the primers (Metabion, Matinsried, Germany) that are used for PCR. The obtained DNA molecules are immobilised on the surface of streptavidin-coated microparticles (diameter 2.0 μm, Polysciences Europe, Eppelheim, Germany) with a density of 150 molecules per particle.

The anti-DIG covered particles are made by coating carboxylated microparticles (G. Kisker GbR, Steinfurt, Germany) with anti-DIG antibodies. The preparation of the microparticles and the synthesis and immobilisation of the DNA molecules are carried out according a protocol developed by Salomo et al. [29].

2.3 Experimental procedure

In order to establish a single DNA duplex, the particle with anti-DIG antibodies is captured by the optical trap and brought in contact with the tip of the micropipette where it is immobilised by capillary forces. Afterwards a second particle (coated with streptavidin and covered with DNA) is trapped by the optical tweezers and brought into the immediate neighbourhood of the anti-DIG-particle so that a visible distance between the particles remains. The binding is established when the particle in the optical trap is slightly pulled out of the focus while retracting the particle at the micropipette. To ensure that only one chain is linked between the two particles, a force–distance dependence of unmodified DNA is recorded (data not shown). After these initial tests, the TmHU protein is flushed into the

sample cell with varying concentrations, while the force on the double-stranded DNA is held constant. The condensation of the DNA is recorded by on-line video detection.

2.4 Atomic force microscopy

TmHU–DNA binding reactions were performed on the mica surface while still in solution. Samples for AFM imaging were prepared by depositing 5 μl of a solution containing 5 ng of DNA, 15 mM MgCl$_2$ and phosphate buffer with 20 mM NaCl (pH 7.0) onto flat freshly cleaved mica. After 2 min, another droplet of 5 μl was added to the one on the surface containing the desired TmHU concentration and 15 mM MgCl$_2$ in the same buffer. The protein concentration values (20–100 μg/ml) refer to the one in the final volume (10 μl). Due to the short incubation time evaporation was not an issue. Various incubation times after mixing were tested, however, and no notable difference for longer times than 5 min was observed. After the binding reaction, the sample was washed with DI-filtered water and blown dry in a gentle stream of nitrogen gas. Samples were imaged at 1.95 nm per pixel resolution in air at room temperature and humidity using tapping mode imaging (cantilever stiffness between 27 and 59 N/m, Nanosensors, Neuchatel, Switzerland) to minimise sample-tip interactions with a Dimension 3000 system with a Nanoscope IIIa controller (Veeco Instruments, Santa Barbara, CA, USA). Image processing including flattening was done using WSxM freeware (www.nanotec.es). AFM imaging was always performed right after the mica had been dried. All experiments were repeated at least three times with new samples on different days to check for reproducibility.

2.5 Molecular model and simulation setup

The SMD[34] simulation is based on the crystal structures of a single TmHU (PDB entry: 1B8Z), which only contains the residues 1 to 52 and 76 to 90 [32]. The missing beta-ribbon arms were added by homology modelling based on the related HU protein of *Anabaena* (AHU, PDB entry: 1P71) [6]. The latter was resolved including the beta-ribbon arms and a pre-bended 19-bp long double-stranded DNA. The DNA from the AHU structure was extended to a total number of 35 bp with the sequence GCCAAAAAATGCAA-CAATTTGTTGCATTTTTTGGC. The middle part of this sequence results from the crystal structure while the rest of the sequence was taken from a computer model of an equilibrated DNA strand added in a quasi-symmetric fashion.

Both the protruding beta-ribbon arms and the DNA, were then combined with the crystal structure of TmHU. Together with approximately 26,500 water molecules, the system fills a rectangular box of about $6 \times 18 \times 8.5$ nm^3. To neutralise the system, 42 Na$^+$ ions were added.

The simulation is performed using NAMD 2.6 [33] together with the CHARMM27 [34] force field, a time step of 1 fs and the PME method for calculating the long-range electrostatic interactions. After an energy minimisation, an equilibration run has been performed at 300 K in a NpT ensemble for 2 ns. Already after 500 ps no large change of the RMSD remains visible. The subsequent 30 ns stretching simulation of the DNA/TmHU complex took place in an NVT ensemble. During this process the protein was kept in place by a cylindrical potential encompassing the helical body only, i.e. the arms of the protein were not constrained. This additional potential is necessary in order to keep the protein in place while stretching the DNA. At the same time the TmHU is kept as flexible as possible

during the simulation. Both free ends of the DNA were pulled away from the protein (in $\pm x$ direction) with a spring constant of 70 pN/nm and a constant velocity of 0.5 m/s. It should be pointed out that the stretching velocity in the experiment is only 5 nm/s. Using the latter velocity would lead to simulation times for the complete process that cannot be covered by current atomistic simulations.

3 Results

In Fig. 1, we show three typical results for the condensation of DNA by TmHU. The DNA with a length of 4,000 bp ($\cong$1.36 μm) is held with a constant force of 2 pN while the protein solution at a concentration of 100 μg/ml is flushed into the sample cell. The force–distance curve of the DNA shows, according to the wormlike chain model, a steep slope for forces higher than 1–2 pN [15]. Thus, every change in force due to protein bindings results in an easily detectable change in length of the DNA. Therefore, a level of 2 pN has been determined as the lowest value to enable the feedback loop to hold the force stable at a preset value. The measurement is carried out while flushing the cell with protein solution perpendicular to the spanned DNA. The influence of the resulting drag force is found to be negligible due to the design of our flow cell with a height of approximately 2 mm, where the inlets and outlets are on a different level than the trapped colloid.

As seen in Fig. 1, the condensation reaction starts after a lag-time of several seconds. The moment of $t = 0$ was located about 10 s before the reaction starts, as the time delay between
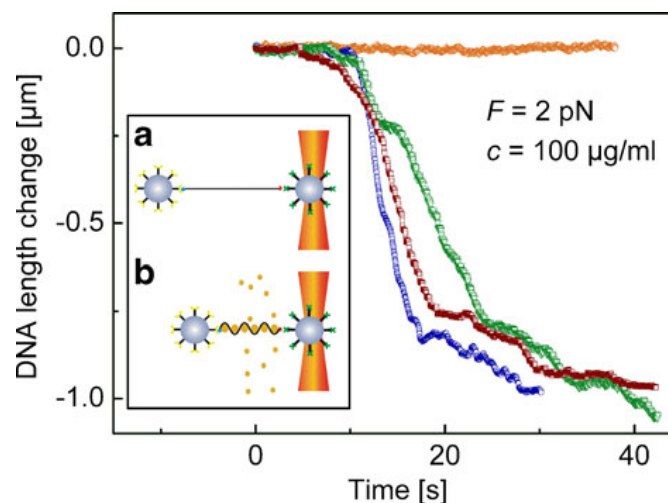

Fig. 1 Condensation reaction at 2 pN. Three typical results for the condensation of DNA by TmHU at a force level of 2 pN with a protein concentration of 100 μg/ml (*blue, red, green*) and a control trace of DNA in the absence of TmHU (*orange*) are displayed. The DNA duplex is hold at a constant force level (± 0.4 pN) while the protein solution is flushed in. The change in length of the DNA under the action of TmHU is recorded, which is defined as the difference to the plateau at $t = 0$–10 s. The moment of $t = 0$ was located about 10 s before the reaction starts. We distinguish two regimes during the reaction, the initial one, where shortening happens linearly with a rate of (70 ± 30) nm/s until a shortening of (0.77 ± 0.12) μm is reached, and the subsequent condensation (for $t > 10$ s) that proceeds at a much slower rate and is less continuous. The reaction comes to a halt at approximately 1 μm shortening. *Inset* shows the scheme of the experiment. (*a*) A single double-stranded DNA is immobilised between two microparticles. One of them is held by the optical trap with a constant force while the other is fixed at the micropipette tip. (*b*) After flushing the protein solution into the sample chamber the condensation of the DNA can be observed

starting the syringe pump and the beginning of the condensation varies significantly due to our setup and the flow cell design. The shortening of the DNA is defined as the change of the end-to-end distance compared to the plateau at $t = 0$–10 s. We distinguish two regimes during the reaction. Initially, the reduction in length happens fast with a rate of (70 ± 30) nm/s until a shortening of (0.77 ± 0.12) μm is reached. The subsequent condensation (for $t > 10$ s) proceeds at a much slower rate and less continuously until the reaction comes to a halt at approximately 1 μm shortening, which corresponds to ∼70% of the initial end-to-end distance of the DNA. All measurements were performed with a new pair of microparticles.

Figure 2 shows the shortening of the DNA due to the binding of TmHU as a function of the applied force. The condensation was carried out at a protein concentration of 100 μg/ml. We detect shortening of the DNA up to a pre-stretching of 40 pN. The maximal change in length decreases exponentially from ∼1 μm (2 pN) to ∼60 nm (40 pN; Fig. 2, inset). The proceeding of the reaction depends on the applied force and, in contrast to the case for 2 pN, above 10 pN no slow shortening is observed.

Furthermore, the influence of TmHU concentration on the DNA condensation at a constant force is investigated. Figure 3 depicts typical results for TmHU concentrations ranging from 20 to 250 μg/ml at a force level of 2 pN. The rate of condensation is defined as the change in DNA length per time between the plateau at $t = 0$ s and the level of 0.5 μm. This level is reached in all experiments at forces lower than 10 pN. The TmHU concentration has a significant impact on the rate of DNA condensation. At concentrations above 50 μg/ml, the DNA shortening up to 0.77 μm is a continuous process with a rate of (70 ± 30) nm/s. At lower protein concentrations the condensation advances much slower and finally reaches a minimum rate of (10 ± 5) nm/s at 20 μg/ml (Fig. 3). Furthermore, the condensation process is less continuous, and is interrupted by pauses. Both the total reduction in length and the rates are shown as a function of protein concentration in the insets of Fig. 3. The dots indicate the averages over all data points at the respective concentration. For concentrations below 20 μg/ml no shortening of the DNA could be observed on the time scale of several minutes. During the whole time protein solution was flushed in continuously. Working in continuous flow ensures that non-specific adhesion

Fig. 2 Force dependence of the condensation reaction. The TmHU-induced condensation of the DNA at different force levels is displayed. With increasing force, the shortening decreases significantly, until at 40 pN almost no condensation is taking place. In contrast to the case for 2 pN, above 10 pN no slow shortening is observed. *Inset* shows mean shortening at different forces. The *error bars* indicate minimal and maximal values
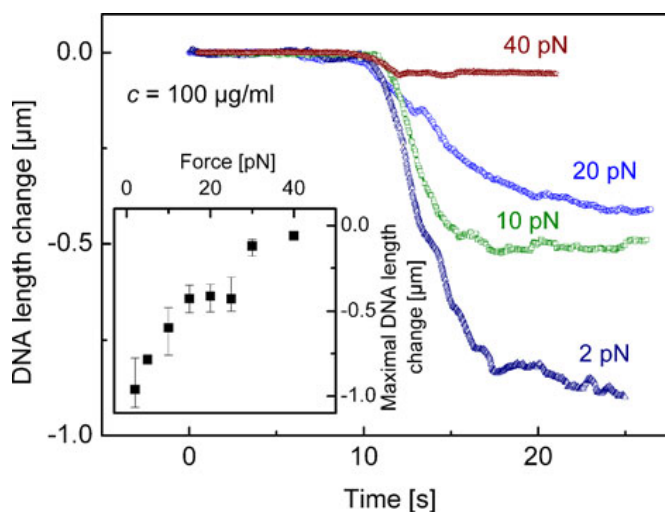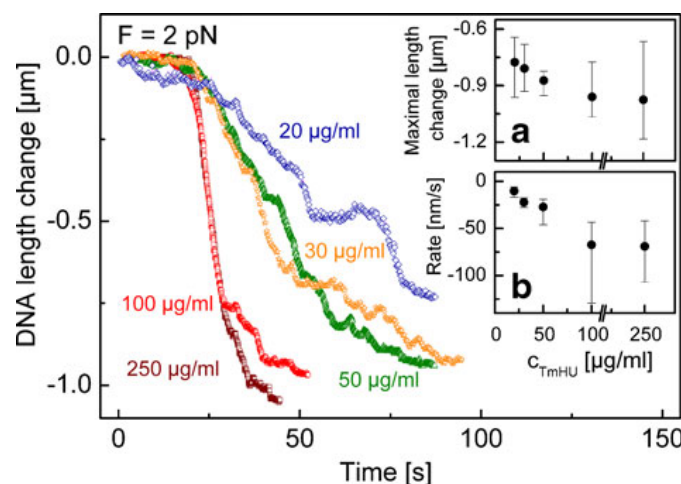
Fig. 3 Concentration dependence of the condensation reaction. The condensation of DNA by TmHU at a force of 2 pN is compared for concentrations between 250 and 20 μg/ml. At smaller protein concentrations the reduction in length proceeds slower and less linearly. *Insets* show the mean values of at least five single measurements of (*a*) the total reduction in length and (*b*) the condensation rate to a shortening of 0.5 μm. The *error bars* are given by minimal and maximal values. Both rate and final extension increase with increasing concentration. At 100 μg/ml, a saturation is observed

to the sample chamber does not inhibit the reaction. However, it has to be noted that the applied tension of 2 pN might be sufficient to impede detectable binding.

Additionally, the TmHU/DNA complex was investigated by AFM. A distinct dependence of the shape of the protein complexes on the protein concentration is found. Figure 4 compares bare DNA (250 bp) with the TmHU/DNA complex at TmHU concentrations of 20 and 100 μg/ml. The bare DNA shows, with the mean end-to-end distance of 70 nm,

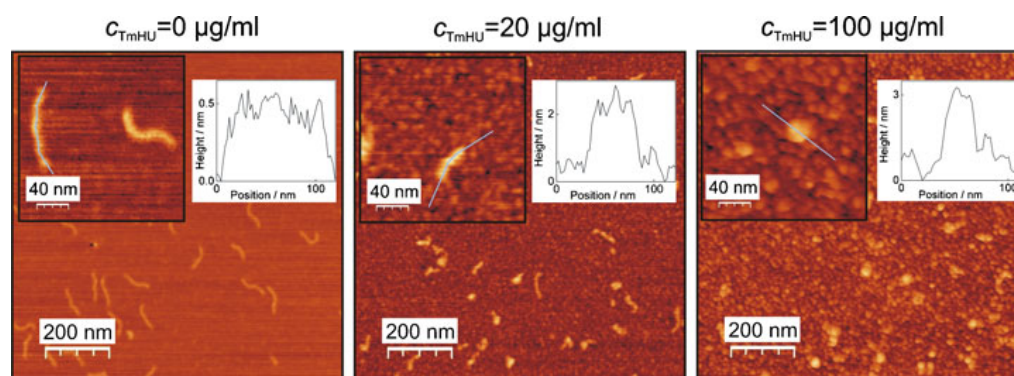**Fig. 4** Condensation of DNA (250 bp) by TmHU observed by AFM at TmHU concentrations of 0 mg/ml, 20 μg/ml and 100 μg/ml. The results presented here are representative for the 30–100 individual complexes that were analysed for each concentration. *Insets* show zooming in and height profile along the *blue line*. *Left* AFM image of double-stranded DNA (250 bp). The DNA shows an extended shape with mean end-to-end distance of 70 nm. The height profile displays a value around 0.5 nm. *Middle* at 20 μg/ml, the complexes still show an extended shape with a mean end-to-end distance of 42 nm. However, the height of the complex is here almost 2 nm. *Right* the structure of the complexes at 100 μg/ml is highly condensed and has a globular shape with a diameter of 38 nm

an extended shape and a height around 0.5 nm. At a TmHU concentration of 20 μg/ml the complex height is increased to ~2 nm. Although the end-to-end distance is reduced to 42 nm on average, the complex still shows an extended shape. At the higher concentration of 100 μg/ml, condensed complexes with globular shape and a diameter of 38 nm are formed, which is another clear indication for a second organisational level.

In addition to the experimental observations, we present here the results of SMD simulations of the stretching of a single TmHU/DNA complex. Salomo et al. observed events of the size of 2–3 nm while stretching a DNA duplex after incubation with TmHU. These events were assigned to the disruption of single TmHU proteins from DNA by comparison with a structural model [29]. SMD simulations allow us to gain valuable insight into the complex dynamics of this unbinding process. As shown in Fig. 5A, forces pointing into opposite directions were applied to both DNA tails contacting a single TmHU protein during a constant velocity simulation. In such a simulation a certain set of atoms is harmonically constrained to a reference point that moves with constant velocity. The DNA has a kinked conformation and is bound to the helical body of the protein (Fig. 5A). From those binding positions, one obtains an effective binding length of 22 bp for the DNA embracing the protein. One can subdivide the simulation into three parts. During the first third of the simulation the force increases almost linearly with the distance between the DNA tails until a force of roughly 180 pN is reached. The DNA remains bound to the helical body of the protein. In the second part of the simulation the unbinding of the DNA from the helical body of the protein takes place. As shown in the graph of Fig. 5B, this may happen in an asymmetric fashion. The thermal fluctuations also present in the simulation
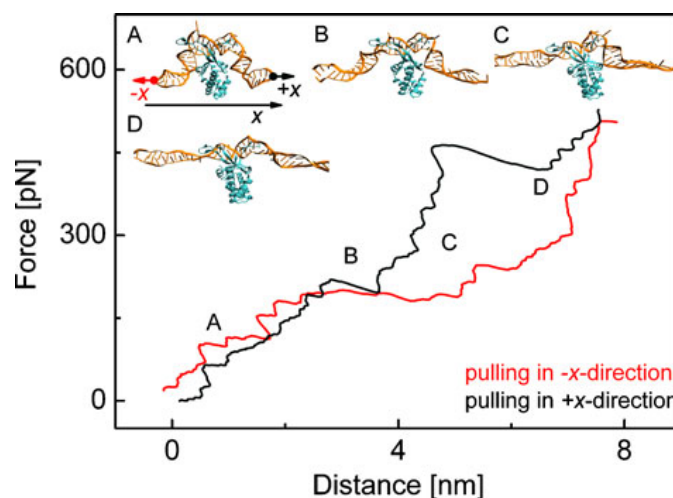

Fig. 5 Force–distance dependence of the SMD-simulated stretching of the TmHU–DNA complex. The 35 bp DNA is stretched with a velocity of 0.5 m/s with a force constant of 70 pN/nm. The snapshots *A–D* show the rupture of bonds between the DNA and the protein. The corresponding parts of the force–distance trace are indicated. *A* Snapshot at $t = 7.5$ ns. The *arrows* indicate the two resulting forces pointing in opposite directions. The force increases almost linearly with the distance of the DNA ends to the protein. The DNA sticks to both sides of the protein. *B* Snapshot at $t = 11.0$ ns. The DNA is disrupted from the left side of the helical body of the protein, which leads to an increase in distance of about 2 nm. Simultaneously, an unwinding of both DNA tails takes place, which yields an additional extension of ~1 nm each. *C* Snapshot at $t = 20.25$ ns. At around 500 pN, the right part of the DNA unbinds from the body of the protein and relaxes for another 2 nm. *D* Snapshot at $t = 25.0$ ns. Both DNA ends are released from the protein and are stretched further

comprise a stochastic element and determine, together with the initial conditions of the simulation, whether the DNA disrupts first only from one side of the protein or from both sides at the same time. For the present simulation, the part of the DNA on the right hand side of the protein remains in contact, while the DNA part on the other side detaches from the protein (Fig. 5B). During this disruption event the distance between the left DNA tail and the protein increases by about 2 nm. At the same time an unwinding of both DNA tails takes place resulting in an additional extension. The unwinding is possible since the forces are only applied to the centres of mass of certain atom selections and is indeed the reason for the first plateau in the force-distance curve between 2.7 and 3.7 nm for the DNA part pulled in the positive x direction. Furthermore, one can see in the force–distance curve as well as in Fig. 5C that the interaction between the DNA and the protein on the right hand side is so strong that the force increases up to values of 500 pN. As expected for these large forces [35], an unwinding of the DNA together with a structural change to a ladder conformation is observed. The reason for this tight binding between DNA and protein is strongly related to the residues LYS41, GLY46, LYS80 and LYS83 of the protein, which interact with the DNA backbone through hydrogen bonds. The residue LYS83 is initially positioned parallel to the backbone of the DNA and in this way stabilises the binding to the DNA. Towards the end of the simulation this part of the DNA also unbinds from the body of the protein and relaxes again for another 2 nm as can be identified by the second plateau for the DNA tail pulled in the $+x$ direction between 4.6 and 6.6 nm (Fig. 5D). This stretching corresponds to the length between the initial binding position of the beta-ribbon arms at the helical body of the protein and the midpoint between the arms. Prior to the just described rupture event, the structure of the DNA between the two protruding beta-ribbon arms is not degenerated. In the final part of the simulation both DNA tails are unbound from the helical body of the protein and stretched further. At this point the two curves in Fig. 5 again show a similar behaviour with increasing force. Moreover, the part of the DNA between the arms is stretched further in a similar fashion. One should note that also in the final part of the simulation the DNA is still connected to the protein at the midpoint between the arms.

4 Discussion

The condensation reaction at 2 pN is found to take place in two regimes. The first one leads to a shortening of 0.77 μm, after which the compaction continues much slower to the final length reduction of 1 μm. From the literature as well as from our present SMD simulation we obtain quantitative information concerning the binding length and the reduction in length due to the binding of one protein to DNA. Therefore, it is possible to estimate a shortening which can then be related to the observed value, in order to assign the regimes to a certain binding mode. It is known from X-ray studies and structural modelling that, as depicted above and displayed in Fig. 5, the DNA is bent around a TmHU protein in an arc [5, 11]. In the common model for a complex with more than one protein binding to DNA, the proteins arrange antiparallel, partly sandwiching the DNA as shown in Fig. 6 [4, 6, 29]. This arrangement allows overcoming a kinetic delay caused by the energetic effort to bend the DNA [29]. The initial state of the SMD simulation allows the precise determination of the length of the DNA that is bound to the protein to be 22 bp. This value agrees quite nicely with the data from the literature where the effective binding length in such a complex was determined experimentally to be 26.8 bp [4], and estimated from the structural model to be 24 bp [29], respectively. In the SMD simulation on DNA with a specific sequence

Fig. 6 Visualisation of the supposed structural formation of the TmHU/DNA complex. The condensation starts with a primary TmHU binding until a shortening of around 0.77 μm is reached. Henceforward, the final complex builds up in higher levels of structural organisation. The total reduction in length compared to the extension of the bare DNA reaches around 1 μm, which corresponds to about 70% of the initial DNA length
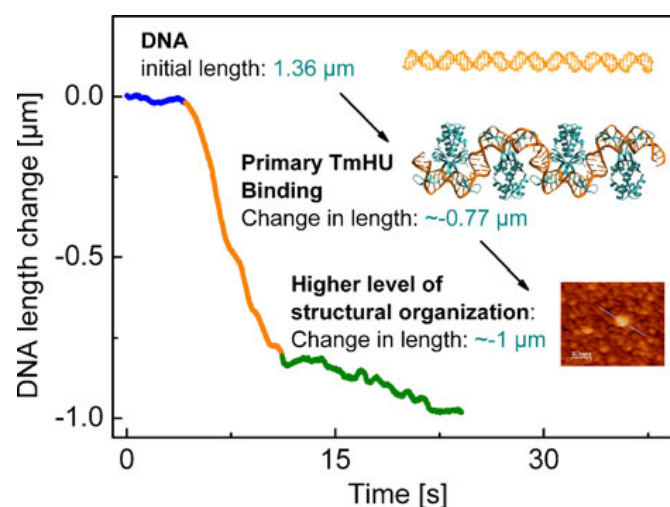
we observe that a one-sided unbinding of DNA and protein causes a lengthening of the end-to-end distance of the DNA of at least 2 nm. With this finding it is possible to assign the experimentally observed disruption events of 2–3 nm from recent experiments [30]. Due to the high forces the unbinding process during the simulation is a combination of an unwinding of the DNA tails and a detaching from the protein. The observed reverse order of unwinding and detaching for pulling in the $+x$ and $-x$ directions is most likely a consequence of the initial setup and conditions together with the thermal/stochastic fluctuations resulting in the asymmetric force profiles in Fig. 5. In the simulation forces of up to 500 pN are reached, which is one order of magnitude higher than encountered under experimental conditions. Concerning this matter one has to keep in mind that, in contrast to the latter one, the simulation proceeds with a pulling rate of 0.5 m/s far out of equilibrium. This causes the observed high forces as it is known from the literature that the unfolding force depends linearly on the logarithm of the pulling speed [36–38]. A similar problem is, for example, faced in the unfolding process of titin sub-domains [39, 40], and in dynamic force spectroscopy studies of DNA [35, 36]. Because of those large forces in our simulation, the DNA parts, which are not attached to the protein, start unwinding before the connections to the protein break. This is not expected to happen in the optical tweezers experiment due to the much smaller forces involved. We also would like to note that the flexibility of a DNA strand exhibits a dependence on the sequence [41, 42]. Although no sequence specificity of TmHU binding is detectable experimentally [10], it is conceivable that changing the DNA sequence might influence the unbinding process.

With the knowledge of the effective binding length found in the SMD calculations (22 bp) and the length change due to the disruption of one protein of at least 4 nm, one can now go back to the model for a complex with more than one TmHU protein binding to DNA and calculate the expected TmHU-induced shortening ΔL for a saturated double-stranded DNA (initial length, 4,000 bp $\cong$ 1.36 μm):

$$\Delta L = 4{,}000 \text{ bp}/22 \text{ bp} \times 4 \text{ nm} \approx 0.73 \text{ μm}.$$

The value matches within the experimental error with our result at 2 pN and a concentration of 100 μg/ml, where the end-to-end distance is decreased by about 0.77 μm. This is remarkable given the different regimes probed by the simulations and measurements.

However, together with the second regime, a total shortening of approximately 1 μm has been observed in our experiments. The simple binding model of antiparallel-arranged proteins is not sufficient to explain this finding. Our experimental results imply that in the first regime the DNA is condensed in a linear manner as proposed in the model, corresponding to a primary level of DNA compaction. The additional shortening observed in the second regime suggests that this primary structure of the TmHU/DNA complex is further compacted in a higher level of organisation (Fig. 6). Large rupture events obtained when stretching the TmHU/DNA complex give only indirect indications concerning the existence of such clusters [30]. This is also consistent with the structure observed by AFM measurements at 100 μg/ml (Fig. 4), showing a compacted, globular shape. Elongated filaments as expected if TmHU proteins were bound like beads-on-a-string are not found in this regime. It is supposed that this higher level of organisation depends strongly on the TmHU concentration. For concentrations smaller than 100 μg/ml a lesser reduction in length is observed and the division into two regimes is no longer possible (Fig. 3). The elongated filaments found by AFM measurements at 20 μg/ml support this assumption. Though the system is in this case constricted to two dimensions and short DNA is used (250 bp), the result is in qualitative agreement with the optical tweezers measurement. These results on the concentration dependence are consistent with the observation of Salomo et al. that large rupture events occur only after incubation with a high TmHU concentration of at least 100 μg/ml [30]. Up to now there are no concrete model representations concerning higher-order organisation of DNA by HU proteins and especially by TmHU. It is presumed that the HU/DNA complexes in the case of the HU protein from *E. coli* are not stable and are of a dynamic nature [43]. Therefore, a similar behaviour in the case of the homologous TmHU protein is very likely. This might be related to the observed slow formation of the second phase of condensation.

The measurements at different force levels show a distinct influence on the condensation of the DNA. At a force of 10 pN the reduction in length of the DNA is only ~0.5 μm. Furthermore, the second regime is not observed, implying that the higher level of structural organisation observed at lower forces and in the AFM images can no longer be formed. Astonishingly, compared with the condensation reaction without force clamp that came to a halt at 25–30 pN [29], a shortening against a pre-stretching of up to 40 pN is observed. The mechanism for protein binding differs for conditions with and without force clamp since in the case of increasing force the DNA is already covered with proteins when 25 pN are reached.

5 Conclusions

The condensation of double-stranded DNA by TmHU under constant force is investigated by usage of an optical tweezers-assisted force clamp. At forces of up to 5 pN, the end-to-end distance is reduced from about 1.36 to ~0.36 μm corresponding to 30% of its initial length on a time scale of seconds. This length-reducing reaction can be split into two regimes. Joining data from our SMD simulation and information from the literature, the first regime is assigned to a primary binding of TmHU. The second regime is therefore suggested to correspond to the formation of a higher level of organisation whose existence was already presumed in the literature [30]. In addition, the results from the SMD simulation precisely describe the process of an unbinding forced by stretching the DNA. This yields a detailed

molecular explanation for the rupture events which were recently observed experimentally [30].

The final DNA length of ∼0.36 μm is comparable to the mean end-to-end distance of ∼0.33 μm of a free DNA molecule in the same buffer solution (persistence length, ∼40 nm). Hence, the effect of TmHU binding to DNA is much stronger compared to that of *E. coli* HU. In the latter case the DNA duplex is compacted to about 50% of its initial length at a force of 1 pN on a time scale of minutes [7]. This leads to the conclusion that the TmHU protein condensates DNA much faster. Therefore, TmHU features not only a higher affinity to DNA but also a faster on-rate. Furthermore, one has to take the fact into account that no homologs of proteins like IHF or H-NS are found in *T. maritima*, though they are abundant in mesophilic bacteria lie *E. coli*. All these facts together show once more the crucial role of TmHU in the nucleoid organisation and in maintaining genomic DNA integrity in extreme environments at 80°C [4, 5, 10].

References

1. Dame, R.T.: The role of nucleoid-associated proteins in the organization and compaction of bacterial chromatin. Mol. Microbiol. **56**(4), 858–870 (2005)
2. Nelson, K.E., Clayton, R.A., Gill, S.R., Gwinn, M.L., Dodson, R.J., Haft, D.H., Hickey, E.K., Peterson, J.D., Nelson, W.C., Ketchum, K.A., McDonald, L., Utterback, T.R., Malek, J.A., Linher, K.D., Garrett, M.M., Stewart, A.M., Cotton, M.D., Pratt, M.S., Phillips, C.A., Richardson, D., Heidelberg, J., Sutton, G.G., Fleischmann, R.D., Eisen, J.A., White, O., Salzberg, S.L., Smith, H.O., Venter, J.C., Fraser, C.M.: Evidence for lateral gene transfer between Archaea and Bacteria from genome sequence of *Thermotoga maritima*. Nature **399**, 323–329 (1999)
3. Huber, R., Langworthy, T.A., König, H., Thomm, M., Woese, C.R., Sleytr, W., Stetter, K.O.: *Thermotoga maritima* sp. nov. represents a new genus of unique extremely thermophilic eubacteria growing up to 90°. Arch. Microbiol. **144**, 324–333 (1986)
4. Mukherjee, A., Sokunbi, A.O., Grove, A.: DNA protection by histone-like protein HU from the hyper-thermophilic eubacterium *Thermotoga maritima*. Nucleic Acids Res. **36**, 3956–3968 (2008)
5. Esser, D., Rudolph, R., Jaenicke, R., Böhm, G.: The HU protein from *Thermotoga maritima*: recombinant expression, purification and physicochemical characterization of an extremely hyperthermophilic DNA-binding protein. J. Mol. Biol. **291**, 1135–1146 (1999)
6. Swinger, K.S., Lemberg, K.M., Zhang, Y., Rice, P.A.: Flexible DNA bending in HU–DNA cocrystal structures. EMBO J. **22**, 3749–3760 (2003)
7. van Noort, J., Verbrugge, S., Goosen, N., Dekker, C., Dame, R.T.: Dual architectural roles of HU: formation of flexible hinges and rigid filaments. Proc. Natl. Acad. Sci. USA **101**, 6969–6974 (2004)
8. Dame, R.T., Goosen, N.: HU: promoting or counteracting DNA compaction? FEBS Lett. **529**, 151–156 (2002)
9. Luijsterburg, M.S., Noom, C.N., Wuite, G.J.L., Dame, R.T.: The architectural role of nucleoid-associated proteins in the organization of bacterial chromatin: a molecular perspective. J. Struct. Biol. **156**, 262–272 (2006)
10. Grove, A., Lim, L.: High-affinity DNA binding of HU protein from the hyperthermophile *Thermotoga maritima*. J. Mol. Biol. **311**, 491–502 (2001)
11. Christodoulou, E., Rypniewski, W.R., Vorgias, C.R.: High-resolution X-ray structure of the DNA-binding protein HU from the hyperthermophilic *Thermotoga maritima* and the determinants of its thermostability. Extremophiles **7**, 111–122 (2002)
12. Ashkin, A.: Acceleration and trapping of particles by radiation pressure. Phys. Rev. Lett. **24**, 156–159 (1970)
13. Marko, J.F., Siggia, E.D.: Stretching DNA. Macromolecules **28**, 8759–8770 (1995)

14. Smith, S.B., Cui, Y., Bustamante, C.: Overstretching B-DNA: the elastic response of individual double-stranded and single-stranded DNA molecules. Science **271**, 795–799 (1996)

15. Salomo, M., Kegler, K., Gutsche, C., Struhalla, M., Reinmuth, J., Skokow, W., Hahn, U., Kremer, F.: The elastic properties of single double-stranded DNA chains of different lengths as measured with optical tweezers. Colloid Polym. Sci. **284**, 1325–1331 (2006)

16. Baumann, C.G., Bloomfield, V.A., Smith, S.B., Bustamante, C., Wang, M.D., Block, S.M.: Stretching of single collapsed DNA molecules. Biophys. J. **78**, 1965–1978 (2000)

17. Tolic-Nørrelykke, S.F., Rasmussen, M.B., Pavone, F., Berg-Sørensen, K., Oddershede, L.B.: Stepwise bending of DNA by a single TATA-box binding protein. Biophys. J. **90**, 3694–3703 (2006)

18. Sischka, A., Toensing, K., Eckel, R., Wilking, S.D., Sewald, N., Ros, R., Anselmetti, D.: Molecular mechanisms and kinetics between DNA and DNA binding ligands. Biophys. J. **88**, 404–411 (2005)

19. Salomo, M., Keyser, U.F., Struhalla, M., Kremer, F.: Optical tweezers to study single protein A/immunoglobulin G interactions at varying conditions. Eur. Biophys. J. **37**, 927–934 (2008)

20. Li, P.T., Collin, D., Smith, S.B., Bustamante, C., Tinoco, I. Jr.: Probing the mechanical folding kinetics of TAR RNA by hopping, force-jump, and force-ramp methods. Biophys. J. **90**, 250–260 (2006)

21. Wen, J.D., Manosas, M., Li, P.T.X., Smith, S.B., Bustamante, C., Ritort, F., Tinoco, I. Jr.: Force unfolding kinetics of RNA using optical tweezers. I. Effects of experimental variables on measured results. Biophys. J. **92**, 2996–3009 (2007)

22. Block, S.M., Goldstein, L.S., Schnapp, B.J.: Bead movement by single kinesin molecules studied with optical tweezers. Nature **348**, 348–352 (1990)

23. Finer, J.T., Simmons, R.M., Spudich, J.A.: Single myosin molecule mechanics: piconewton forces and nanometre steps. Nature **368**, 113–119 (1994)

24. Wen, J.D., Lancaster, L., Hodges, C., Zeri, A.C., Yoshimura, S.H., Noller, H.F., Bustamante, C., Tinoco, I.: Following translation by single ribosomes one codon at a time. Nature **452**, 598–603 (2008)

25. Bennink, M.L., Leuba, S.H., Leno, G.H., Zlatanova, J., de Grooth, B.G., Greve, J.: Unfolding individual nucleosomes by stretching single chromatin fibers with optical tweezers. Nat. Struct. Biol. **8**, 606–610 (2001)

26. Pope, L.H., Bennink, M.L., van Leijenhorst-Groener, K.A., Nikova, D., Greve, J., Marko, J.F.: Single chromatin fiber stretching reveals physically distinct populations of disassembly events. Biophys. J. **88**, 3572–3583 (2005)

27. Brower-Toland, B.D., Smith, C.L., Yeh, R.C., Lis, J.T., Peterson, C.L., Wang, M.D.: Mechanical disruption of individual nucleosomes reveals a reversible multistage release of DNA. Proc. Natl. Acad. Sci. USA **99**, 1960–1965 (2002)

28. Dame, R.T., Noom, M.C., Wuite, G.J.L.: Bacterial chromatin organization by H-NS protein unravelled using dual DNA manipulation. Nature **444**, 387–390 (2006)

29. Salomo, M., Kroy, K., Kegler, K., Gutsche, C., Struhalla, M., Reinmuth, J.,Skokov, W., Immisch, C., Hahn, U., Kremer, F.: Binding of TmHU to single dsDNA as observed by optical tweezers. J. Mol. Biol. **359**, 769–776 (2006)

30. Salomo, M., Keyser, U.F., Kegler, K., Gutsche, C., Struhalla, M., Immisch, C., Hahn, U., Kremer, F.: Kinetics of TmHU binding to DNA as observed by optical tweezers. Microsc. Res. Tech. **70**, 938–943 (2007)

31. Otto, O., Gutsche, C., Kremer, F., Keyser, U.: Optical tweezers with 2.5 kHz bandwidth video detection for single-colloid electrophoresis. Rev. Sci. Instrum. **79**, 023710 (2008)

32. Christodoulou, E., Vorgias, C.E.: Cloning, overproduction, purification and crystallization of the DNA binding protein HU from the hyperthermophilic eubacterium *Thermotoga maritima*. Acta Crystallogr. D **54**, 1043–1045 (1998)

33. Phillips, J.C., Braun, R., Wang, W., Gumbart, J., Tajkhorshid, E., Villa, E., Chipot, C., Skeel, R.D., Kale, L., Schulten, K.: Scalable molecular dynamics with NAMD. J. Comput. Chem. **26**, 1781–1802 (2005)

34. MacKerell, A.D., Foloppe, N.: All-atom empirical force field for nucleic acids: I. Parameter optimization based on small molecule and condensed phase macromolecular target data. J. Comput. Chem. **21**, 86–104 (2000)

35. Morfill, J., Kühner, F., Blank, K., Lugmaier, R.A., Sedlmair, J., Gaub, H.E.: B-S transition in short oligonucleotides. Biophys. J. **60**, 2400–2409 (2007)

36. Strunz, T., Orosylan, K., Schäfer, R., Güntherodt, H.J.: Dynamic force spectroscopy of single DNA molecules. Proc. Natl. Acad. Sci. USA **96**, 11277–11282 (1999)

37. Evans, E., Ritchie, K.: Strength of a weak bond connecting flexible polymer chains. Biophys. J. **76**, 2439–2447 (1999)

38. Lee, E.H., Hsin, J., Sotomayor, M., Cornellas, G., Schulten, K.: Discovery through the computational microscope. Structure **17**, 1295–1306 (2009)

39. Lu, H., Isralewitz, B., Krammer, A., Vogel, V., Schulten, K.: Unfolding of titin immunoglobulin domains by steered molecular dynamics simulation. Biophys. J. **75**, 662–671 (1998)

40. Gräter, F., Shen, J., Jiang, H., Gautel, M., Grubmüller, H.: Mechanically induced titin kinase activation studied by force-probe molecular dynamics simulations. Biophys. J. **88**, 790–804 (2005)

41. Lankaš, F., Šponer, J., Hobza, P., Langowski, J.: Sequence-dependent elastic properties of DNA. J. Mol. Biol. **299**(3), 695–709 (2000)

42. Scipioni, A., Anselmi, C., Zuccheri, G., Samori, B., De Santis, P.: Sequence-dependent DNA curvature and flexibility from scanning force microscopy images. Biophys. J. **83**(5), 2408–2418 (2002)

43. Broyles, S.S., Pettijohn, D.E.: Interaction of the *Escherichia coli* HU protein with DNA. J. Mol. Biol. **187**, 47–60 (1986)

Curriculum Vitae

Personal Data

Name	*Carsten Olbrich*
Birthday	*14-Feb-1982*
Place of birth	*Burgstädt, Germany*
Email	*c.olbrich@jacobs-university.de*
Nationality	*German*

Scientific Career

10-2006 – 09-2011	PhD thesis in the group of Prof. Dr. Ulrich Kleinekathöfer, Jacobs University Bremen
	Title of the PhD thesis: *Time-dependent atomistic view on the electronic relaxation in light-harvesting systems*
05-2006 – 10-2006	Research assistant in the group of Prof. Dr. Gotthard Seifert, Dresden University of Technology
	Topic: *Modeling and simulation of deranged magnetic surfaces*
10-2001 – 09-2006	Bachelor and Master studies in *Computational Science*, Chemnitz University of Technology
	Title of the Master thesis: *Simulation of transport properties in quasi two-dimensional electron systems with impurities*
	Title of the Bachelor thesis: *Simulation of molecular aggregates on structured surfaces using the Ising model*

List of Publications

Publications

[1] C. Loppacher, U. Zerweck, L. Eng, S. Gemming, G. Seifert, C. Olbrich, K. Morawetz and M. Schreiber. *Adsorption of PTCDA on a partially KBr covered Ag(111) substrate*. Nanotechnology **17** (2006) 1568.

[2] S. Gemming, R. Luschtinetz, I. Chaplygin, G. Seifert, C. Loppacher, L. M. Eng, T. Kunze and C. Olbrich. *Polymorphism in ferroic functional elements*. The European Physical Journal - Special Topics **149** (2007) 145.

[3] K. Morawetz, C. Olbrich and S. Gemming. *Reduction of surface coverage of finite systems due to geometrical steps*. Eur. Phys. J. B **62** (2008) 311.

[4] C. Olbrich and U. Kleinekathöfer. *Time-dependent atomistic view on the electronic relaxation in light-harvesting system II*. The Journal of Physical Chemistry B **114** (2010) 12427.

[5] C. Olbrich, J. Liebers and U. Kleinekathöfer. *Modeling of light-harvesting in purple bacteria using a time-dependent hamiltonian approach*. physica status solidi (b) **248** (2011) 393.

[6] C. Olbrich, J. Strümpfer, K. Schulten and U. Kleinekathöfer. *Quest for spatially correlated fluctuations in the FMO light-harvesting complex*. The Journal of Physical Chemistry B **115** (2011) 758.

[7] C. Wagner, C. Olbrich, H. Brutzer, M. Salomo, U. Kleinekathöfer, U. Keyser and F. Kremer. *DNA condensation by TmHU studied by optical tweezers, AFM and molecular dynamics simulations*. Journal of Biological Physics **37** (2011) 117.

[8] C. Olbrich, T. L. C. Jansen, J. Liebers, M. Aghtar, J. Strümpfer, K. Schulten, J. Knoester and U. Kleinekathöfer. *From atomistic modeling to excitation transfer and two-dimensional spectra of the fmo light-harvesting complex*. The Journal of Physical Chemistry B **115** (2011) 8609.

[9] C. Olbrich, J. Strümpfer, K. Schulten and U. Kleinekathöfer. *Theory and simulation of the environmental effects on FMO electronic transitions*. The Journal of Physical Chemistry Letters **2** (2011) 1771.

Poster Presentations

[1] C. Olbrich and U. Kleinekathöfer. *Stretching of a DNA/HU-protein complex in SMD simulations*. DPG Spring Meeting, Regensburg (2007).

[2] C. Olbrich and U. Kleinekathöfer. *Stretching of a DNA/HU-protein complex in SMD simulations*. DPG Spring Meeting, Berlin (2008).

[3] C. Olbrich and U. Kleinekathöfer. *Stretching of DNA/HU-protein complexes in SMD simulations*. DPG Spring Meeting, Dresden (2009).

[4] C. Olbrich, M. Schreiber and U. Kleinekathöfer. *Calculation of optical properties from molecular-dynamics simulations of light-harvesting systems*. DPG Spring Meeting, Dresden (2009).

[5] C. . Olbrich and U. Kleinekathöfer. *Calculation of optical properties from molecular-dynamics simulations of light-harvesting systems*. Light-Harvesting Processes, Banz (2009).

[6] C. Olbrich, M. Schreiber and U. Kleinekathöfer. *Calculation of optical properties from molecular-dynamics simulations of light-harvesting systems*. WEH Summer School: Quantum and Classical Simulation of Biological Systems and their Interaction with Technical Material, Bremen (2009).

[7] C. Olbrich, M. Schreiber and U. Kleinekathöfer. *Calculation of optical properties from molecular-dynamics simulations of light-harvesting systems*. Symposium für Theoretische Chemie, Neuss am Rhein (2009).

[8] C. Olbrich and U. Kleinekathöfer. *Stretching of DNA/HU-protein complexes in SMD simulations*. Expanding the frontiers of molecular dynamics simulations in biology, Barcelona, Spain (2009).

[9] C. Olbrich, J. Liebers and U. Kleinekathöfer. *Optical properties of light-harvesting systems determined by molecular-dynamics simulations*. Biophysical Society Meeting, San Francisco (CA,USA) (2010).

[10] C. Olbrich and U. Kleinekathöfer. *Stretching of DNA/TmHU-protein complexes in smd simulations*. DPG Spring Meeting, Regensburg (2010).

[11] C. Olbrich, J. Liebers, M. Schreiber and U. Kleinekathöfer. *Optical properties of light-harvesting systems determined by molecular-dynamics simulations*. DPG Spring Meeting, Regensburg (2010).

[12] C. Olbrich, J. Liebers and U. Kleinekathöfer. *Simulation of spectra and exciton transfer in light-harvesting systems*. European Conference on Nonlinear Optical Spectroscopy, Bremen (2010).

[13] C. Olbrich, J. Strümpfer, K. Schulten and U. Kleinekathöfer. *Quest for spatially correlated fluctuations in light-harvesting systems*. DPG Spring Meeting, Dresden (2011).

Oral Presentations

[1] C. Olbrich and U. Kleinekathöfer. *MD-simulations of the HU/DNA-complexes*. Seminar talk, Leipzig (2008).

[2] C. Olbrich and U. Kleinekathöfer. *MD-simulations of the HU/DNA-complexes*. Workshop on Computer Simulation and Theory of Macromolecules, Hünfeld (2009).

[3] C. Olbrich and U. Kleinekathöfer. *Time-dependent atomistic view on the electronic relaxation in light-harvesting systems*. Seminar talk, Freiburg (2010).

[4] C. Olbrich and U. Kleinekathöfer. *Time-dependent atomistic view on the electronic relaxation in light-harvesting systems*. NanoFun Retreat, Clausthal-Zellerfeld (2011).

[5] C. Olbrich, T. L. C. Jansen, J. Liebers, M. Aghtar, J. Strümpfer, K. Schulten, J. Knoester and U. Kleinekathöfer. *Atomistic modeling of LH complexes*. DPG Spring Meeting, Dresden (2011).